

# Seismic Response of Base Isolated Buildings Considering Pounding to Moat Walls

by  
Armin Masroor and Gilberto Mosqueda

Technical Report MCEER-13-0003

February 26, 2013

## NOTICE

This report was prepared by the University at Buffalo, State University of New York as a result of research supported primarily by the George E. Brown, Jr. Network for Earthquake Engineering Simulation (NEES) Program of the National Science Foundation, NEESR award numbers CMMI-0724208 and CMMI-1113275. Neither MCEER, associates of MCEER, its sponsors, the University at Buffalo, State University of New York, nor any person acting on their behalf:

- a. makes any warranty, express or implied, with respect to the use of any information, apparatus, method, or process disclosed in this report or that such use may not infringe upon privately owned rights; or
- b. assumes any liabilities of whatsoever kind with respect to the use of, or the damage resulting from the use of, any information, apparatus, method, or process disclosed in this report.

Any opinions, findings, and conclusions or recommendations expressed in this publication are those of the author(s) and do not necessarily reflect the views of MCEER, the National Science Foundation, or other sponsors.

## Seismic Response of Base Isolated Buildings Considering Pounding to Moat Walls

by

Armin Masroor<sup>1</sup> and Gilberto Mosqueda<sup>2</sup>

Publication Date: February 26, 2013

Submittal Date: December 19, 2012

Technical Report MCEER-13-0003

NSF Grant Number CMMI-1113275

- 1 Graduate Student, Department of Civil, Structural and Environmental Engineering, University of Buffalo, State University of New York
- 2 Associate Professor, University of California at San Diego; Former Associate Professor, Department of Civil, Structural and Environmental Engineering, University of Buffalo, State University of New York

MCEER

University at Buffalo, State University of New York

133A Ketter Hall, Buffalo, NY 14260

Phone: (716) 645-3391; Fax (716) 645-3399

E-mail: [mceer@buffalo.edu](mailto:mceer@buffalo.edu); Website: <http://mceer.buffalo.edu>

---



## Preface

MCEER is a national center of excellence dedicated to the discovery and development of new knowledge, tools and technologies that equip communities to become more disaster resilient in the face of earthquakes and other extreme events. MCEER accomplishes this through a system of multidisciplinary, multi-hazard research, in tandem with complimentary education and outreach initiatives.

Headquartered at the University at Buffalo, The State University of New York, MCEER was originally established by the National Science Foundation in 1986, as the first National Center for Earthquake Engineering Research (NCEER). In 1998, it became known as the Multidisciplinary Center for Earthquake Engineering Research (MCEER), from which the current name, MCEER, evolved.

Comprising a consortium of researchers and industry partners from numerous disciplines and institutions throughout the United States, MCEER's mission has expanded from its original focus on earthquake engineering to one which addresses the technical and socio-economic impacts of a variety of hazards, both natural and man-made, on critical infrastructure, facilities, and society.

The Center derives support from several Federal agencies, including the National Science Foundation, Federal Highway Administration, National Institute of Standards and Technology, Department of Homeland Security / Federal Emergency Management Agency, and the State of New York, other state governments, academic institutions, foreign governments and private industry.

The report is a product of the "NEESR-SG: TIPS - Tools to Facilitate Widespread Use of Isolation and Protective Systems, a NEES/E-Defense Collaboration," funded by the National Science Foundation through the George E. Brown, Jr. Network for Earthquake Engineering Simulation (NEES) program. The project team includes the University of Nevada, Reno as the lead institution, with subawards to the University of California, Berkeley; University of Wisconsin, Green Bay; and the University at Buffalo, State University of New York.

The NEES TIPS project is a collaborative effort between researchers in the U.S and Japan to create and promote tools that will facilitate adoption of isolation and protective systems. The vision is that in the future, losses and disruptive societal impacts associated with earthquakes will be substantially reduced due to the widespread use of isolation systems, which provide the capability to control both structural and nonstructural damage by simultaneously reducing accelerations and displacements. Isolation systems will become a realistic option for any building regardless of size, occupancy, and importance, based on the following outcomes:

Knowledge gaps regarding the behavior of isolation devices and overall system performance are addressed; based on innovative tests using state-of-the-art facilities and improved modeling capabilities. Practitioners and stakeholders will have improved access to

information through the creation of a worldwide database of information about isolation systems. Tested and validated strategies will allow for substantially reduced costs associated with the design and construction of an isolation system.

Rational analysis tools will be able to convey the long term benefits of isolation systems in terms of performance, life cycle costs, and sustainability. Seismic isolation technology will be promoted by engineering and design firms throughout the United States. A national audience will be educated regarding the societal impacts of earthquakes and the potential benefits of seismic isolation and protective systems.

*This study investigates the pounding phenomenon in base isolated buildings by conducting shake table pounding experiments, developing analytical models for impact to moat walls, and evaluating the adequacy of code specifications for the gap distance of moat walls. The experiments indicated that the contact forces generated during pounding can induce yielding in the superstructure and amplify the response acceleration at all stories of the building. The response amplification and damage depends on the gap distance, moat wall properties, and impact velocity. A detailed finite element model of the test setup was developed in OpenSees and an analytical study on the dynamic behavior of the moat walls resulted in proposing a new impact element. The numerical simulation showed good agreement with the experimental results. Finally, a series of collapse studies using the FEMA P695 methodology was conducted to determine the collapse probability of the base isolated models and the effect of moat wall gap distance on the probability of collapse. These studies verified that pounding to moat walls at the gap distance required by ASCE7-05 results in an acceptable probability of collapse for flexible and ductile moment frame models. However, the braced frame showed a notable drop in collapse margin ratio because of pounding to the moat wall at the required gap distance and requires increasing the gap distance by 17%.to achieve an acceptable collapse probability.*

## ABSTRACT

Seismic isolation offers a simple and direct opportunity to control or even eliminate damage to structures subjected to ground shaking by simultaneously reducing deformations and acceleration demands. A base isolation system decouples the superstructure from the ground resulting in elongation of fundamental period of the structure and reducing the accelerations transferred to superstructure during ground shaking. However, increasing the fundamental period of the structure is mostly accompanied by increased displacement demands. In base isolated structures, this large displacement is concentrated at base level where seismic isolation devices are installed and designed to handle these large deformations without damage. A typical base isolated basement design requires a space in which the building is free to move sideways without hitting the surrounding structure. This space is commonly referred to as the "moat".

Structural design codes such as ASCE 7-05 that regulate the design of buildings incorporating seismic base isolation systems require the minimum moat wall clearance distance equal to the maximum displacement at the base of the structure under the Maximum Considered Earthquake (MCE), although the superstructure is designed for design basis earthquake (DBE) level. Despite the cautious regulation for moat wall gap distance, pounding of base isolated buildings to moat walls has been reported in previous earthquakes. In conventional structures, the pounding problem between adjacent structures of buildings and highway bridges has been a major cause of seismic damage, even collapse, during earthquakes in the past several decades. Current design specifications may not adequately account for the large forces generated during impact in base isolated buildings. This study investigates the pounding phenomenon in base isolated buildings from both experimental and analytical perspectives by conducting shake table pounding experiments, developing effective models for impact to moat walls and evaluating the adequacy of code specifications for the gap distance of moat walls.

A series of prototype base isolated moment and braced buildings designed by professional engineers for the purpose of this project is presented and one of the models was selected for a quarter scale shake table test with moat walls. The pounding experiments indicate that the contact forces generated during pounding can induce yielding in the superstructure and amplify

the response acceleration at all stories of the building. The response amplification and damage depends on the gap distance, moat wall properties, and impact velocity.

A detailed finite element model of the test setup is developed in OpenSees. An analytical study on the dynamic behavior of the moat walls resulted in proposing a new impact element. Numerical simulation using the proposed impact element compares well with experimental results.

A series of collapse studies using the Methodology in FEMA P695 was conducted for both prototype models at various gap distances. The collapse probability of base isolated models used in this study and the effect of moat wall gap distance on the probability of collapse for base isolated structures is investigated. These studies verify that pounding to moat walls at the required gap distance by ASCE7-05 result in acceptable probability of collapse for the flexible and ductile moment frame models examined. However, the braced frame shows a notable drop in collapse margin ratio because of pounding to moat wall at the required gap distance and requires increasing the gap distance by 17%. to have an acceptable collapse probability.

## **ACKNOWLEDGEMENTS**

This work is part of the NEES TIPS project supported by the National Science Foundation (NSF) under Grants No. CMMI-0724208 and CMMI-1113275. The authors are grateful to Drs. Keri Ryan (PI), Stephen Mahin, (CO-PI) for their input.



# TABLE OF CONTENTS

Section	Title	Page
<b>1</b>	<b>INTRODUCTION.....</b>	<b>1</b>
1.1	Problem Description .....	1
1.2	Objectives and Scope of Research .....	2
1.3	Outline of Report .....	3
<b>2</b>	<b>STRUCTURAL POUNDING IN BASE ISOLATED BUILDINGS .....</b>	<b>7</b>
2.1	Base Isolated Structure .....	7
2.1.1	Design of Base Isolated Structure .....	8
2.1.2	Dynamic Analysis Procedure .....	12
2.2	Structural Pounding .....	15
2.2.1	Analytical and Numerical Studies .....	17
2.2.2	Experimental Studies .....	23
2.3	Pounding of Base Isolated Building to a Moat Wall .....	27
<b>3</b>	<b>PROTOTYPE BUILDING MODEL .....</b>	<b>31</b>
3.1	Introduction .....	31
3.2	Design Assumptions .....	31
3.3	Ground Motion .....	38
<b>4</b>	<b>DESCRIPTION OF SHAKE TABLE TESTING PROGRAM.....</b>	<b>43</b>
4.1	Introduction .....	43
4.2	Description of Model Structure .....	44
4.3	Description of the Moat Wall .....	50
4.4	Instrumentation .....	51
4.5	Earthquake Records .....	57
4.6	System Identification .....	60
4.7	Test Schedule .....	63
<b>5</b>	<b>SHAKE TABLE TEST RESULTS .....</b>	<b>69</b>
5.1	Introduction .....	69
5.2	Results for Fixed Base Structure .....	69
5.3	Results for Isolated Base Structure without Moat Wall .....	75
5.4	Results for Isolated Base Structure with Moat Wall .....	87
5.4.1	Test Results for Base Isolated IMRF with 2 in. Concrete Moat Wall at 6 in. Gap Distance .....	87
5.4.2	Test Results for Base Isolated IMRF with 6 in. Concrete Moat Wall at 4 in. Gap Distance .....	90
5.4.3	Test Results for Base Isolated IMRF with Welded Steel Moat Wall at 4 in. Gap Distance .....	93
5.5	Effects of Wall Stiffness and Gap Distance .....	97
5.6	Shake Table Performance .....	103

## TABLE OF CONTENTS (CONT'D)

Section	Title	Page
5.6.1	Comparison of Acceleration Time Histories .....	106
5.6.2	Cumulative Relative Root Square Error .....	106
5.6.3	Elastic Response Spectra .....	107
5.6.4	Shake Table Actuator Force.....	108
<b>6</b>	<b>ANALYTICAL PREDICTION OF RESPONSE .....</b>	<b>111</b>
6.1	Introduction.....	111
6.2	Analytical Modeling of Structural Impact .....	112
6.2.1	Classical Theory of Impact .....	112
6.2.2	Local Deformation Phase Produced by Impact .....	113
6.2.3	Vibration Aspect of Impact.....	115
6.3	Moat Wall Impact Model.....	116
6.3.1	Uniform Moat Wall.....	116
6.3.2	Non-uniform Moat Wall .....	122
6.3.3	Proposed Impact Element .....	123
6.3.4	Concrete Moat Wall Parameters .....	125
6.3.5	Steel Moat Wall Parameters.....	128
6.4	Description of Superstructure Analytical Model .....	129
6.4.1	Concentrated Plastic Hinges .....	129
6.4.2	Panel Zones .....	131
6.4.3	Structural Damping.....	132
6.4.4	Transient Integration Scheme .....	132
6.5	Numerical Simulation Results .....	134
6.5.1	Fixed Base Model .....	134
6.5.2	Base Isolated Model without Moat Wall .....	137
6.5.3	Base Isolated Model with Moat Wall .....	141
6.6	Sensitivity Analysis .....	147
<b>7</b>	<b>POUNDING IN THREE DIMENSIONAL BASE ISOLATED BUILDINGS .....</b>	<b>149</b>
7.1	Introduction.....	149
7.2	3D Moat Wall Model .....	149
7.2.1	Soil Backfill .....	150
7.2.2	Local Impact Element .....	153
7.2.3	Internal Shear Elements .....	153
7.3	Base Isolated IMRF Building .....	161
7.3.1	Plastic Hinges.....	162
7.3.2	Panel Zone Flexibility.....	164
7.3.3	Isolator Model.....	164
7.4	Base Isolated OCBF Building.....	166
7.4.1	Brace Elements .....	166
7.5	Response of IMRF and OCBF Models in MCE Event (2/50 YEAR) .....	167

## TABLE OF CONTENTS (CONT'D)

Section	Title	Page
7.5.1	Detailed Response of OCBF Model under Input Motion GM9 .....	168
7.5.2	Base Isolated IMRF Model .....	174
7.5.3	Base Isolated OCBF Model .....	181
7.5.4	Base Isolated IMRF and OCBF Comparison .....	187
<b>8</b>	<b>COLLAPSE EVALUATION OF SEISMICALLY ISOLATED STRUCTURE CONSIDERING POUNDING TO A MOAT WALL .....</b>	<b>193</b>
8.1	Introduction .....	193
8.2	Background Study and Objectives .....	193
8.3	Scope of the Collapse Evaluation Methodology Proposed by FEMA P695 .....	195
8.4	Approach and Assumptions .....	196
8.4.1	Ground Motion Set .....	197
8.4.2	MCE Spectrum .....	201
8.4.3	Period-based Ductility .....	203
8.4.4	Total System Collapse Uncertainty .....	204
8.4.4.1	Record-to-Record Uncertainty (RTR) .....	205
8.4.4.2	Design Requirements Uncertainty (DR) .....	205
8.4.4.3	Test Data Uncertainty (TD) .....	205
8.4.4.4	Modeling Uncertainty (MDL) .....	206
8.4.5.	Dimensional Analysis .....	206
8.4.6	Collapse Criteria .....	206
8.5	Collapse Assessment .....	207
8.5.1	IMRF Model .....	207
8.5.1.1	Static Pushover Analysis .....	207
8.5.1.2	Collapse Assessment Parameters .....	209
8.5.1.3	Nonlinear Dynamic Analysis .....	210
8.5.2	OCBF Model .....	214
8.5.2.1	Static Pushover Analysis .....	214
8.5.2.2	Collapse Assessment Parameters .....	216
8.5.2.3	Nonlinear Dynamic Analysis .....	216
8.6	Base Isolated IMRF and OCBF Models Comparison .....	221
<b>9</b>	<b>SUMMARY AND CONCLUSION .....</b>	<b>223</b>
<b>10</b>	<b>REFERENCES .....</b>	<b>229</b>



## LIST OF ILLUSTRATIONS

<b>Figure</b>	<b>Title</b>	<b>Page</b>
2-1	Principals of seismic isolation (Constantinou et al. 2007).....	7
2-2	Different types of seismic isolation system (Constantinou et al. 2007) .....	8
2-3	Acceleration and displacement response spectra.....	14
2-4	Typical moat wall configuration in base isolated building (Arnold 2009).....	15
2-5	(a) Barrier rail damage during the 1994 Northridge earthquake; (b) Pounding between a six-story building and a two-story building in Golcuk, causing damage to the column of the six-story building (EERI 2000) .....	16
2-6	Pounding of base isolated Christchurch women’s hospital to moat wall (Gavin et al. 2010) .....	17
2-7	Classical theory of impact.....	18
2-8	Linear spring element. ....	19
2-9	Kelvin-Voigt element.....	20
2-10	Modified Kelvin-Voigt element.....	21
2-11	Hertz element.....	22
2-12	Hertz damped element. ....	23
2-13	Sketches of the theoretical and experimental models for modeling pounding between two adjacent structures (Chau et al. 2003). ....	24
2-14	Setup of the impact experiment by Jankowski (2010).....	25
2-15	Photographs of the bridge model: (a) Bridge model; (b) Expansion joint without contact Point; and (c) Expansion joint with contact point (Guo et al. 2009). ....	26
2-16	Test specimen by Sato et al. (2011) (unit: mm): (a) Specimen; (b) Elevation. ....	27
3-1	3D View for moment frame and braced frame models.....	32
3-2	Plan view for SMRF and IMRF model.....	33
3-3	Plan view with typical geometry for RBS (Sayani et al. 2011).....	34
3-4	(a) Plan view of braced buildings; elevation view of (b) Conventional and (c) Isolated buildings.....	35
3-5	MCE and target spectrum for assumed site location .....	38
3-6	Median of 20 ground motions in comparison with the target and MCE spectra .....	41
3-7	The average of SRSS of the 2 components of 20 ground motions in compare with the MCE spectrum .....	41
4-1	The position of the selected internal bay for shake table testing .....	44
4-2	The scaled IMRF used in shake table study.....	46
4-3	Photograph of gravity frame connection.....	48
4-4	Illustration and photograph of shake table test setup.....	48
4-5	Photograph of especial beam to gravity frame connection.....	49
4-6	Photograph of concrete block attached to base level to simulate contact surface.....	49

## LIST OF ILLUSTRATIONS (CONT'D)

<b>Figure</b>	<b>Title</b>	<b>Page</b>
4-7	Illustration of single friction pendulum used in this study (Mosqueda et al. 2004). .....	50
4-8	Photograph of different types of moat wall used in impact purpose. ....	51
4-9	Elevation and top view of accelerometers positions. ....	54
4-10	Elevation and top view of string potentiometer positions. ....	55
4-11	Impact load cells. ....	56
4-12	Location of strain gages on the moment frame. ....	57
4-13	Spectral acceleration for individual scaled motions and target spectra for scaled model. ....	58
4-14	Transfer function amplitude obtained from white noise excitation of fixed base frame. ....	61
4-15	Single friction isolator hysteresis loop under sinusoidal excitation. ....	63
5-1	Story drift ratio for fixed base model under GM15-2 record. ....	70
5-2	Story drift ratio for fixed base model under GM16-2 record. ....	71
5-3	Normalized shear force versus peak story drift ratio for fixed base IMRF. ....	74
5-4	Normalized base shear versus peak roof drift ratio for isolated structure .....	81
5-5	Isolator hysteresis behavior for record GM7-1 .....	82
5-6	Isolator hysteresis behavior for record GM11-1 .....	82
5-7	Isolator hysteresis behavior for record GM15-2 .....	83
5-8	Isolator hysteresis behavior for record GM16-2 .....	83
5-9	Isolator hysteresis behavior for record GM17-1 .....	84
5-10	Isolator hysteresis behavior for record GM17-2 .....	84
5-11	Base level velocity versus displacement for different record at MCE level .....	86
5-12	Isolator hysteresis behavior for record GM17-1 at MCE and 2 in. concrete walls installed at 6 in. gap .....	88
5-13	Base level acceleration for record GM17-1 at MCE and 2 in. concrete walls installed at 6 in. gap .....	88
5-14	Base level velocity versus displacement for record GM17-1 at MCE and 2 in. concrete walls installed at 6 in. gap .....	89
5-15	Impact force for record GM17-1 at MCE and 2 in. concrete walls installed at 6 in. gap .....	89
5-16	Moat wall displacement for record GM17-1 at MCE and 2 in. concrete walls installed at 6 in. gap .....	90
5-17	Isolator hysteresis behavior for record GM17-1 at MCE and 6 in. concrete walls installed at 4 in. gap .....	91
5-18	Base level acceleration for record GM17-1 at MCE and 6 in. concrete walls installed at 4 in. gap .....	91
5-19	Base level velocity versus displacement for record GM17-1 at MCE and 6 in. concrete walls installed at 4 in. gap .....	92
5-20	Impact force for record GM17-1 at MCE and 6 in. concrete walls installed at 4 in. gap .....	92

## LIST OF ILLUSTRATIONS (CONT'D)

Figure	Title	Page
5-21	Moat wall displacement for record GM17-1 at MCE and 6 in. concrete walls installed at 4 in. gap .....	93
5-22	Isolator hysteresis behavior for record GM17-1 at MCE and steel wall with weld installed at 4 in. gap .....	94
5-23	Base level velocity versus displacement for record GM17-1 at MCE and steel wall with weld installed at 4 in. gap .....	95
5-24	Base level acceleration for record GM17-1 at MCE and steel wall with weld installed at 4 in. gap .....	95
5-25	Impact force for record GM17-1 at MCE and steel wall with weld installed at 4 in. gap.....	96
5-26	Moat wall displacement for record GM17-1 at MCE and steel wall with weld installed at 4 in. gap .....	96
5-27	Impact force for different moat wall types: (a) Impact force versus contact time, (b) Impact force versus moat wall relative displacement .....	97
5-28	The effect of different wall types installed at 4 in. gap distance on base level velocity.....	99
5-29	The effect of different wall types on superstructure response .....	100
5-30	Minimum and maximum acceleration and story drift ratio under MCE level of GM17-1 (Erzincan NS) ground motion.....	102
5-31	Minimum and maximum acceleration and story drift ratio under MCE level of Northridge at Sylmar Station (GM11-1) and LA33 (GM7-1) ground motions.....	103
5-32	NEES at buffalo shake table facility used to conduct the experimental program.....	105
5-33	Acceleration time history comparison a) without impact b) with impact.....	106
5-34	Relative root square error of shake table response .....	107
5-35	a) Displacement response spectra, b) Acceleration response spectra .....	108
5-36	Horizontal actuator force .....	109
6-1	Classical theory of impact.....	112
6-2	Contact force-penetration relationship for Hertz and Hertz damped models. ....	115
6-3	Schematic side view of a moat wall and representing beam. ....	118
6-4	Predicted nonlinear moment-rotation relationship for concrete wall. ....	120
6-5	Schematic of the new impact element. ....	124
6-6	Variation of impact element properties with changing of concentrated spring stiffness for 2 in. moat wall.....	126
6-7	Relative wall displacement for 2 in. concrete wall due to impact force. ....	128
6-8	Schematic of numerical simulation of experimental setup (McKenna et al. 2000). ....	129
6-9	Modified Ibarra – Krawinkler deterioration model; (a) Monotonic curve; (b) Basic modes of cyclic deterioration and associated definitions (Lignos et al. 2011).....	130

## LIST OF ILLUSTRATIONS (CONT'D)

Figure	Title	Page
6-10	Analytical model for panel zone (Gupta et al. 1999).....	131
6-11	Sequence of applied ground motion on fixed base model .....	135
6-12	Story drift ratio (SDR) for fixed base model. ....	136
6-13	Absolute acceleration response for fixed base model.....	137
6-14	Base level displacement and acceleration for base isolated model for GM17-1.....	138
6-15	Base level velocity versus displacement under GM17-1.....	139
6-16	Total isolators hysteresis under GM17-1.....	139
6-17	Story drift ratio for base isolated model under GM17-1.....	140
6-18	Absolute acceleration response for base isolated model under GM17-1.....	141
6-19	Impact force for 2 in. concrete wall installed at 6 in. gap distance: (a) Impact force versus contact time, (b) Impact force versus penetration displacement. ....	142
6-20	Impact force for 4 in. concrete wall installed at 6 in. gap distance: (a) Impact force versus contact time, (b) Impact force versus penetration displacement. ....	143
6-21	Impact force for 6 in. concrete wall installed at 4 in. gap distance: (a) Impact force versus contact time, (b) Impact force versus penetration displacement. ....	143
6-22	Impact force for steel wall installed at 4 in. gap distance: (a) Impact force versus contact time, (b) Impact force versus penetration displacement. ....	144
6-23	Impact force for steel wall installed at 6 in. gap distance: (a) Impact force versus contact time, (b) Impact force versus penetration displacement. ....	144
6-24	Base level velocity versus displacement for steel wall installed at 4 in gap distance.....	146
6-25	Superstructure acceleration and story drift ratio.....	146
6-26	Effect of changing impact model parameters on structural response. ....	148
7-1	Moat wall model using beam element .....	150
7-2	Logarithmic-Spiral passive wedge and corresponding force-displacement relationship (Shamsabadi et al. (2007)) .....	151
7-3	Hyperbolic force-displacement parameters (Shamsabadi et al. (2007)).....	152
7-4	Side view of moat wall element.....	153
7-5	Plan view of the prototype model a) Continues moat wall and soil backfill b) District moat wall model .....	154
7-6	Different Contact scenarios between Base Level and Moat Wall .....	156
7-7	Single wall pushover in ABAQUS .....	158
7-8	Comparison of behavior of a cantilever wall in OpenSees and ABQUS .....	158
7-9	Pushing on center of continues moat wall: deformations and rebar stress .....	159
7-10	Pushover of continues moat wall (middle section).....	160
7-11	Pushing continues moat wall (corner section) and rebar stress .....	160
7-12	Pushover of continues moat wall (corner section).....	161
7-13	Cyclic behavior of column section W 14x176.....	163
7-14	Modified Ibarra Krawinkler deterioration model (Lignos et al. 2011).....	164

## LIST OF ILLUSTRATIONS (CONT'D)

Figure	Title	Page
7-15	(a) Isolator model; (b) Lateral force-deformation; (c) Vertical force-deformation in the isolation devices (Sayani et al. 2011) .....	165
7-16	(a) Brace model using two nonlinear frame elements with initial camber; (b) connection geometry and modeling details; and (c) Cyclic axial force–deformation relationship for a representative brace element (Erduran et al. 2011) .....	167
7-17	Impact force in line 1 for OCBF model under GM9. ....	169
7-18	Moat wall displacement in line 1 for OCBF model under GM9. ....	170
7-19	Displacement of 4 corners of the base level for OCBF model under GM9.....	171
7-20	Acceleration response for OCBF model (a) X direction (b) Y direction.....	172
7-21	Story drift ratio for OCBF model under GM9. ....	173
7-22	Second floor brace force-deformation of OCBF model under GM9.....	174
7-23	(a) Base level master node displacement and (b) Base level corner node displacement for IMRF model without moat wall.....	175
7-24	Maximum impact force generated at IMRF model.....	175
7-25	(a) Base level master node displacement (b) Base level corner node displacement for IMRF model with wall.....	176
7-26	Maximum master node acceleration of IMRF model.....	177
7-27	SRSS of x and y-component displacement spectra for 20 ground motions.....	178
7-28	Maximum story drift ratio (SDR) of IMRF model.....	180
7-29	Maximum plastic rotation of (a) Beam elements (b) Column elements of IMRF model.....	181
7-30	(a) Base level master node displacement (b) Base level corner node displacement for OCBF model without moat wall .....	182
7-31	Maximum impact force generated at OCBF model.....	182
7-32	(a) Base level master node displacement (b) Base level corner node displacement for OCBF model with wall .....	183
7-33	Maximum master node acceleration of OCBF model. ....	184
7-34	Maximum story drift ratio (SDR) of OCBF model .....	185
7-35	Number of buckled braces (a) First floor (b) Second floor (c) Third floor of OCBF model.....	186
7-36	Maximum plastic rotation of (a) Beam elements (b) Column elements of OCBF model.....	187
7-37	Median and 84% of (a) Acceleration (b) SDR for IMRF model under 20 ground motions .....	189
7-38	Median and 84% of (a) Acceleration (b) SDR for OCBF model under 20 ground motions .....	189
7-39	Median and 84% of (a) Acceleration (b) SDR for IMRF model under 18 ground motions .....	191
7-40	Median and 84% of (a) Acceleration (b) SDR for OCBF model under 18 ground motions .....	191

## LIST OF ILLUSTRATIONS (CONT'D)

Figure	Title	Page
8-1	Moat wall force displacement model used in FEMA P695 case study (FEMA 2009b).....	194
8-2	The 22 unscaled ground motions spectra and median spectrum.....	197
8-3	Ground motion spectra and median spectrum for 22 normalized records .....	200
8-4	The normalized 22 ground motion spectra scaled to MCE spectrum.....	201
8-5	MCE spectrum for model site location and FEMA SDC Dmax.....	202
8-6	Idealized nonlinear static pushover curve (FEMA 2009b).....	204
8-7	Nonlinear static pushover curve for fixed-base IMRF in (a) X direction (b) Y direction.....	208
8-8	Nonlinear static pushover curve for base-isolated IMRF in (a) X direction and (b) Y direction.....	208
8-9	IDA curve for maximum direction of IMRF model and different moat wall situations .....	211
8-10	Collapse fragility curve for IMRF model from IDA .....	212
8-11	Adjusted collapse fragility curve for 3D IMRF model.....	213
8-12	Nonlinear static pushover curve for (a) Fixed base (b) Base isolated OCBF model.....	215
8-13	IDA curve for maximum direction of OCBF model and different moat wall situations .....	217
8-14	Collapse fragility curve for OCBF model from IDA.....	219
8-15	Adjusted collapse fragility curve for base isolated OCBF model.....	220
8-16	Ratio of adjusted collapse margin ratio (ACMR) to accepted ACMR for 10% probability of collapse.....	222

## LIST OF TABLES

<b>Table</b>	<b>Title</b>	<b>Page</b>
3-1	Member sizes for conventional SMRF.....	33
3-2	Member sizes for base-isolated IMRF.....	33
3-3	Member sizes for conventional SCBF.....	35
3-4	Member sizes for base-isolated OCBF.....	35
3-5	Model weight based on level.....	36
3-6	Fundamental periods of moment frame models.....	36
3-7	Fundamental periods of braced frame models.....	36
3-8	Design parameters for isolation systems.....	37
3-9	List of the 20 ground motions.....	40
4-1	Comparison of required and provided scale factors for scaled model.....	45
4-2	Comparison of prototype and scaled model element properties.....	47
4-3	The superstructure weight at each level.....	48
4-4	List of accelerometers and their location.....	52
4-5	List of string potentiometer and their location.....	53
4-6	List of ground motion properties used in scaled model experiment testing.....	59
4-7	System identification test results summary.....	62
4-8	Test log for date 9/3/2010 - Fixed base IMRF.....	64
4-9	Test log for date 9/7/2010 – Fixed base IMRF.....	64
4-10	Test log for date 10/4/2010 – Base isolated IMRF without moat wall.....	65
4-11	Test log for date 10/19/2010 – Base isolated IMRF with 2 in. concrete moat wall at 6 in. gap distance.....	66
4-12	Test log for date 11/4/2010 – Base isolated IMRF with 4 in. concrete moat wall at 6 in. gap distance.....	66
4-13	Test log for date 11/16/2010 – Base isolated IMRF with 6 in. concrete moat wall at 4 in. gap distance.....	67
4-14	Test log for date 11/23/2010 – Base isolated IMRF with steel moat wall without weld at 6, 5 and 4 in. gap distances.....	68
4-15	Test log for date 12/3/2010 - Base isolated IMRF with steel moat wall with weld at 6 and 4 in. gap distance.....	68
5-1	Summary of fixed base IMRF shake table test results for GM15-2.....	72
5-2	Summary of fixed base IMRF shake table test results for GM16-2.....	73
5-3	Summary of isolated base IMRF shake table test results for GM11-1.....	76
5-4	Summary of isolated base IMRF shake table test results for GM15-2.....	77
5-5	Summary of isolated base IMRF shake table test results for GM16-2.....	78
5-6	Summary of isolated base IMRF shake table test results for GM17-1.....	79
5-7	Summary of isolated base IMRF shake table test results for GM17-2.....	80
6-1	List of proposed impact element parameters for different wall types.....	127
7-1	Modified Bilin model parameters for fiber section.....	163

## LIST OF TABLES (CONT'D)

<b>Table</b>	<b>Title</b>	<b>Page</b>
8-1	Ground motion set for collapse assessment (from FEMA P695) .....	198
8-2	Collapse margin ratio for IMRF models .....	212
8-3	Adjusted collapse margin ratio for IMRF models .....	214
8-4	Collapse margin ratio for OCBF models .....	218
8-5	Adjusted collapse margin ratio for OCBF models.....	221

# SECTION 1 INTRODUCTION

## 1.1. Problem Description

Seismic isolation offers a simple and direct opportunity to control or even eliminate damage to structures subjected to ground shaking by simultaneously reducing deformations and accelerations. Installing a base isolation system decouples the superstructure from the ground resulting in elongation of fundamental period of the structure and reducing the acceleration transferred to superstructure during ground motion. However, increasing the fundamental period of the structure is mostly accompanied by increased displacement demands. In base isolated structures, however, this large displacement is concentrated at the base level where seismic isolation devices are installed and designed to handle these large deformations without damage. A typical base isolated basement design requires a space in which the building is free to move sideways without hitting the surrounding structure. This space is commonly referred to as the "moat". Any services that enter the building must make provision for these large displacements, either by flexible joints or large radius expansion loops. The moat must be covered, either by sacrificial material or have the ability to slide over the adjoining supports.

Structural design codes such as the International Building Code IBC (ICC 2006) and ASCE 7-05 (ASCE 2005) that regulate the design of buildings incorporating seismic base isolation systems require the minimum moat wall clearance distance equal to the maximum displacement at the base of the structure under the Maximum Considered Earthquake (MCE), although the superstructure is designed for Design Basis Earthquake (DBE) level. Despite the cautious regulation for moat wall gap distance, pounding of base isolated building to moat walls has been reported in previous earthquakes. The base-isolated Fire Command and Control (FCC) building in Los Angeles experienced pounding to its moat wall during strong motion of 1994 Northridge earthquake. The evaluation studies after this earthquake showed that the base isolated FCC building performed well, except for impact, which increased structure shear and drift demands (Nagarajaiah et al. 2001). In the more recent 2011 Christchurch earthquake, evidence revealed pounding to moat wall in the only base isolated building in the region of strong shaking,

resulting in damage to sacrificial non-structural components at the seismic gaps (Gavin et al. 2012).

The pounding problem between adjacent structures of buildings and highway bridges has been a major cause of seismic damage, even collapse, of civil infrastructure during earthquakes in the past several decades. Seismic pounding is known to cause localized damage, and even contribute to the collapse of structures. Pounding incidences between fixed-base buildings due to strong earthquakes motivated relevant research, which led to seismic-code reforms in order to mitigate the risks from poundings of adjacent structures. However, very limited research work has been carried out for internal poundings of seismically isolated buildings, which exhibit quite different dynamic characteristics from fixed base buildings. Pounding in base isolated buildings has not been a major issue in past earthquakes since there are few buildings with this technology and, particularly in areas that have experienced strong shaking.

Current design specifications may not adequately account for the large forces generated during impact in base isolated buildings. This study investigates the pounding phenomenon in base isolated buildings from both experimental and analytical perspectives by conducting shake table pounding experiments, developing effective models for impact to moat walls and evaluating the adequacy of code specifications for the gap distance of moat walls.

This research is part of the National Science Foundation (NSF) funded NEES TIPS project (Network for Earthquake Engineering Simulation (NEES), Tools for Isolation and Protective Systems); a collaborative effort of researchers in the U.S and Japan to create and promote tools that will facilitate adoption of isolation and protective systems (Ryan et al. 2008). This particular study focuses on modeling and evaluation of limit-states in base isolated buildings.

## **1.2. Objectives and Scope of Research**

The goal of this study is to determine the effects of pounding on the global response of base isolated buildings through realistic experimental testing and the development of reliable analytical models for moat wall pounding. For the first time, a series of shake table experiments were conducted on base isolated buildings impacting the moat wall and damaging the superstructure. The experiments provide a wealth of data to better understand the dynamics of

impact that can lead to further development of new impact element for moat walls and other applications. A reliable base isolated and moat wall model will be used for a comprehensive comparative and collapse study of base isolated building.

The specific objectives of this research are:

- Conduct a series of shake table test to assess limit states in base isolated buildings under strong ground motion.
- Explore the response of base isolated buildings pounding to a surrounding moat wall.
- Investigate experimentally the effect of moat wall gap distance, stiffness and damping on response of base isolated structure during impact.
- Propose a new impact element to simulate pounding of base isolated building and moat wall.
- Compare response of base isolated structures with and without moat wall.
- Evaluate the collapse probability of base isolated buildings for different moat wall gap distances.
- Evaluate the efficacy of code specifications in accounting for pounding in base isolated buildings.

### **1.3. Outline of Report**

This report is organized into nine sections with the following contents:

Section 2 presents an overview of seismic pounding in base isolated buildings. The possibility of pounding in base isolated structures is investigated based on specifications required for this type of buildings. Various analytical models used to simulate impact are presented. Past research on seismic pounding is also summarized.

The summary of prototype base isolated buildings designed by professional engineers for purpose of this project is presented in Section 3. Two base isolated moment and braced frame steel buildings are considered for purpose of the NEES TIPS project. The detailed design

assumptions, final geometry and section properties as well as ground motion set used in this study are summarized in this section.

The experimental test setup is described in Section 4. Detail properties of a quarter scale base-isolated moment frame building model with moat walls designed for shake table testing is provided. The building model is scaled down from the prototype model and tested in fixed base and base isolated conditions. Scaling similitude and dimensional analysis as applied to the reduced scale model are explained. The properties of the isolation bearings and a detailed description of the different moat wall configurations are described. At the end of this Section, the experimental testing schedule is presented.

Section 5 presents a summary of experimental results for the building in three configurations including fixed base, base isolated without moat wall, and base isolated with moat wall. Detailed results are presented for one of the ground motions applied on the shake table while the other ground motions results can be accessed in the NEES website under the NEES TIPS project directory (<https://nees.org/warehouse/project/571>). At the end of this Section, a summary of all experimental testing is provided and the effects of pounding in base isolated buildings are summarized based on experimental observations.

Numerical simulations of the experiments are presented in Section 6. A Detail finite element model of the test setup is modeled in OpenSees. The assumptions and properties of numerical simulation for 2-dimensional (2D) impact are explained in this Section. An analytical study on dynamic behavior of the moat walls resulted in proposing a new impact element described in this Section. Numerical simulation using the proposed impact element is compared with experimental results.

The proposed impact element in 2D analysis is extended to 3D simulation in Section 7. A surrounding moat wall is constructed by connecting multiple impact elements in plane by shear key element. The behavior of these shear keys are calibrated based on finite element simulations of a continuous walls in ABAQUS. The response of the 3-story moment and braced prototype models presented in Section 3 is examined considering impact to a surrounding moat wall at the base level by implementing the proposed impact element. The effect of pounding to moat wall in

both prototype buildings were investigated by comparing the superstructure response with and without presence of the moat wall. These studies provide critical information for the design of base isolated buildings, particularly the moat wall clearance and its potential effect on the superstructure response.

A series of collapse studies using the fragility curve concept was conducted for both prototype models and for various gap distances in Section 8. The objective of this section is to evaluate the collapse probability of base isolated models used in this study and also investigate the effect of moat wall gap distance on the probability of collapse for base isolated structures. For this purpose the numerical models developed in Section 7 were used following the Methodology presented in FEMA P695 (FEMA 2009b).

The findings from the study are summarized and areas of future research are suggested in Section 9.



## SECTION 2 STRUCTURAL POUNDING IN BASE ISOLATED BUILDINGS

### 2.1. Base Isolated Structure

Base isolation has been proven to be an effective strategy to reduce both story drift ratio and accelerations in structures during ground shaking. Inter story drift ratio and acceleration are two key measures of structural response during earthquakes. High inter-story drifts can cause severe damage to structural frames, piping and ductwork, facade, windows, and partitions. High floor accelerations can cause damage to ceilings and lights, building equipment, elevators, and other building contents. Unlike traditional design strategies that aim to increase the design capacity and stiffness of the structure to accommodate foreseeable lateral forces, base isolation systems introduce a flexible level between structure and foundation in order to isolate the structure from ground movement. Increasing stiffness in structures shifts the fundamental period of the structure to higher acceleration zone in response spectrum resulting in higher demand in building. Installing base isolation system results in elongation of period to lower demand acceleration zone. However, increasing fundamental period of the structure is always accompanied by increasing in displacement demand (Figure 2-1). This large displacement is concentrated at base level where seismic isolation devices are installed. Increasing damping at base level such as using additional viscous damper devices in conjunction with base isolation system is an option to reduce this large demand displacement, although they may be costly.

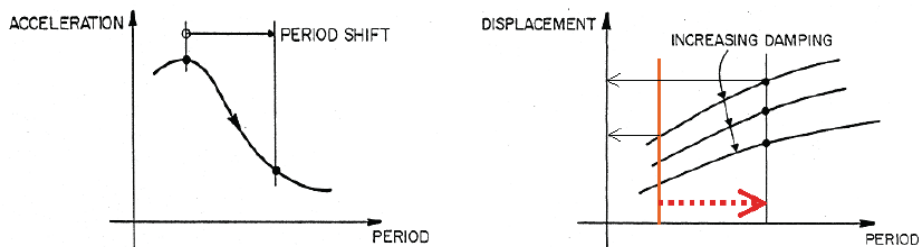
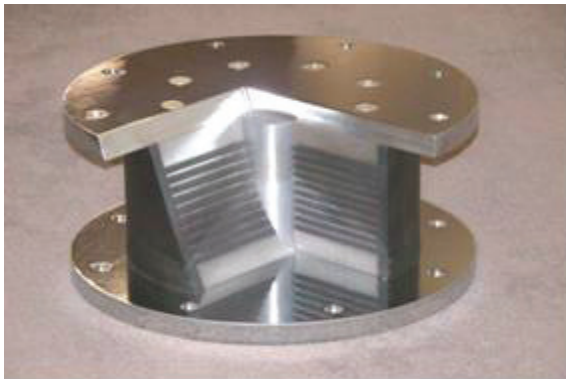


**Figure 2-1 Principles of seismic isolation (Constantinou et al. 2007)**

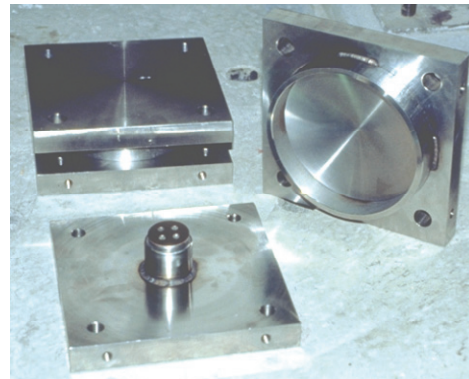
Although patents on seismic isolators can be traced back to the 1800s, the use of seismic isolation for protecting bridges and buildings is somewhat recent in the United States. The first application of modern seismic isolation was completed in 1985 for a retrofit of Sierra Point Overpass, in San Francisco, California (Constantinou et al. 2007).

The number of base isolated building in Asian countries, especially Japan, far surpasses the number in the United States. The number of base isolated buildings in Japan is in order of the thousands while the number in the U.S. remains around one hundred. Unlike its use in Japan, isolation technology in the U.S. has remained within mainly essential, public buildings such as hospitals, city halls or emergency response centers. The technology has not spread to use in typical office or residential buildings, which may also see increased safety and performance benefits (Nakashima et al. 2010).

There are two common types of seismic isolation bearings in the United States, elastomeric bearings (low- and high-damping rubber; lead rubber) and sliding bearings (spherical sliding or Friction Pendulum bearings; flat sliding bearings). Two common types of seismic isolation devices are shown in Figure 2-2. These bearings are designed to be relatively flexible and accommodate large displacements in the horizontal direction while sustaining the gravity loads from the superstructure.



(a) Lead rubber bearing



(b) Friction pendulum bearing

**Figure 2-2 Different types of seismic isolation system (Constantinou et al. 2007)**

### *2.1.1. Design of Base Isolated Structure*

Structural design codes such as the International Building Code IBC (ICC 2006) and ASCE 7-05 (ASCE 2005) regulate the design of buildings incorporating seismic base isolation systems. The concept of design standards in these codes is to design the structure for a single earthquake intensity with 10% probability of occurring in 50 years. These codes require that seismic isolated structure remains elastic during this event. Although the code guidelines allow analysis

of the isolated building system by several procedures: the equivalent lateral force method, response spectrum analysis and nonlinear response history analysis, use of the equivalent lateral force method for final design has been limited by the codes to a narrow class of structures. However, static analysis is the logical starting point for the conceptual design phase, and furthermore, the codes require that the response determined from an acceptable dynamic analysis procedure does not fall below limits determined by static analysis. Thus, accessibility to static equations that can simply and accurately predict important response parameters, such as the deformation demand of the isolation system, is a critical aspect of design.

Base isolated structures should fulfill requirements in Chapter 17 of ASCE7-05 “*SEISMIC DESIGN REQUIREMENTS FOR SEISMICALLY ISOLATED STRUCTURES*”. This chapter requires design of the superstructure for the forces obtained from design basis earthquake (DBE) while isolation devices should be designed for displacement obtained from maximum considered earthquake (MCE) analysis. The MCE is defined as an earthquake with 2% probability of occurrence in 50 years, or a 2500-year return period. The DBE is defined as 2/3 of the MCE. In earthquake prone regions such as the west coast, the DBE has approximately 10% probability of occurring in 50 years (475 years return period).

The equivalent lateral force design method consists of recursive steps to get to the final design parameters equal to initial assumed values. Minimum lateral earthquake design displacements and forces on seismically isolated structures should be based on the deformation characteristics of the isolation system. First, the design displacement is calculated using Equation 17.5-1 of ASCE 7-05:

$$D_D = \frac{gS_{D1}T_D}{4\pi^2B_D} \quad (2-1)$$

Where  $S_{D1}$  is 5% damped DBE spectral acceleration parameter at 1-s period dependent on building location,  $B_D$  is numerical coefficient related to the effective damping of the isolation system at design displacement obtained from Table 15.5-1 of ASCE 7-05, and  $T_D$  is effective period of seismically isolated structure at design displacement:

$$T_D = 4\pi \sqrt{\frac{W}{k_{Dmin}g}} \quad (2-2)$$

To calculate the effective period of the isolated structure,  $W$  is the total weight of the structure on top of isolators and  $k_{Dmin}$  is minimum effective stiffness of the isolation system at the design displacement.

The isolation system, the foundation, and all structural elements below the isolation system should be designed and constructed to withstand a minimum lateral seismic force,  $V_b$  using all of the appropriate requirements for a nonisolated structure where

$$V_b = k_{Dmax}D_D \quad (2-3)$$

and  $k_{Dmax}$  is the maximum effective stiffness of the isolation system at the design displacement. The structures above the isolation system should be designed to tolerate a minimum shear force,  $V_s$ , using:

$$V_s = \frac{k_{Dmax}D_D}{R_I} \quad (2-4)$$

where  $R_I$  is response modification factors related to the type of seismic force-resisting system above the isolation system. The  $R_I$  factor should be based on the type of seismic force-resisting system used for the structure above the isolation system and should be three-eighths of the  $R$  value given in Table 12.2-1 of ASCE7-05 with an upper-bound value not to exceed 2.0 and a lower-bound value not to be less than 1.0.

The maximum displacement of the isolation system,  $D_M$ , in the most critical direction of horizontal response should be calculated in accordance with the formula:

$$D_M = \frac{gS_{M1}T_M}{4\pi^2B_M} \quad (2-5)$$

where  $S_{M1}$  is maximum considered 5% damped spectral acceleration parameter at 1 sec period,  $T_M$  is effective period of seismic isolated structure at maximum displacement calculating using Equation 2-6 , and  $B_M$  is a numerical coefficient related to the effective damping of the isolation system at the maximum displacement.

$$T_M = 4\pi \sqrt{\frac{W}{k_{Mmin}g}} \quad (2-6)$$

In the equation above,  $k_{Mmin}$  is minimum effective stiffness of the isolation system at maximum displacement.

The total maximum displacement,  $D_{TM}$ , of the isolation system elements should include additional displacement due to actual and accidental torsion calculated from the spatial distribution of the lateral stiffness of the isolation system and the most disadvantageous location of eccentric mass. The total maximum displacement,  $D_{TM}$ , of elements of an isolation system with uniform spatial distribution of lateral stiffness should not be taken as less than that prescribed by the following equations:

$$D_{TM} = D_M \left[ 1 + y \frac{12e}{b^2 + d^2} \right] \quad (2-7)$$

where  $y$  is the distance between the centers of rigidity of the isolation system and the element of interest measured perpendicular to the direction of seismic loading under consideration,  $e$  is the actual eccentricity measured in plan between the center of mass of the structure above the isolation interface and the center of rigidity of the isolation system, plus accidental eccentricity, taken as 5 percent of the longest plan dimension of the structure perpendicular to the direction of force under consideration,  $b$  and  $d$  are the shortest and longest plan dimension of the structure.

The isolation system should not be configured to include a displacement restraint that limits lateral displacement due to the maximum considered earthquake to less than the total maximum displacement,  $D_{TM}$ , unless the seismically isolated structure is designed in accordance with the following criteria, which are more strict than the requirements described earlier:

1. Maximum considered earthquake response is calculated in accordance with the dynamic analysis requirements of Section 17.6 of ASCE 7-05 (Dynamic Analysis Procedure) explicitly considering the nonlinear characteristics of the isolation system and the structure above the isolation system.

2. The ultimate capacity of the isolation system and structural elements below the isolation system should exceed the strength and displacement demands of the maximum considered earthquake.
3. The structure above the isolation system is checked for stability and ductility demand of the maximum considered earthquake.
4. The displacement restraint does not become effective at a displacement less than 0.75 times the total design displacement unless it is demonstrated by analysis that earlier engagement does not result in unsatisfactory performance.

The accuracy of equivalent-linear systems to estimate seismic demands has been documented for general nonlinear systems (Fajfar 1999; Chopra et al. 2000) and specifically for isolation systems (Anderson et al. 1998; Franchin et al. 2001; Dicleli et al. 2007). Because the equivalent linear approach cannot characterize the isolation system based on its physical parameters, often requires iteration, and potentially suffers from inaccuracy, other approaches to estimate the deformation demand of the isolation system are worth investigating.

There are some other restraints on using equivalent lateral procedure such as structure height (less than 65 ft), the effective period of the isolated structure at the maximum displacement,  $T_M \leq 3.0 \text{ sec}$ , the structure location at a site with  $S_1$  less than 0.60g, etc. which are listed in Section 17.4 of ASCE 7-05. These situations, which are very possible in design of seismic isolated structure, persuade using of nonlinear time history analysis as a design tool.

### *2.1.2. Dynamic Analysis Procedure*

Dynamic analysis in design of seismic isolated structure is inevitable in many cases. Where dynamic analysis is used to design seismically isolated structures, the mathematical models of the isolated structure including the isolation system, the seismic force-resisting system, and other structural elements should conform to Section 12.7.3 and to the requirements of Sections 17.6.2.1 and 17.6.2.2 of ASCE 7-05. For the purpose of dynamic time history analysis, a suite of not fewer than three appropriate ground motions should be used in the analysis. Ground motions should consist of pairs of appropriate horizontal ground motion acceleration components that

should be selected and scaled from individual recorded events. Appropriate ground motions should be selected from events having magnitudes, fault distance, and source mechanisms that are consistent with those that control the maximum considered earthquake.

For each pair of horizontal ground-motion components, a square root of the sum of the squares (SRSS) spectrum should be constructed by taking the SRSS of the 5 percent damped response spectra for the scaled components (where an identical scale factor is applied to both components of a pair). Each pair of motions should be scaled such that for each period between  $0.5T_D$  and  $1.25T_M$  (where  $T_D$  and  $T_M$  are defined in Equations 2-2 and 2-6) the average of the SRSS spectra from all horizontal component pairs does not fall below 1.3 times the corresponding ordinate of the design response spectrum by more than 10 percent.

Note that the criteria in ASCE 7-05 represent minimum requirements. Even when scaled motions meet these criteria, it does not mean that the scaled motions correctly represent the target MCE spectrum. To verify, the maximum direction spectrum of each scaled pair of ground motion components should be constructed. Then the average of the maximum direction spectra of the scaled motions should be constructed and compared to the target MCE spectrum. The two spectra should be reasonably close.

There are various procedures for scaling records to represent a spectrum. One is to perform “spectral matching” in which the record is modified in frequency content and amplitude so that its response spectrum matches the target spectrum within a range of periods and with a specified degree of accuracy. Another is to simply scale the amplitude of the record and maintain the frequency content unchanged. The simplest version of this procedure is to scale the record so that its response spectrum matches the target spectrum at a particular period, say 1 second or at the fundamental period of the structure to be analyzed. Another is to utilize a “weighted average” scaling process in which several periods are considered (Constantinou et al. 2011).

The weighted average procedure utilizes information on spectral acceleration at a number of periods. It is more difficult to apply but should, in principle; result in better matching of the target spectra. Note that the scaling procedure only scales the amplitude of the seed motions. It does not involve changes in the frequency content of the seed motions. This procedure is

especially appropriate for evaluation of different structures with wide range of fundamental periods.

Figure 2-3 shows the acceleration and displacement response spectra for 20 ground motions used for time history analysis in the NEES TIPS project (Ryan et al. 2008) and MCE spectrum that all the ground motions are scaled to based on the procedure described earlier. It can be seen that average SRSS of 20 ground motions are above the MCE spectrum. On the right, the median displacement spectrum for the two components of each pair of scaled ground motions is shown. The solid thick line corresponds to the median of all the motions. It can be seen that some ground motions resulted in substantially larger displacement demands than the median curve. The median curve is the basis of determining the minimum gap size for displacement restraint in ASCE 7-05 for isolated structures. It can be concluded that conducting dynamic analysis using ground motions scaled to MCE spectrum complying to ASCE 7-05 requirements results in displacement demand more than minimum displacement restraint limit in some motions. This requires modeling these displacement restraints in dynamic analysis in order to better capture the expected behavior of base isolated buildings.

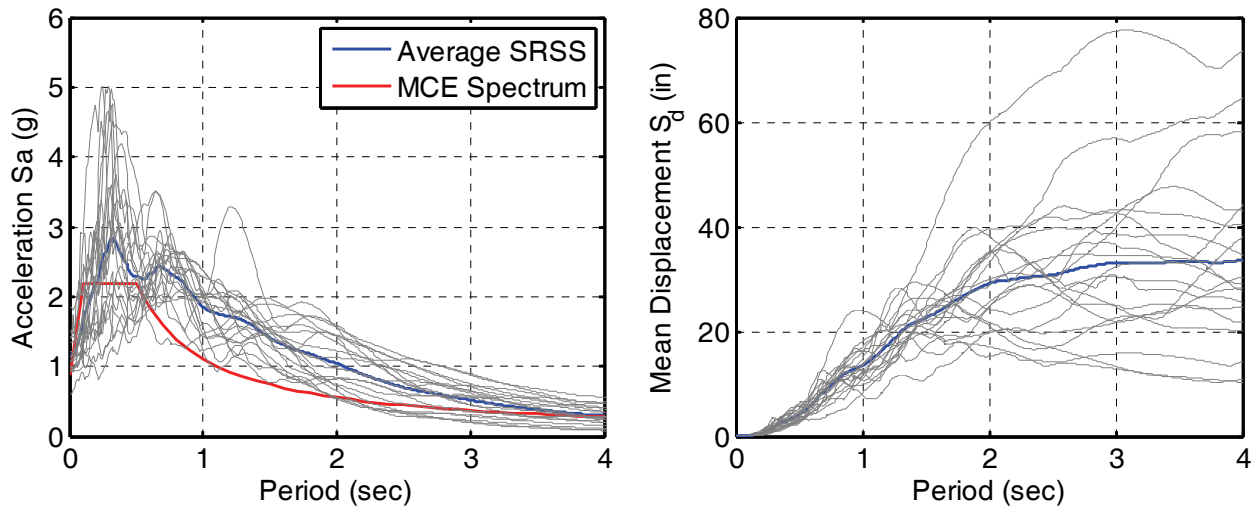


**Figure 2-3 Acceleration and displacement response spectra**

This displacement restraint can be moat wall or retaining wall around the base level of a base isolated building. A typical base isolated basement design requires a space of not less than  $D_{TM}$  in which the building is free to move sideways without hitting the surrounding structure. This

space is commonly referred to as the "moat". Any services that enter the building must make provision for these large displacements, either by flexible joints or large radius expansion loops. The moat must be covered, either by sacrificial material or have the ability to slide over the adjoining supports. Figure 2-4 shows the typical arrangement of a base isolated building with the isolators located below the basement floor.

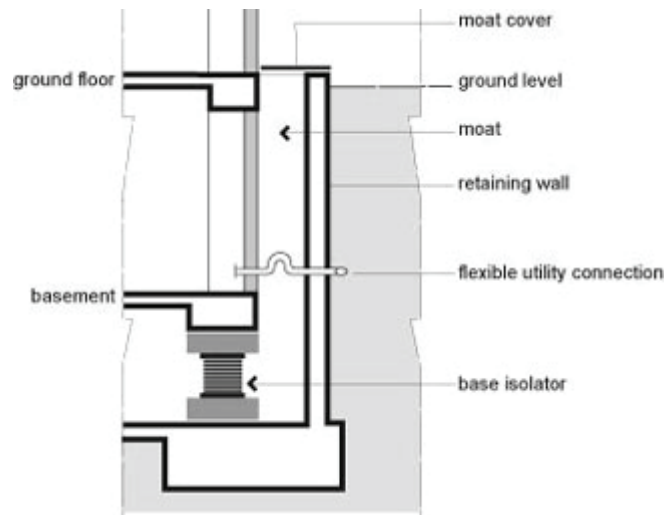


**Figure 2-4 Typical moat wall configuration in base isolated building (Arnold 2009)**

The dynamic analysis of base isolated building should explicitly include the elements to represent the behavior of the moat wall due to the high probability of base level displacement exceeding the gap distance under scaled ground motions. Although numerous studies have been conducted on modeling of superstructure and isolators elements, a few efforts have been made to model the dynamic behavior of retaining walls and soil backfill. In the following subsections, a review of previous studies on structural pounding between adjacent structures and also the different methods to model this pounding force are presented.

## **2.2. Structural Pounding**

The pounding problem between adjacent structures of buildings and highway bridges has been a major cause of seismic damage, even collapse, of civil infrastructures during earthquakes in the past several decades. Pounding damage in buildings and highway bridges has been widely reported in almost all major earthquakes in the literature, such as the 1989 Loma Prieta

earthquake (Priestley et al. 1996), the 1994 Northridge earthquake (EERI 1995a; Nagarajaiah et al. 2001), the 1995 Kobe earthquake (EERI 1995b) and the 1999 Chichi earthquake (EERI 2001). Especially in the 1985 Mexico City earthquake, the post-earthquake survey showed that over 40% of the 330 severely damaged or collapsed buildings were induced by the structural pounding (Rosenblueth 1986).

Although most structural pounding occurred between two adjacent fixed base structures at top floors or bridge decks due to lack of sufficient gap distance (Figure 2-5), a few cases of pounding have been reported in base isolated buildings.



(a)



(b)

**Figure 2-5 (a) Barrier rail damage during the 1994 Northridge earthquake; (b) Pounding between a six-story building and a two-story building in Golcuk, causing damage to the column of the six-story building (EERI 2000)**

The Christchurch Women’s Hospital, completed in March 2005, is the only base-isolated building in the South Island of New Zealand. The displacement capacity of the base-isolation system and the superstructure ductility capacity are designed to meet 2000-year return-period demands. Detailed structural evaluations after the 2010 Darfield Earthquake and the 2011 Christchurch Earthquake revealed damage only to sacrificial non-structural components at the seismic gaps (Gavin et al. 2010; Gavin et al. 2012). Figure 2-6 shows the moat wall damage due

to pounding at the base level of this building. Rolling trolleys, items falling from shelves, clocks falling from walls, items falling out of refrigerators, and sloshing of water from a full birthing pool to a distance of 6 to 9 ft from the pool was reported from the hospital staff during the ground motion (Gavin et al. 2012).



**Figure 2-6 Pounding of base isolated Christchurch women’s hospital to moat wall (Gavin et al. 2010)**

The base-isolated Fire Command and Control (FCC) building in Los Angeles experienced strong motion during the 1994 Northridge earthquake. The California Strong Motion Instrumentation Program has instrumented the building and recorded the data during the Northridge earthquake (Shakal et al. 1994). Impact was observed in the base-isolated FCC building during the Northridge earthquake. Nagarajaiah et al. (2001) evaluated the seismic performance of the base-isolated FCC building during the 1994 Northridge earthquake and the effect of impact. They showed that the base isolated FCC building performed well, except for impact, which increased structure shear, and drift demands. The effectiveness of base isolation was reduced because of impact.

### *2.2.1. Analytical and Numerical Studies*

Previous studies related to structural pounding have been mainly analytical, based on two techniques, the stereomechanical approach and contact element approach.

The classical theory of impact, called stereomechanics, is based preliminary on the impulse-momentum law for rigid bodies, which specifies of initial and terminal velocity states (Figure 2-7). In this theory, velocities of the colliding bodies after collision are calculated from:

$$v_{1t} = v_{1i} - (1+e) \frac{m_2(v_{1i} - v_{2i})}{m_1 + m_2} \quad (2-8a)$$

$$v_{2t} = v_{2i} + (1+e) \frac{m_1(v_{1i} - v_{2i})}{m_1 + m_2} \quad (2-8b)$$

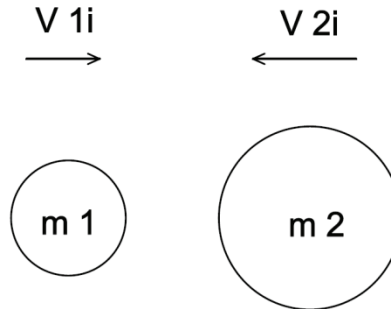


**Figure 2-7 Classical theory of impact.**

In this equation  $v_i$ ,  $v_t$  are the velocities before and after collision, the subscripts 1 and 2 identify the two colliding bodies, and  $e$  is the coefficient of restitution. The coefficient of restitution accounts for energy loss during impact, and is usually defined as the ratio of final to initial relative velocity. This approach has been used to model impact by several researchers (Papadrakakis et al. 1991; DesRoches et al. 1997). It has been shown that the variation in ( $e$ ) has a relatively minor effect on the structural response due to pounding (DesRoches et al. 1997). Using this approach, Malhotra (1998) investigated the effect of earthquake-induced pounding at thermal expansion joints of concrete bridges. Examining collinear impact between concrete rods of the same cross section but different lengths showed that the coefficient of restitution depends only on the length ratio and the damping ratio of the rod material and the duration of impact is equal to the fundamental period of axial vibration of the shorter rod.

From Equations 2-8, it is evident that this theory does not account for impact duration, transient forces, and local deformations at the contact point and further assumes that a negligible fraction of the initial kinetic energy of the system is transferred into local vibrations of colliding bodies. These assumptions limit the application of stereomechanics theory in accurately capturing structural collisions.

On the other hand, the contact element approach considers the impact force generated during the collision of two adjacent structures by assuming a combination of springs and dashpots between them. The contact element approach is a very widely used formulation because of its easy adaptability and logical nature to model impact. Various contact elements have been used in the past including the linear spring element, Kelvin-Voigt element, the Hertz contact element and the Hertz damped element.

The linear spring element (Figure 2-8) is the simplest contact element used to model impact. The spring is implemented in series with a gap element to consider the distance between two bodies. Obviously, this model suffers from lack of energy dissipation during impact. Maison et al. (1992) have used this model to study pounding between adjacent buildings. They conclude that pounding generates drifts, shears, and overturning moments in the stories above the pounding location that are greater than those from the case where pounding is ignored.

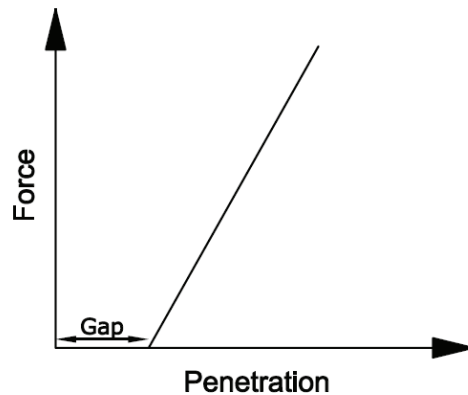


**Figure 2-8 Linear spring element.**

Figure 2-9 shows the Kelvin-Voigt element which is represented by a linear spring in parallel with a damper. Many researchers have used this element to generate forces during pounding of adjacent bodies (Wolf et al. 1980; Anagnostopoulos et al. 1992; Jankowski et al. 1998). Unlike the linear spring model the damper in this model accounts for the energy loss during impact. The damping coefficient ( $c_k$ ) can be related to the coefficient of restitution ( $e$ ), by equating the energy losses during impact.

$$c_k = 2\xi \sqrt{k_k \frac{m_1 m_2}{m_1 + m_2}} \quad (2-9a)$$

$$\xi = -\frac{\ln e}{\sqrt{\pi^2 + (\ln e)^2}} \quad (2-9b)$$

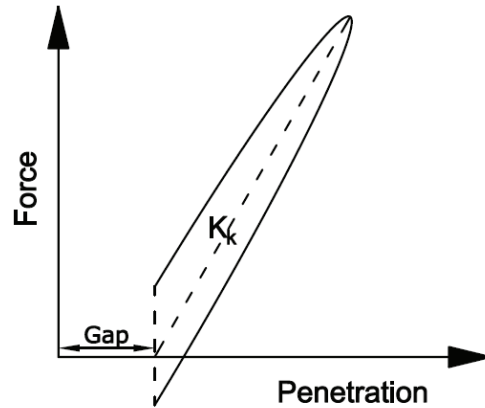


**Figure 2-9 Kelvin-Voigt element.**

As it can be seen in this figure, energy dissipated during the contact is modeled using a damper element in parallel with a linear spring. However, this model exhibits an initial jump of the impact force values upon impact due to the damper. Furthermore, the damping force causes negative impact forces that pull the colliding bodies together, during the unloading phase, instead of pushing them apart.

In order to avoid the tensile impact forces that arise between the colliding structures at the end of the restitution period, due to the damping term, a minor adjustment is proposed by Komodromos et al. (2007) for the linear viscoelastic model. In particular, when the impact force is about to change sign, the impact spring and dashpot are removed, considering that the two bodies are detached from each other. A permanent deformation is considered, assuming some remaining plastic deformations, which increase the corresponding available width of the gap (Figure 2-10).

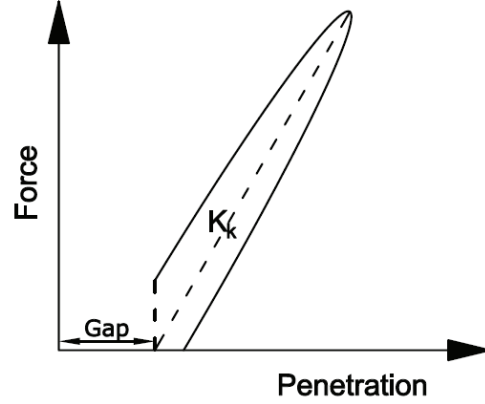


**Figure 2-10 Modified Kelvin-Voigt element.**

A nonlinear spring based on the Hertz contact law can be used to model impact between two bodies. The Hertz contact law (Goldsmith 2001) was originally proposed for static contact of two bodies, in which stresses and deformations near the contact point are described as a function of the geometric and elastic properties of the bodies. The contact force is related to the relative indentation of two bodies with a nonlinear spring of stiffness  $K_h$  calculated as

$$K_h = \frac{4}{3\pi} \left( \frac{1}{\lambda_1 + \lambda_2} \right) \sqrt{\frac{R_1 R_2}{R_1 + R_2}} \quad (2-10a)$$

$$K_h = \frac{4}{3\pi} \left( \frac{1}{\lambda_1 + \lambda_2} \right) \sqrt{R_1} \quad (2-10b)$$

respectively, for two colliding spheres of radii  $R_1$  and  $R_2$ , and colliding of a sphere of radius  $R_1$  to a massive plane surface. In these formula,  $\lambda_i$  is a material parameter defined as:

$$\lambda_i = \frac{1 - \nu_i^2}{\pi E_i} \quad (2-11)$$

where  $E_i$  and  $\nu_i$  are modulus of elasticity and Poisson's ratio, respectively. For other geometric shapes, an equivalent sphere radius can be used. The contact force can then be expressed as:

$$F_c = K_h \delta^n \quad (2-12)$$

where  $\delta$  is relative penetration and  $n$ , is typically taken as 3/2 for nonlinear behavior.

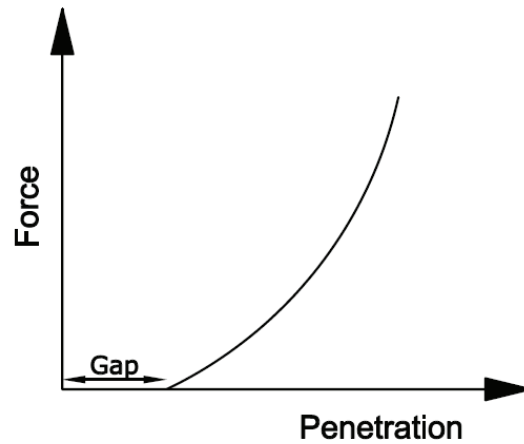


**Figure 2-11 Hertz element.**

The use of the Hertz model for dynamic impact has been justified on the basis that it appears to predict accurately most of the impact parameters that can be experimentally verified (Goldsmith 2001). However, the original model does not capture the energy dissipated during contact. To overcome this limitation, a nonlinear damper in conjunction with the Hertz model was proposed (Hunt et al. 1975; Lankarani et al. 1990; Marhefka et al. 1999; Muthukumar et al. 2006) with contact force given by (Figure 2-12):

$$F_c = K_h \delta^{3/2} + C_h \dot{\delta} \quad (2-13)$$

where  $C_h$  is the damping coefficient, and  $\dot{\delta}$  is penetration velocity. The damping coefficient is related to penetration using Equation 2-14 in order to prevent tensile forces after the two bodies separate.

$$C_h = \xi \delta^{3/2} \quad (2-14)$$

In this equation,  $\xi$  is damping constant which is expressed as (Ye et al. 2009):

$$\xi = \frac{8 K_h (1-e)}{5 e \dot{\delta}_0} \quad (2-15)$$

Jankowski (2007) determined a range of the coefficient of restitution ( $e$ ) for different building materials, such as: steel, concrete, timber and ceramics, based on the results of impact experiments. A general trend observed for all materials is that the coefficient of restitution decreases with an increase in the prior impact velocity. A range of  $e$  from 0.75 to 0.50 for impact velocity of 0.91 in/s to 14.6 in/s was suggested for concrete materials.

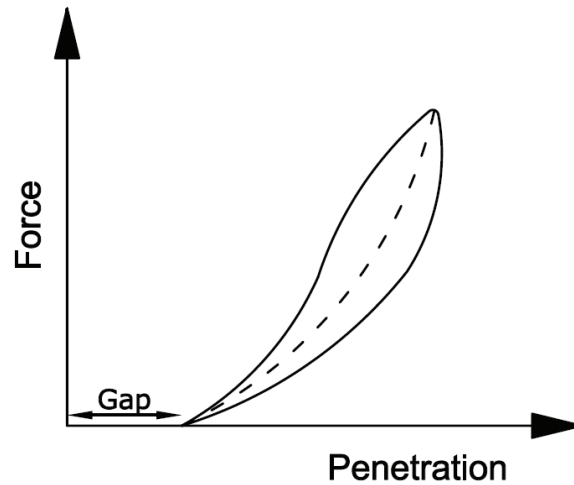


**Figure 2-12 Hertz damped element.**

### 2.2.2. Experimental Studies

Although many researchers have been using the analytical and numerical approach for structural pounding, only a few experimental studies have been conducted on this topic. Filiatrault *et al.* (1995) performed a series of shaking table tests on the dynamic impact between adjacent three- and eight-story single-bay steel frames. The experimental displacements and impact forces could

be properly estimated from analytical models based on a linear elastic spring, but the acceleration at contact locations was not well predicted.

Shaking table tests have been carried out by Chau et al. (2003) to investigate the pounding phenomenon between two steel towers of different natural frequencies and damping ratios, subject to different combinations of stand-off distance and seismic excitations. Both analytical and numerical predictions of the relative impact velocity, the maximum stand-off distance, and the excitation frequency range for pounding occurrences were made and found to be comparable with the experimental observations in most of the cases. Pounding appears to amplify the response of the stiffer structure but suppress that of the more flexible structure; and this agrees qualitatively with previous shaking table tests and theoretical studies.

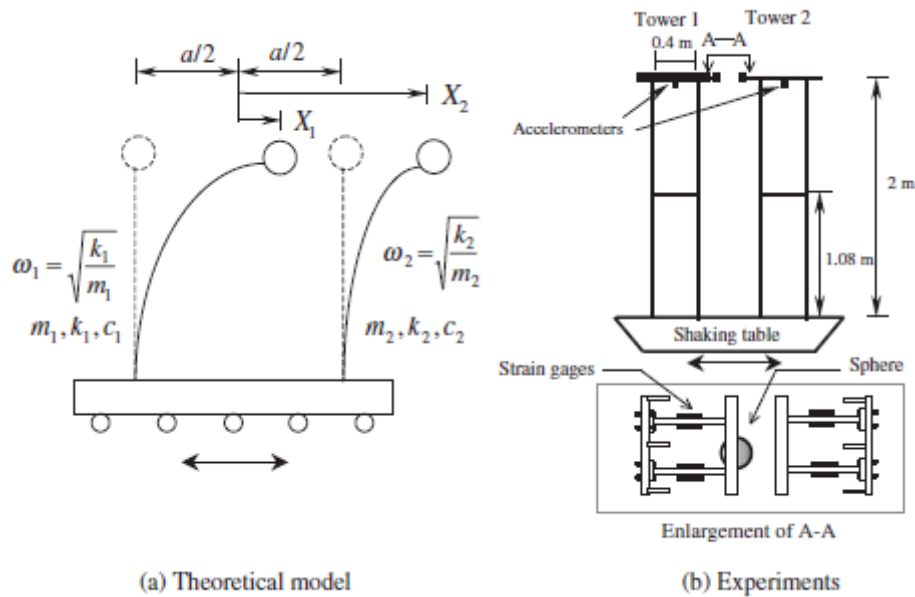


**Figure 2-13 Sketches of the theoretical and experimental models for modeling pounding between two adjacent structures (Chau et al. 2003).**

In a more basic study, Goldsmith (Goldsmith 2001) reported results from experimental tests on collisions between spheres, the impact of spheres on plates, and some other tests on bars and elastic beams, and proposed the stiffness parameter of the Hertz model as a function of the elastic properties and geometry of the two colliding bodies.

The two experiments focused on interactions between elements made of steel, concrete, timber and ceramic are presented in Jankowski (2010). The first experiment was conducted by dropping balls from different height levels onto a rigid surface, whereas the second one was focused on pounding-involved response of two tower models excited on a shaking table. The results of the impact experiment show that the value of the coefficient of restitution depends substantially on the pre-impact velocity as well as on the material of colliding elements. The general trend for all materials shows the decrease in the coefficient of restitution as the impact velocity increases with the highest values for ceramic-to-ceramic impact and the lowest for timber-to-timber. The results of the shaking table experiment confirm the general conclusions obtained from the numerical simulations that structural pounding may lead to the considerable amplification of the response as well as reducing vibrations in some cases.



**Figure 2-14 Setup of the impact experiment by Jankowski (2010).**

There have also been some experimental studies examining pounding of isolated bridges (Vlassis et al. 2001; Guo et al. 2009; Sun et al. 2011). Guo *et al.* (Guo et al. 2009) conducted a series of shaking table tests on a 1:20 scaled base-isolated bridge model to investigate the effects of pounding between adjacent superstructures on the system dynamics response. Based on the test results, the parameters of the linear and the nonlinear viscoelastic impact models were identified and results compared well with numeric models. The results showed that pounding between

adjacent superstructures of the highway bridge significantly increases the structural acceleration responses. Compared to buildings, however, bridge decks are relatively rigid superstructures.

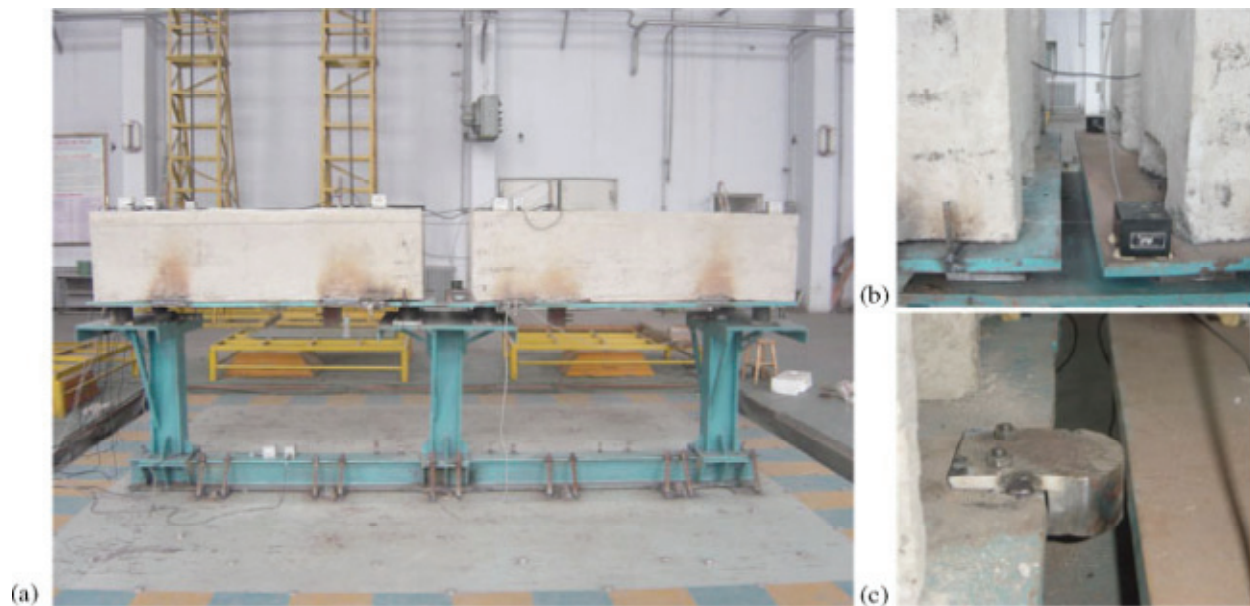


**Figure 2-15 Photographs of the bridge model: (a) Bridge model; (b) Expansion joint without contact Point; and (c) Expansion joint with contact point (Guo et al. 2009).**

Sato et al. (2011) conducted a series of full-scale shaking table tests using the E-Defense shaking table facility on a base-isolated four-story RC hospital structure. A variety of furniture items, medical appliances, and service utilities are placed on the hospital specimen in as realistic a manner as possible. In this test, natural rubber bearings with a parallel U-shaped steel damper (designated as NRB+U) was adopted. The other was high-damping rubber bearings (designated as HDRB), in which the bearing itself dissipates energy. For NRB+U, the clearance between the superstructure and surrounding blocks was set at 500 mm (20 in), while for HDRB, it was set at 300 mm (12 in), intending to allow slight pounding during the test. In this test, pounding occurred once, but the velocity at the instant of pounding was close to zero (0.06m/s). The floor acceleration increased to 0.57g, which was about twice as large as the maximum floor acceleration of 0.26g, observed when no pounding occurred. The increased acceleration, however, lasted only for 0.2 s, and it had no effect on responses except for the following case; a high-oxygen pressure unit placed on the first floor moved horizontally by 20mm in the case of pounding.

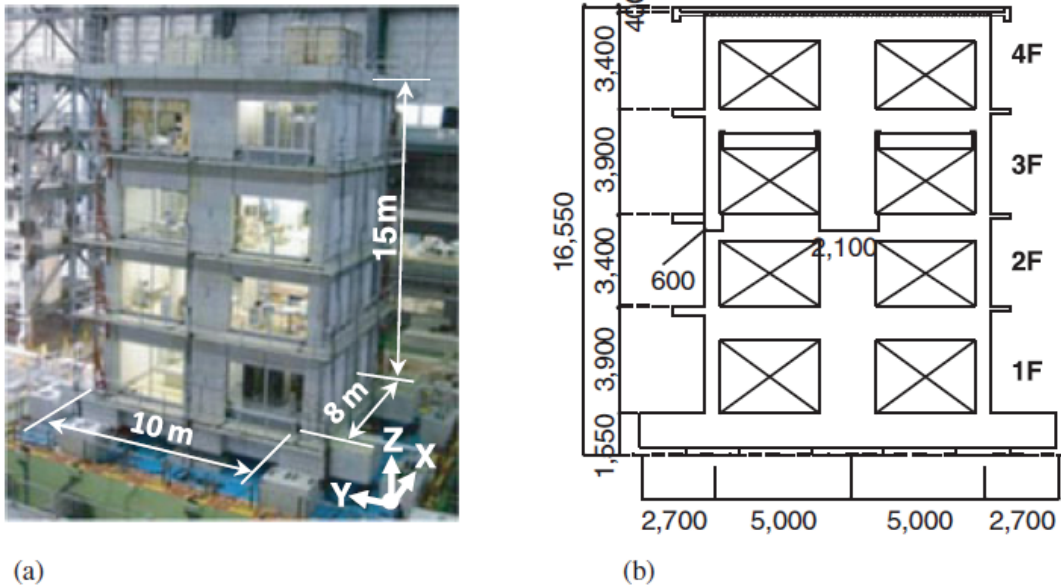


**Figure 2-16 Test specimen by Sato et al. (2011) (unit: mm): (a) Specimen; (b) Elevation.**

### 2.3. Pounding of Base Isolated Building to a Moat Wall

As defined earlier, a moat wall is a retaining wall separating base isolated building from the adjacent structure. The minimum required gap distance between a base isolated building and the surrounding moat wall is determined by  $D_{TM}$  in ASCE 7-05 which is based on probabilistic estimation of maximum displacement in the base level of an isolated building under MCE event multiplied by a scale factor to consider effects of torsion. This minimum required gap distance in the design of most isolated buildings is considered by practitioner due to the economic surcharge of increasing this distance.

Although there is a potential of pounding between the base level of isolated building and moat wall under ground motions at MCE level, the effect of this pounding and extra forces generated at the impact surface has not been carefully investigated. Very limited research work has been carried out for poundings of seismically isolated buildings to moat wall. In most of these numerical studies, the moat wall was replaced with one of impact elements described earlier and the response of base isolated structure is investigated due to pounding in the impact elements under various ground motions.

Tsai (1997) simulated the superstructure of an isolated building as a continuous shear beam in order to investigate the effects of poundings on structural response. In this study, the building is modeled as an elastic or inelastic shear beam and the moat wall is simplified as elastic or inelastic stops. Numerical results indicate that the impact wave induced by the bumping can create an extremely high acceleration response in the shear beam (up to 70 times of input motion), if the shear beam remains elastic. A non-linear elastic stop model is observed to reduce the acceleration response. If the shear beam yields, the impact wave cannot propagate through the shear beam and the shear beam remains in the low acceleration response except for the base.

Malhotra (1997) used linear spring element as the moat wall and concluded that for elastic systems the base shear generated by impacts can be higher than the weight of the building; base shear increases with increase in the stiffness of the retaining wall, stiffness of the building and the mass of the base mat. A significant fraction of the initial kinetic energy of the system is lost by impact; energy loss increases with increase in the stiffness of the retaining wall, system damping and mass of the base mat.

The seismic response of multi-story buildings supported on various base isolation systems during impact with adjacent structures was investigated by Matsagar et al. (2003). The isolated building was modeled as a shear type structure with lateral degree-of-freedom at each floor. An impact element in the form of spring and dashpot was used to model the adjacent structure (i.e. retaining wall or entry bridge). The impact response of the isolated building is studied under the variation of important system parameters such as size of gap, stiffness of impact element, superstructure flexibility and number of stories in the base-isolated building. It is concluded that the response of base-isolated structures is affected when impact takes place with the surrounding foundation structures and hence need to be avoided. The effects of impact are found to be severe for the system with flexible superstructure, increased number of stories and greater stiffness of the moat wall.

Komodromos et al. (2007) conducted a series of parametric studies to investigate the influence of potential poundings of seismically isolated buildings with adjacent structures on the effectiveness of seismic isolation. The numerical simulations demonstrated that poundings may substantially increase floor accelerations, especially at the base floor where impacts occur.

Higher modes of vibration are excited during poundings, increasing the story deflections, instead of retaining an almost rigid-body motion of the superstructure as is expected with seismic isolation. Impact stiffness seems to affect significantly the acceleration response at the isolation level, while the displacement response is less sensitive to the variation of the impact stiffness. Finally, the results indicated that providing excessive flexibility at the isolation system to minimize the floor accelerations may lead to a building vulnerable to poundings, if the available seismic gap is limited.

In a more recent study, the effects of seismic pounding on the structural performance of a base-isolated reinforced concrete (RC) building are investigated by Pant et al. (2012). In particular, seismic pounding of a typical four-story base-isolated RC building with retaining walls at the base and with a four-story fixed-base RC building is studied. Three-dimensional finite element analyses are carried out considering material and geometric nonlinearities. The structural performance of the base-isolated building is evaluated considering various earthquake excitations. It is found that the performance of the base-isolated building is substantially influenced by the pounding. The investigated base-isolated building shows good resistance against shear failure and the predominant mode of failure due to pounding is flexural.

As mentioned in Section 1, this study investigates the pounding phenomenon in base isolated buildings from both experimental and analytical perspectives by conducting shake table pounding experiments, developing effective models for impact to moat walls and evaluating the adequacy of code specifications for the gap distance of moat walls. The goal of this study is to determine the effects of pounding on the global response of base isolated buildings through realistic experimental testing and the development of reliable analytical models for moat wall pounding. For the first time, a series of shake table experiments were conducted on base isolated buildings impacting the moat wall and damaging the superstructure. The experiments provide a wealth of data to better understand the dynamics of impact that can lead to further development of new impact element for moat walls and other applications. A reliable model of a base isolated building and moat wall model developed based on experimental observations is used for a comprehensive comparative and collapse study of base isolated building.



## **SECTION 3 PROTOTYPE BUILDING MODEL**

### **3.1. Introduction**

As part of the NEESTips project, a series of conventional and base-isolated buildings were professionally designed by Forell/Elsesser Engineers inc. and adapted here for use in the experimental and numerical studies on structural pounding. The 3-story building models include a conventional Special Moment Resistant Frame (SMRF), a base-isolated Intermediate Moment Resistant Frame (IMRF), a conventional Special Concentric Braced Frame (SCBF), and a base-isolated Ordinary Concentric Braced Frame (OCBF).

The objective of this section is to describe the properties and assumptions in the design of the 3-story IMRF and also OCBF models that are used extensively throughout this study. The three-story IMRF model was selected for the experimental study while IMRF and OCBF models are used in numerical studies in Sections 7 and 8. The scaled experimental model is described in Section 4.

### **3.2. Design Assumptions**

Hypothetical 3-story conventional and base-isolated buildings were designed by Forell/Elsesser Engineers Inc. for use in this project (Figure 3-1). These buildings were designed for occupancy category II and importance factor  $I = 1.0$  according to ASCE 7-05(ASCE 2005). These office buildings were designed by the Equivalent Lateral Force Method to meet the requirements of 2006 International Building Code (ICC 2006), ASCE 7-05 (ASCE 2005), and AISC 341-05 (AISC 2005). The buildings were designed for a Los Angeles, California, location (34.50 N, 118.2 W) on stiff soil (site class D with reference shear wave velocity of 180 to 360 m/s). The mapped spectral accelerations for this location are  $S_s = 2.2$  g for short periods and  $S_1 = 0.74$  g for a 1-s period.

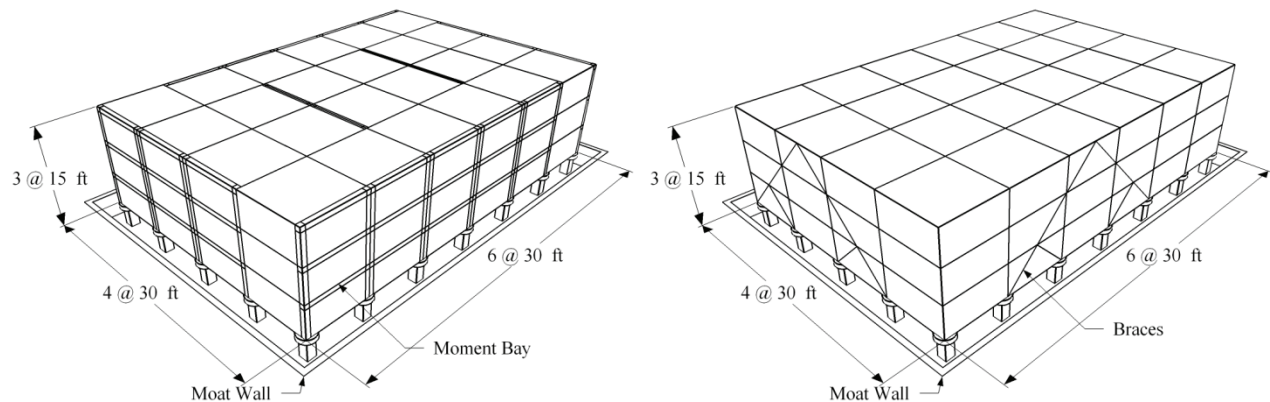


**Figure 3-1 3D View for moment frame and braced frame models**

The moment frame building configurations are based on the plan layout for the 3-story buildings designed for the SAC Steel Project (FEMA 2000a) with modifications. Figure 3-2 shows the plan view of the both IMRF and SMRF models. The model layout is 6 by 4 bays with 30 ft width in both directions. The height of each story is equal to 15 ft. Lateral resistance is provided by two 5-bay perimeter moment frames in the X-direction and two 3-bay perimeter and two 2-bay interior moment frames in the Y-direction; moment-resisting bays are indicated by bold lines in Figure 3-2. Figure 3-4 shows the plan and elevation view of braced buildings. The model dimensions of the braced frame are the same as for the moment frame. The lateral loads of the conventional SCBF are carried by a single braced bay on each side of the building perimeter, while the remaining elements were designed to resist gravity loads only. The bracing in the isolated OCBF is fanned outward from the top down to the base to maximize the resistance to local uplift at the isolation level.

The fixed-based moment frame building was detailed for high ductility as SMRF and uses reduced beam section (RBS) connections, which are prequalified according to AISC 341-05 (AISC 2005). However, the isolated building has lower ductility requirements and was detailed as an intermediate moment-resisting frame (IMRF) utilizing welded unreinforced flange, welded web (WUF-W) beam-column connections. As such, design force reduction factors were  $R = 8$  for the SMRF, and  $R_I = 1.67$  for the isolated IMRF assuming a design yield strength of 50 ksi for structural steel. Design drift limits were 2.5% for the SMRF and 1.5% for the isolated IMRF,

and the design of both buildings was drift controlled. However, the code factor  $C_d$  by which elastic drift is amplified is 5.5 for the SMRF and only 1.67 (equal to  $R_I$ ) for the IMRF.

Moment frame member sections are summarized in Table 3-1 and Table 3-2 respectively for conventional the SMRF and base-isolated IMRF models. The beam and column section for all moment frame lines are similar in each story level.

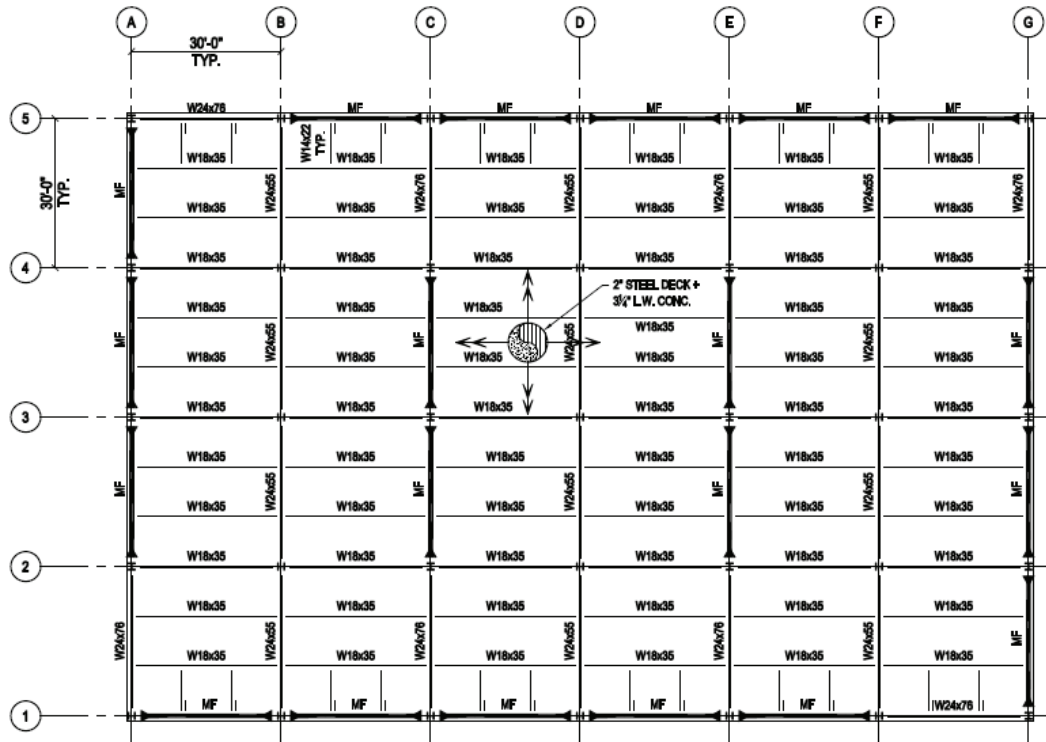


Figure 3-2 Plan view for SMRF and IMRF model

Table 3-1 Member sizes for conventional SMRF.

Story	Columns	Beams
Roof	W14 x 211	W27 x 102
2	W14 x 370	W33 x 130
1	W14 x 370	W33 x 141

Table 3-2 Member sizes for base-isolated IMRF.

Story	Columns	Beams
Roof	W14 x 109	W18 x 60
2	W14 x 176	W24 x 76
1	W14 x 176	W24 x 84

The RBS approach was developed as an improved connection following the unexpected brittle failures of steel moment frame connections in the Northridge earthquake, and is now used extensively (FEMA 2000b). In the RBS configuration, portions of the beam flanges at a section away from the beam end are tapered. This approach has been observed to effectively eliminate brittle fractures by transferring the zone of plasticity away from the column (FEMA 2000b), as well as improve the overall ductility capacity of the beam-to-column assembly. The typical geometry of a circular RBS as they were applied for this project is depicted in Figure 3-3, with only half of the beam is drawn because of symmetry. The flange is tapered starting  $3b_f/4$  ( $b_f$  = beam flange width) from the face of the column over a length  $3d_b/4$  ( $d_b$  is beam depth), and the flange width is reduced by up to 50% in the middle of the taper.

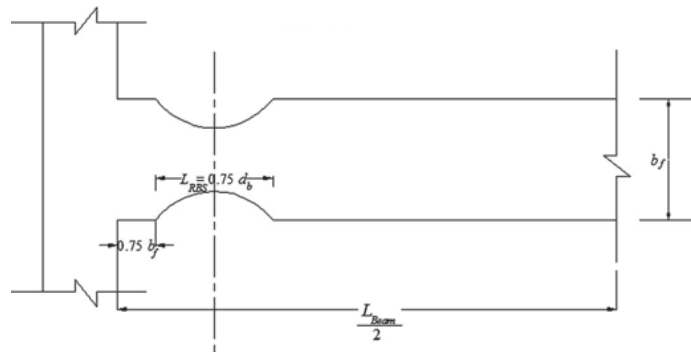


**Figure 3-3 Plan view with typical geometry for RBS (Sayani et al. 2011)**

The fixed-based braced building was designed and detailed as a special concentric braced frame (SCBF), with force reduction factor  $R=6$  and a drift ratio limit of 2.5%, whereas the isolated braced building was designed and detailed as an ordinary concentric braced frame (OCBF) with  $R=1$  and a drift ratio limit of 1.5%. Using an OCBF, which allows for relaxation of brace slenderness ratio and gusset plate detailing requirements, is permitted in Seismic Design Category  $D$  with the restriction that  $R=1$ . The design of both braced buildings was force-controlled, wherein the characteristic yield strength of steel was assumed to be 50 ksi for frame members and 46 ksi for brace members. Table 3-3 and Table 3-4 lists the steel sections for all frame members of both braced buildings.

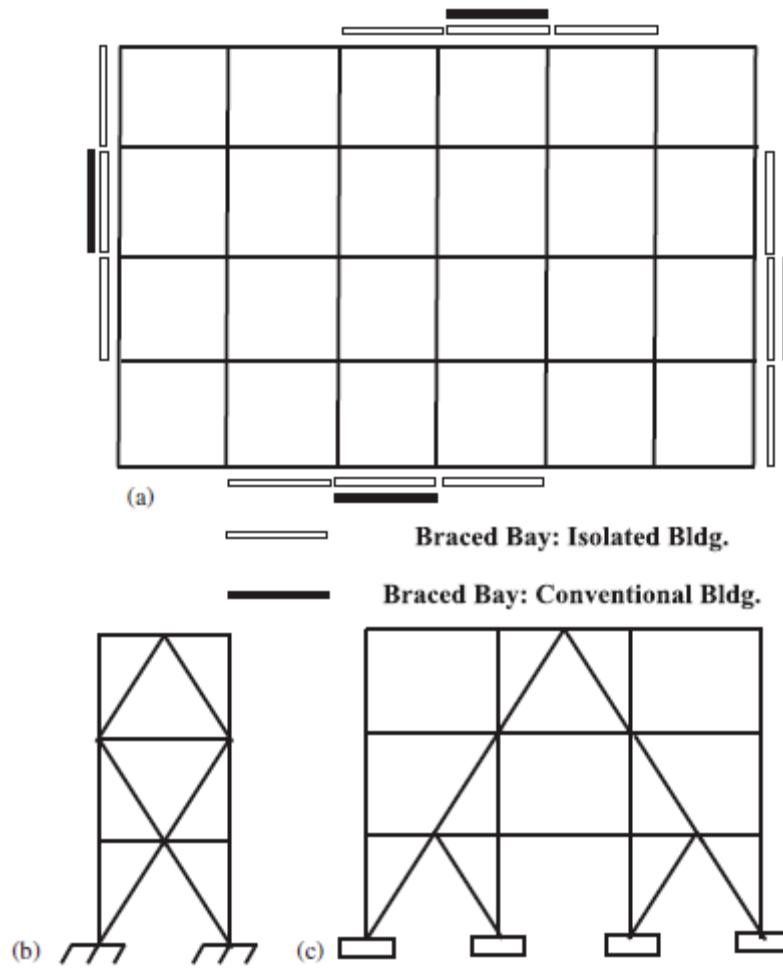


**Figure 3-4 (a) Plan view of braced buildings; elevation view of (b) Conventional and (c) Isolated buildings.**

**Table 3-3 Member sizes for conventional SCBF.**

Story	Column	Girder	Brace
Roof	W14 x 109	W27 x 84	HSS 8 x 8 x 1/2
2	W14 x 176	W30 x 99	HSS 10 x 10 x 5/8
1	W14 x 176	W27 x 84	HSS 12 x 12 x 5/8

**Table 3-4 Member sizes for base-isolated OCBF.**

Story	Column	Girder	Brace
Roof	W12 x 53	W18 x 60	HSS 7 x 7 x 5/8
2	W12 x 72	W24 x 76	HSS 8 x 8 x 5/8
1	W12 x 72	W24 x 84	HSS 10 x 10 x 5/8

Floor slabs for both systems are composed of 3.25-in. thick lightweight concrete over 2-in. thick corrugate steel deck. Seismic mass properties were calculated from anticipated gravity loads on the floors and roof, which include: self-weight of framing, floor/roof dead loads computed from slabs = 42 psf; superimposed floor dead load = 23 psf; superimposed roof dead load = 25 psf; and exterior cladding load = 20 psf. Table 3-5 shows the weight of each model at each level in kips.

**Table 3-5 Model weight based on level.**

Story	SMRF	IMRF	SCBF	OCBF
Roof	2005	1962	1867	1838
2	1918	1812	1789	1768
1	1924	1817	1790	1779
Base Level	-	1745	-	1702

Table 3-6 and Table 3-7 summarize the fundamental periods of each frame. The numbers in this table are obtained from analytical model considering the effect of panel zone flexibility, rigid end offsets to account for clear length dimensions of beams and columns (FEMA 2000a), and for the conventional SMRF only, a multielement approach was used to simulate the behavior of RBS. The fundamental period  $T \approx 1.5$  s for the IMRF superstructure and  $T \approx 0.4$  s for the OCBF superstructure were obtained from a model fixed at the base without considering the isolators.

**Table 3-6 Fundamental periods of moment frame models.**

Period (s)	Conventional SMRF	Base-isolated IMRF at MCE level	Mode
T1	0.83	3.10	Lateral Torsional
T2	0.81	2.99	Bidirectional Lateral
T3	0.52	2.59	Torsional

**Table 3-7 Fundamental periods of braced frame models.**

Period (s)	Conventional SCBF	Base-isolated OCBF at MCE level	Mode
T1	0.43	3.11	Coupled Lateral Torsional
T2	0.43	2.88	Bidirectional Lateral
T3	0.24	2.55	Coupled Lateral Torsional

The maximum displacement and total maximum displacement of the isolation system is calculated from Equations 17.5-1 and 17.5-3 in (ASCE 2005):

$$D_D = \frac{gS_{D1}T_D}{4\pi^2B_D}, \quad D_M = \frac{gS_{M1}T_M}{4\pi^2B_M} \quad (3-1)$$

where  $T_D$ ,  $T_M$  are effective isolation periods at DBE and MCE level;  $B_D$ ,  $B_M$  are coefficients that modify 5% damping spectrum for a specific desired damping (Table 17.5-1 in (ASCE 2005)),  $S_{D1}$ ,  $S_{M1}$  are 1-s spectral accelerations for DBE and MCE events. Based on base-isolated period presented in Table 3-6, Table 3-8 summarizes the design parameters for the isolation system. These parameters are comparable for both systems of IMRF and OCBF since the total weight of the two systems are very close.

**Table 3-8 Design parameters for isolation systems.**

Isolator Properties	DBE Event	MCE Event
Effective period (s)	$T_D = 2.77$	$T_M = 3.1$
Effective Damping (%)	$\beta_D = 24.2$	$\beta_M = 15.8$
Isolator Displacement (in)	$D_D = 12.7$	$D_M = 24.3$
Total Displacement (in)	$D_{TD} = 15.3$	$D_{TM} = 29.4$

The total isolator displacement in Table 2 accounts for displacement amplification attributable to accidental torsion (Equations 17.5-5 and 17.5-6 of ASCE (2005)):

$$D_{TD} = D_D \left[ 1 + y \frac{12e}{b^2 + d^2} \right], \quad D_{TM} = D_M \left[ 1 + y \frac{12e}{b^2 + d^2} \right] \quad (3-2)$$

where  $e$  is the actual eccentricity measured in plan between the center of mass of the structure above the isolation system, plus accidental eccentricity taken as 5 percent of the longest plan dimension of the structure perpendicular to the direction of force under consideration, and  $b$  and  $d$  are the shortest and longest plan dimension of the structure, respectively. The isolation devices were not designed in detail so that the study is neutral with respect to isolation system.

The equivalent lateral load design for both models conducted using base shear coefficients of:

$$C_{S, \text{fixed base}} = \frac{S_{D1}}{TR}, \quad C_{S, \text{isolated base}} = \frac{K_D D_D}{WR_1} \quad (3-3)$$

Where  $K_D$  is secant stiffness of the isolators corresponding to the design period and seismic weight of 7336 kips (7087 kips for OCBF) above the isolated level.

### 3.3. Ground Motion

For the purpose of conducting dynamic time history analysis on prototype models, a hazard curve was defined that quantifies ground motion intensity versus frequency of occurrence, and individual points along the hazard curve represent earthquake scenarios ranging from frequent to rare events (FEMA 2009a). For 2% probability of exceedance (PE) in 50 years (2/50) target spectra was generated and ground motions were selected and amplitude scaled to best match the target spectra. The United States Geological Survey (USGS) national seismic hazard maps (Frankel et al. 2000) were consulted to generate uniform hazard spectra (target spectra) for the three selected events. The target spectra list spectral ordinates at periods  $T = 0.1, 0.2, 0.3, 0.5, 1.0$  and  $2.0$  s. Values at  $0.2$  and  $1.0$  s for the 2/50 event correspond to  $S_S$  and  $S_1$  values for the MCE.

The target spectrum is based on a reference shear wave velocity  $V_s = 2,493$  ft/s, and were thus modified to reflect the assumed site conditions site class D with  $V_s$  from  $591$  to  $1,181$  ft/s. To modify the target spectra, spectral site modification factors that depend on both ground motion intensity and period were developed from next generation attenuation (NGA) relations. This approach is consistent with site modification factors  $F_a$  and  $F_v$  used in building codes but reflects the additional periods accounted for in the target spectra. Specifically, site factors were computed as the ratios of spectral acceleration at  $2,493$  ft/s and  $886$  ft/s, with all other factors held constant. Site factors were restricted not to fall below  $1.0$ , even in the short period range. The target spectrum is plotted in Fig. 6 compared with the MCE spectrum for the same location.

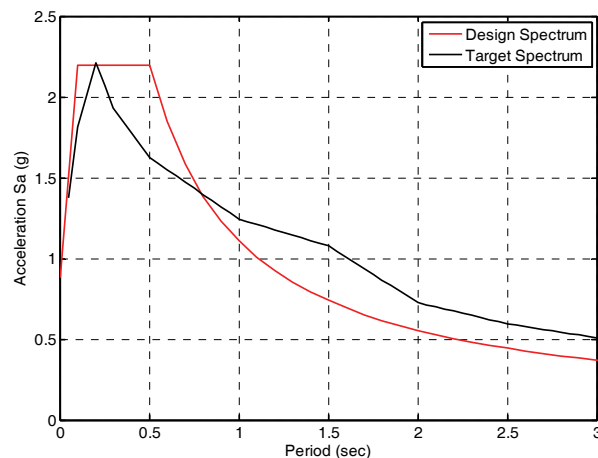


**Figure 3-5 MCE and target spectrum for assumed site location**

For the selected hazard level (2/50) 10 recorded natural ground motions that conform to the magnitude, distance, and site class were selected from the Pacific Earthquake Engineering Research Center (PEER) NGA database (Chiou et al. 2008). Although using recorded ground motions was considered to be ideal, 10 pairs of ground motions from SAC steel project Los Angeles (SAC-LA) ground motion sets were added to obtain a better match between the target hazard spectra and the median response spectra in the long period range. These SAC motions were originally selected for similar location and site conditions and frequency modified to match the target spectra (Somerville et al. 1998). Using USGS seismic deaggregation data (Frankel et al. 2000), ground motions were selected according to the percentage contribution of magnitude and distance pairs to the seismic hazard for the given scenario, which was determined by averaging the deaggregation data over the various periods. Each pair of records was amplitude scaled by a common factor that minimized the difference of the mean spectrum of the components and the target spectrum in the least square sense from  $T = 0$  to 3 s. The selection and scaling procedures were based on a range of periods, since the motions were applied to buildings with significantly different fundamental periods. The ground motions selected for the nonlinear response history analyses for the 2/50 events, are listed in Table 3-9. In this table, the first 10 ground motions are from SAC steel projects and the next 10 are from PEER data base.

Figure 3-6 compares 5% damped acceleration spectra (median of the x and y components) of the 20 pairs of scaled motions along with their median with the target spectra for each hazard level and Design spectrum. A large variance in spectra for individual motions relative to the median is observed. In particular, this includes some motions with peak accelerations that are 2–3 times the target values at high frequencies. The 2/50 event contains at least one motion with very large spectral accelerations in the long period range. However, the median spectrum falls somewhat short of the target spectrum beyond  $T = 1.5$  s despite the introduction of frequency modified motions.

**Table 3-9 List of the 20 ground motions.**

NO.	Record Tag	Record Name	Magnitude	Distance (km)	Number of Points	$\Delta t$ (sec)	PGA (g)
GM-1	LA21 & LA22	1995 Kobe	6.9	3.4	3000	0.02	1.28
GM-2	LA23 & LA24	1989 Loma Prieta	7	3.5	2500	0.01	0.47
GM-3	LA25 & LA26	1994 Northridge	6.7	7.5	2990	0.005	0.94
GM-4	LA27 & LA28	1994 Northridge	6.7	6.4	3000	0.02	1.33
GM-5	LA29 & LA30	1974 Tabas	7.4	1.2	2500	0.02	0.99
GM-6	LA31 & LA32	Elysian Park (simulated)	7.1	17.5	3000	0.01	1.30
GM-7	LA33 & LA34	Elysian Park (simulated)	7.1	10.7	3000	0.01	0.78
GM-8	LA35 & LA36	Elysian Park (simulated)	7.1	11.2	3000	0.01	1.10
GM-9	LA37 & LA38	Palos Verdes (simulated)	7.1	1.5	3000	0.02	0.78
GM-10	LA39 & LA40	Palos Verdes (simulated)	7.1	1.5	3000	0.02	0.62
GM-11	NGA1084	Northridge-01 1994	6.69	5.35	8000	0.005	0.71
GM-12	NGA0527	N. Palm Springs 1986	6.06	12.07	4030	0.005	0.21
GM-13	NGA1106	Kobe, Japan 1995	6.9	0.96	2400	0.02	0.71
GM-14	NGA1054	Northridge-01 1994	6.69	7.46	4425	0.005	0.51
GM-15	NGA1044	Northridge-01 1994	6.69	5.92	2000	0.02	0.70
GM-16	NGA1120	Kobe, Japan 1995	6.9	1.47	4095	0.01	0.65
GM-17	NGA0821	Erzican, Turkey 1992	6.69	4.38	4260	0.005	0.49
GM-18	NGA1605	Duzce, Turkey 1999	7.14	6.58	5175	0.005	0.43
GM-19	NGA1141	Dinar, Turkey 1995	6.4	3.36	5595	0.005	0.30
GM-20	NGA	Parkfield 2004	6	4.8	1048	0.02	0.82

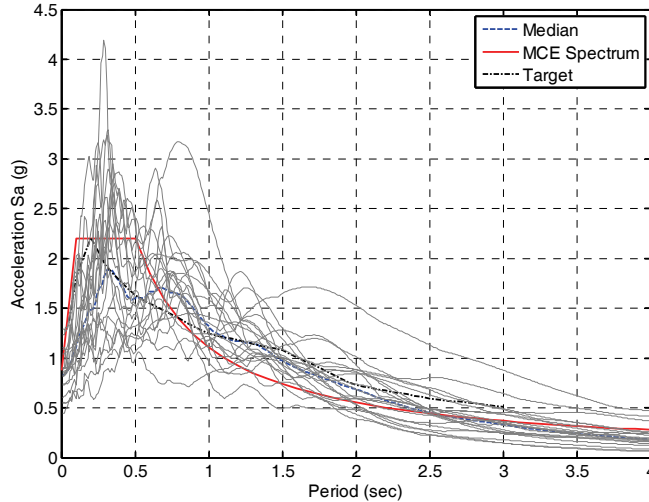


**Figure 3-6 Median of 20 ground motions in comparison with the target and MCE spectra**

It's important to mention that the procedure used in this study for scaling the ground motions complies to the requirements of ASCE7-05 (2005) for scaling ground motions. ASCE7-05 (2005) requires that the average of the SRSS spectra of the fault-normal and fault-parallel components of the scaled motions not be less than 1.3 times the MCE spectrum by more than 10% in the period range of  $0.5T_D$  to  $1.25T_M$ . Figure 2-1 compares the average of SRSS spectra of the fault-normal and fault-parallel components of the 20 ground motions pairs with 90% of 1.3 times MCE spectrum. It can be seen that the average of the SRSS of the two components of the 20 ground motions are not less than 90% of 1.3 times MCE spectrum in the specified range.

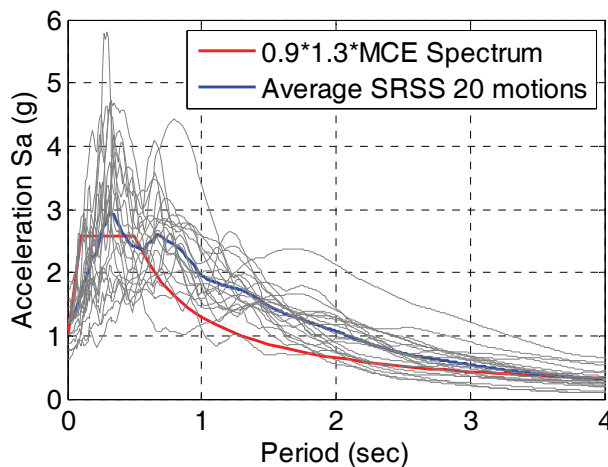


**Figure 3-7 The average of SRSS of the 2 components of 20 ground motions in compare with the MCE spectrum**



## **SECTION 4**

### **DESCRIPTION OF SHAKE TABLE TESTING PROGRAM**

#### **4.1. Introduction**

This section describes an experimental program designed to capture the behavior of base isolated buildings impacting against their surrounding moat wall under extreme ground motions. The test program consist of shake table testing of a quarter-scale model representative of the three-story IMRF described in Section 3 using the NEES equipment site at the Structural Engineering and Earthquake Simulation Laboratory (SEESL) at the University at Buffalo. The base isolated IMRF model was selected for the experimental program due to availability of scaled members and simplicity in fabrication. However, both base isolated buildings including the IMRF and OCBF are used in numerical simulations presented latter in this report. The principal objective of these experiments was to generate experimental data for base isolated building pounding a moat wall, specifically the impact force and the superstructure response. This data is subsequently used to validate the numerical models of structural pounding. In addition to generating unique data on structural pounding, the behavior of a base isolated building impacting different types of moat wall installed at different gap distance was also of investigated.

The shake table testing described herein occurred in three phases. The first stage examined the response of fixed-base three-story IMRF model. The data generated in this phase was used to validate numerical model of IMRF and also examined the response of superstructure in the inelastic range. In the second phase, isolation devices were installed at the base level of the IMRF model and the response of base isolated model was examined under different level of ground motion. The third and last phase of the testing examine the response of the base isolated three-story IMRF including pounding to a moat wall. For this purpose, different types of moat walls were installed at various gap distances relative to base level of isolated model and different ground motions were applied to capture the variation in response with moat wall stiffness and impact velocity.

In this section, the scaled IMRF superstructure is first described considering similitude and dimensional analysis. Then, the properties of the isolation device and a detailed description of

the moat walls are provided. Following the description of the test setup components, the experimental testing schedule is presented.

## 4.2. Description of Model Structure

The experimental building model was scaled by 1/4 in length of the three-story prototype to satisfy the limitations of the earthquake simulator at the University at Buffalo, considering the potential impact forces. The test specimen represents a single bay of an internal moment frame in the prototype structure excited in one horizontal direction. Figure 4-1 shows the position of the selected internal frame that was scaled down for purpose of shake table testing.

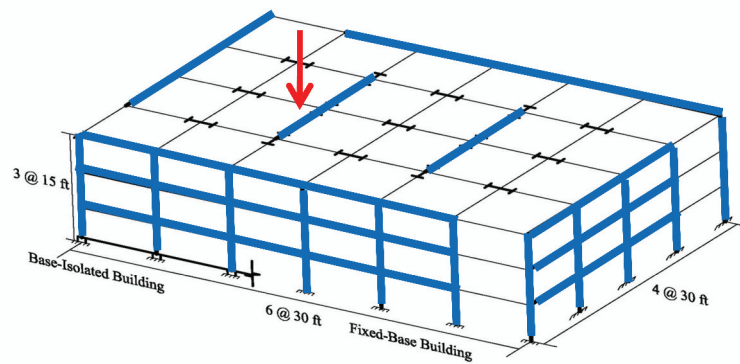


**Figure 4-1 The position of the selected internal bay for shake table testing**

The selected prototype frame was reduced to a quarter-scale model according to the geometric similitude law. The scale factor for length was chosen  $\lambda_L = 4$ , and for acceleration  $\lambda_a = 1$ . Since the same material is used for the prototype and model, the scale factor for elastic modulus also has a value of unity,  $\lambda_E = 1$ . Following the principles of similitude and dimensional analysis described in Bracci *et al.* (1992), all other scale factors are dependent on these three aforementioned factors. The complete list of scale factors is provided in Table 4-1.

Based on the three independent predefined scale factors, the required scaling factor for material density is  $\lambda_p^{req} = 1/\lambda_L = 1/4$ . However, the model structure is the same as the prototype, meaning that the provided material density is the same as the prototype or  $\lambda_p^{prov} = 1$ . Since the required and provided material densities are different, additional mass must be added to the model so that the dependent quantities (mass, gravitational force and frequency) are scaled

properly. This extra mass is referred to artificial mass. To satisfy similitude laws, artificial mass (steel plates and concrete blocks) equal to 10.7 kips was added to the structure at each floor.

**Table 4-1 Comparison of required and provided scale factors for scaled model**

Quantity	General Case	Same Material and Acceleration	
		Required	Provided
Geometric Length, l	$\lambda_l = ?$	$\lambda_l = 4.00$	$\lambda_l = 4.00$
Elastic Modulus, E	$\lambda_E = ?$	$\lambda_E = 1.00$	$\lambda_E = 1.00$
Acceleration, a	$\lambda_a = ?$	$\lambda_a = 1.00$	$\lambda_a = 1.00$
Density, $\rho$	$\lambda_\rho = \lambda_E / \lambda_l \lambda_a$	$\lambda_\rho = 0.25$	$\lambda_\rho = 1.00$
Velocity, v	$\lambda_v = \sqrt{\lambda_l \cdot \lambda_a}$	$\lambda_v = 2.00$	$\lambda_v = 2.00$
Forces, f	$\lambda_f = \lambda_E \cdot \lambda_l^2$	$\lambda_f = 16.00$	$\lambda_f = 16.00$
Stress, $\sigma$	$\lambda_\sigma = \lambda_E$	$\lambda_\sigma = 1.00$	$\lambda_\sigma = 1.00$
Strain, $\epsilon$	$\lambda_\epsilon = 1.00$	$\lambda_\epsilon = 1.00$	$\lambda_\epsilon = 1.00$
Area, A	$\lambda_A = \lambda_l^2$	$\lambda_A = 16.00$	$\lambda_A = 16.00$
Volume, V	$\lambda_V = \lambda_l^3$	$\lambda_V = 64.00$	$\lambda_V = 64.00$
Second Moment of Area, I	$\lambda_I = \lambda_l^4$	$\lambda_I = 256.00$	$\lambda_I = 256.00$
Mass, m	$\lambda_m = \lambda_\rho \cdot \lambda_l^3$	$\lambda_m = 16.00$	$\lambda_m = 64.00$
Impulse, i	$\lambda_i = \lambda_l^3 \cdot \sqrt{\lambda_\rho \cdot \lambda_E}$	$\lambda_i = 32.00$	$\lambda_i = 64.00$
Energy, e	$\lambda_e = \lambda_E \cdot \lambda_l^3$	$\lambda_e = 64.00$	$\lambda_e = 64.00$
Time (Period), t	$\lambda_t = \sqrt{\lambda_l / \lambda_a}$	$\lambda_t = 2.00$	$\lambda_t = 2.00$
Gravitational Acceleration, g	$\lambda_g = 1.00$	$\lambda_g = 1.00$	$\lambda_g = 1.00$
Gravitational Forces	$\lambda_{fg} = \lambda_\rho \cdot \lambda_l^3$	$\lambda_{fg} = 16.00$	$\lambda_{fg} = 64.00$
Critical Damping, $\xi$	$\lambda_\xi = 1.00$	$\lambda_\xi = 1.00$	$\lambda_\xi = 1.00$

Base on scale factors described in Table 4-1 the bay width for moment frame is 96 in. with story height of 47.25 in. at each of the three stories. Columns were constructed from S5x10 section and S4x9.5, 4x7.7, and 3x7.5 sections were used for first, second, and third floor beams respectively. Figure 4-2 shows the scaled moment resisting frame used in this study and sections used for each member.

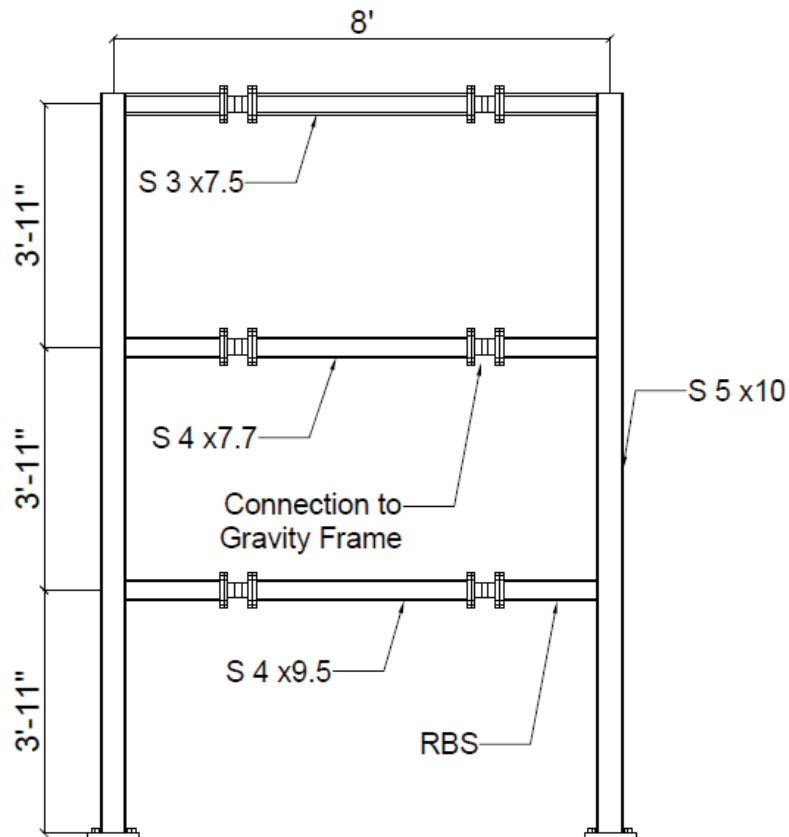


**Figure 4-2 The scaled IMRF used in shake table study.**

Unlike most previous seismic isolation experiments, the limit state tests planned here have a significant potential to yield the superstructure. In order to yield the superstructure at realistic load levels and mechanisms, further constraints were imposed in properly scaling the strength and stiffness of the frame relative to the bearings properties. For this purpose, reduced sections were used at both ends of the beams to obtain the desired strength based on FEMA 350 (2000c). The moment frame was designed such that the scaled strength and stiffness distribution of beams and columns is comparable to the prototype. Four identical moment frames were constructed for

the test series, and were replaced within the gravity frame after experiencing major damage so that comparisons could be made between undamaged nominally identical specimens.

**Table 4-2 Comparison of prototype and scaled model element properties**

	Section	I (in <sup>4</sup> )	I/I <sub>beam1</sub>	Target (Prototype)	B <sub>f</sub> (in)	Z (in <sup>3</sup> )	Z/Z <sub>beam1</sub>	Target (Prototype)
Column	S5X10	12.3	1.8	0.9	3.00	5.6	1.61	1.43
Beam1	S4X9.5	6.79	1.0	1.0	2.10 <sup>1</sup>	3.3	1.00	1.00
Beam2	S4X7.7	6.08	0.9	0.9	1.75 <sup>1</sup>	2.8	0.85	0.89
Beam3	S3X7.5	2.93	0.4	0.4	1.55 <sup>1</sup>	2.0	0.60	0.55

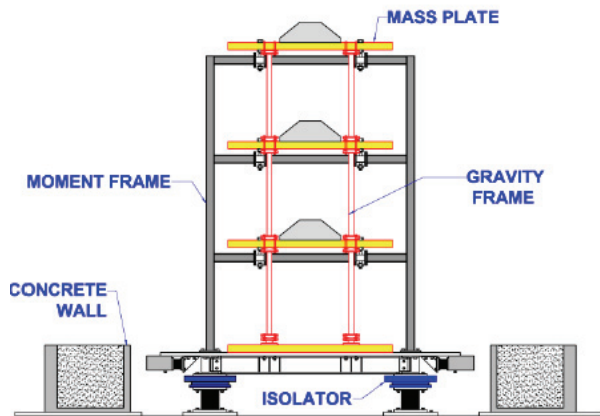
<sup>1</sup> Reduced beam section

Table 4-2 summarized the properties of scaled model element properties and compared them with target value from the prototype structure. In order to yield the superstructure at realistic load levels and mechanisms, relative plastic section modulus of each member to first level beam section was compared with corresponding value in the prototype model. The flange width in this table includes the reduced beam section width in order to have equivalent lateral strength in comparison to the prototype.

The lateral resisting frame was coupled with a gravity frame that provides the inertia for the shake table specimen; the lateral resisting frame is the only component that needs to be replaced if the superstructure is damaged. The gravity frame was developed for collapse simulations and has not been previously used on a seismically isolated building, requiring some modifications (Kusumastuti et al. 2005). The gravity frame is one bay by one bay frame which is braced for out of plane direction. For in plane direction, the gravity frame has no resistance in order to investigate the behavior of the main frame (moment frame). For this purpose, at both ends of the gravity frame columns, concave plates were designed in order to rotate easily without any resistance. Figure 4-3 shows the end of the gravity frame columns. The final shake table model is a unidirectional model with a single 1 bay by 1 bay gravity frame providing the dynamic inertia supported by a single bay steel moment frame installed in the centerline of the gravity frame (Figure 4-4). The superstructure weight at each level is shown in Table 4-3 .



**Figure 4-3 Photograph of gravity frame connection.**



**Figure 4-4 Illustration and photograph of shake table test setup.**

**Table 4-3 The superstructure weight at each level**

Level	Weight (kips)
Base floor	18.482
First floor	10.927
Second floor	10.927
Third floor	10.732

The unidirectional IMRF was connected to the gravity frame at two points of the beams in each level with a special vertical pin connection that tied the structures together in the horizontal direction but did not transfer forces in the vertical direction by allowing slip (Figure 4-5).



**Figure 4-5 Photograph of especial beam to gravity frame connection.**

The base floor of the isolated building model was constructed from a steel frame and steel plates for added mass. This base level frame designed and built for purpose of this project. A concrete block was attached at each end of the base plate in order to simulate the material contact interface for the pounding experiments (Figure 4-6).

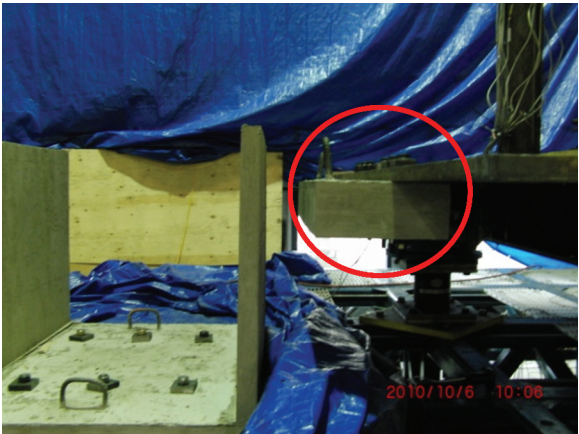


**Figure 4-6 Photograph of concrete block attached to base level to simulate contact surface.**

Four single FP isolators were used with the inner radius of 32 in and the maximum displacement capacity of 8.0 in. Figure 4-7 shows the dimension and properties of the single FP used in this study.

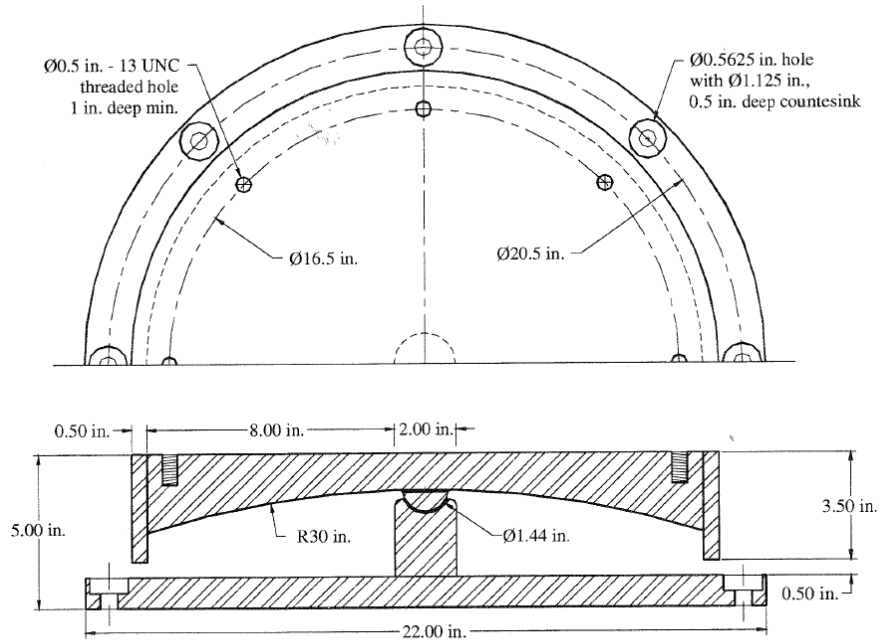


**Figure 4-7 Illustration of single friction pendulum used in this study (Mosqueda et al. 2004).**

### 4.3. Description of the Moat Wall

For the test involving pounding, the moat wall was modeled as either a concrete wall with soil backfill (Figure 4-8(a)) or a rigid steel plate (Figure 4-8(b)). Different scaled concrete wall thicknesses of 2, 4, and 6 in were tested to examine the effect of wall stiffness on the pounding behavior. A rigid steel wall was also used to cover a wider range of wall properties. The rigid steel wall was connected to the shake table using 4 long bolts which provided some flexibility in the connection in earlier tests due to rocking at the base. In latter tests, the steel wall connection was reinforced with welds at the points indicated in Figure 4-8(b) in order to increase the effective wall stiffness.



**Figure 4-8 Photograph of different types of moat wall used in impact purpose.**

The concrete moat walls were built in “U” shape with width of 48 in. and a distance of 36 in (Figure 4-6) between two sides. Four sets of concrete walls with different front and back wall thicknesses were built to examine effect of wall thickness on impact force. Each concrete wall was installed on the shake table using four long steel rods. The space between two sides of the wall was filled with a large sand bag and fastened with two plywood sheets on each open side to contain the sand (Figure 4-8(a)).

The steel walls were also used to cover a wide range of wall stiffness. The steel walls were attached to shake table extension using four long steel rods providing some flexibility. The steel walls sit on four 9 in. steel pedals to level the walls with concrete blocks attached to the base plate of structure. Later, linear welding was used to stiffen the connections of steel walls to the shake table. The long slotted holes on the two sides of these steel walls allowed for easy adjustment of the gap distance.

#### **4.4. Instrumentation**

Several instruments were used to record the structural response of the model, primarily acceleration, displacement, and force at each level of the building model in the main direction of testing. Acceleration and displacement transducers were also installed on the moat wall to measure its response during impact. Most of the accelerometers installed in the structure had a frequency range of 0-400 Hz; six high performance accelerometers calibrated to frequency range exceeding 2000Hz were placed at each level of the frame and at the moat walls in order to obtain more reliable measurements at key points during pounding. Table 4-4 and Table 4-5 list all

accelerometers and string potentiometers used in this study. Their locations on the shake table model are indicated in the table. Accelerometers A16-20 are the six high performance accelerometers used to capture acceleration during impact phenomena. The linear potentiometer has 43 inches of maximum length capacity, a predicted life of 1 million full-stroke cycles and it is operational in a environment temperature of  $-4^{\circ}$  to  $212^{\circ}$  F. The accelerometer used was the model JTF general purpose accelerometer and it is a piezoresistive type; a strain gage based, the same as a piezoelectric one but with a built in resistor used in standard signal conditioner. Figure 4-9 and Figure 4-10 show the elevation view and top view of accelerometers and string potentiometer positions on the shake table model.

**Table 4-4 List of accelerometers and their location.**

Channel No.	Designation	Direction	Measurement
1	A1	East-West	South corner of base plate
2	A2	East-West	North corner of base plate
3	A3	East-West	East Column, Level1
4	A4	East-West	East Column, Level2
5	A5	East-West	East Column, Level3
6	A6	East-West	South corner of mass plate, Level1
7	A7	East-West	North corner of mass plate, Level1
8	A8	East-West	South corner of mass plate, Level2
9	A9	East-West	North corner of mass plate, Level2
10	A10	East-West	South corner of mass plate, Level3
11	A11	East-West	North corner of mass plate, Level3
12	A12	Vertical	Vertical acceleration of base plate on West
13	A13	Vertical	Vertical acceleration of base plate on East
14	A14	South-North	East corner of base plate
15	A15	South-North	West corner of base plate
16	A16	East-West	base plate
17	A17	East-West	Center of mass plate, Level1
18	A18	East-West	Center of mass plate, Level2
19	A19	East-West	Center of mass plate, Level3
20	A20	East-West	East Front Wall
21	A21	East-West	East Back Wall
22	A22	East-West	West Front Wall
23	A23	East-West	West Back Wall

**Table 4-5 List of string potentiometer and their location.**

Channel No.	Designation	Direction	Measurement
1	S1	East-West	South corner of base plate
2	S2	East-West	North corner of base plate
3	S3	East-West	West Column, Level1
4	S4	East-West	West Column, Level2
5	S5	East-West	West Column, Level3
6	S6	East-West	South corner of mass plate, Level1
7	S7	East-West	North corner of mass plate, Level1
8	S8	East-West	South corner of mass plate, Level2
9	S9	East-West	North corner of mass plate, Level2
10	S10	East-West	South corner of mass plate, Level3
11	S11	East-West	North corner of mass plate, Level3
12	S12	Vertical	Vertical displacement of base plate on West
13	S13	Vertical	Vertical displacement of base plate on East
14	S14	South-North	East corner of base plate
15	S15	South-North	West corner of base plate
16	S16	East-West	West Front Wall
17	S17	East-West	West Back Wall
18	S18	East-West	East Front Wall(negative)
19	S19	East-West	East Back Wall(negative)
20	S20	East-West	West gap
21	S21	East-West	East gap

A five-component load cell was located under each bearing to measure the axial force, shear force and moment during testing. These multiaxial 12 inches five component load cells, have maximum load capacity of 100 kips in axial, 20 kips in shear and 220 kip-in in moment. Two uniaxial load cells were designed and installed behind each of the concrete impact bumper blocks to measure the magnitude and duration of the impact force (Figure 4-11).

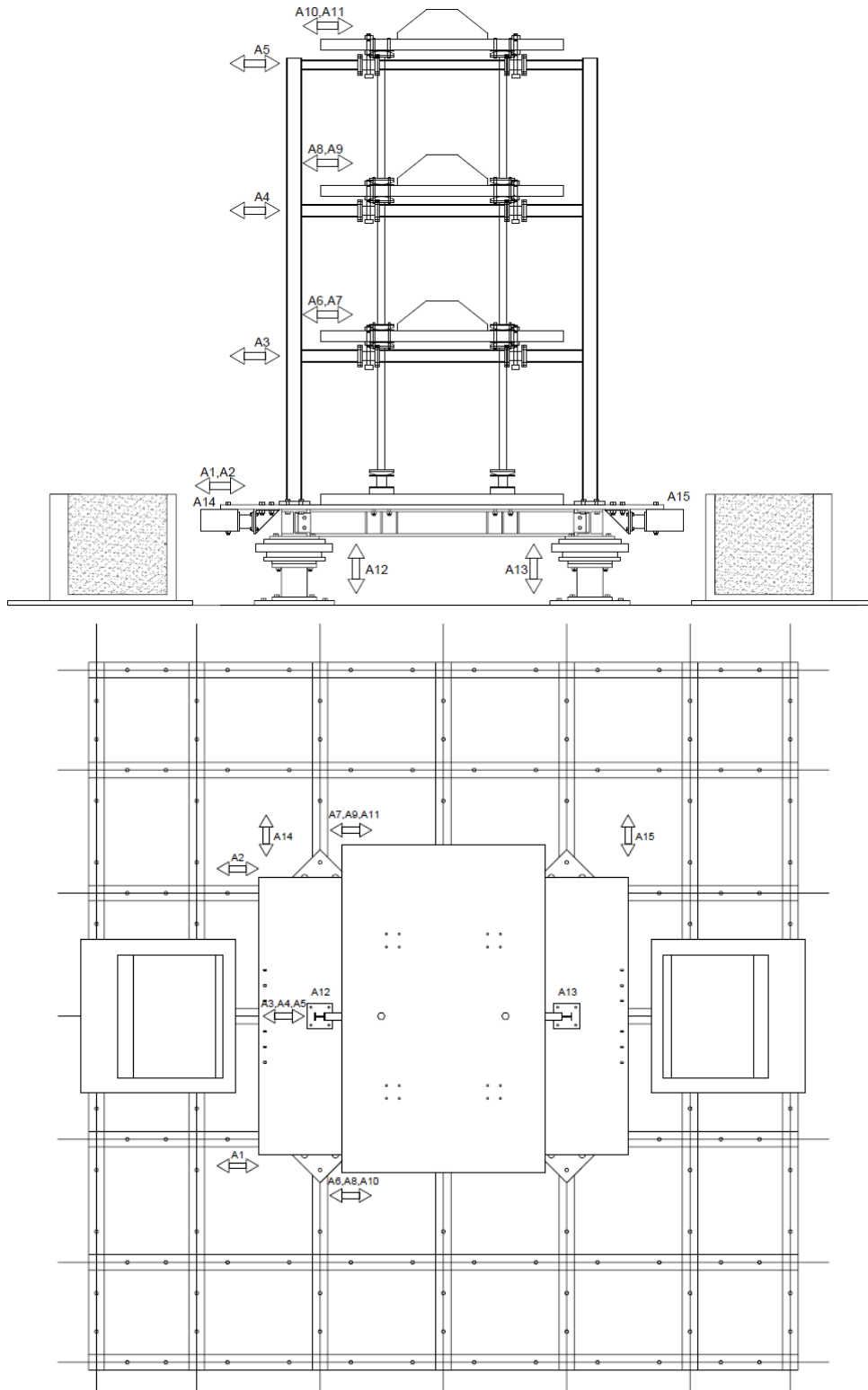


**Figure 4-9 Elevation and top view of accelerometers positions.**

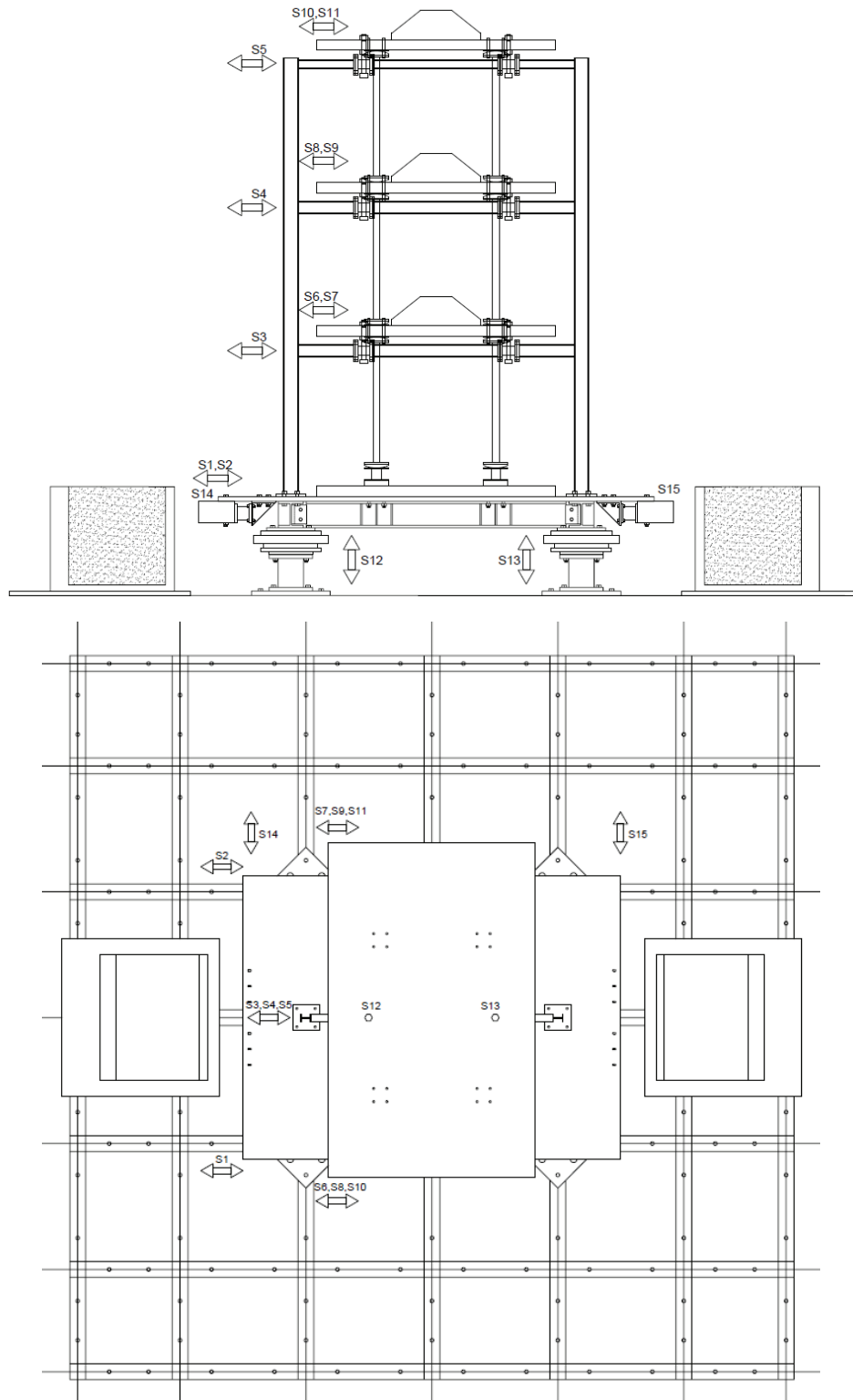


**Figure 4-10 Elevation and top view of string potentiometer positions.**

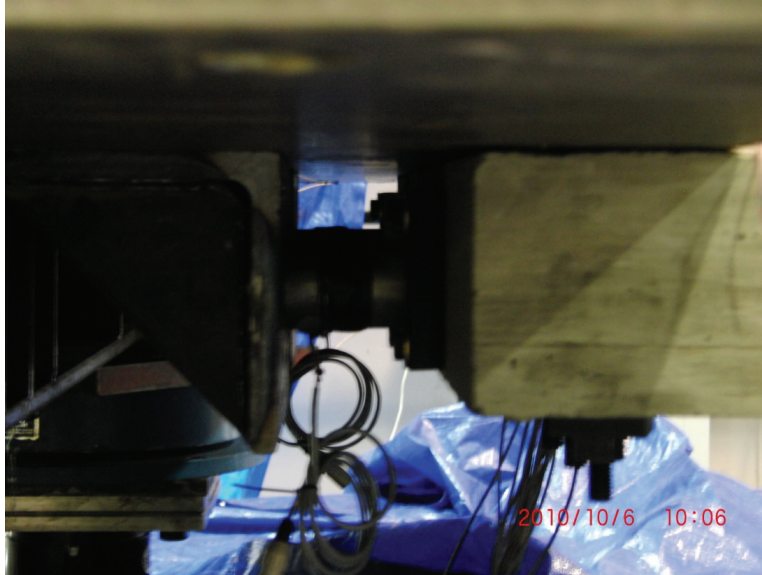


**Figure 4-11 Impact load cells.**

Strain gages were installed on the moment frame to measure strain during testing. The strain gages were installed on first story column and each level beam. Figure 4-12 shows location of the strain gages on the moment frame. This figure shows half of the frame with the other half having similar instrumentation.

In total, 108 channels of data were recorded at a rate of 2500 Hz during the impact testing, while a sampling rate of 256 Hz was used for tests without impact.

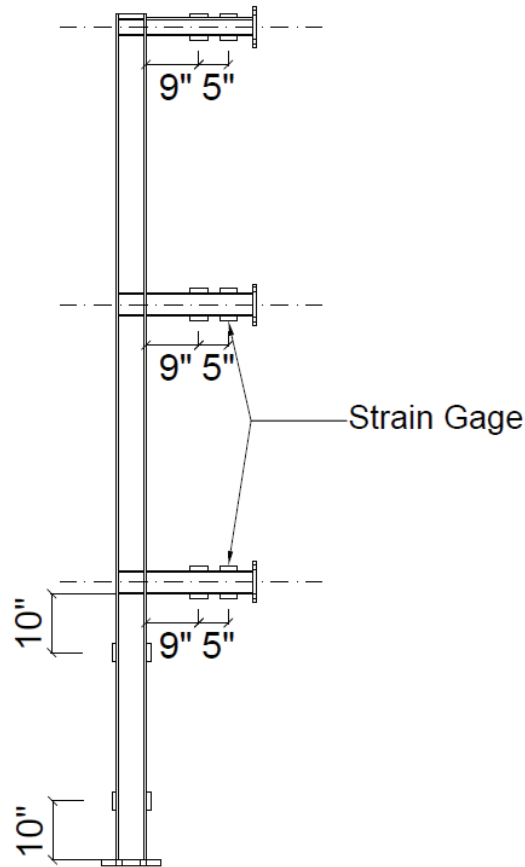


**Figure 4-12 Location of strain gages on the moment frame.**

#### **4.5. Earthquake Records**

Based on the  $\pm 6$  in. displacement capacity limit of the earthquake simulator, six ground motions were selected from the earthquake record bin of the NEES TIPS project (Table 3-8). Target spectra were generated for the Maximum Considered Earthquake (MCE) event, then each record was amplitude scaled by a factor that minimized the difference of the spectrum of the record and the target spectrum in the least square sense from  $T = 0$  to 3 sec. The selection and scaling procedures were based on a range of periods since the motions were applied to fixed and isolated buildings with significantly different fundamental periods. Table 4-6 lists the properties of these six ground motions. It is important to note that the SAC motions were originally selected for similar location and site conditions, and the frequency content was modified to match the target spectra (Somerville et al. 1998). Figure 4-13 shows acceleration spectra for individual scaled

motions used in this study and compares them with target spectrum obtained based on mapped spectral accelerations for the scaled model.

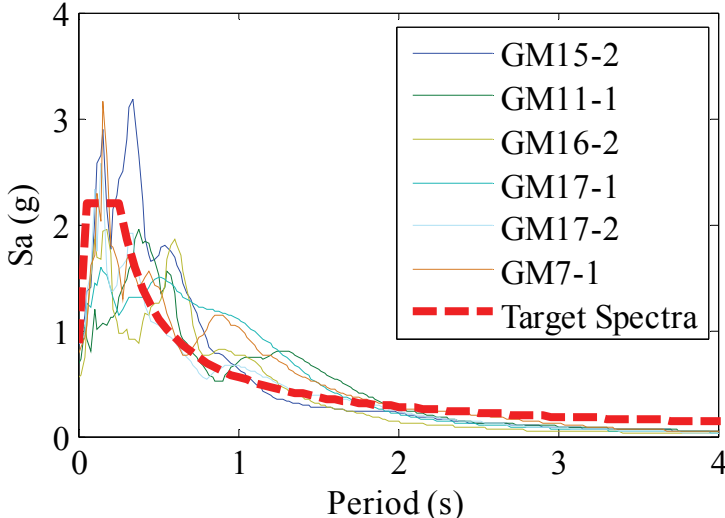


**Figure 4-13 Spectral acceleration for individual scaled motions and target spectra for scaled model.**

**Table 4-6 List of ground motion properties used in scaled model experiment testing.**

Record ID	Record Title	Earthquake	MCE Amplitude Scale Factor	Original Earthquake (full scale)				Scaled Earthquake (max. level) (1/4 scale)			
				PGA (g)	PGD (in)	Duration* (s)	PGA (g)	PGD (in)	Duration* (s)		
GM7-1	LA33	Simulated	1.00	0.78	19.7	5.6	0.78	4.9	2.8		
GM11-1	Sylmar	1994 Northridge	1.11	0.61	21.4	5.5	0.68	5.9	2.8		
GM15-2	Newhall	1994 Northridge	1.46	0.59	15.0	15.1	0.86	5.5	7.5		
GM16-2	Takatori	1995 Kobe	0.89	0.62	12.9	9.9	0.55	2.8	4.9		
GM17-1	Erzincan NS	1992 Erzincan	1.76	0.52	10.9	7.5	0.91	4.8	3.7		
GM17-2	Erzincan EW	1992 Erzincan	1.76	0.50	8.6	7.3	0.88	3.8	3.7		

\* Duration is determined as time interval between 5-95% of Arias intensity.

## 4.6. System Identification

Initial experimental tests were performed to identify the structural and dynamic properties of the scaled fixed base building model through dynamic testing. The tests included pull-back (3 tests), snap-back (2 tests), white-noise (1 test), sine-sweep (1 tests), and Impulse (1 tests). The testing follows the work of Bracci *et al.* (1992). The data was analyzed with DADISP and further interpreted to identify modal frequencies and shapes, as well as determining the stiffness and damping matrices.

The model was tested with 5 types of loadings: pull-back (PB1, PB2, PB3); snap-back (SB1, SB2), white-noise (WN), sine-sweep (SS), and Table Impulse (TBI). Afterward, the data collected was analyzed using DADISP 2002 software for each loading. For the pullback test, the displacement-force functions at each level of the frame and the flexibility vector for the pullback load were determined. For the snap-back test, the transfer function at each external joint of the frame at each level to the excitation force was calculated. The transfer function is defined as an output structural response normalized by a superimposed input base motion in the frequency domain. The first three modal frequencies could be found considering the peaks of the transfer functions of the accelerometers of each story. The damping ratios for each mode through the logarithmic decrement can be determined in Snap Back tests for each frequency band of +/-20% of modal frequency. The damping ratios were calculated based on half band theory in all other tests. Using ratios of amplitude of transfer functions at modal frequencies, the modal shapes of the frame can be found at each floor. To determine the sign of modal shape, the phase of the transfer function is considered. Using the above information, the stiffness and damping matrix of the structure is derived in terms of mass and the orthogonal modal shape matrix.

A wide band frequency response (0.1~50 Hz) white noise excitation with amplitude of 0.1g was applied on the fixed base model. This test was repeated after each dynamic test presented in the next section in order to measure changes in dynamic properties that could indicate possible damage in the structure. Figure 4-14 shows the transfer function obtained from white noise excitation for each story.

The model was also imposed to sine sweep excitation in a range covering first three modal frequencies of the model. The properties of the sine sweep were selected in such a way that maximum displacement of the table extension is limited to 5 inches, which is almost its capacity. The starting frequency was set at 0.25 Hz and it is bounded to 16 Hz for a total of seven octaves. The amplitude is 0.05g and the time for each octave is three seconds.

Based on results of eigenvalue analysis from numerical model and also from white noise system identification test results, three sine impulse signals produced with frequencies close to first three frequencies of the model. These table impulses applied on shake table and acceleration and displacement response of the moment frame was obtained from instrumentations. Table 4-7 summarizes all system identification test results. Modal Frequencies, modal shape, stiffness matrix, damping ratios, and damping matrix are shown in this table.

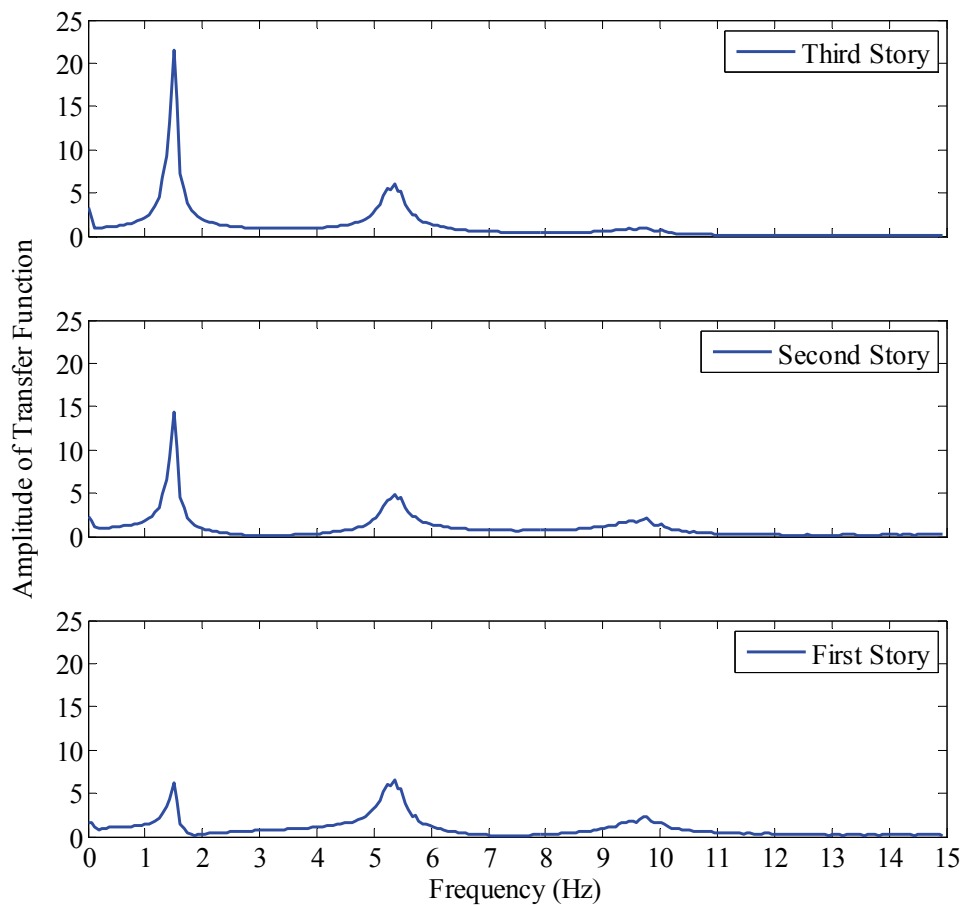


**Figure 4-14 Transfer function amplitude obtained from white noise excitation of fixed base frame.**

Table 4-7 System identification test results summary.

Test	$f_i$ (Hz)	$\phi_{ij}$	$K_{ij}$ (kips/in)	$\xi_{ij}$ (%)	$C_{ij}$ (kips*s/in)
Pull Back	[1.51]	[1.00 -0.78 0.15]	[16.33 -27.82 13.74]	-	-
	[6.02]	[0.61 1.00 -0.62]	[-27.81 79.81 -84.59]		
	[14.40]	[0.23 0.74 1.00]	[13.72 -84.53 168.04]		
Snap Back	[1.58]	[1.00 -0.78 0.35]	[17.58 -25.73 7.18]	[2.4]	[0.098 -0.033 0.003]
	[5.53]	[0.66 0.74 -0.98]	[-25.73 58.97 -39.39]	[2.5]	[-0.033 0.142 -0.032]
	[10.06]	[0.29 1.00 1.00]	[7.18 -39.39 67.58]	[7.0]	[0.003 -0.032 0.156]
White Noise	[1.5]	[1.00 -0.84 0.32]	[15.38 -21.22 3.60]	[5.8]	[0.040 -0.020 0.008]
	[5.25]	[0.67 0.73 -0.99]	[-21.22 51.98 -34.24]	[2.7]	[-0.020 0.081 -0.040]
	[9.31]	[0.35 1.00 1.00]	[3.60 -34.24 57.67]	[4.0]	[0.008 -0.040 0.084]
Sine Sweep	[1.44]	[1.00 -0.84 0.31]	[15.92 -22.88 6.23]	[9.5]	[0.043 -0.002 0.009]
	[5.31]	[0.68 0.80 -0.91]	[-22.88 52.17 -36.94]	[1.7]	[-0.002 0.051 -0.015]
	[9.69]	[0.30 1.00 1.00]	[6.23 -36.94 65.18]	[2.0]	[0.009 -0.015 0.050]
Impulse	[1.5]	[1.00 -0.80 0.34]	[16.31 -23.77 6.99]	[4.8]	[0.031 -0.011 0.004]
	[5.31]	[0.67 0.76 -0.95]	[-23.77 54.01 -37.25]	[2.0]	[-0.011 0.049 -0.019]
	[9.75]	[0.29 1.00 1.00]	[6.99 -37.25 64.38]	[2.2]	[0.004 -0.019 0.054]

A three-cycle sinusoidal input motion was generated at a frequency equal to post yield frequency of single concave friction pendulum isolators in order to investigate the properties of these bearings. This test was repeated at different input sinusoidal amplitude. Figure 4-15 shows the hysteresis loop for the friction pendulum isolators used in this study under sinusoidal excitation. The average friction coefficient was estimated to 8% for the Teflon sliders used in these isolators.

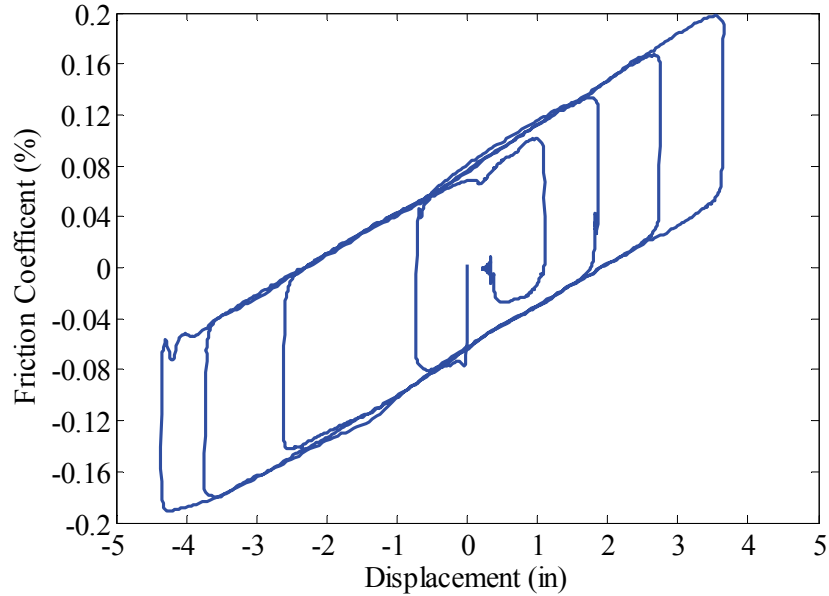


**Figure 4-15 Single friction isolator hysteresis loop under sinusoidal excitation.**

#### 4.7. Test Schedule

The experimental testing program was conducted in three main configurations: (1) fixed-base building to investigate the linear and nonlinear frame behavior; (2) base isolated building without moat wall to investigate properties of isolation device and superstructure under MCE motions; and (3) base isolated structure with moat wall having variable stiffness and gap displacements to examine effects of impact. The testing schedule and date of testing are presenting. In the tables below, *Test Type* shows the type of testing which is either dynamic simulation of a ground motion record in East-West direction of shake table or white noise excitation to identify potential damages and yielding (period shifting) in superstructure. *Test Name* is the file name of the saved data, *Description* is name of the ground motion or amplitude of white noise excitation, scale factor is the factor used to amplitude scale the MCE scaled ground motion record listed in Table

4-6, *PGA* is the corresponding peak ground acceleration for the record consider the scale factor and *Remarks* column highlights important details about the test.

**Table 4-8 Test log for date 9/3/2010 - Fixed base IMRF.**

Test#	Test Name	Description	Scale Factor	PGA(g)	Remarks
1	FBWN1	PGA(g)=0.1g	N/A	0.1	Freq. Range: 0.1-50Hz,
2	FBGM162S1	GM16-2	0.2	0.17	
3	FBWN2	PGA(g)=0.1g	N/A	0.1	Freq. Range: 0.1-50Hz,
4	FBGM152S1	GM15-2	0.2	0.11	
5	FBWN3	PGA(g)=0.1g	N/A	0.1	Freq. Range: 0.1-50Hz,
6	FBGM162S2	GM16-2	0.4	0.34	
7	FBWN4	PGA(g)=0.1g	N/A	0.1	Freq. Range: 0.1-50Hz,

**Table 4-9 Test log for date 9/7/2010 – Fixed base IMRF.**

Test#	Test Name	Description	Scale Factor	PGA(g)	Remarks
1	FBGM152S2	GM15-2	0.4	0.22	
2	FBWN5	PGA(g)=0.1g	N/A	0.1	Freq. Range: 0.1-50Hz,
3	FBGM162S3	GM16-2	0.67	0.56	DBE
4	FBWN6	PGA(g)=0.1g	N/A	0.1	Freq. Range: 0.1-50Hz,
5	FBGM152S3	GM15-2	0.67	0.36	DBE
6	FBWN7	PGA(g)=0.1g	N/A	0.1	Freq. Range: 0.1-50Hz,
7	FBGM162S4	GM16-2	0.85	0.73	
8	FBWN8	PGA(g)=0.1g	N/A	0.1	Freq. Range: 0.1-50Hz,
9	FBGM162S5	GM16-2	1	0.86	MCE
10	FBWN9	PGA(g)=0.1g	N/A	0.1	Freq. Range: 0.1-50Hz,
11	FBGM152S4	GM15-2	1	0.55	MCE
12	FBWN10	PGA(g)=0.1g	N/A	0.1	Freq. Range: 0.1-50Hz,

Table 4-8 and Table 4-9 show the test log for fixed base structure conducted in two separate days. Two ground motions (GM15-2, and GM16-2) were first used to investigate the post-yield behavior of the fixed-base structure. Each ground motion was scaled in amplitude to 20, 40, 67(DBE), and 100% of MCE level and applied in order of increasing amplitude, alternating between both earthquakes. The GM16-2 record was also applied at 85% of MCE level. The

white noise excitation was applied between each test to compare the natural frequencies and damping ratios with benchmark white noise conducted in initial system identification testing.

In the second phase of shake table testing, the IMRF model was replaced with a new frame and four FP bearings were installed at the base of the structure. Six ground motions were used for dynamic testing of the isolated structure. Five ground motions were scaled to 40, 67, and 100% of MCE level while the GM7-1 record was only applied at MCE level. Table 4-10 lists the tests conducted on base isolated model without any moat wall.

**Table 4-10 Test log for date 10/4/2010 – Base isolated IMRF without moat wall.**

Test#	Test Name	Description	Scale Factor	PGA(g)	Remarks
1	FPWN1	PGA(g)=0.1g	N/A	0.1	Freq. Range: 0.1-50Hz,
2	FPGM152S1	GM15-2	0.4	0.34	
3	FPGM152S2	GM15-2	0.67	0.58	DBE
4	FPGM152S3	GM15-2	1	0.86	MCE
5	FPWN2	PGA(g)=0.1g	N/A	0.1	Freq. Range: 0.1-50Hz,
6	FPGM162S1	GM16-2	0.4	0.22	
7	FPGM162S2	GM16-2	0.67	0.37	DBE
8	FPGM162S3	GM16-2	1	0.55	MCE
9	FPWN3	PGA(g)=0.1g	N/A	0.1	Freq. Range: 0.1-50Hz,
10	FPGM111S1	GM11-1	0.4	0.27	
11	FPGM111S2	GM11-1	0.67	0.46	DBE
12	FPGM111S3	GM11-1	1	0.68	MCE
13	FPWN4	PGA(g)=0.1g	N/A	0.1	Freq. Range: 0.1-50Hz,
14	FPGM172S1	GM17-2	0.4	0.35	
15	FPGM172S2	GM17-2	0.67	0.58	DBE
16	FPGM172S3	GM17-2	1	0.87	MCE
17	FPWN5	PGA(g)=0.1g	N/A	0.1	Freq. Range: 0.1-50Hz,
18	FPGM171S1	GM17-1	0.4	0.36	
19	FPGM171S2	GM17-1	0.67	0.61	DBE
20	FPGM171S3	GM17-1	1	0.91	MCE
21	FPWN6	PGA(g)=0.1g	N/A	0.1	Freq. Range: 0.1-50Hz,
22	FPGM71S3	GM7-1	1	0.78	MCE

To investigate the effects of pounding at the base level of isolated structures, moat wall models were installed on the simulator platform at both sides of the structure. The gap distance between

the base of the structure and the moat wall were varied between 4-6 in to induce pounding at various impact velocities. Different thicknesses for the concrete moat wall model were also considered to investigate the effect of the wall stiffness on the behavior of the superstructure. The preliminary tests results of base isolated model without moat wall show that the GM17-1 is the only ground motion record which induces base level displacement more than 6 in, for this reason, this record is used in impact testing with 6 in. gap while other records listed in Table 4-6 are used for gap distance less than 6 in. In the first phase of impact test, concrete moat walls with front impact wall thickness of 2 inches and back wall thickness of 4 inches were installed on two sides (East-West) of the base isolated model at 6 in. gap distance and filled with sand to simulate soil backfill. Table 4-11 shows three tests conducted using 2 in. concrete moat wall.

**Table 4-11 Test log for date 10/19/2010 – Base isolated IMRF with 2 in. concrete moat wall at 6 in. gap distance.**

Test#	Test Name	Description	Scale Factor	PGA(g)	Remarks-Gap Distance
1	FPI62WN1	PGA(g)=0.1g	N/A	0.1	Freq. Range: 0.1-50Hz,
2	FPI62GM171S1	GM17-1	0.67	0.61	2” concrete wall – 6”
3	FPI62WN2	PGA(g)=0.1g	N/A	0.1	Freq. Range: 0.1-50Hz,
4	FPI62GM171S2	GM17-1	0.85	0.77	2” concrete wall – 6”
5	FPI62WN3	PGA(g)=0.1g	N/A	0.1	Freq. Range: 0.1-50Hz,
6	FPI62GM171S3	GM17-1	1	0.91	2” concrete wall – 6”
7	FPI62WN4	PGA(g)=0.1g	N/A	0.1	Freq. Range: 0.1-50Hz,

The impact test continued by flipping the moat walls and having the 4 in. concrete wall in front. The gap distance was kept to 6 in. and GM17-1 was applied to the shake table to see the effect of changing in wall thickness on response of base isolated structure during impacting moat wall. Table 4-12 shows the tests description using 4 in. concrete walls installed at 6 in. gap distance.

**Table 4-12 Test log for date 11/4/2010 – Base isolated IMRF with 4 in. concrete moat wall at 6 in. gap distance.**

Test#	Test Name	Description	Scale Factor	PGA(g)	Remarks-Gap Distance
1	FPI64GM171S2a	GM17-1	0.85	0.77	4” concrete wall – 6”
2	FPI64WN1	PGA(g)=0.1g	N/A	0.1	Freq. Range: 0.1-50Hz,
3	FPI64GM171S3a	GM17-1	1	0.91	4” concrete wall – 6”
4	FPI64WN2	PGA(g)=0.1g	N/A	0.1	Freq. Range: 0.1-50Hz,

The IMRF model was replaced with a new identical one due to potential damages during past impact tests. Concrete walls were replaced with a new set of 6 in. front wall thickness and 3 in. back wall thickness. The new concrete walls were installed at 4 in. gap distance to examine effect of changing the gap distance on impact force. Table 4-13 shows the sequence of tests conducted in this step. GM11-1 and GM7-1 records are also used at this gap distance since the maximum displacement these records induced at the base level exceeds the 4 in. gap distance.

**Table 4-13 Test log for date 11/16/2010 – Base isolated IMRF with 6 in. concrete moat wall at 4 in. gap distance.**

Test#	Test Name	Description	Scale Factor	PGA(g)	Remarks-Gap Distance
1	FPI46WN1	PGA(g)=0.1g	N/A	0.1	Freq. Range: 0.1-50Hz,
2	FPI46GM171S3	GM17-1	1	0.91	6” concrete wall – 4”
3	FPI46WN2	PGA(g)=0.1g	N/A	0.1	Freq. Range: 0.1-50Hz,
4	FPI46GM171S2	GM17-1	1	0.77	6” concrete wall – 4”
5	FPI46GM111S3	GM11-1	1	0.68	6” concrete wall – 4”
6	FPI46WN4	PGA(g)=0.1g	N/A	0.1	Freq. Range: 0.1-50Hz,
7	FPI46GM71S3	GM7-1	1	0.78	6” concrete wall – 4”
8	FPI46WN5	PGA(g)=0.1g	N/A	0.1	Freq. Range: 0.1-50Hz,

As mentioned in the description of the moat walls, steel walls were also used to cover a wide range of moat wall stiffness. In the first configuration, moat walls were installed at 5 in. gap distance using four long steel rods. The gap distance was changed to 4 in. after a couple of tests (Table 4-14).

In the first series of rigid steel wall testing, it was noticed that the wall was uplifting at impact due to bolt elongation. The steel walls were welded to minimize rocking at the base and several tests were repeated as listed in Table 4-15.

**Table 4-14 Test log for date 11/23/2010 – Base isolated IMRF with steel moat wall without weld at 6, 5 and 4 in. gap distances.**

Test#	Test Name	Description	Scale Factor	PGA(g)	Remarks-Gap Distance
1	FP6RWN1	PGA(g)=0.1g	N/A	0.1	Freq. Range: 0.1-50Hz,
2	FP6RGM171S3	GM17-1	1	0.91	Steel w/o weld wall – 5”
3	FP5RWN1	PGA(g)=0.1g	N/A	0.1	Freq. Range: 0.1-50Hz,
4	FP5RGM171S3	GM17-1	1	0.91	Steel w/o weld wall – 5”
5	FP5RWN2	PGA(g)=0.1g	N/A	0.1	Freq. Range: 0.1-50Hz,
6	FP4RGM171S2	GM17-1	0.85	0.77	Steel w/o weld wall – 4”
7	FP4RWN1	PGA(g)=0.1g	N/A	0.1	Freq. Range: 0.1-50Hz,
8	FP4RGM171S3	GM17-1	1	0.91	Steel w/o weld wall – 4”
9	FP4RWN2	PGA(g)=0.1g	N/A	0.1	Freq. Range: 0.1-50Hz,
10	FP4RGM111S3	GM11-1	1	0.68	Steel w/o weld wall – 4”
11	FP4RWN3	PGA(g)=0.1g	N/A	0.1	Freq. Range: 0.1-50Hz,
12	FP4RGM71S3	GM7-1	1	0.78	Steel w/o weld wall – 4”
13	FP4RWN4	PGA(g)=0.1g	N/A	0.1	Freq. Range: 0.1-50Hz,

**Table 4-15 Test log for date 12/3/2010 - Base isolated IMRF with steel moat wall with weld at 6 and 4 in. gap distance.**

Test#	Test Name	Description	Scale Factor	PGA(g)	Remarks-Gap Distance
1	FP6RNGM171S3	GM17-1	1	0.91	Steel with weld wall – 6”
2	FP6RNWN1	PGA(g)=0.1g	N/A	0.1	Freq. Range: 0.1-50Hz,
3	FP4RNGM171S3	GM17-1	1	0.91	Steel with weld wall – 4”
4	FP4RNWN1	PGA(g)=0.1g	N/A	0.1	Freq. Range: 0.1-50Hz,
5	FP4RNGM111S3	GM11-1	1	0.68	Steel with weld wall – 4”
6	FP4RNWN3	PGA(g)=0.1g	N/A	0.1	Freq. Range: 0.1-50Hz,
7	FP4RNGM71S3	GM7-1	1	0.78	Steel with weld wall – 4”
8	FP4RNWN4	PGA(g)=0.1g	N/A	0.1	Freq. Range: 0.1-50Hz,

## **SECTION 5**

### **SHAKE TABLE TEST RESULTS**

#### **5.1. Introduction**

The experimental results and data analysis from the shake table testing program of the 1/4-scale model structure are described in this section. Test results are presented for three main configurations: (1) fixed-base building to investigate the linear and nonlinear frame behavior; (2) base isolated building without moat wall to investigate properties of isolation device and superstructure under MCE motions; and (3) base isolated structure with moat wall having variable stiffness and gap displacements to examine effects of impact. A summary of processed experimental results for these three configurations can be found in this section while raw data and detailed processed results can be accessed in the NEES website under the NEES TIPS project directory (<https://nees.org/warehouse/project/571>).

#### **5.2. Results for Fixed Base Structure**

The GM15-2 and GM16-2 earthquake motions listed in Table 3-9 were first used to investigate the post-yield behavior of the fixed-base structure. Each ground motion was scaled in amplitude to 20, 40, 67(DBE), and 100% of MCE level and applied in order of increasing amplitude, alternating between both earthquakes. The GM16-2 record was also applied at 85% of MCE level. Figure 5-1 and Figure 5-2 show the story drift ratio (SDR) of the fixed base model under GM15-2 and GM16-2, respectively. SDR is defined as the relative displacement between the top and bottom level divided by height of each level. As expected, the SDR increases by increasing the amplitude of the ground motion. It can be seen that peak SDR under GM15-2 occurs in positive direction while it is negative for GM16-2. The East-West direction in which these two records were applied was chosen in such a way that each one recovered previous residual drift in order to prevent progressive collapse due to cumulative residual drift. This helped to continue the fixed base testing model up to MCE level of the records.

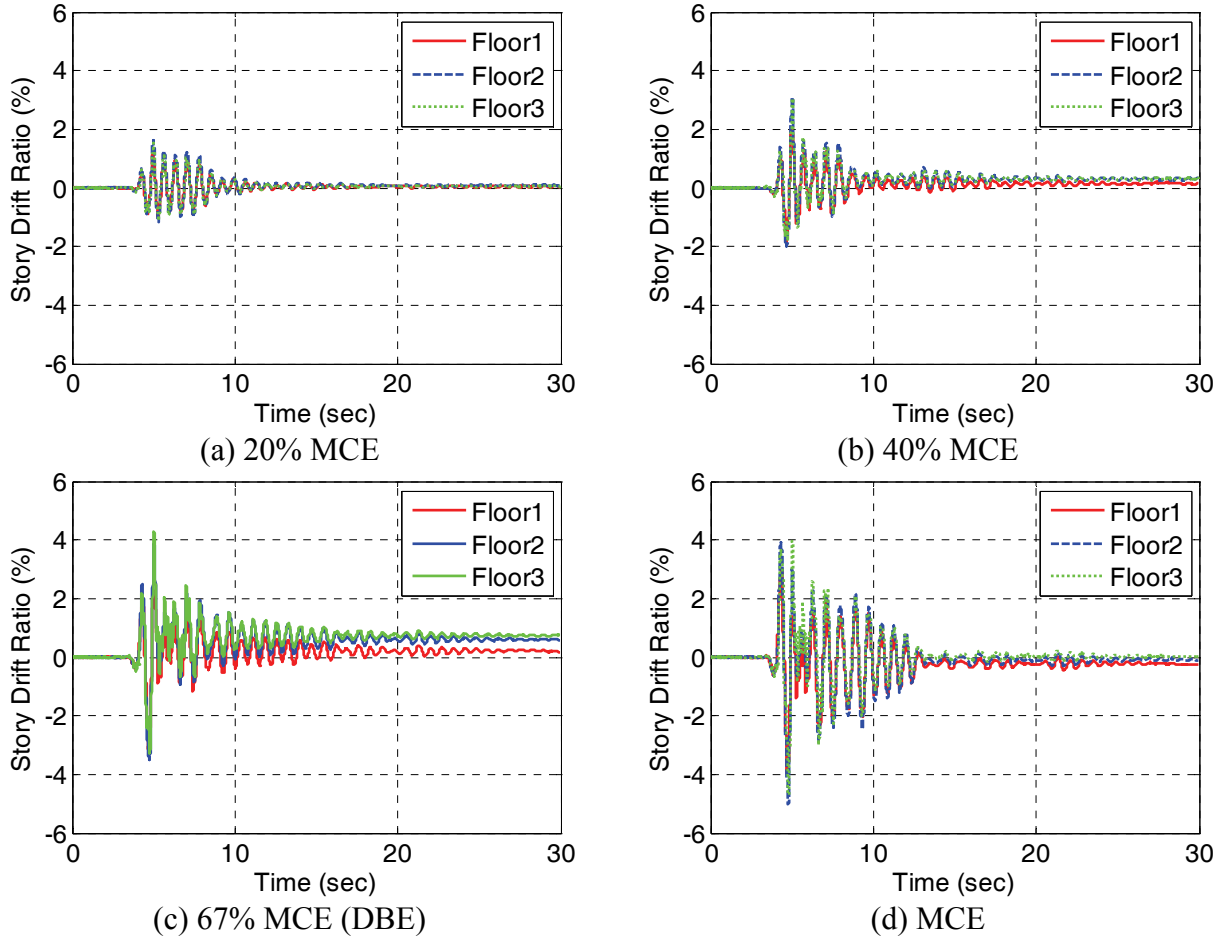
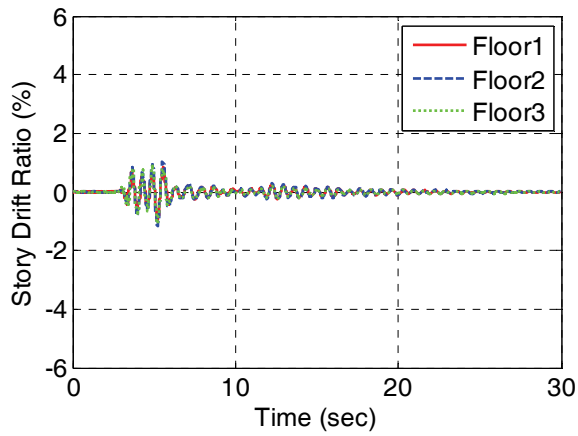
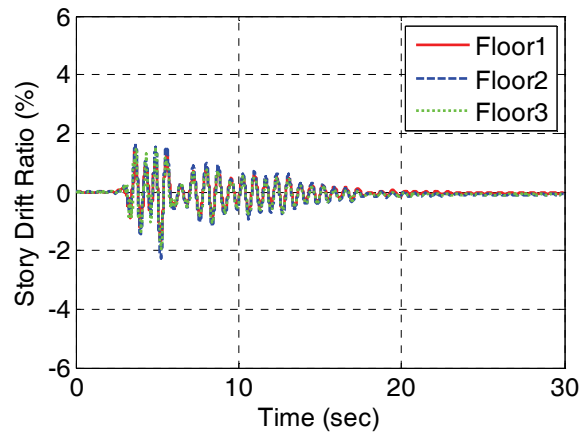


**Figure 5-1 Story drift ratio for fixed base model under GM15-2 record.**

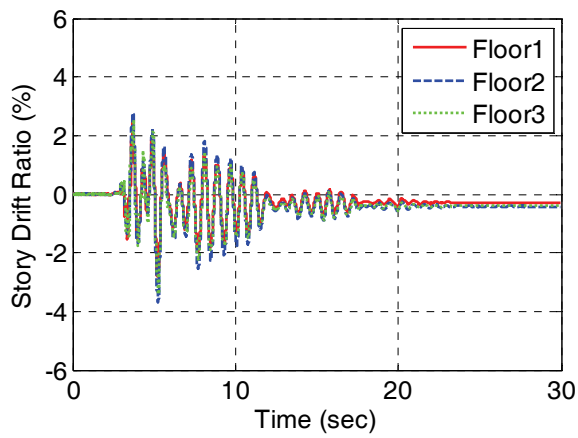
Table 5-1 and Table 5-2 summarize the test results for fixed base IMRF under these two records. Peak Ground Acceleration (PGA) for the input motion is peak measured acceleration on the shake table extension platform and the peak floor shear is calculated using mass at each floor multiply by peak floor acceleration at the same level (inertia force) while peak base shear force is read from 4 load cells under the base frame.



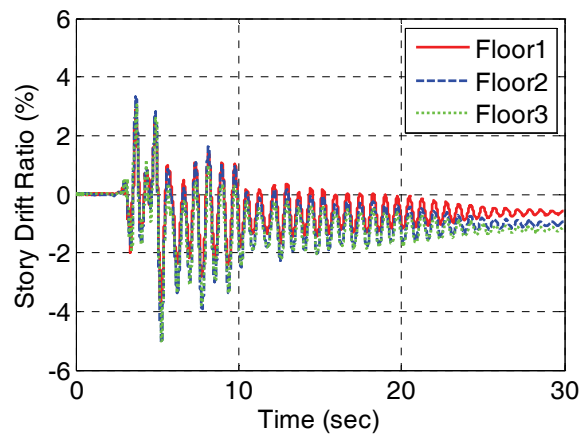
(a) 20% MCE



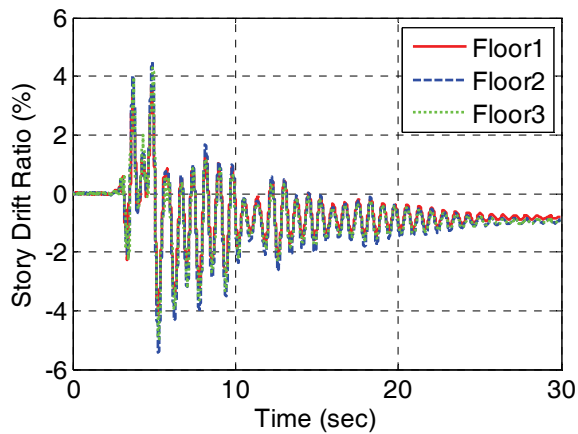
(b) 40% MCE



(c) 67% MCE (DBE)



(d) 85% MCE



(e) MCE

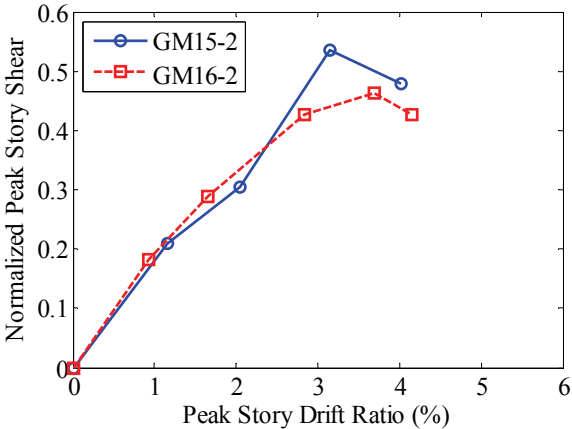
**Figure 5-2 Story drift ratio for fixed base model under GM16-2 record.**

**Table 5-1 Summary of fixed base IMRF shake table test results for GM152-2.**

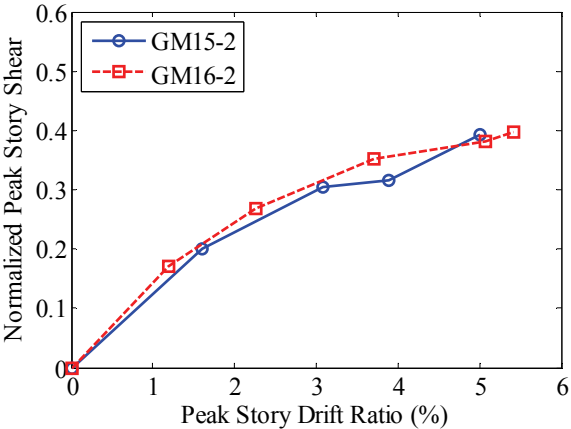
	Unit	GM152-20%	GM152-40%	GM152-67%	GM152-100%
PGA (Input Motion)	g	0.23	0.44	0.77	1.04
Peak Base Shear	kips	8.55	15.40	20.81	23.39
Peak Floor1 Acceleration	g	0.38	0.75	0.95	1.10
Peak Floor2 Acceleration	g	0.39	0.60	0.75	1.06
Peak Floor3 Acceleration	g	0.53	0.88	1.12	1.20
Peak Floor1 Shear	kips	8.08	14.63	19.32	21.30
Peak Floor2 Shear	kips	7.17	11.75	14.72	14.46
Peak Floor3 Shear	kips	5.68	9.39	12.01	12.84
Peak Floor1 SDR	in	0.55	0.97	1.49	1.90
Peak Floor2 SDR	in	0.76	1.46	1.84	2.37
Peak Floor3 SDR	in	0.72	1.45	2.03	2.21
Peak Roof SDR	in	1.97	3.81	4.91	6.30
Residual Floor1 SDR	in	0.02	0.07	0.10	-0.11
Residual Floor2 SDR	in	0.03	0.14	0.29	-0.04
Residual Floor3 SDR	in	0.03	0.14	0.35	0.01
Residual Roof SDR	in	0.08	0.36	0.74	-0.14



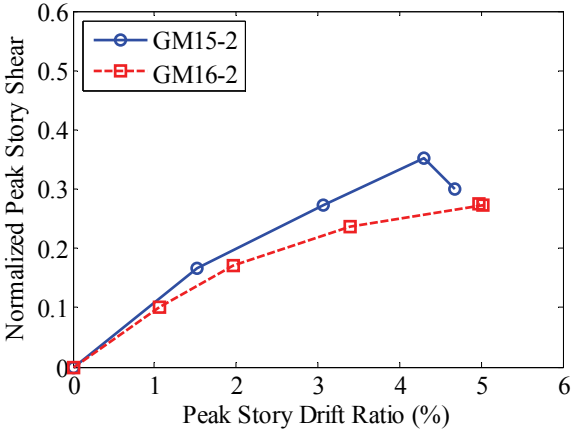
Figure 5-3 plots the maximum absolute story drift ratio for each floor and the corresponding story shear normalized by the total weight of superstructure (32 kips) for each test. The last point corresponds to the MCE level motion. Story shear forces were assumed equal to inertia forces calculated by multiplying corresponding floor acceleration by story mass. From Figure 5-3, it is observed that the maximum story drift ratio exceeding 5% drift occurs at the middle level, and that all levels start to show softening behavior due to yielding by 2% drift.



(a) First Floor



(b) Second Floor



(c) Third Floor

**Figure 5-3 Normalized shear force versus peak story drift ratio for fixed base IMRF.**

The results obtained from the fixed base IMRF tests were used to calibrate numerical model for the frame as explained in following sections.

### **5.3. Results for Isolated Base Structure without Moat Wall**

In the second phase of shake table testing, the IMRF model was replaced with a new frame and four FP bearings were installed at the base of the structure. The model was first excited by a sinusoidal displacement command at a frequency equal to the isolation frequency to characterize the bearing properties. The sliding friction coefficient of the isolators was estimated to be approximately 8%. Six ground motions were used for dynamic testing of the isolated structure. Five ground motions were scaled to 40, 67, and 100% of MCE level while the GM7-1 record was only applied at MCE level. A summary of test results for each record at the three levels are presented in Table 5-3 to Table 5-7. Peak ground acceleration corresponds to the peak measured acceleration at shake table extension level while Peak Base Acceleration (PBA) is the peak measured acceleration at base level of the building model (top of isolator level). Both maximum and minimum base plate displacement are reported in this table in order to count possible pounding to east (positive displacement) and west (negative displacement) walls when moat walls are installed. The base shear is obtained from the summation of 4 load cells installed under the isolators while floor shears are calculated from inertia force (mass times measured story acceleration). As expected in base isolated building, the peak floor acceleration is reduced relative to the PGA for all levels of shaking. The peak ground acceleration is 0.91g for GM17-1 at MCE level and the resulting peak acceleration at the third floor is 0.54g. The reduction ratio increases with increasing amplitude of excitation. This can be explained by considering the initial shear force required to activate the friction isolators. For low amplitude input excitation, the structure behaves essentially as a fixed-based structure, but for higher input motion the isolators are activated,.

**Table 5-3 Summary of isolated base IMRF shake table test results for GM11-1.**

	Unit		40% MCE		67% MCE		100% MCE	
PGA (Input Motion)	g		0.35		0.55		0.79	
PBA (Peak Base Acc.)	g		0.28		0.36		0.31	
Max Base Disp.	in		0.85		2.21		4.88	
Min Base Disp.	in		-0.53		-2.41		-4.42	
Peak Base Shear	kips		5.35		7.80		11.86	
Peak Floor1 Acceleration	g		0.28		0.27		0.34	
Peak Floor2 Acceleration	g		0.27		0.28		0.34	
Peak Floor3 Acceleration	g		0.37		0.39		0.47	
Peak Floor1 Shear	kips		5.83		7.44		9.83	
Peak Floor2 Shear	kips		5.42		6.34		8.50	
Peak Floor3 Shear	kips		3.99		4.21		5.00	
Peak Floor1 SDR	in	%	0.33	0.69	0.51	1.08	0.79	1.66
Peak Floor2 SDR	in	%	0.48	1.02	0.65	1.38	0.92	1.95
Peak Floor3 SDR	in	%	0.42	0.90	0.54	1.15	0.73	1.55
Peak Roof SDR	in	%	1.21	0.85	1.70	1.20	2.43	1.72
Residual Floor1 SDR	in	%	0.00	-0.01	0.00	0.01	0.01	0.01
Residual Floor2 SDR	in	%	-0.01	-0.02	0.00	0.00	0.02	0.05
Residual Floor3 SDR	in	%	0.00	-0.01	0.00	-0.01	0.01	0.02
Residual Roof SDR	in	%	-0.01	-0.01	0.00	0.00	0.04	0.03

**Table 5-4 Summary of isolated base IMRF shake table test results for GM15-2.**

	Unit		40% MCE		67% MCE		100% MCE	
PGA (Input Motion)	g		0.51		0.79		1.09	
PBA (Peak Base Acc.)	g		0.32		0.29		0.40	
Max Base Disp.	in		1.11		2.61		4.24	
Min Base Disp.	in		-0.81		-1.70		-3.41	
Peak Base Shear	kips		5.91		8.28		11.03	
Peak Floor1 Acceleration	g		0.31		0.36		0.43	
Peak Floor2 Acceleration	g		0.35		0.34		0.40	
Peak Floor3 Acceleration	g		0.38		0.44		0.53	
Peak Floor1 Shear	kips		5.86		7.85		9.41	
Peak Floor2 Shear	kips		4.85		6.56		8.62	
Peak Floor3 Shear	kips		4.12		4.70		5.70	
Peak Floor1 SDR	in	%	0.32	0.69	0.47	0.99	0.70	1.48
Peak Floor2 SDR	in	%	0.42	0.89	0.62	1.32	0.90	1.91
Peak Floor3 SDR	in	%	0.41	0.86	0.54	1.14	0.79	1.67
Peak Roof SDR	in	%	1.08	0.76	1.60	1.13	2.36	1.67
Residual Floor1 SDR	in	%	-0.01	-0.01	-0.01	-0.01	-0.03	-0.07
Residual Floor2 SDR	in	%	-0.01	-0.02	0.00	-0.01	-0.06	-0.13
Residual Floor3 SDR	in	%	0.00	0.01	-0.01	-0.02	-0.05	-0.10
Residual Roof SDR	in	%	-0.01	-0.01	-0.02	-0.01	-0.14	-0.10

**Table 5-5 Summary of isolated base IMRF shake table test results for GM16-2.**

	Unit		40% MCE		67% MCE		100% MCE	
PGA (Input Motion)	g		0.28		0.45		0.66	
PBA (Peak Base Acc.)	g		0.30		0.31		0.35	
Max Base Disp.	in		1.18		2.24		2.83	
Min Base Disp.	in		-0.81		-1.12		-1.75	
Peak Base Shear	kips		5.65		7.18		7.97	
Peak Floor1 Acceleration	g		0.41		0.41		0.46	
Peak Floor2 Acceleration	g		0.46		0.51		0.53	
Peak Floor3 Acceleration	g		0.40		0.45		0.49	
Peak Floor1 Shear	kips		7.66		7.51		8.37	
Peak Floor2 Shear	kips		6.46		6.45		5.87	
Peak Floor3 Shear	kips		4.29		4.78		5.21	
Peak Floor1 SDR	in	%	0.41	0.87	0.43	0.90	0.49	1.03
Peak Floor2 SDR	in	%	0.60	1.27	0.61	1.29	0.52	1.11
Peak Floor3 SDR	in	%	0.51	1.08	0.50	1.07	0.48	1.01
Peak Roof SDR	in	%	1.50	1.06	1.49	1.05	1.31	0.93
Residual Floor1 SDR	in	%	0.00	0.01	0.01	0.01	0.00	0.00
Residual Floor2 SDR	in	%	0.01	0.03	0.01	0.02	0.00	0.00
Residual Floor3 SDR	in	%	0.01	0.03	0.01	0.02	0.00	0.00
Residual Roof SDR	in	%	0.03	0.02	0.02	0.02	-0.01	0.00

**Table 5-6 Summary of isolated base IMRF shake table test results for GM17-1.**

	Unit		40% MCE		67% MCE		100% MCE	
PGA (Input Motion)	g		0.52		0.85		1.17	
PBA (Peak Base Acc.)	g		0.30		0.37		0.37	
Max Base Disp.	in		1.42		3.43		5.90	
Min Base Disp.	in		-2.18		-4.32		-6.62	
Peak Base Shear	kips		7.36		11.10		14.12	
Peak Floor1 Acceleration	g		0.29		0.35		0.45	
Peak Floor2 Acceleration	g		0.31		0.38		0.48	
Peak Floor3 Acceleration	g		0.38		0.44		0.55	
Peak Floor1 Shear	kips		8.29		10.55		12.53	
Peak Floor2 Shear	kips		6.26		7.79		9.07	
Peak Floor3 Shear	kips		4.03		4.68		5.86	
Peak Floor1 SDR	in	%	0.52	1.10	0.70	1.49	0.96	2.04
Peak Floor2 SDR	in	%	0.65	1.37	0.81	1.70	1.06	2.24
Peak Floor3 SDR	in	%	0.49	1.03	0.65	1.38	0.83	1.75
Peak Roof SDR	in	%	1.63	1.15	2.12	1.50	2.74	1.93
Residual Floor1 SDR	in	%	0.00	-0.01	0.01	0.02	0.01	0.02
Residual Floor2 SDR	in	%	-0.01	-0.03	0.02	0.05	0.03	0.07
Residual Floor3 SDR	in	%	0.01	0.01	0.00	0.00	0.02	0.04
Residual Roof SDR	in	%	-0.01	-0.01	0.03	0.02	0.06	0.04

**Table 5-7 Summary of isolated base IMRF shake table test results for GM17-2.**

	Unit	40% MCE		67% MCE		100% MCE		
PGA (Input Motion)	g	0.46		0.73		0.98		
PBA (Peak Base Acc.)	g	0.50		0.51		0.51		
Max Base Disp.	in	0.31		1.61		3.36		
Min Base Disp.	in	-0.68		-1.69		-2.77		
Peak Base Shear	kips	5.47		7.04		9.16		
Peak Floor1 Acceleration	g	0.30		0.31		0.34		
Peak Floor2 Acceleration	g	0.27		0.29		0.31		
Peak Floor3 Acceleration	g	0.37		0.40		0.41		
Peak Floor1 Shear	kips	7.42		8.04		8.62		
Peak Floor2 Shear	kips	6.18		6.73		6.72		
Peak Floor3 Shear	kips	3.96		4.34		4.35		
Peak Floor1 SDR	in	%	0.48	1.01	0.50	1.05	0.52	1.11
Peak Floor2 SDR	in	%	0.59	1.24	0.65	1.38	0.67	1.41
Peak Floor3 SDR	in	%	0.48	1.02	0.50	1.07	0.50	1.06
Peak Roof SDR	in	%	1.55	1.09	1.64	1.15	1.67	1.18
Residual Floor1 SDR	in	%	-0.02	-0.04	-0.01	-0.02	0.00	0.00
Residual Floor2 SDR	in	%	-0.01	-0.02	-0.01	-0.02	0.00	0.00
Residual Floor3 SDR	in	%	-0.01	-0.03	0.00	-0.01	-0.01	-0.01
Residual Roof SDR	in	%	-0.04	-0.03	-0.02	-0.01	-0.01	-0.01

The maximum SDR recorded at MCE level motions are in the range of 1.5 to 2%, which indicates slight yielding in superstructure. Insignificant residual SDR at the end of each event also verifies that the yielding in superstructure is minor.

The peak base shear normalized by the total weight of the isolated model (51 kips) versus roof drift ratio is plotted in Figure 5-4 for all tests. The maximum roof drift ratio occurs under GM17-1 record and is less than 2%. Examining story drift ratios of each story under the GM17-1 record it can be concluded that as expected, the isolation system decreased the superstructure response. For example for 2 cases of GM15-2 and 16-2 maximum story drift ratio at MCE level decreased from 5% at the fixed base model to less than 2% for base isolated frame. It can be conclude that

the base isolation model with sufficient displacement capacity can withstand this MCE level ground motion with only slight yielding at the second story. It is interesting to note that for two of the ground motions, GM15-2 and GM17-2, the peak base shear increased with increasing intensity, but the roof drift ratio remained almost constant and in one case, decreased. The displacements at the base level and the base shear increased as expected.

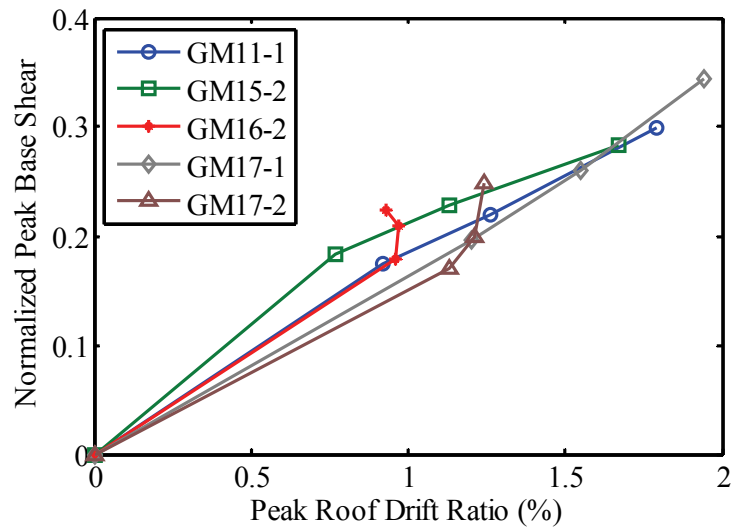


**Figure 5-4 Normalized base shear versus peak roof drift ratio for isolated structure**

Figure 5-5 to Figure 5-10 show each isolator hysteresis response at MCE level of each record. In these figures load cell 1 to load cell 4 are located at North-West, North-East, South-West and South-East of the shake table, respectively. The effect of overturning moment on axial force applied on each bearing is obvious in these figures. Moving the base plate in positive direction (East direction) leads to increasing the axial force on isolators 2 and 4, resulting in higher amplitude shear force while decreasing axial force for isolators 1 and 3 leads to narrower hysteresis loop. The effect of overturning moment due to upper floor mass also could lead to uplift in bearings. The effect of uplift on hysteresis response of isolators can be seen in Figure 5-9, for record GM17-1 at MCE level. The amount of uplift in this test was insignificant and could not be observed during testing.

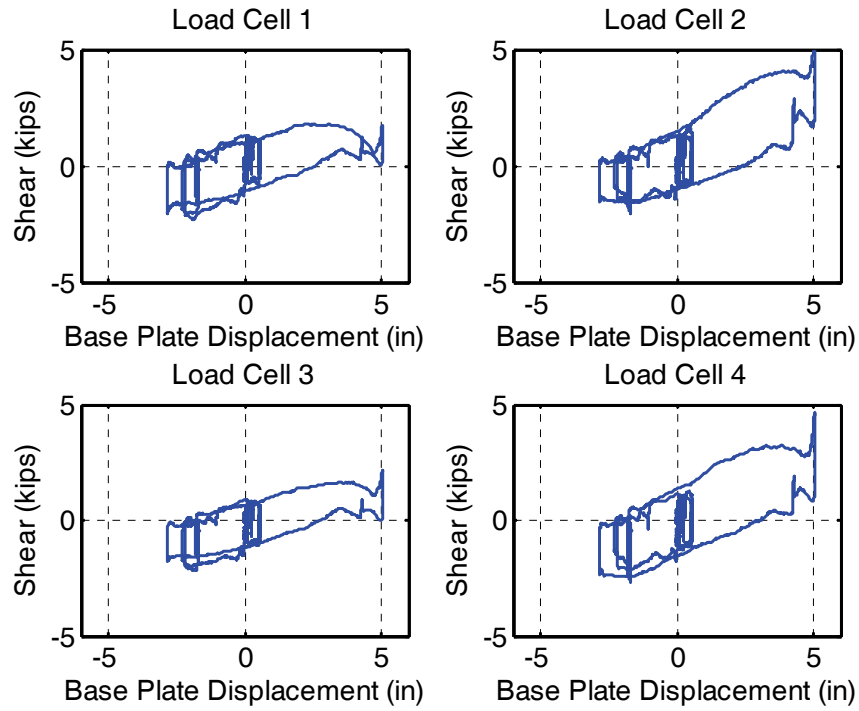


**Figure 5-5 Isolator hysteresis behavior for record GM7-1**

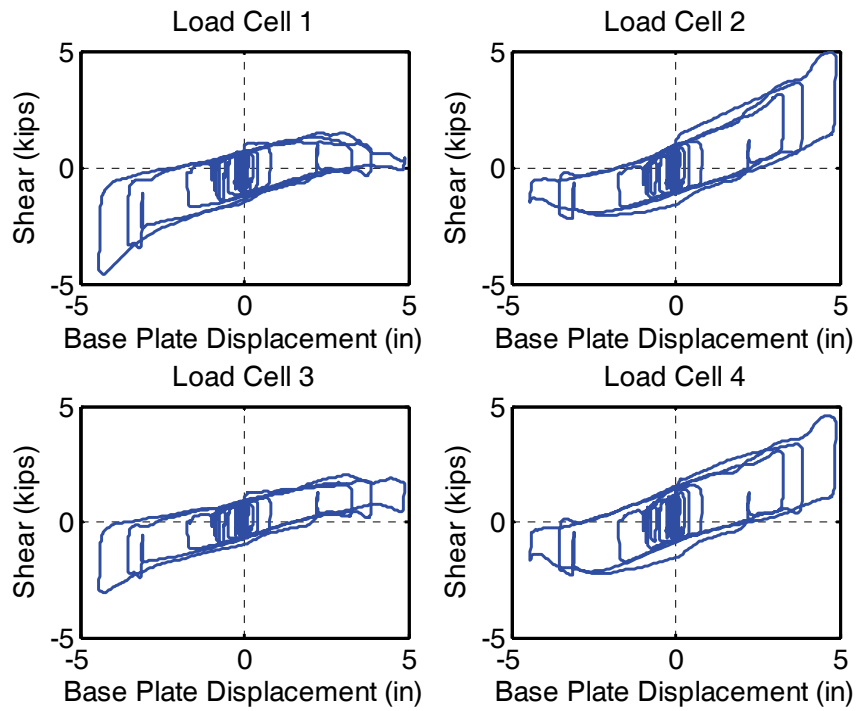


**Figure 5-6 Isolator hysteresis behavior for record GM11-1**

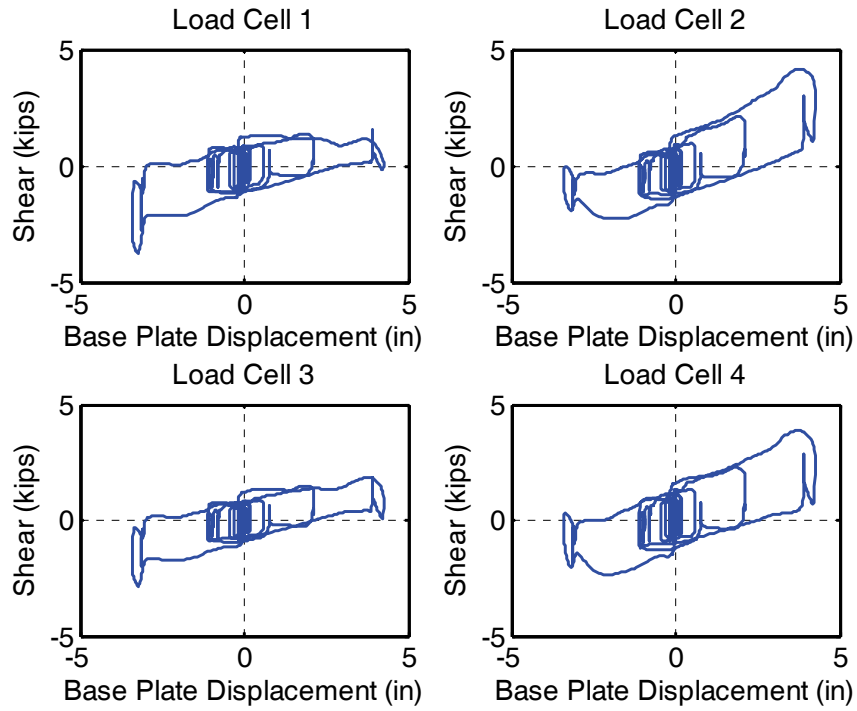


**Figure 5-7 Isolator hysteresis behavior for record GM15-2**

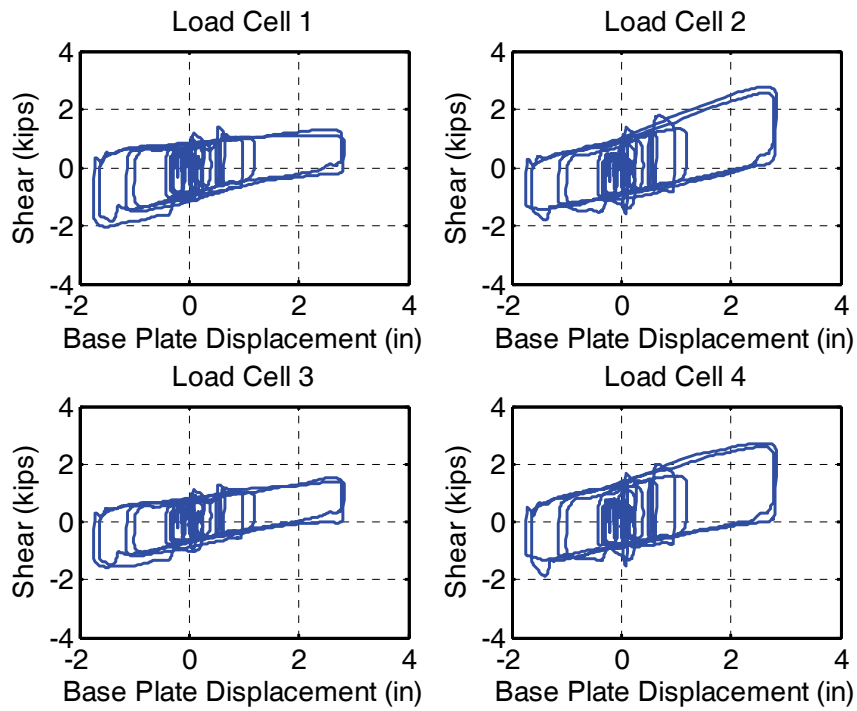


**Figure 5-8 Isolator hysteresis behavior for record GM16-2**

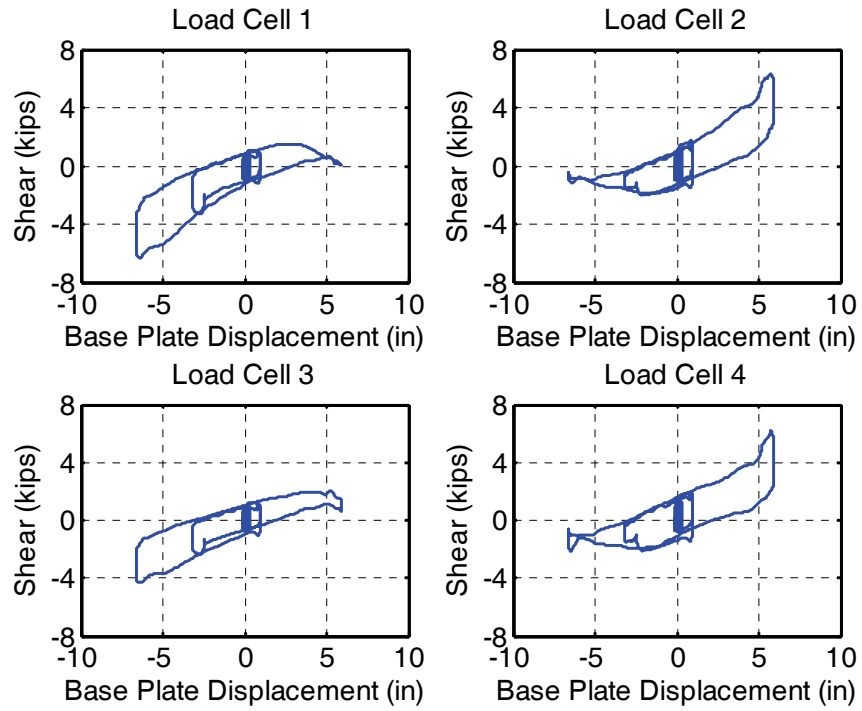


**Figure 5-9 Isolator hysteresis behavior for record GM17-1**

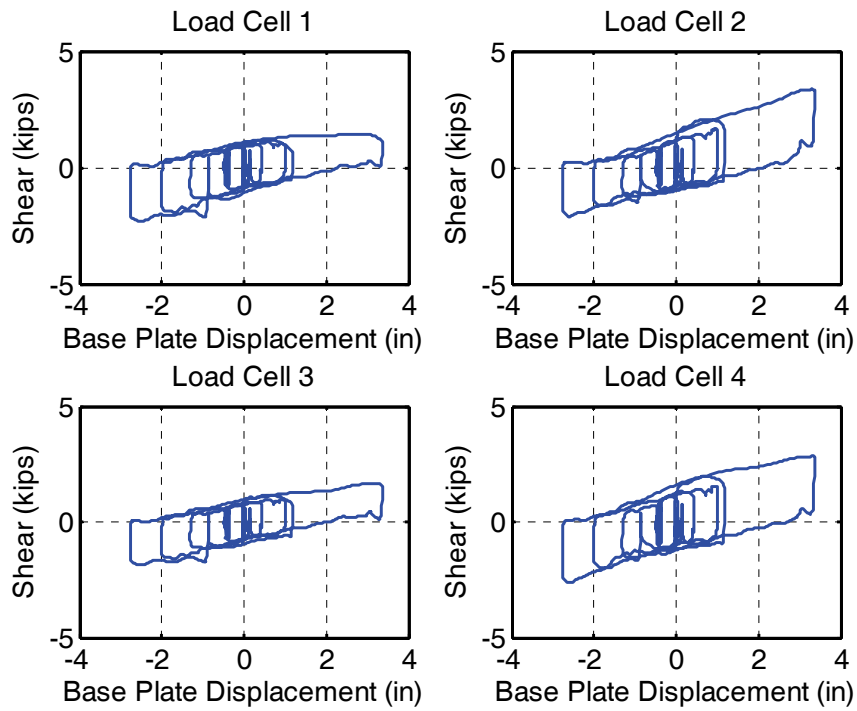
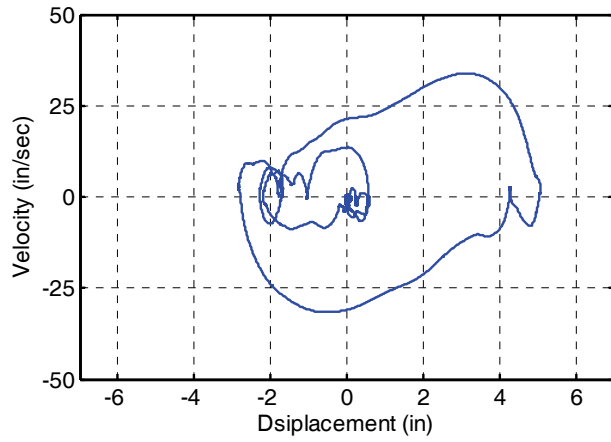
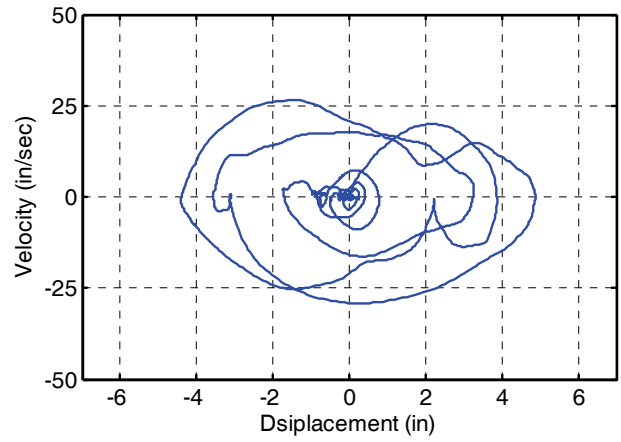


**Figure 5-10 Isolator hysteresis behavior for record GM17-2**

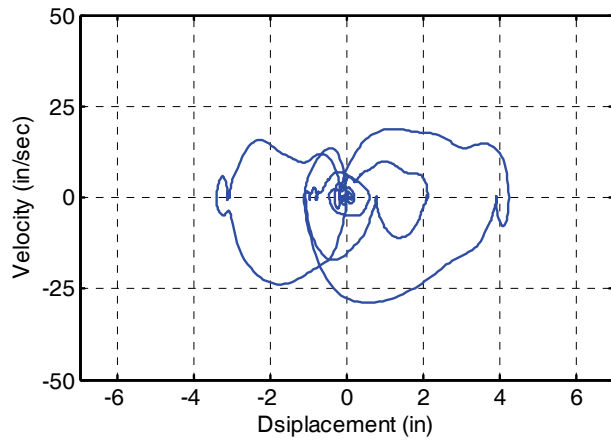
Figure 5-11 shows the base level velocity versus displacement for all six ground motion records applied to the isolated IMRF without moat wall. In this study, velocity was calculated from numerical differentiation of the displacement data. These plots show the maximum displacement of the base level and also an approximate impact velocity in case there would be a wall at a certain gap distance. Since GM17-1 was the only ground motion that produced displacements large enough to impact the moat walls for the 6 in gap, this was the primary ground motion used in the impact testing while GM7-1 and GM11-1 records were also used for the 4 in gap configuration. Applying GM17-1 moves the base level in the west direction beyond the 6 in. gap. Based on Figure 5-11 (e), installing moat walls at 6 in gap distance (scaled MCE displacement) leads to one impact to west wall (negative displacement). Installing the moat wall at 4 in. gap, pounding is expected to to both the east and west wall under GM17-1 and GM11-1 records and one impact to east wall under GM7-1 record. The impact velocity would be 15 in/sec for a moat wall at 6 in. gap distance and 25 in/sec when the moat walls are installed at 4 in. gap under GM17-1 records.



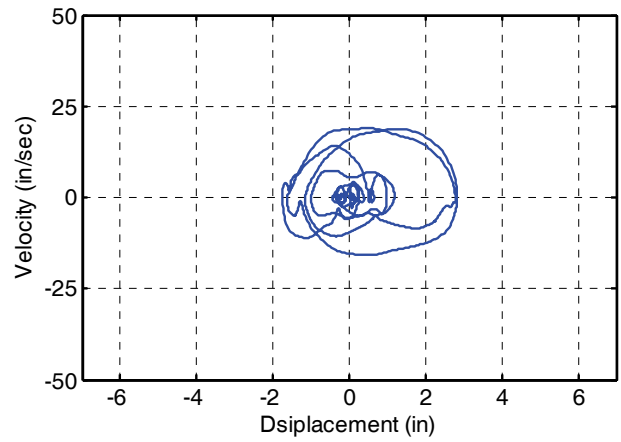
(a) GM7-1



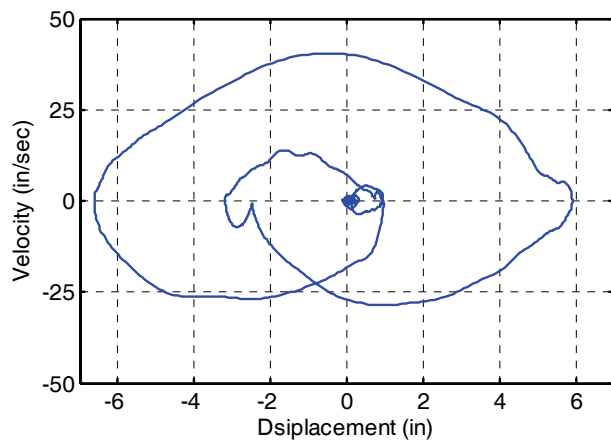
(b) GM11-1



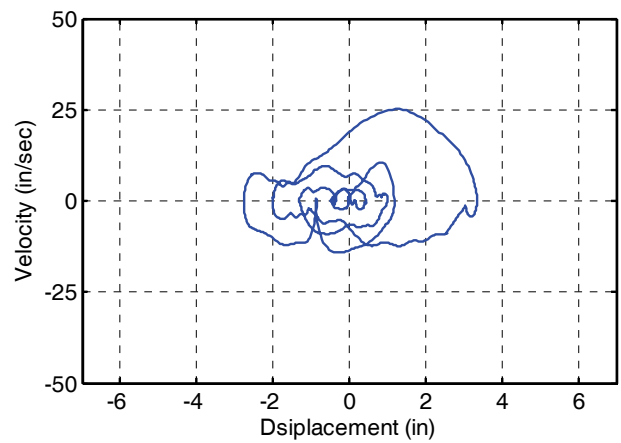
(c) GM15-2



(d) GM16-2



(e) GM17-1



(f) GM17-2

**Figure 5-11 Base level velocity versus displacement for different record at MCE level**

## 5.4. Results for Isolated Base Structure with Moat Wall

To investigate the effects of pounding at the base level of isolated structures, moat wall models were installed on the simulator platform at both sides of the structure. The gap distance between the base of the structure and the moat wall were varied between 4-6 in. to induce pounding at various impact velocities. Different thicknesses for the concrete moat wall model were also considered to investigate the effect of the wall stiffness on the behavior of the superstructure. The concrete moat wall models are U-shaped and filled with sand to simulate soil backfill as show in section 4. The bottom slab was bolted tightly to the shake table to prevent slip at the base during impact. A rigid steel wall was also bolted to simulate a rigid wall; in the first series of testing, it was noticed that the wall was uplifting due to bolt elongation and was welded to minimize rocking at the base. Table 3-14 through Table 3-17 list all impact tests conducted in this study. The moment frame was replaced during testing when permanent damage was observed such as major yielding in the beams and residual displacements. The experimental results for three cases of impact are presented in detail for input motion GM17-1 at MCE level for the following cases: the 2 in. concrete moat wall installed at 6 in. gap; 6 in. concrete moat wall installed at 4 in. gap; and steel moat wall with weld installed at 4 in. gap distance. All impact test results can be accessed in the NEES website under the NEES TIPS project directory (<https://nees.org/warehouse/project/571>).

### *5.4.1. Test Results for Base Isolated IMRF with 2 in. Concrete Moat Wall at 6 in. Gap Distance*

The 2 in thickness concrete walls were installed at 6 in gap distance. GM17-1 was simulated on the shake table to induce large displacement at the base level of the isolated model, leading to pounding to moat walls. Figure 5-12 shows the hysteresis behavior of each isolator and also indicates the displacement at which contact between the moat wall and concrete blocks mounted on base level of the superstructure occurs. Although moat walls were installed at 6 in gap distance, the east moat wall moved due to damaged during previous tests and also during installation on the shake table.

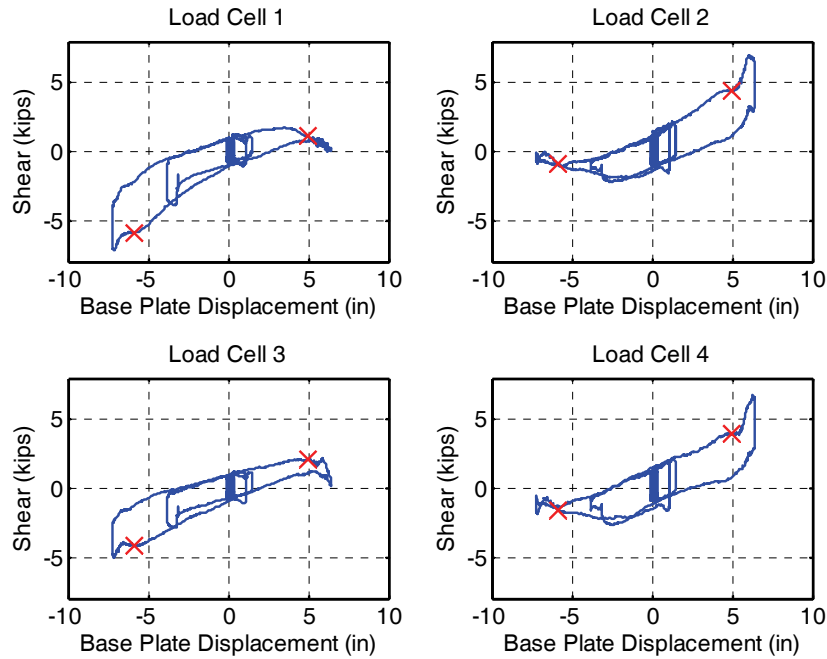


**Figure 5-12 Isolator hysteresis behavior for record GM17-1 at MCE and 2 in. concrete walls installed at 6 in. gap**

Figure 5-13 shows the base level acceleration with large spikes at the time of two impacts. The magnitude of this spike is different between different accelerometers installed on base plate and depends on the location of the sensor and distance to the pounding surface. Figure 5-14 shows the base level velocity versus displacement. It can be seen that the velocity did not change significantly at the time of impact indicating that the 2 in concrete moat walls are too weak to stop the movement of the structure.

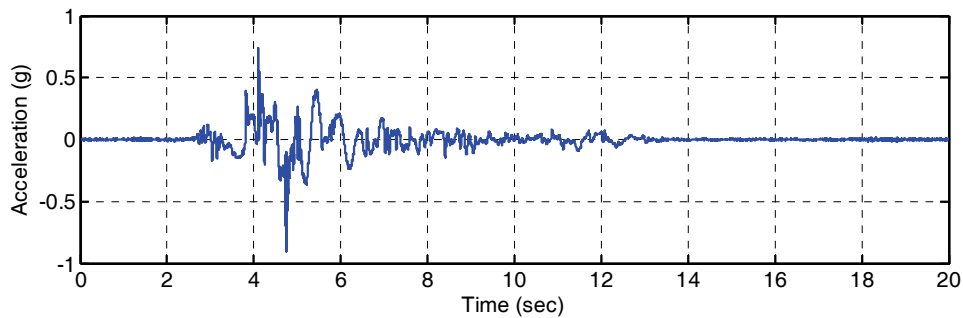


**Figure 5-13 Base level acceleration for record GM17-1 at MCE and 2 in. concrete walls installed at 6 in. gap**

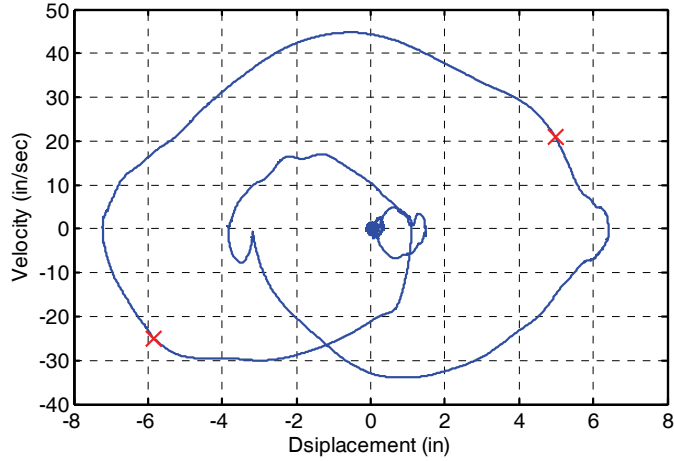


**Figure 5-14 Base level velocity versus displacement for record GM17-1 at MCE and 2 in. concrete walls installed at 6 in. gap**

The impact force generated during the contact of the concrete block mounted on the base level and the concrete moat walls are shown in Figure 5-15. The maximum magnitude of 5 kips was observed due to this impact. Figure 5-16 shows both sides of the moat walls displacement due to impact for both the east and west walls. Large displacements were observed in the front side of concrete walls while smaller displacements are shown for the back side wall due to compression of soil between the two concrete walls.

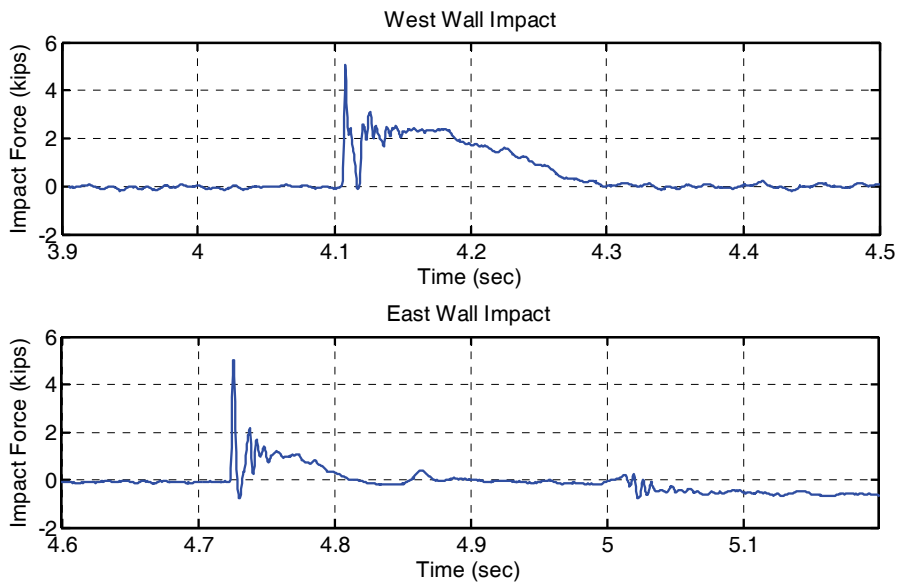


**Figure 5-15 Impact force for record GM17-1 at MCE and 2 in. concrete walls installed at 6 in. gap**

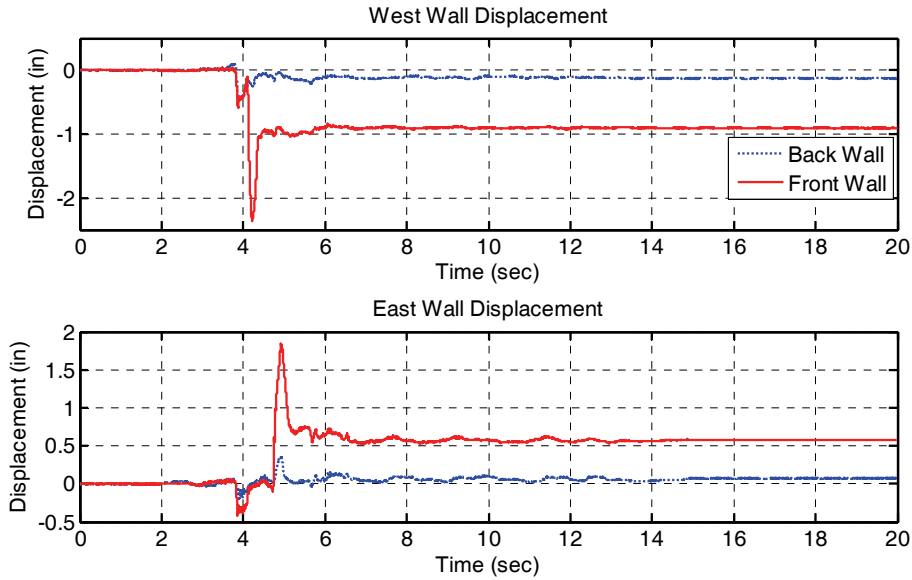


**Figure 5-16 Moat wall displacement for record GM17-1 at MCE and 2 in. concrete walls installed at 6 in. gap**

*5.4.2. Test Results for Base Isolated IMRF with 6 in. Concrete Moat Wall at 4 in. Gap Distance*

The 6 in concrete moat walls were installed at 4 in gap distance and the model structure was subjected to GM17-1. A large level of noise was recorded in shear load cells under each isolator after pounding to moat walls (Figure 5-17) although shape of hysteresis loops are similar to those shown in Figure 5-12

Larger spikes in compare to the case with 2 in moat wall are observed at the time of impact in base level acceleration resulting to peak base level acceleration in range of 4g (Figure 5-18).

A gradually drop in base level velocity can be seen in Figure 5-19 after contact. Although the moat walls were installed at 4 in gap distance, the maximum displacement in base level exceeds more than 6 in for both directions showing that concrete walls did not have sufficient strength capacity to limit displacements.

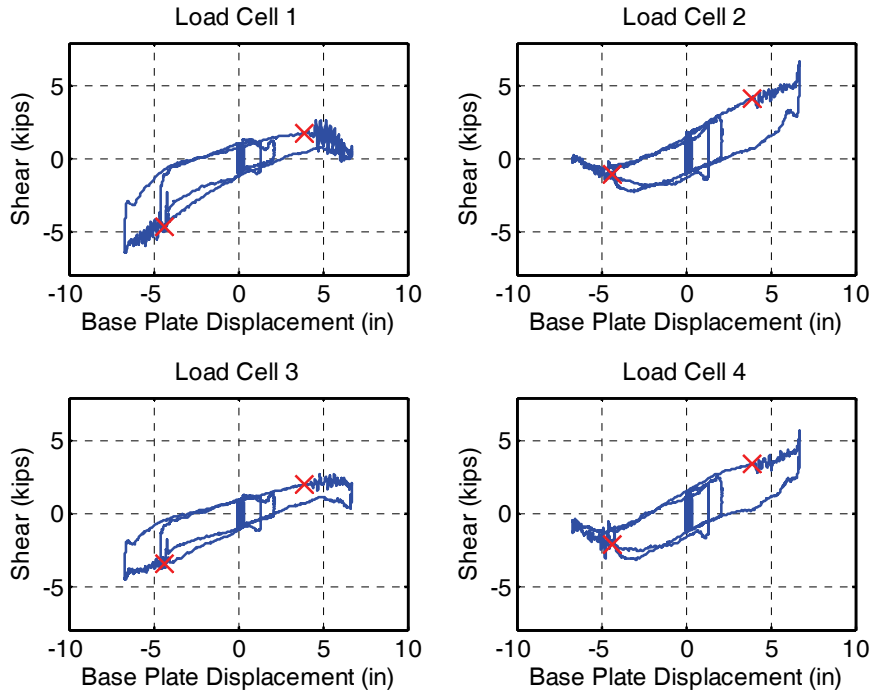


**Figure 5-17 Isolator hysteresis behavior for record GM17-1 at MCE and 6 in. concrete walls installed at 4 in. gap**

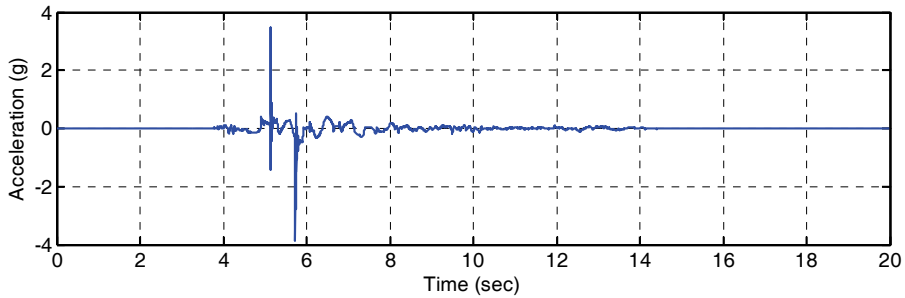


**Figure 5-18 Base level acceleration for record GM17-1 at MCE and 6 in. concrete walls installed at 4 in. gap**

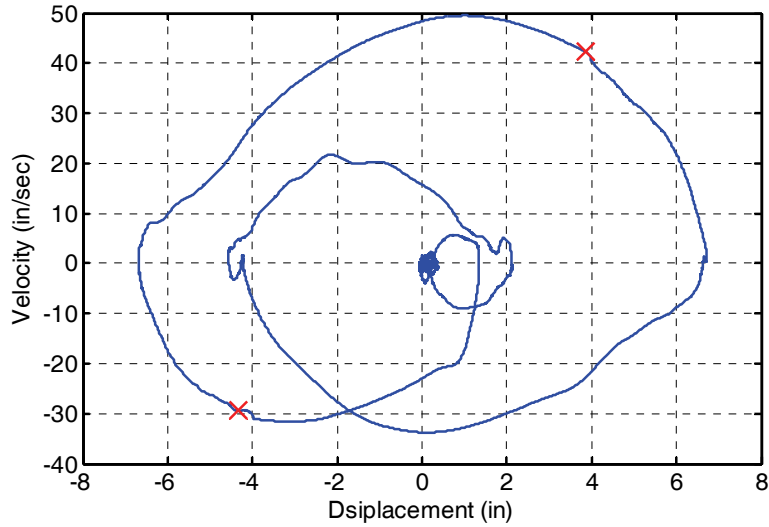


**Figure 5-19 Base level velocity versus displacement for record GM17-1 at MCE and 6 in. concrete walls installed at 4 in. gap**

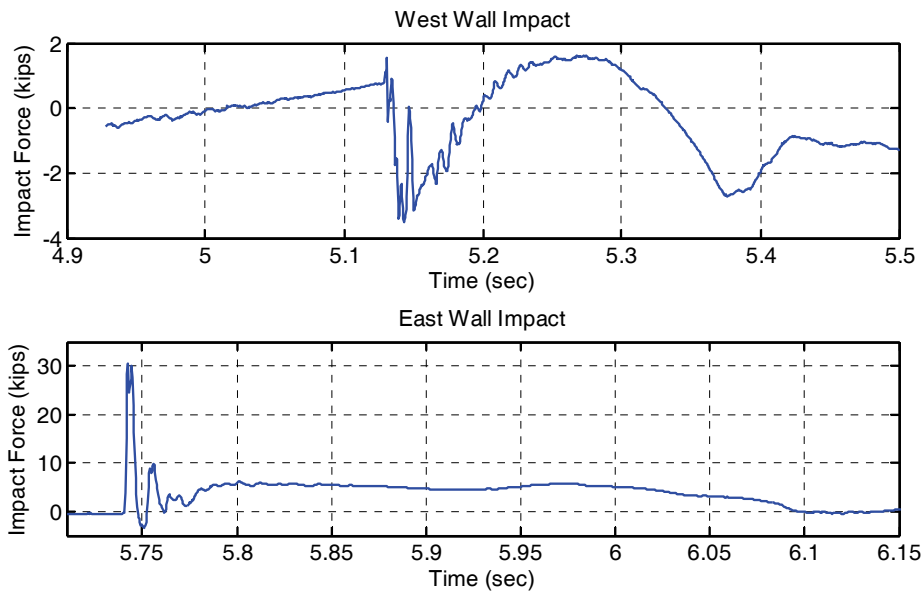


**Figure 5-20 Impact force for record GM17-1 at MCE and 6 in. concrete walls installed at 4 in. gap**

Figure 5-20 shows impact forces for east and west walls. The load cells at the west wall were relocated during testing program and did not properly record the impact force. The impact force to the east wall shows a large initial impulse magnitude in range of 30 kips while after that

dropped to an approximately constant number of 8 kips due to compression in soil backfill. The initial high amplitude force is due to a local impact phase which will be described in Section 6.

Front and back side wall displacements are shown in Figure 5-21. As expected from Figure 5-19 large displacements occur in the front walls on both sides. This large deformations in concrete moat walls resulted in residual displacement about 1 in. for both sides.

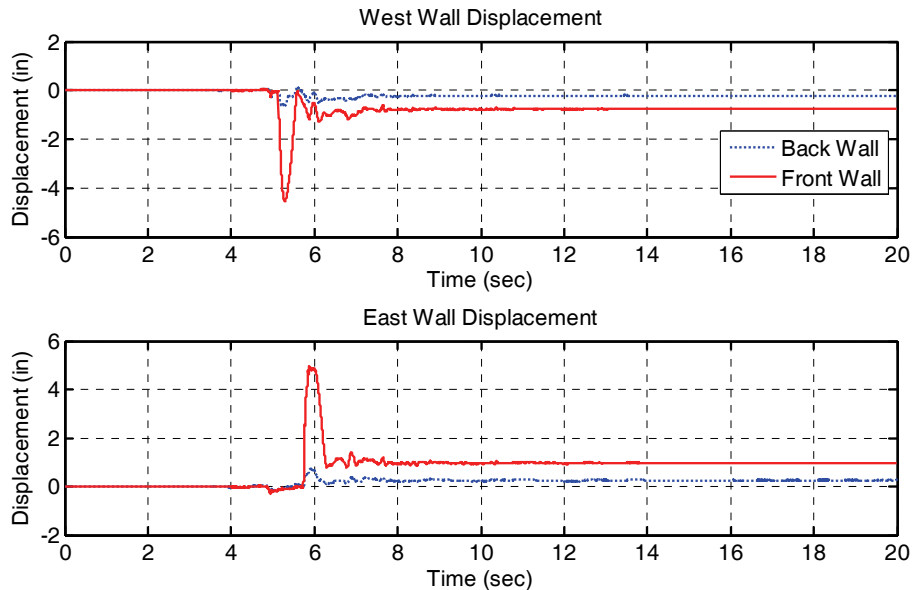


**Figure 5-21 Moat wall displacement for record GM17-1 at MCE and 6 in. concrete walls installed at 4 in. gap**

#### *5.4.3. Test Results for Base Isolated IMRF with Welded Steel Moat Wall at 4 in. Gap Distance*

The low stiffness and strength of concrete walls persuaded the use of stronger moat walls to investigate impact over a wider range of moat wall properties. Steel moat walls were installed and impact testing was repeated using GM17-1 input motion. In the initial installation, base uplift was observed in the steel moat walls at the connection point to the shake table platform at the instant of impact. The steel moat walls were welded at their base to prevent this uplift. The results for welded steel wall installed at 4 in gap distance under GM17-1 input motion are shown here; the results of steel wall without welding and also under different gap distance and various input motion are shown in the NEES website under the NEES TIPS project directory (<https://nees.org/warehouse/project/571>).

Hysteresis loops for each isolator are shown in Figure 5-22. This figure shows that although hysteresis loops are narrowing in tension region, the data does not show uplift in isolators unlike the other two tests on 2 and 6 in concrete walls. This indicates that uplift occurs due to large displacements and not because of impact. In Figure 5-12 and Figure 5-17 uplift was observed in isolators because of large displacement in base level, but in the case of installing the steel walls, large displacement at base level was prevented.

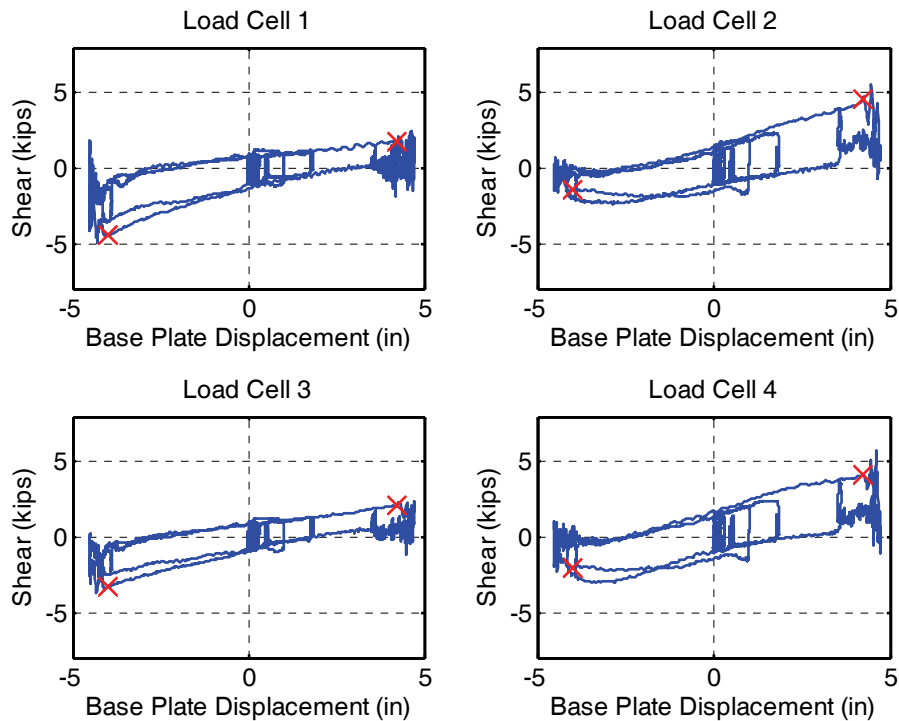


**Figure 5-22 Isolator hysteresis behavior for record GM17-1 at MCE and steel wall with weld installed at 4 in. gap**

A sudden drop in velocity can be seen in Figure 5-23 at the instant of impact to both sides. This drop was not clear in the case of concrete moat walls. Small displacements beyond the gap distance were observed in this test confirming the high stiffness of the steel moat wall.

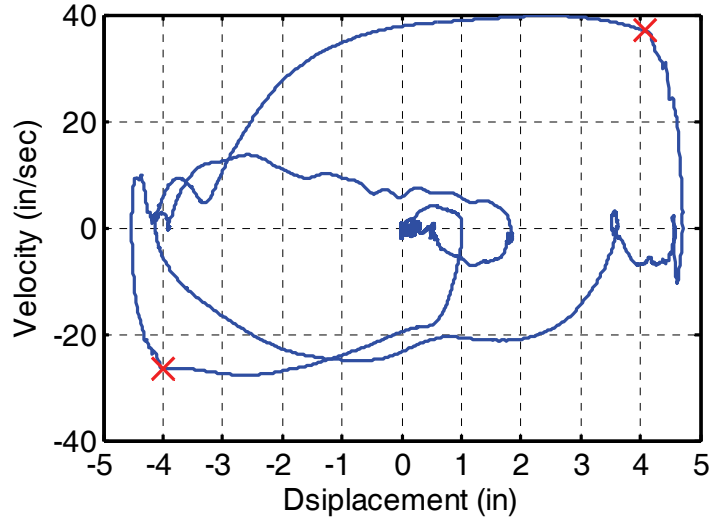


**Figure 5-23 Base level velocity versus displacement for record GM17-1 at MCE and steel wall with weld installed at 4 in. gap**

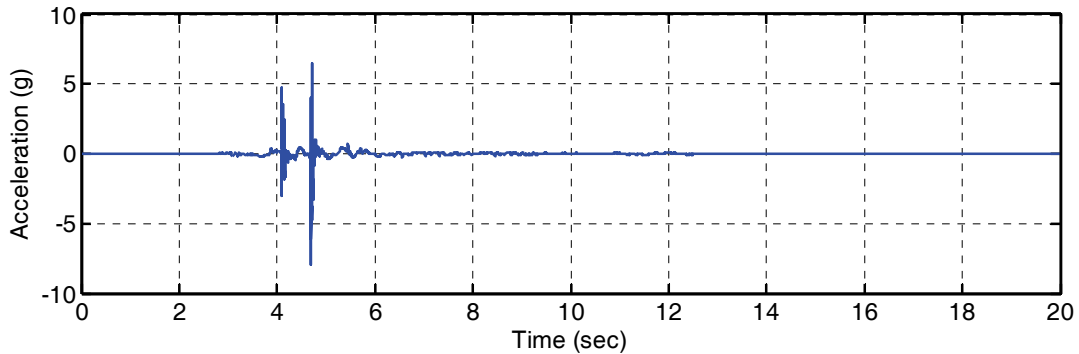


**Figure 5-24 Base level acceleration for record GM17-1 at MCE and steel wall with weld installed at 4 in. gap**

The impact forces are shown in Figure 5-25. High forces (in range of 30-60kips) are generated at the base level of structure during contact with the steel walls. The main difference between impact to steel wall and concrete walls is shown in this figure. For steel, the high amplitude impact force lasts during the contact duration as opposed to the concrete moat walls in which the high amplitude force is applied during a very short duration in the beginning of impact and followed by a longer duration low amplitude force resulting from yielding in the concrete wall and compression in soil backfill. This leads to different superstructure response, which will be discussed next.

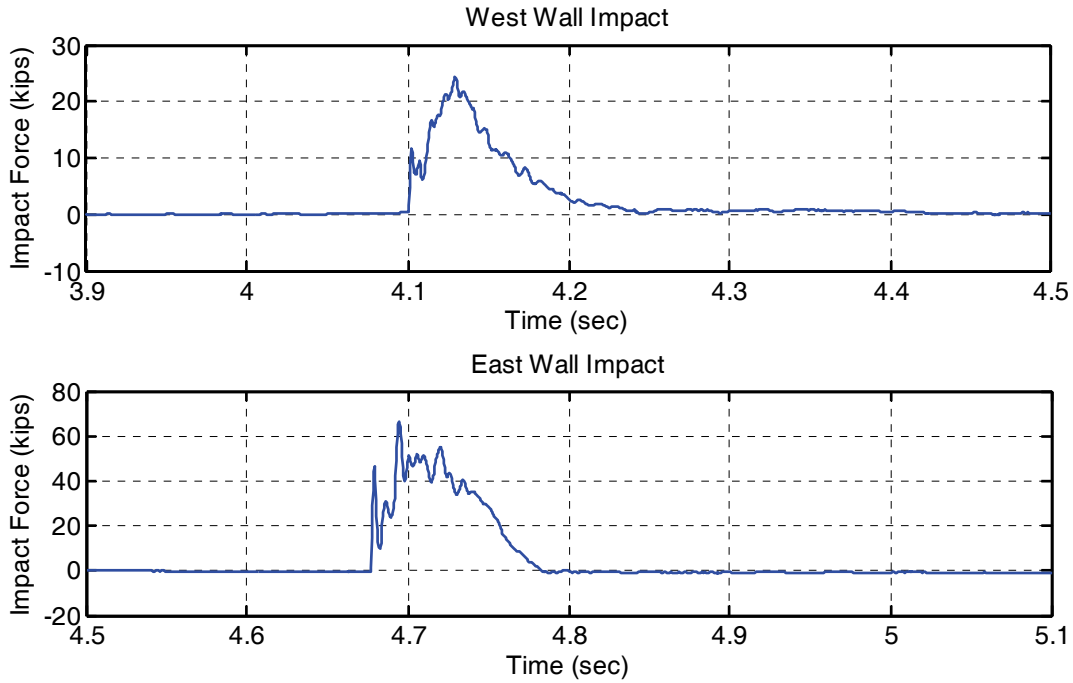


**Figure 5-25 Impact force for record GM17-1 at MCE and steel wall with weld installed at 4 in. gap**

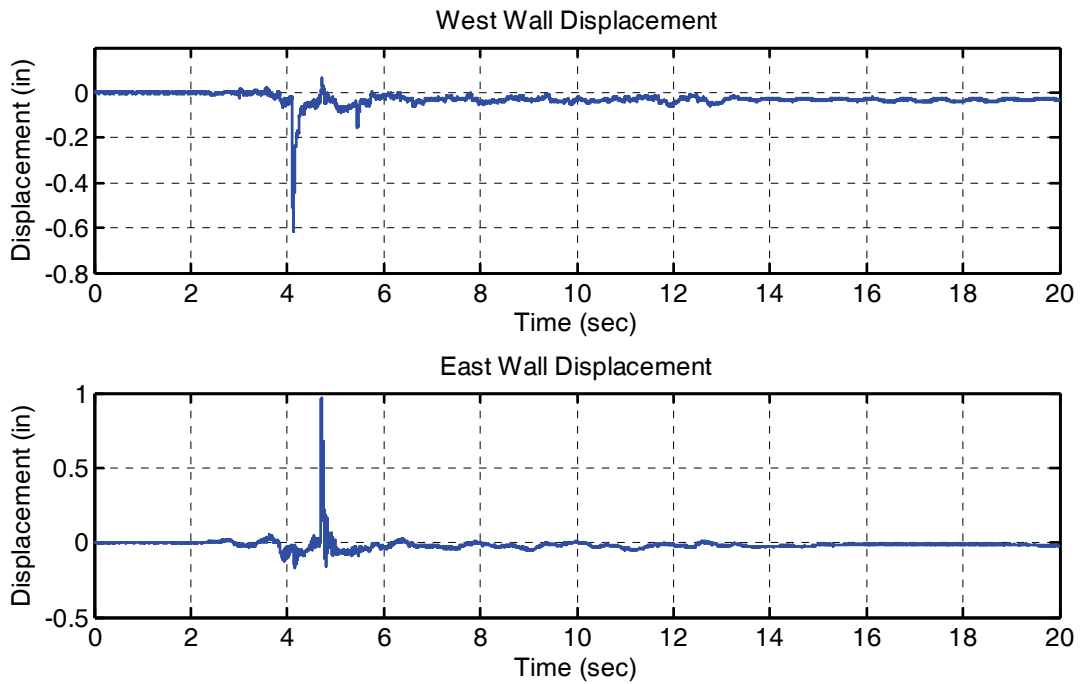


**Figure 5-26 Moat wall displacement for record GM17-1 at MCE and steel wall with weld installed at 4 in. gap**

## 5.5. Effects of Wall Stiffness and Gap Distance

Different types of moat walls having a wide range of stiffness were placed at various gap distances in the experimental simulations. The effect of these various walls on the impact force and response of the superstructure is evaluated in this section. Figure 5-27 shows the impact force for three types of the moat walls with a 6 in. gap: 6 in. thick concrete wall with soil backfill and steel wall with and without weld reinforcement. In the experiments, the impact force was obtained from two load cells installed behind the concrete block at the base. Note that the time in Figure 5-27(a) is a pseudo time shifted so that in all cases, initiation of impact occurs at the origin to provide a better comparison. It can be seen that each impact force consists of two separate phases. The first phase of impact consists of a short duration (less than 10 ms), high amplitude impulse, with all three walls providing approximately the same force amplitude and duration. In the second phase, which is at least one order of magnitude longer in duration than the first phase, the three resisting forces show substantially different behavior and appear to be highly dependent on the stiffness of the wall.

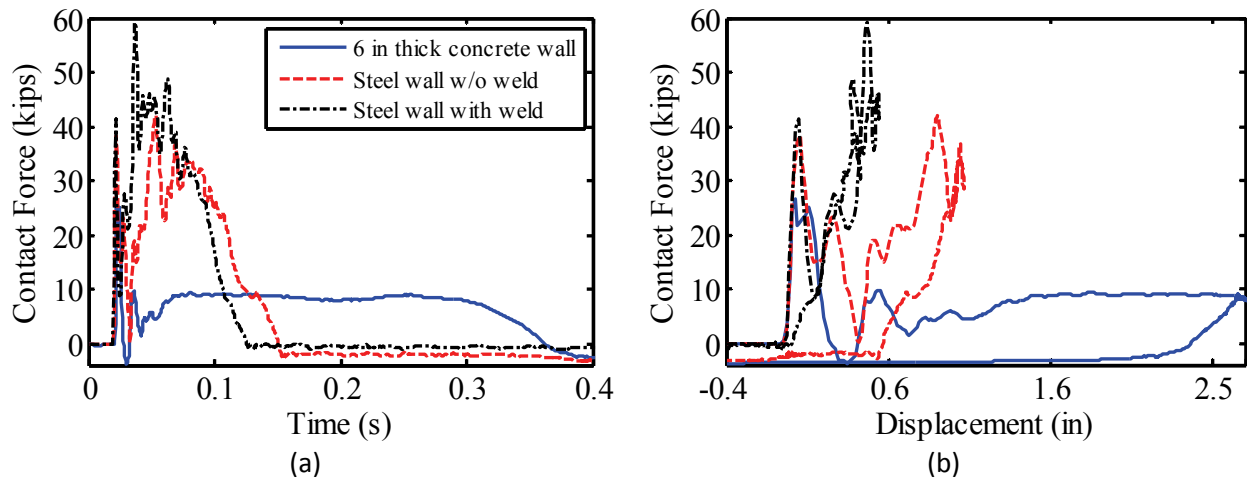


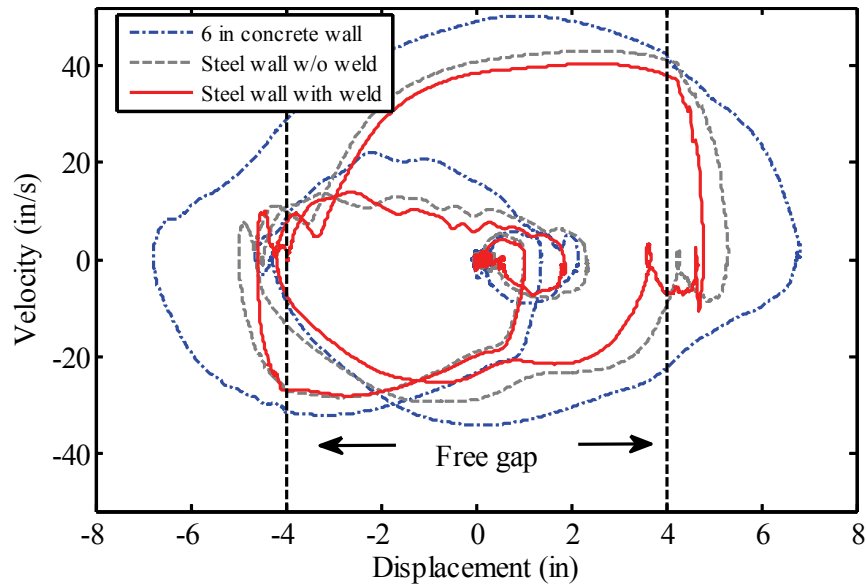
**Figure 5-27 Impact force for different moat wall types: (a) Impact force versus contact time, (b) Impact force versus moat wall relative displacement**

The observed forces in seismic pounding can be further explained by considering this as a problem of dynamic impact (Goldsmith 2001). In a structural collision as observed in these experiments, contact between two objects consists first a local phase followed by a second global

response phase. The first phase occurring over a short period of time is the local impact phase which includes the indentation of two objects at the point of the contact. The contact force generated in this phase is generally a function of the shape and material properties of colliding objects as well as impact velocity. The contact forces act over a short period of time, where energy is dissipated as heat due to random molecular vibrations and the internal friction of the colliding bodies. In this phase, due to the fact that the time of contact is short, it can be assumed that the characteristics of external seismic forces (direction, frequency, etc.) do not affect the displacement and duration of impact. Thus, this first phase consists mainly of a free colliding system with initial velocity. The second phase occurs after the first impact during which the two bodies stay in contact, sometimes followed by a short separation after phase 1, and push or generate forces against each other. The contact force in this second phase can be affected by external seismic forces, and dynamic properties of the two objects including mass and stiffness.

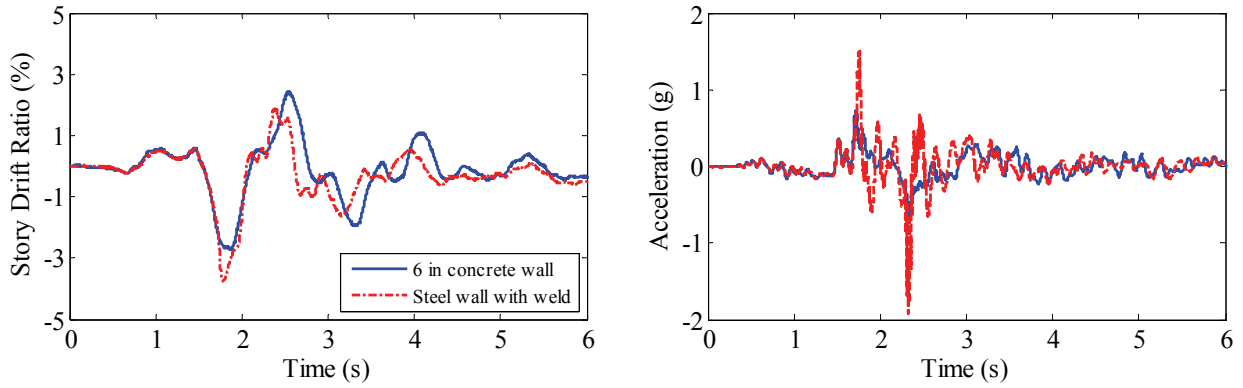
The second phase of impact is more evident in Figure 5-27(b), which plots impact force versus deformation of the moat wall while the base level is in contact with the wall. The stiffness variation for different moat walls is apparent in this figure. A slight slip can be seen in the steel wall without weld reinforcement although its stiffness is very close to the case with welded connections. The concrete wall shows relatively low resistance after first phase of the impact, mainly from compression of soil behind the wall since the concrete wall formed a plastic hinge at its base where the bending moment is maximum.

Figure 5-28 shows base level velocity versus displacement for a 4 in. nominal gap distance to the wall for different wall types under MCE level of GM17-1 (Erzincan NS) earthquake. The effect of the wall stiffness on the distance that base level travels beyond the gap distance and the velocity drop at the instance of the impact is evident in this figure. The stiffer the wall, the less distance the base plate moves beyond the gap, producing a sharper drop in velocity after impact.

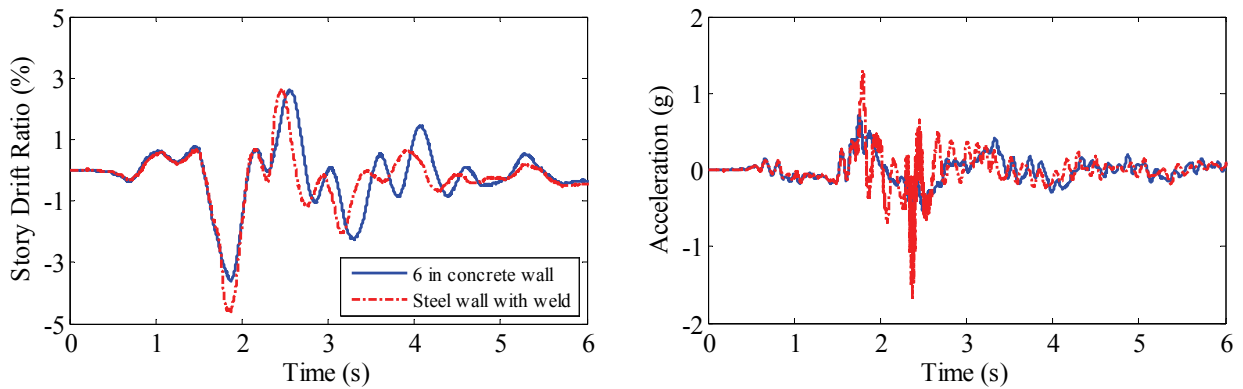


**Figure 5-28 The effect of different wall types installed at 4 in. gap distance on base level velocity**

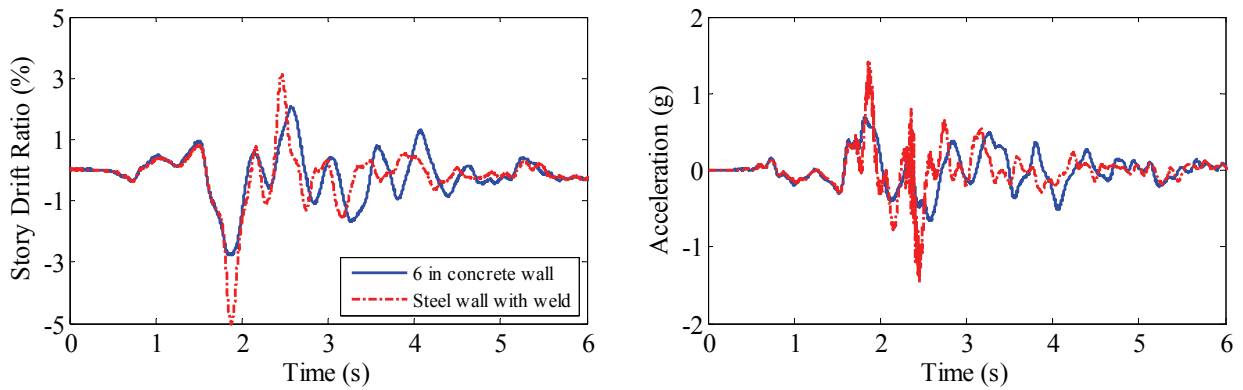
The effect of different wall types on superstructure response under GM17-1 (Erzincan NS) record at MCE level for 4 in. gap distance is shown in Figure 5-29. The results for two wall types, namely the 6 in concrete wall and steel wall with weld reinforcement are compared in this figure. It should be noted that the steel walls without weld reinforcement results are very close to the case presented here with weld reinforced connections. The maximum story drift ratio occurred at the second and third level for the case of the impact to the concrete wall and steel wall respectively. Significant differences are evident in the acceleration response under these two different moat walls, particularly when examining the frequency. In both cases, the maximum acceleration is captured at the first story closest to the point of impact. The data presented clearly show that both displacement and acceleration response of the superstructure are highly dependent on stiffness of the moat wall. The higher forces generated by the stiffer wall increases both acceleration and displacement.



(a) First story



(b) Second story



(c) Third story

**Figure 5-29 The effect of different wall types on superstructure response**

Figure 5-30 summarized the superstructure response for all impact tests under GM17-1 (Erzincan NS) ground motion at MCE level for different wall types and compares them with the case without impact. Minimum and maximum acceleration and story drift ratio are plotted in separate figures to investigate effects of each impact. Minimum negative drifts and maximum positive

accelerations occurred after the first impact to the west wall while the second impact to the east wall leads to maximum positive drifts and minimum negative accelerations. It can be seen that by increasing the moat wall stiffness, both acceleration and drift increased at all stories of the model, although the effects of the moat wall stiffness is more apparent on lower floor accelerations and upper floor drifts. Response acceleration increased in all stories of the structure after both impacts. The peak floor acceleration occurred at the lower story with impact while the peak floor acceleration occurred at the top floor without impact. The acceleration amplification in lower levels could be under influence of internal material wave propagation in the model due to impact. Not considering the base level, the maximum floor acceleration is in the range of 1-2g, which is a significant increase in comparison to the case without impact.

The effect of impact on story drift is apparent after the first impact to the west wall, which yields the superstructure in the negative direction, while maximum positive drifts are influenced by both west and east wall impacts. While it is expected that a harder impact to the east wall should result in larger amplification of positive drifts, exceeding the response in the negative direction as observed for the 2 and 4 in concrete walls, the stiffer moat wall yielded the superstructure after the first impact and affects the drifts after second impact. Lower levels of impact (Figure 5-30 (a), (b), and (c)) amplify the drift ratios after each impact and keeps the shape of maximum drifts the same as first modal shape, while stronger impacts (Figure 5-30 (d), and (e)) increased the upper story drift ratio relative to lower stories.

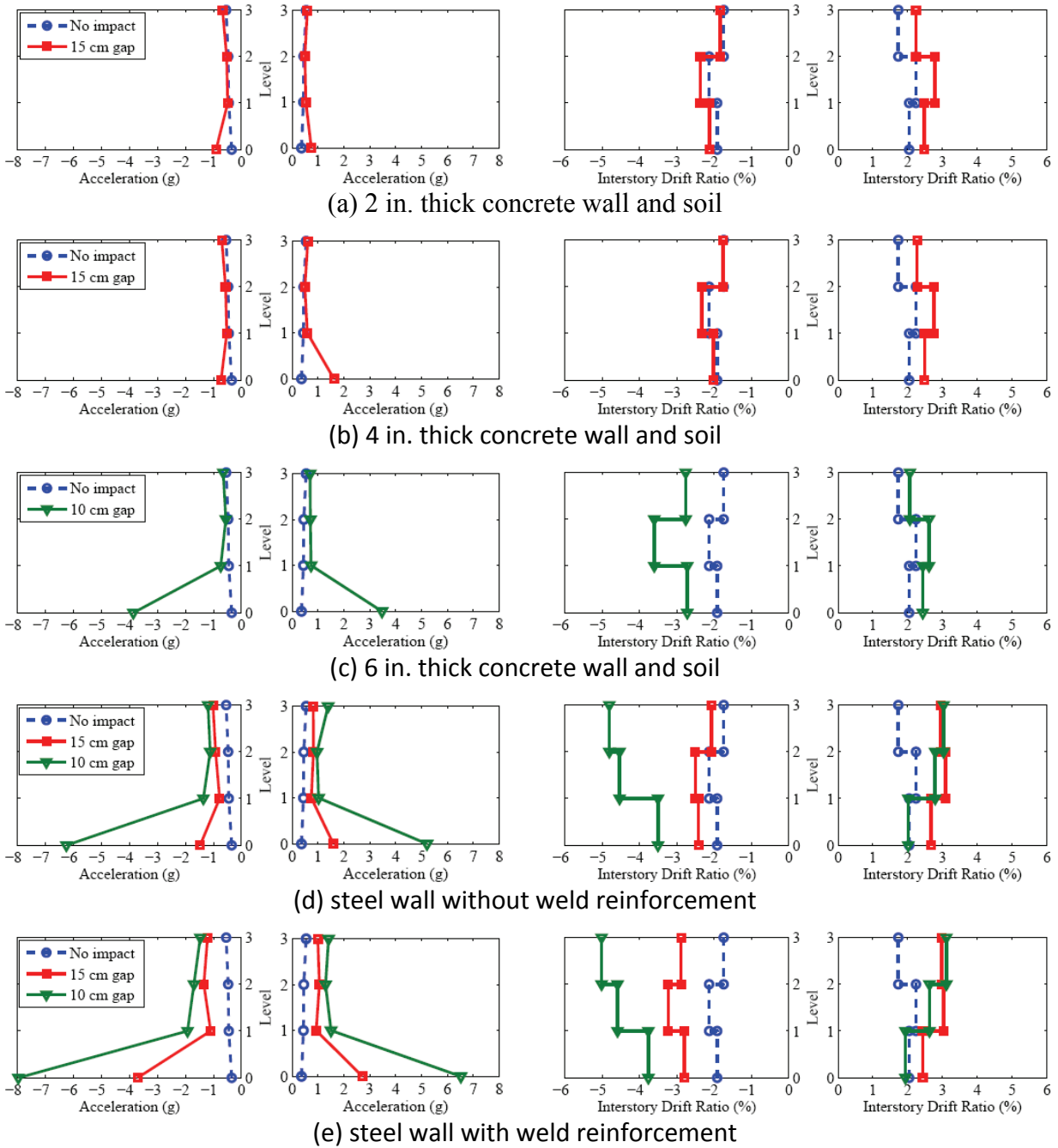


**Figure 5-30 Minimum and maximum acceleration and story drift ratio under MCE level of GM17-1 (Erzincan NS) ground motion**

Figure 5-31 shows the superstructure response under the same ground motions for different wall types installed at 4 in. gap distance. The GM7-1 (LA33) record induced one hard impact to east wall, except for the steel wall without weld reinforcement; rebound from the east wall induced a

second impact at low velocity to west wall. This one-sided impact amplifies the response of the structure in one direction (positive story drift ratio and negative acceleration) while the other direction responses remains similar to the case with no impact. The impact test results under GM11-1 (Sylmar) and GM7-1 (LA33) records show that increasing wall stiffness increases the acceleration and drifts in all story levels which is in agreement with results obtained for GM17-1 (Erzincan NS) record.

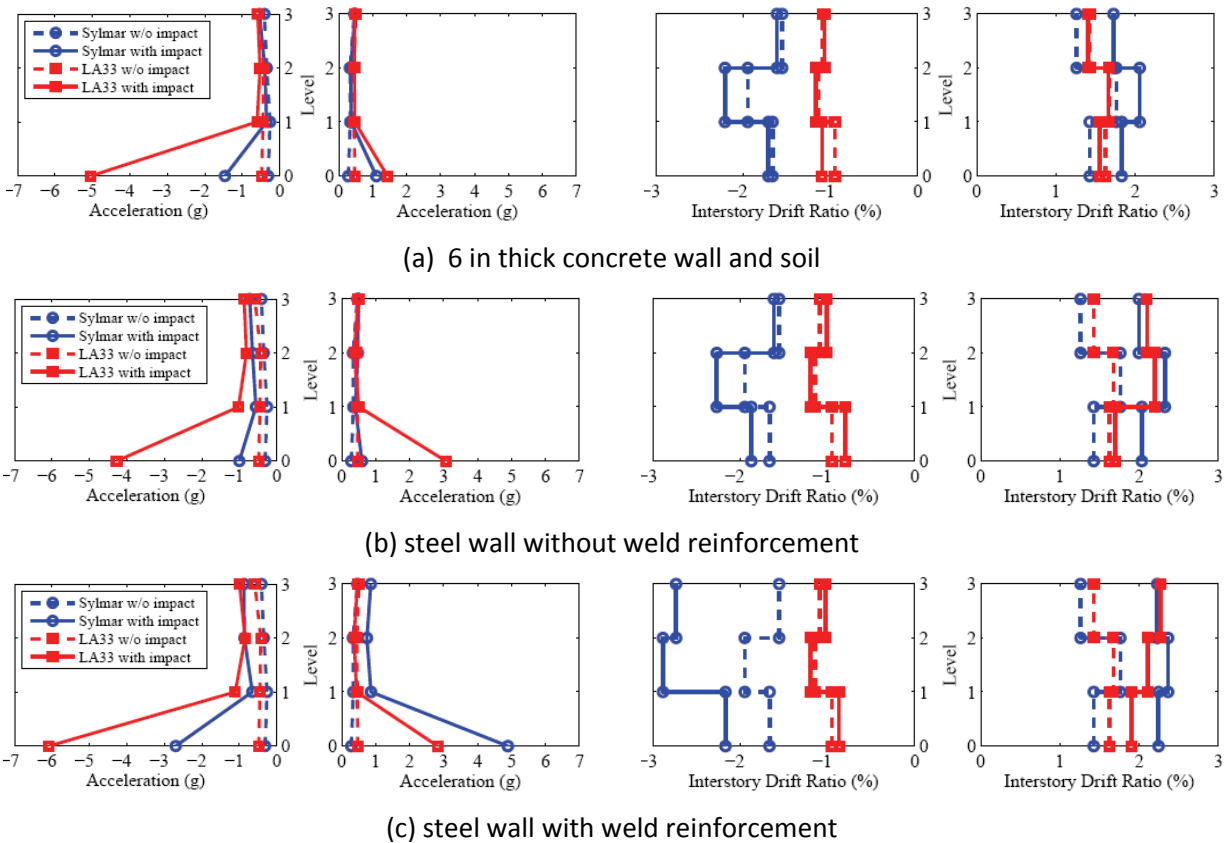


**Figure 5-31 Minimum and maximum acceleration and story drift ratio under MCE level of Northridge at Sylmar Station (GM11-1) and LA33 (GM7-1) ground motions**

## 5.6. Shake Table Performance

Modern shaking tables are considered one of the most realistic means of evaluating the response of a structure subjected to earthquake ground motions. Particularly for impact simulations as described here, shake tables are perhaps the best way to fully capture the dynamic impact forces experimentally and their effect on superstructure response. The main limitation is the reduced

scale of the model to comply within the capacity of the earthquake simulator. For the tests presented here, the impact forces on the moat wall models need to be absorbed by the shaking table and if sufficiently large, can damage the equipment. In addition, the impact forces will be recorded by the feedback control system and can alter the shake table response. In this section, the safety and performance of the shake table during impact testing is examined.

The accuracy of the shake table simulation, or the level of fidelity to which the achieved motion matches the desired earthquake motion has been examined by many researchers. The frequency content of recorded earthquakes, strong dynamic cross coupling between degrees of freedom, existence of non-linearities in the hydraulic and mechanical system components, and the dynamic interaction of the specimen and table system all contribute to the challenge of achieving high fidelity motions (Nowak et al. 2000).

The tests were conducted on the shake tables at the NEES site at the University at Buffalo. This site includes two movable, six degrees-of-freedom simulators; only one table was used for these tests and loading was applied in one horizontal direction. The payload capacity of each table is 80 kips, and the model weighs about 60 kips. Each shake table is driven by the following hydraulic actuators:

1. Horizontal (X and Y-axis) hydraulic actuators (quantity = 2 each axis). MTS Model 244.4 Hydraulic Actuator with a dynamic force rating of 50 kips and a dynamic stroke of 12 in ( $\pm 6$  in).
2. Vertical (Z-axis) hydraulic actuator (quantity =4). MTS Model 206.S Hydraulic Actuator with a dynamic force rating of 60 kips and a dynamic stroke of 6 in ( $\pm 3.5$  in).



**Figure 5-32 NEES at buffalo shake table facility used to conduct the experimental program**

The performance of the UB-NEES shake table during the MCE ground motion and impact of superstructure is evaluated by direct comparisons of the acceleration time histories, peak accelerations error, elastic response spectra for the achieved and desired acceleration time histories, and actuator forces. To provide a quantitative measure, the cumulative measure of the error based on the RMS error measure is applied (Luco et al. 2010):

$$\varepsilon_{rel} = \frac{\sqrt{(1/N) \sum_{n=1}^N (\ddot{x}_{fbk}(n) - \ddot{x}_{des}(n))^2}}{\sqrt{(1/N) \sum_{n=1}^N (\ddot{x}_{des}(n))^2}} \quad (5-1)$$

In Equation 5-1,  $\ddot{x}_{des}$ =desired (command) acceleration;  $\ddot{x}_{fbk}$ =achieved (feedback) acceleration; and N denotes the number of data point within the time window chosen to calculate the error. For earthquake records, this time window was chosen to be the time interval between the 5 and 95% contributions of the desired acceleration time histories to the Arias intensity ( $\int \ddot{x}_{des}^2 dx$ ).

To investigate the effect of pounding in the model on the performance of the shake table, the result of two tests are presented here: base isolated model without moat wall and base isolated model and welded steel walls with 6 in. gap. Both results are from the GM17-1 (Erzincan NS) ground motion at MCE level. The corresponding time interval considered for this ground motion is 9-13 sec.

### 5.6.1. Comparison of Acceleration Time Histories

To get an overview of the performance of the table during the ground motion with impact, the desired and achieved acceleration time histories are first compared. Figure 5-33 shows the measured acceleration time history within the time window defined earlier. The results from (a) the base isolated case without any pounding and (b) the case that superstructure hits the moat wall twice are compared with the target acceleration. The time of the impacts are indicated in the figure. It can be seen that in Figure 5-33, the achieved motion and target motion agreed well except at the peak acceleration which shows a 33% overshoot. In Figure 5-33(b), two spikes are observed in the measured acceleration at the instance of impact. Although the occurrence of impact leads to overshooting followed by a reverse peak in the opposite direction, the achieved acceleration is comparable to the test without impact in other regions. Note that the maximum measured acceleration occurs at the instance of the peak ground acceleration demand and not at the time of impact. The relative peak acceleration error is approximately equal to the error in the test without impact and is equal to 36%.

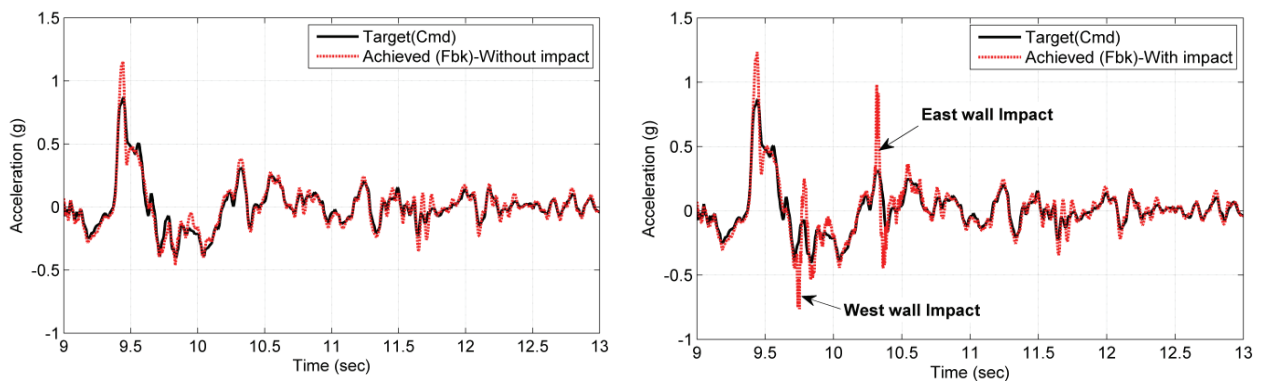


**Figure 5-33 Acceleration time history comparison a) without impact b) with impact**

### 5.6.2. Cumulative Relative Root Square Error

The cumulative relative root square error defined as the summation of square error of achieved motion at each step normalized by the summation of the squared desired value over the total length:

$$\varepsilon_{rel}(\tau) = \frac{\sqrt{\sum_{n=1}^{N_\tau} (\ddot{x}_{fbk}(n) - \ddot{x}_{des}(n))^2}}{\sqrt{\sum_{n=1}^N (\ddot{x}_{des}(n))^2}} \quad (5-2)$$

In Equation 5-2  $N_\tau$ , and  $N$  denote the number of data points up to time  $\tau$  and total length of the time window respectively. This formula converges to relative RMS error in Equation 5-1 as the  $N_\tau$  goes to  $N$ . In this way, one can see the portion of the error at each time step with respect to total RMS error.

Figure 5-34 shows the cumulative root square error for test with and without impact. The limit values of the both curves show the relative RMS error for the total time window of interest. The RMS error with and without impact at 6 in. gap is calculated to be 28 and 46% respectively. The first jump in the Figure 5-34 corresponds to peak acceleration in target ground motion which is almost equal for both cases, while the second and third jump occurs only in the case with impact at the time of impact.

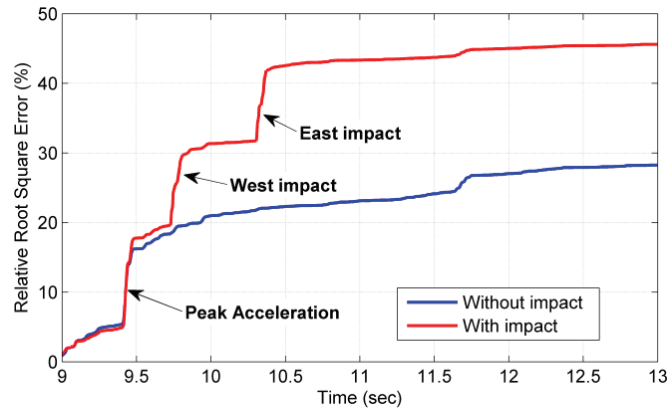


**Figure 5-34 Relative root square error of shake table response**

### 5.6.3. Elastic Response Spectra

The capability of the shake table to reproduce the response spectrum of the target acceleration time history is another important measure of the performance of the table, as it provides some insight into how the structure is excited dynamically. The linear displacement and pseudo acceleration spectra from achieved acceleration time histories were calculated and compared with the response spectra of the target acceleration records. Figure 5-35 shows the resulting

response spectra for both tests compared to the target spectrum. It can be seen that the displacement demands in the large period range are less than the target demand for both cases. In addition, the displacement response for the case including impact is larger than the case without impact. Since the effective isolated base period of the structure is about 1.5 sec, these plots provide some insight into why the larger displacements were observed at the base of the structure in the test including impact.

In Figure 5-35(b), the response acceleration is higher for the test including impact than the achieved response from the test without impact. Both tests have larger acceleration demands compared to the target motion in the low period range. It can be concluded that although response spectra of the achieved motions do not perfectly match the response spectra of the target motion, pounding in the superstructure did not induce a significant difference in the response of the shake table.

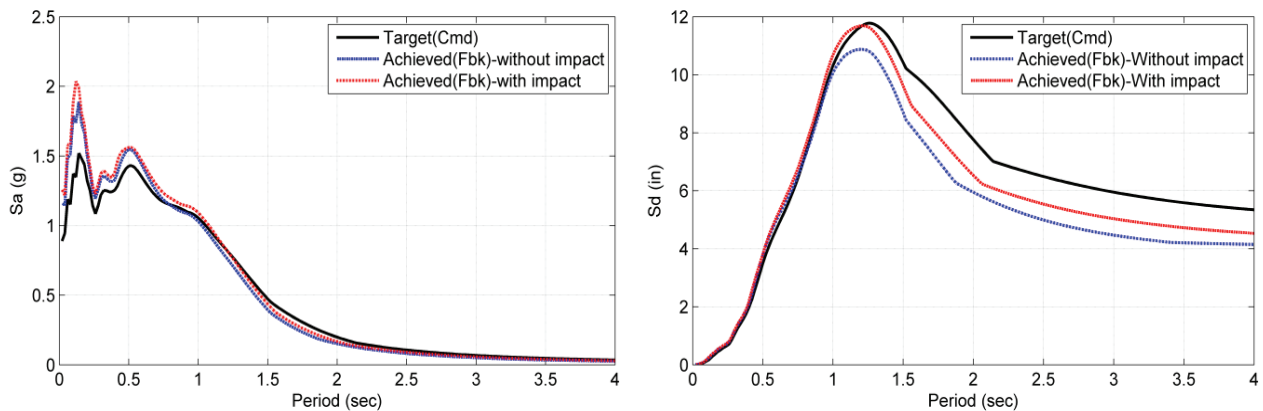


**Figure 5-35 a) Displacement response spectra, b) Acceleration response spectra**

#### 5.6.4. Shake Table Actuator Force

Figure 5-36 shows the force in one of two horizontal actuators in main direction of testing during the selected time window. It can be seen that maximum force occurs at the time corresponding to maximum acceleration in the target motion and is almost equal to the rated force capacity of the actuator. Two spikes in the case with impact are indicated with arrows for west and east wall pounding. The increase in actuator force due to impact is on the order of 25 kips, and because of the low acceleration demands at the time of impact, does not approach the capacity of the

actuator. Thus, for this particular test series and the payload selected, the shake table equipment including actuators was not at risk of damage.

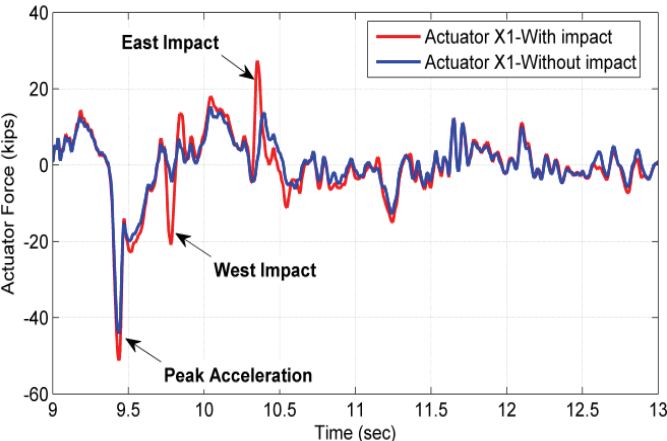


**Figure 5-36 Horizontal actuator force**



## **SECTION 6**

### **ANALYTICAL PREDICTION OF RESPONSE**

#### **6.1. Introduction**

The experimental testing program of a base isolated building was conducted with pounding on various moat wall configurations and different ground motions. The analytical prediction of response of base isolated structures pounding to a moat wall is presented in this section. To better understand the consequences of impact on the superstructure, an impact element considering moat wall compliance is proposed based on impact theory and observations during experimental simulations. It is demonstrated that numerical simulations using the proposed impact element can capture the dominant characteristics of the contact force observed in experiments for both concrete walls with soil backfill and rigid steel walls. The contact force is dependent on impact velocity, geometry and material properties at the contact surface, as well as the global dynamic flexibility characteristic of the moat wall. Properties of the moat wall impact element are derived here based on mechanics-based models considering material properties and geometric measurements of the experimental setup. For this purpose, the moat wall is modeled as a flexural column with a concentrated hinge at its base with soil backfill considered through a damped elastic foundation.

The main objective of this section is to propose a new impact element that can simulate contact force during impact of base isolated structure to a moat wall. The proposed impact element is able to capture both local deformation and vibration response of the moat wall. The classic contact mechanics of impact of a striker object to a column representing the moat wall is investigated and equations for calculating required parameters for the proposed simplified impact element are derived. The impact force obtained from numerical simulation for different wall types are compared with earthquake simulator test results from section 5. It is demonstrated that the proposed impact element with parameters derived from the mechanical properties of the walls is able to capture the main characteristics of the contact force and the effects on superstructure response.

## 6.2. Analytical Modeling of Structural Impact

### 6.2.1. Classical Theory of Impact

The classical theory of impact, called stereomechanics, is based preliminary on the impulse-momentum law for rigid bodies, which specifies of initial and terminal velocity states (Figure 6-1). In this theory, velocities of the colliding bodies after collision are calculated from:

$$v_{1t} = v_{1i} - (1+e) \frac{m_2(v_{1i} - v_{2i})}{m_1 + m_2} \quad (6-1a)$$

$$v_{2t} = v_{2i} + (1+e) \frac{m_1(v_{1i} - v_{2i})}{m_1 + m_2} \quad (6-1b)$$

In this equation  $v_i$ ,  $v_t$  are the velocities before and after collision, the subscripts 1 and 2 identify the two colliding bodies, and  $e$  is the coefficient of restitution. The coefficient of restitution accounts for energy loss during impact, and is usually defined as the ratio of final to initial relative velocity. Using this approach, Malhotra (1998) investigated the effect of earthquake-induced pounding at thermal expansion joints of concrete bridges. Examining collinear impact between concrete rods of the same cross section but different lengths showed that the coefficient of restitution depends only on the length ratio and the damping ratio of the rod material and the duration of impact is equal to the fundamental period of axial vibration of the shorter rod.

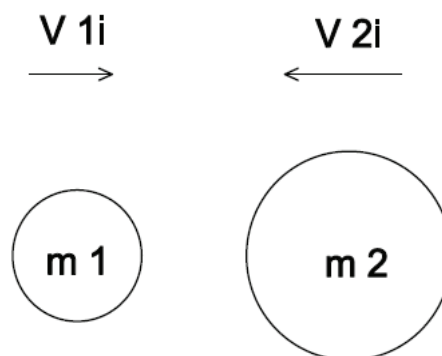


**Figure 6-1 Classical theory of impact.**

From Equations 6-1, it is evident that this theory does not account for impact duration, transient forces, and local deformations at the contact point and further assumes that a negligible fraction of the initial kinetic energy of the system is transferred into local vibrations of colliding bodies. These assumptions limit the application of stereomechanics theory in accurately capturing structural collisions consisting of two phases discussed next.

### 6.2.2. Local Deformation Phase Produced by Impact

In a majority of collisions, at least one of the participating objects will be bounded by a curved surface at the contact location. However, even in smooth planes located normal to the direction of impact, there are some factors including the existence of microscopic surface irregularities, which prevent achieving contact between two perfectly plane surfaces. In this case, the two bodies will undergo a relative indentation in the vicinity of the impact point. The energy required to produce this local deformation may be an appreciable fraction of the initial kinetic energy. Most research related to structural impact has proposed force-displacement models to capture this phenomenon such as a linear spring, Kelvin, Hertz, and Hertz model with nonlinear dampers. The linear model is straight forward and can be easily implemented in commercial software, although lack of energy loss during impact leads to unrealistic results. The Kelvin model consists of a linear spring and damper in parallel to simulate the energy loss due to permanent deformation at the contact point, but shows tension forces due to damping even after two objects have separated.

The Hertz contact law was originally proposed for static contact of two bodies, in which stresses and deformations near the contact point are described as a function of the geometric and elastic properties of the bodies (Goldsmith 2001). The contact force is related to the relative indentation of two bodies with a nonlinear spring of stiffness  $K_h$  calculated as:

$$K_h = \frac{4}{3\pi} \left( \frac{1}{\lambda_1 + \lambda_2} \right) \sqrt{\frac{R_1 R_2}{R_1 + R_2}} \quad (6-2a)$$

$$K_h = \frac{4}{3\pi} \left( \frac{1}{\lambda_1 + \lambda_2} \right) \sqrt{R_1} \quad (6-2b)$$

respectively, for two colliding spheres of radii  $R_1$  and  $R_2$ , and collision of a sphere of radius  $R_1$  to a massive plane surface. In these formula,  $\lambda_i$  is a material parameter defined as:

$$\lambda_i = \frac{1 - \nu_i^2}{\pi E_i} \quad (6-3)$$

where  $E_i$  and  $\nu_i$  are modulus of elasticity and Poisson's ratio, respectively. For other geometric shapes, an equivalent sphere radius can be used. The contact force can then be expressed as:

$$F_c = K_h \delta^n \quad (6-4)$$

where  $\delta$  is relative penetration and  $n$ , is typically taken as 3/2 for nonlinear behavior.

The use of the Hertz model for dynamic impact has been justified on the basis that it appears to predict accurately most of the impact parameters that can be experimentally verified (Goldsmith 2001). However, the original model does not capture the energy dissipated during contact. To overcome this limitation, Muthukumar *et al.* (2006) proposed a nonlinear damper in conjunction with the Hertz model with contact force given by (Figure 6-2):

$$F_c = K_h \delta^{3/2} + C_h \dot{\delta} \quad (6-5)$$

where  $C_h$  is the damping coefficient, and  $\dot{\delta}$  is penetration velocity. The damping coefficient is related to penetration using Equation 6-6 in order to prevent tensile forces after the two bodies separate.

$$C_h = \xi \delta^{3/2} \quad (6-6)$$

In this equation,  $\xi$  is damping constant which is expressed as (Ye et al. 2009):

$$\xi = \frac{8 K_h (1-e)}{5 e \dot{\delta}} \quad (6-7)$$

Jankowski (2007) determined a range of the coefficient of restitution ( $e$ ) for different building materials, such as: steel, concrete, timber and ceramics, based on the results of impact experiments. A general trend observed for all materials is that the coefficient of restitution decreases with an increase in the prior impact velocity. A range of  $e$  from 0.75 to 0.50 for impact velocity of 0.25 m/s to 4 m/s was determined for concrete materials.

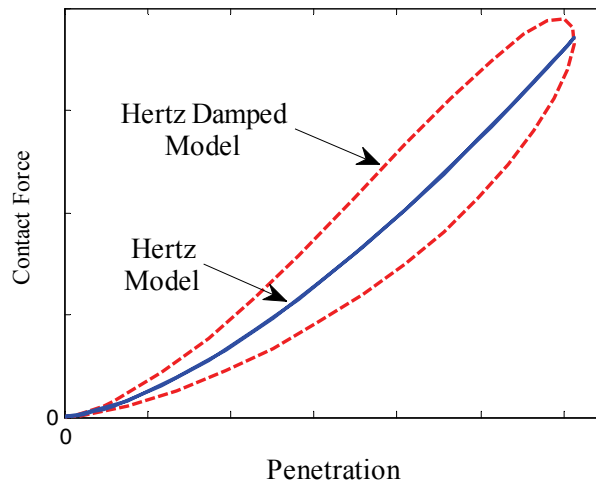


**Figure 6-2 Contact force-penetration relationship for Hertz and Hertz damped models.**

### 6.2.3. *Vibration Aspect of Impact*

In the stereomechanical treatment of impact, the colliding objects may be regarded essentially as single mass points or rigid bodies uniformly undergoing an instantaneous change in velocity. For elastic bodies, the disturbance generated at the contact point propagates into the interior of the bodies with a finite velocity and its reflection from the boundaries produces oscillations or

vibrations in the solids. The predictions of the stereomechanical theory may produce errors when a significant percentage of total energy is converted into vibrations (Goldsmith 2001). In general, this effect will be small when the duration of the contact is large compared to the period of the lowest natural frequency of either body such as collision of two spheres at moderate velocities. On the other hand, a considerable amount of energy is transformed into vibrations in the collision of bodies with low natural frequencies. Such objects generally exhibit a high ratio of surface area to volume, as in the case for rods and beams (Goldsmith 2001). Simulating pounding at the base level of a base isolated building to a moat wall includes impact of a solid base slab to a cantilever column in which the vibration aspect of impact is important. To consider the vibration effects of a moat wall during the impact, dynamic behavior of the moat wall needs to be modeled.

### **6.3. Moat Wall Impact Model**

In order to consider the potential and effect of pounding in a time history analysis of base isolated buildings under shaking, the moat wall model should include both local deformation and global vibration aspects of structural impact. The local aspect of impact can be implemented using a Hertz damped element at the contact location. The vibration response of the moat wall can be of varying complexity ranging from a detailed finite element model to an equivalent single Degree of Freedom (SDF) system. A generalized SDF moat wall model is proposing here considering both local and vibration aspect of impact. This model can be easily implemented in common structural analysis software, is the least computationally expensive, and provides good correlation to experimental results as will be shown later.

#### *6.3.1. Uniform Moat Wall*

To investigate the behavior of a cantilever moat wall under impact from the base slab in a base isolated building, a continuous cantilever beam supported by an elastic foundation and external distributed damping was assumed. A rotational spring was assumed at the base of the beam to capture the post-elastic behavior due to the formation of a plastic hinge (Figure 6-3). To consider both local deformation and vibration aspect of impact to the moat wall, first, the vibration equation of the moat wall model is solved, then coupled with local deformation at the impact point.

The most elementary description of flexure waves considers only strain energy of bending and transverse inertia results in well-known equation of beam vibration:

$$\frac{\partial^2}{\partial x^2} \left( EI(x) \frac{\partial^2 v}{\partial x^2} \right) + \bar{C} \frac{\partial v}{\partial t} + \bar{K}v + m(x) \frac{\partial^2 v}{\partial t^2} = F(x, t) \quad (6-8)$$

where  $v$  is lateral displacement of the beam,  $EI(x)$  is the flexural stiffness and  $m(x)$  is the mass per unit length of the beam. The uniform stiffness and damping of the elastic support foundation is characterized by  $\bar{K}$  and  $\bar{C}$ , and  $K_\theta$  is stiffness of the rotational spring. A linear elastic spring using an effective stiffness can be assigned to  $K_\theta$  to simplify the formulation while accounting for post elastic behavior of the moat wall during impact.

For simplicity, the flexural stiffness and the mass per unit length are assumed constant throughout the length of the beam and set equal to  $EI$  and  $\rho A$ , respectively. Considering only the impact force at the free end in Equation 6-8,  $F(x, t)$  is replaced with  $F(t)$  to further simplify the equation as follows:

$$EI \frac{\partial^4 v}{\partial x^4} + \bar{C} \frac{\partial v}{\partial t} + \bar{K}v + \rho A \frac{\partial^2 v}{\partial t^2} = F(t) \quad (6-9)$$

The solution of this equation must satisfy the prescribed boundary conditions:

$$\begin{aligned} v_{(x=0)} &= 0; & EI \frac{\partial^2 v}{\partial x^2} \Big|_{(x=0)} &= \pm K_\theta \frac{\partial v}{\partial x} \Big|_{(x=0)} \\ \frac{\partial^2 v}{\partial x^2} \Big|_{(x=L)} &= 0; & \frac{\partial^3 v}{\partial x^3} \Big|_{(x=L)} &= 0 \end{aligned} \quad (6-10)$$

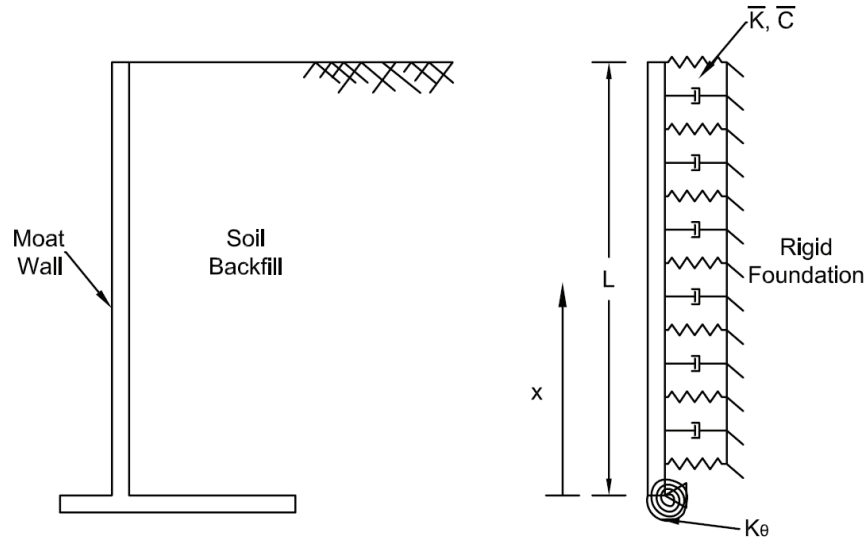


**Figure 6-3 Schematic side view of a moat wall and representing beam.**

To solve Equation 6-9, the homogeneous solution is first considered ( $F(t) = 0$ ) and solved by separation of variables:

$$v(x, t) = X(x)Y(t) \quad (6-11)$$

which yields two ordinary differential equations

$$\frac{\partial^4 X}{\partial x^4} - \zeta^4 X = 0 \quad (6-12a)$$

$$\frac{\rho A}{EI} \frac{\partial^2 Y}{\partial t^2} + \frac{\bar{C}}{EI} \frac{\partial Y}{\partial t} + \left( \frac{\bar{K}}{EI} + \zeta^4 \right) Y = 0 \quad (6-12b)$$

where  $\zeta$  is a number to be determined. Solving Equation 6-12a yields the general solution

$$X(x) = A_1 \cosh(\zeta x) + A_2 \sinh(\zeta x) + A_3 \cos(\zeta x) + A_4 \sin(\zeta x) \quad (6-13)$$

Substituting Equation 6-13 in the boundary conditions (6-10), a set of four homogeneous equations are obtained in the constants  $A_i$ . Since the system is homogeneous, for the existence of a nontrivial solution, the determinant of coefficients must be equal to zero. This procedure yields the frequency equation to calculate  $\zeta$

$$\zeta L (\sinh(\zeta L) \cdot \cos(\zeta L) - \sin(\zeta L) \cdot \cosh(\zeta L)) + K'_\theta (1 + \cos(\zeta L) \cdot \cosh(\zeta L)) = 0 \quad (6-14)$$

in which it is assumed that

$$K'_\theta = \frac{K_\theta L}{EI} \quad (6-15)$$

Solving Equation 6-14 for a given  $K'_\theta$  produces infinite values for  $\zeta$ , corresponding to an infinite number of mode shape for a distributed beam. The  $K'_\theta$  ratio could vary between a small number to infinity for the case of an elastic cantilever moat wall. The frequency equation is changed to Equation 6-16 for elastic cantilever moat wall.

$$1 + \cos(\zeta L) \cdot \cosh(\zeta L) = 0 \quad (6-16)$$

In order to consider nonlinear deformation in the moat wall assuming that plasticity is concentrated at the base of the column where bending is maximum, an elastic spring with effective stiffness for an assumed rotation or an idealized bilinear rotational spring can be considered for  $K_\theta$ . Figure 6-4 shows the nonlinear moment-rotation relationship for concrete walls. The effective stiffness for an assumed rotation in this nonlinear hinge is shown in this figure.

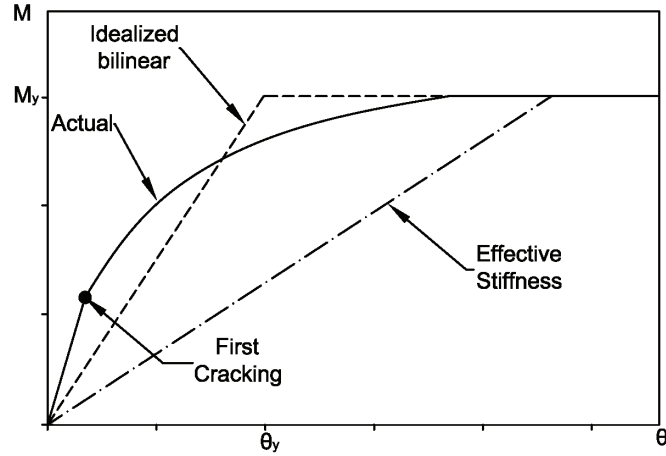


**Figure 6-4 Predicted nonlinear moment-rotation relationship for concrete wall.**

Substituting  $\zeta_i$  obtained from the frequency equation in Equation 6-12b and 6-13 results in modal frequencies and shape functions

$$\omega_i = \sqrt{\frac{\bar{K}}{\rho A} + \frac{EI}{\rho A} \zeta_i^4} \quad (6-17)$$

$$X(x) = \sum_{i=1}^{\infty} A_i \left( \begin{array}{l} \cosh(\zeta_i x) + \frac{\sin(\zeta_i L) - \sinh(\zeta_i L) + \frac{2\zeta_i L}{K'_\theta} \cos(\zeta_i L)}{\cos(\zeta_i L) + \cosh(\zeta_i L)} \sinh(\zeta_i x) \\ -\cos(\zeta_i x) + \frac{\sinh(\zeta_i L) - \sin(\zeta_i L) + \frac{2\zeta_i L}{K'_\theta} \cosh(\zeta_i L)}{\cos(\zeta_i L) + \cosh(\zeta_i L)} \sin(\zeta_i x) \end{array} \right) \quad (6-18)$$

Substituting Equation 6-18 in Equation 6-11 yields the lateral displacement of the beam in terms of infinite number of mode shapes

$$v(x,t) = \sum_{i=1}^{\infty} X_i(x) Y_i(t) \quad (6-19)$$

To solve the vibration equation for the considered column, Equation 6-19 is substituted in Equation 6-9:

$$v(x,t) = \sum_{i=1}^{\infty} X_i(x) Y_i(t) \quad (6-20)$$

$$\rho A \sum_{i=1}^{\infty} X_i \frac{\partial^2 Y_i(t)}{\partial t^2} + \bar{C} \sum_{i=1}^{\infty} X_i \frac{\partial Y_i(t)}{\partial t} + EI \sum_{i=1}^{\infty} \frac{\partial^4 X_i}{\partial x^4} Y_i(t) + \bar{K} \sum_{i=1}^{\infty} X_i Y_i(t) = F(t) \quad (6-21)$$

Modal orthogonality provides the means for decoupling Equation 6-21. Multiplying each side of Equation 6-21 by  $X_n(x)$  and integrating along column height gives

$$\begin{aligned} & \left( \rho A \int_0^L X_n^2 dx \right) \frac{\partial^2 Y_n(t)}{\partial t^2} + \left( \bar{C} \int_0^L X_n^2 dx \right) \frac{\partial Y_n(t)}{\partial t} \\ & + \left( EI \int_0^L \frac{\partial^4 X_n}{\partial x^4} X_n dx + \bar{K} \int_0^L X_n^2 dx \right) Y_n(t) = F(t) X_n(L) \end{aligned} \quad (6-22)$$

Considering  $A_i$  in Equation 6-18 in such a way that corresponding mode shape displacement at free end of the column is equal to one, and also defining

$$M_n = \rho A \int_0^L X_n^2 dx \quad (6-23)$$

$$C_n = \bar{C} \int_0^L X_n^2 dx \quad (6-24)$$

simplifies Equation 6-22 into

$$M_n \frac{\partial^2 Y_n(t)}{\partial t^2} + C_n \frac{\partial Y_n(t)}{\partial t} + M_n \omega_n^2 Y_n(t) = F(t) \quad (6-25)$$

Equation 6-25 describes generalized forced vibration equation associated with  $n$ th mode of the column in Figure 6-3, where  $F(t)$  is the contact force at the free end of the column. Thus, Equation 6-25 describes the equation of motion for the distributed column in Figure 6-3 under external force  $F(t)$  as an infinite number of Single Degree of Freedom (SDF) system with mass, damping and stiffness respectively equal to  $M_n$ ,  $C_n$  and  $M_n \omega_n^2$ .

The right hand side of the Equation 6-25,  $F(t)$ , can be replaced with the force generated due to local deformation of two bodies during impact of a striker to the head of the moat wall. This force can be obtained using Equation 6-5. These two phases of impact should be combined in one element for implementation in dynamic structural analysis.

### 6.3.2. Non-uniform Moat Wall

Using the relatively rigid steel triangle walls in the experimental testing program requires developing vibration equations for this kind of shape. Since flexural stiffness and mass per unit length of the steel walls are not constant along the height of the wall due to its triangle geometric shape, the properties for the impact model are determined as follows.

Assuming that the static deformation of the cantilever column due to a transverse force at free end,  $f(x)$ , is geometrically equal to its dynamic deformation due to an impact force leads to the column deflection  $v = f(x)Y(L,t)$ , where  $Y(L,t)$  is the dynamic deflection at free end of the column and  $f(L) = 1$ . The kinetic energy (T) and potential energy (V) of the column may be written as

$$T = \frac{1}{2} \int_0^L m(x) \left( \frac{\partial v}{\partial t} \right)^2 dx \quad (6-26)$$

$$V = \frac{1}{2} \int_0^L EI(x) \left( \frac{\partial^2 v}{\partial x^2} \right)^2 dx + \frac{1}{2} K_\theta \left( \frac{\partial v}{\partial x}(0) \right)^2 \quad (6-27)$$

where  $K_\theta$  is rotational stiffness at the end of the column due to axial deformation of the connecting rods,  $m(x)$  and  $EI(x)$  are calculated for triangle geometric shape of walls. The Lagrangian equations of motion are usually written in the form

$$\frac{d}{dx} \left[ \frac{\partial T}{\partial \dot{q}_i} \right] - \frac{\partial T}{\partial q_i} + \frac{\partial V}{\partial q_i} = F(t) \quad (6-28)$$

where  $F(t)$  is the generalized force corresponding to generalized coordinate  $q_i$ . Substituting for kinetic and potential energy in the Lagrangian equation of motion yields an equation of motion for an equivalent SDF considering a non-uniform column.

### 6.3.3. Proposed Impact Element

Simulation of impact forces in structural analysis should consider the two phases of impact to capture both the effects of local deformation at the impact point and the vibration aspect of the colliding objects. Equation 6-5 captures forces during the first phase of impact, which includes the local deformation of two objects and assumes that the force is a function of material properties and initial velocity. The force obtained in the first phase can be implemented in Equation 6-25 to find lateral displacement of the wall and also resisting force imposed on the striker body. The second phase occurs after the first initial impact, sometimes followed by a quick separation, during which the two bodies stay in contact and push or generate forces against each other. The force in this second phase is primarily influenced by the dynamic properties of the moat wall described in Equation 6-8.

To simulate both phases of impact, a new impact model consisting of two elements in series is proposed as shown in Figure 6-5. The first element simulates the local deformations at the contact point dependent mainly on material properties of two objects, which can be defined by a Hertz damped model. Since the Hertz model is not common in structural analysis software such as OpenSees (McKenna et al. 2000), Muthukumar (2003) showed that a bilinear spring can provide a reasonable substitute. The first and second slope stiffness for this uniaxial gap spring should be determined such that the area enclosed for a certain penetration equals to corresponding dissipated energy in the Hertz damped model for a given coefficient of restitution. The second element in Figure 6-5 captures the vibration aspects of the impact wall and consists of a SDF representing the first mode shape of the distributed cantilever column described in Figure 6-3. Vibration properties of this system to model a moat wall can be calculated using Equations 6-14 to 6-25. These equations lead to the first modal mass,  $M$ , and stiffness,  $K$ , to define the SDF system. If an idealized nonlinear behavior is assigned to the rotational spring at the base of the wall, the corresponding yielding criteria should be assigned to the spring in the equivalent SDF system.

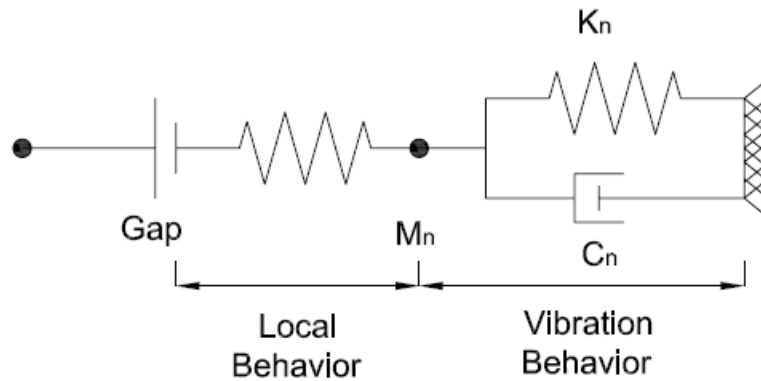


**Figure 6-5 Schematic of the new impact element.**

The damping coefficient,  $C$ , is usually calculated by assuming a damping ratio,  $\xi = C/2M\omega$  since mechanical interpretation of damping coefficient is difficult. The damping ratio should be assumed to include energy dissipated by soil backfill. A higher damping ratio is expected when using an elastic spring with effective stiffness to represent nonlinearity in the column and the associated hysteretic energy dissipation.

#### 6.3.4. Concrete Moat Wall Parameters

The proposed impact model was used to simulate the moat wall behavior in a numerical study. Here, the moat wall model parameters are calibrated based on physical properties of the moat walls used in the experimental setup.

The concrete moat walls with 2 in. front wall thickness and 4 in. back wall thickness were installed at 6 in. gap distance and filled with loose sand in between. To implement the proposed impact element in the numerical simulation, the properties of the moat wall for both local deformation and vibration response are required. Local deformation parameter including the Hertz damped stiffness  $K_h = 4500 \text{ kips/in}^{3/2}$  was calculated using Equation 6-2b assuming  $R_1$  as the radius of an equivalent sphere to concrete block volume, and  $e=0.7$  was assumed.

To calculate the dynamic frequency of the moat wall, Equation 6-14 requires a value for  $K'_\theta$ , which is the ratio of concentrate hinge stiffness at the base of the wall to  $EI/L$ . An elastic spring is assumed with the concentrate hinge stiffness obtained from section analysis of the wall over an assumed hinge length. Here, the post concrete crack stiffness (Figure 6-4) is used since the concrete walls were damaged in previous tests and during installation on shake table resulting in  $K'_\theta = 0.23$ . Substituting this value in Equation 6-14 and solving for  $\zeta L$  yields  $\zeta L = 0.957$  for the first modal shape.

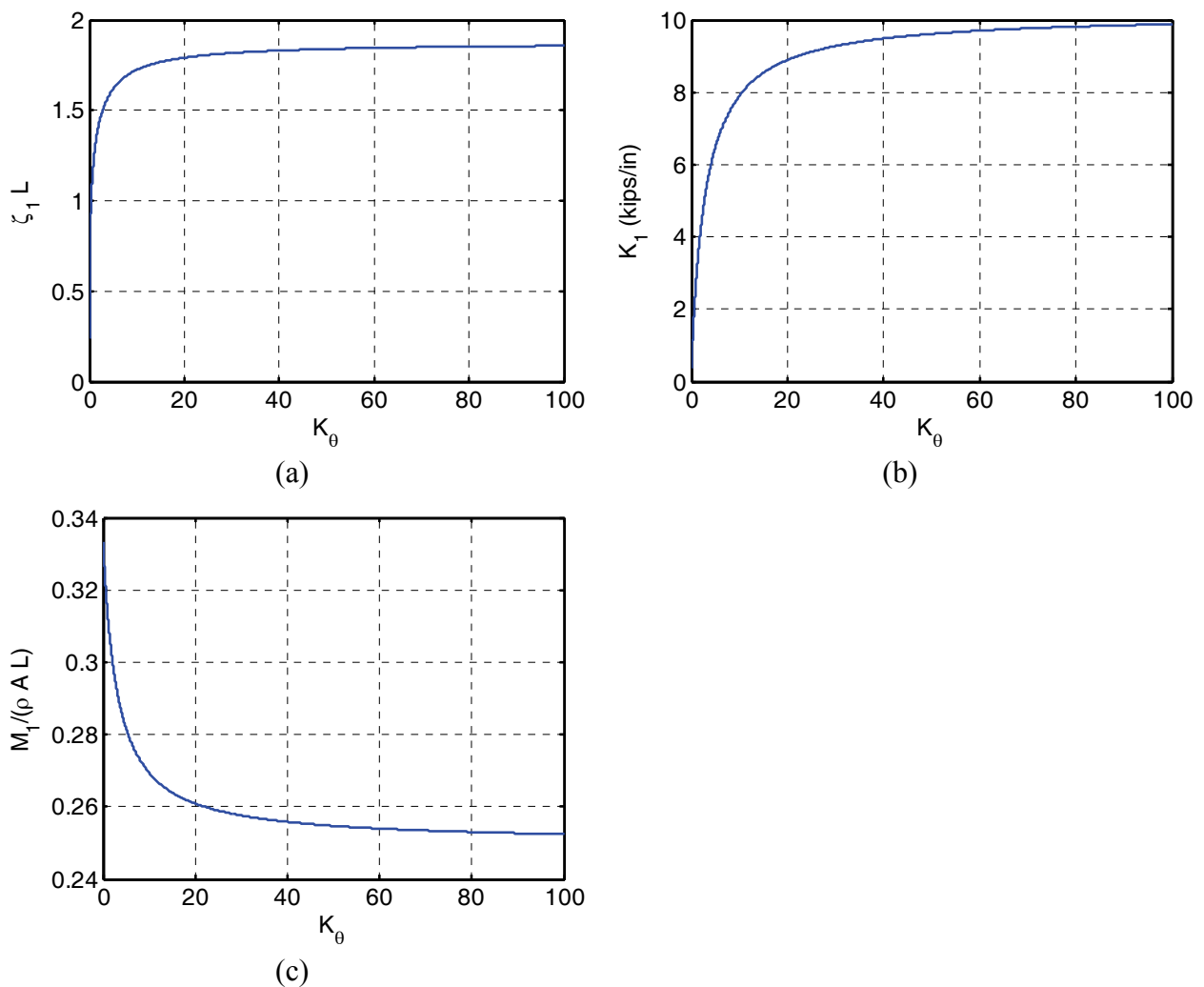
The elastic foundation behind the cantilever column representing soil backfill was modeled as Winkler springs (Scott 1973) with stiffness

$$\bar{K} = \frac{8G(1-\nu)}{L(1-2\nu)} \quad (6-29)$$

where  $G$  and  $\nu$  are the shear modulus (500 psi) and Poisson's ratio (0.4) for the soil, respectively.  $L$  is the length of soil, which is equal to distance between two sides of the U-shape concrete walls (35 in) in this test program. This stiffness was also affected by the flexibility of the back concrete wall, resulting in  $\bar{K} = 0.05 \text{ kips/in}^2$ . Applying these numbers to Equations 6-

17 leads to the first mode frequency. Substituting  $\zeta$  in Equation 6-18 also leads to calculate first mode shape, which can be used in Equation 6-23 to calculate corresponding effective modal mass in the first mode of vibration ( $M = 0.32\rho AL$ ). The corresponding stiffness can be calculated as

$$K = M \omega^2 = 1.05 \text{ kips/in} \quad (6-30)$$



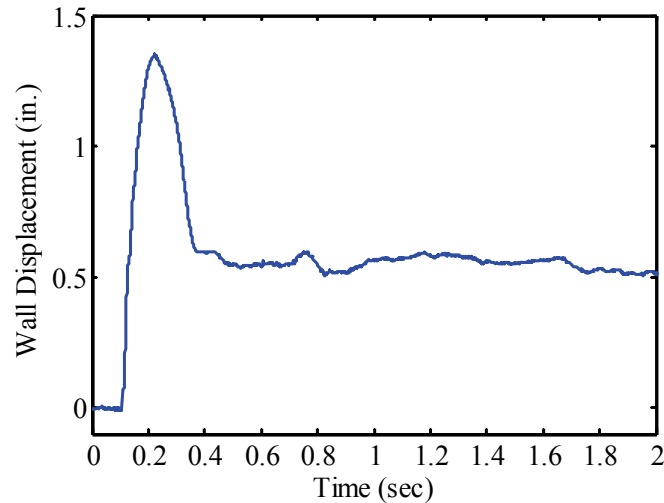
**Figure 6-6 Variation of impact element properties with changing of concentrated spring stiffness for 2 in. moat wall.**

Figure 6-6 shows the variation of impact element properties regarding to change in concentrated spring stiffness ratio,  $K'_\theta$ . It can be seen that first modal stiffness is converging to ultimate elastic stiffness ( $K = 3EI/L^3$ ) by increasing the concentrated spring stiffness ratio,  $K'_\theta$ . The mass ratio participating in the first modal dynamic of the system is between 25 to 33% of the total mass of the wall.

The parameters for the proposed impact element for different type of moat walls are summarized in Table 6-1. In this table, local parameters include the Hertz damped model stiffness and coefficient of restitution and vibration parameters include ratio of concentrate hinge stiffness at the end of the wall to  $EI/L$ , and the first modal mass, stiffness and damping ratio of the moat wall. Vibration parameters for concrete walls in Table 6-1 are calculated following the same procedure presented earlier for the 2 in. concrete wall. All the parameters in this table are calculated from physical properties of moat walls except the damping ratio,  $\xi$ , which is calibrated from experimental results that clearly show over-damped response. This behavior of the moat wall was expected due to large plastic deformation in moat wall and compression of loose soil backfill. Figure 6-7 shows the front surface of the 2 in. concrete moat wall displacement under the impact force. It can be seen that the wall settles at a residual displacement without oscillating after contact. The high damping ratio implies that soil behind the wall and the plastic hinge at the base of wall play a vital role in damping the impact energy.

**Table 6-1. List of proposed impact element parameters for different wall types.**

Wall type	Wall thickness (in)		Local parameters		Vibration parameters			
	Front wall	Back wall	$K_h$ (kips/in <sup>3/2</sup> )	e	$K'_\theta$	M (lbs)	K (kips/in)	$\xi$ (%)
Concrete	2	4	4000	0.7	0.23	90	1.1	180
	4	2	4000	0.7	0.10	200	1.8	160
	6	4	4000	0.7	0.02	292	2.4	200
Steel	2	NA	8000	0.7	-	405	100	40



**Figure 6-7 Relative wall displacement for 2 in. concrete wall due to impact force.**

From Table 6-1, it can be seen that the stiffness ratio,  $K'_\theta$ , is decreasing as the thickness of the concrete wall increases. As described for the 2 in. concrete wall,  $K'_\theta$  is the ratio of the concentrate hinge stiffness at the bottom of the wall model to flexural stiffness of the wall. Since the reinforcement ratio for all wall thicknesses are the same, the post concrete crack stiffness is decreasing with increasing wall thickness, and therefore the stiffness of the concentrate hinge decreases.

### 6.3.5. Steel Moat Wall Parameters

The relatively rigid steel triangle wall was installed at a 4 in. gap distance from the isolated structure to examine a wider range of moat wall stiffness values. Four 25 in. long rods were used to attach the steel wall to the shake table platform. Initial experiments indicated rocking of the steel wall, thus the bolted connection was reinforced with a 2 in. linear weld to prevent slip and uplift at the base of the steel wall. Since flexural stiffness and mass per unit length of the steel walls are not constant along the height of the wall due to its triangle geometric shape, the properties for the impact model are determined using equations explained in section 6.3.2.

The corresponding mass,  $M$ , and stiffness,  $K$ , are shown in Table 6-1. The damping ratio in this table is obtained from calibrating the numerical analysis with the proposed impact element

against experimental results. The damping ratio is lower in comparison with the nonlinear concrete walls with soil backfill as expected.

#### 6.4. Description of Superstructure Analytical Model

To simulate the impact force using proposed impact element a numerical model of the experimental setup was developed in OpenSees (McKenna et al. 2000) that could capture the response of the superstructure under large drifts and impact forces. This required a detailed model of the structural frame and moat walls. The 3-story, 1-bay steel moment resisting frame is modeled with elastic beam-column elements and zero length nonlinear rotation spring elements at the location of the RBS (Figure 6-8). P-Delta effects were simulated by a leaning column with gravity loads linked to the moment frame by truss elements.

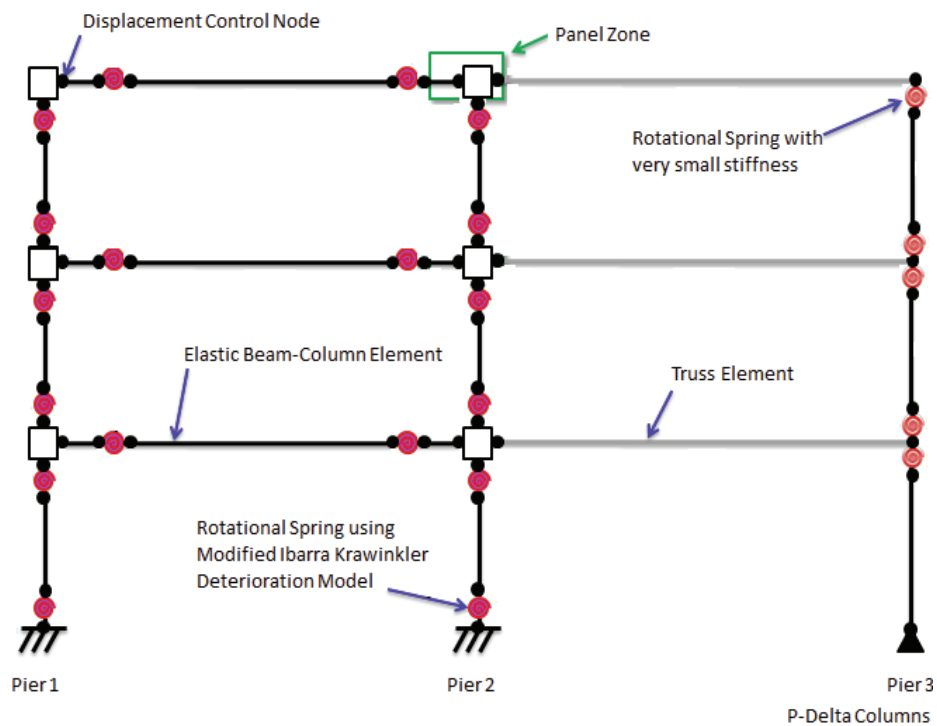


**Figure 6-8 Schematic of numerical simulation of experimental setup (McKenna et al. 2000).**

##### 6.4.1. Concentrated Plastic Hinges

The steel moment resisting frame is modeled with elastic beam-column elements connected by zero length elements which serve as rotational springs to represent the structure's nonlinear

behavior. The springs follow a bilinear hysteretic response based on the Modified Ibarra Krawinkler Deterioration Model (Lignos et al. 2011).

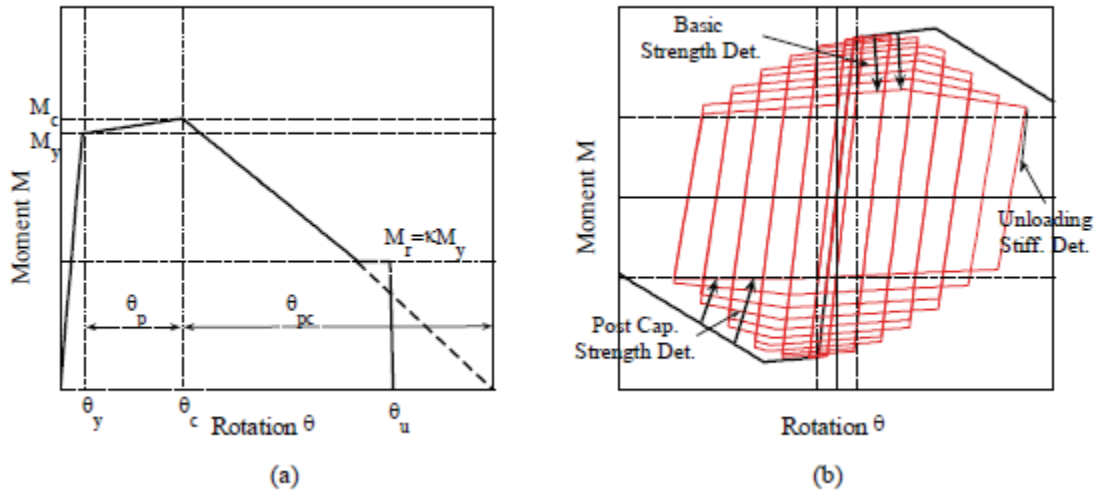


**Figure 6-9 Modified Ibarra – Krawinkler deterioration model; (a) Monotonic curve; (b) Basic modes of cyclic deterioration and associated definitions (Lignos et al. 2011).**

The required parameters were calibrated using test results from the fixed-base experimental tests. The stiffness of these components composed of elastic element connected in series with rotational spring at both ends must be modified so that the equivalent stiffness of this assembly is equivalent to the stiffness of the actual frame member (McKenna et al. 2000). The approach described by Ibarra and Krawinkler (2005) was implemented here. Since a frame member is modeled as an elastic element connected in series with rotational springs at either end, the stiffness of these components must be modified so that the equivalent stiffness of this assembly is equivalent to the stiffness of the actual frame member. Using the approach described in Appendix B of Ibarra and Krawinkler (2005), the rotational springs are made “n” times stiffer than the rotational stiffness of the elastic element in order to avoid numerical problems and allow all damping to be assigned to the elastic element. To ensure the equivalent stiffness of the assembly is equal to the stiffness of the actual frame member, the stiffness of the elastic element must be “(n+1)/n” times greater than the stiffness of the actual frame member. This is accomplished by making the elastic element’s moment of inertia “(n+1)/n” times greater than the actual frame member’s moment of inertia.

In order to make the nonlinear behavior of the assembly match that of the actual frame member, the strain hardening coefficient (the ratio of post-yield stiffness to elastic stiffness) of the plastic hinge must be modified. If the strain hardening coefficient of the actual frame member is denoted  $\alpha_{s,mem}$  and the strain hardening coefficient of the spring is denoted  $\alpha_{s,spring}$  (the ratio of  $M_c$  and  $M_y$  in Figure 6-9) then  $\alpha_{s,spring} = \alpha_{s,mem} / (1 + n*(1 - \alpha_{s,mem}))$ .

#### 6.4.2. Panel Zones

Gupta *et al.* (1999) showed the importance of modeling panel zones in moment resisting frame in order to better predict lateral displacement of the frame. A model with eight elastic beam-column elements and one zero length element which serves as rotational spring to represent shear distortions in the panel zone was used for this purpose. This model consists of the rectangular area of the column web that lies between the flanges of the connecting beam(s). The panel zone deforms primarily in shear due to the opposing moments in the beams and columns. To capture these deformations, the panel zone is explicitly modeled using a rectangle composed of eight very stiff elastic beam-column elements with one zero length element which serves as rotational spring to represent shear distortions in the panel zone (Figure 6-10). At the three corners of the panel zone without a spring, the elements are joined by a simple pin connection to constrain both translational degrees of freedom. The spring has a trilinear backbone which is created with the Hysteretic material. The spring's backbone curve is derived using the principle of virtual work applied to a deformed configuration of the panel zone (Gupta and Krawinkler 1999).

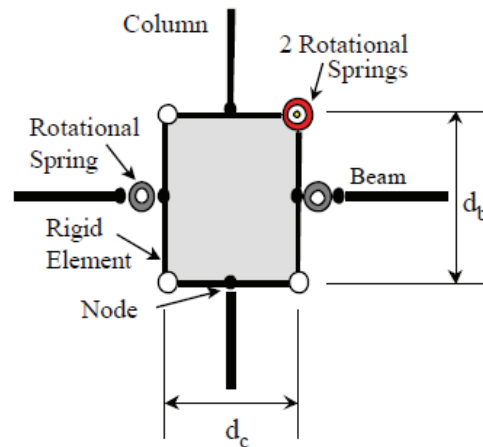


**Figure 6-10 Analytical model for panel zone (Gupta et al. 1999)**

### *6.4.3. Structural Damping*

This model uses Rayleigh damping which formulates the damping matrix as a linear combination of the mass matrix and stiffness matrix ( $c = a_0*m + a_1*k$ ), where  $a_0$  is the mass proportional damping coefficient and  $a_1$  is the stiffness proportional damping coefficient. A damping ratio of 2%, which is obtained from system identification tests on superstructure, is assigned to the first two modes of the structure. The Rayleigh command allows the user to specify whether the initial, current, or last committed stiffness matrix is used in the damping matrix formulation. In this study, only the initial stiffness matrix is used.

To properly model the structure, stiffness proportional damping is applied only to the frame elements and not to the highly rigid truss elements that link the frame and leaning column, nor to the leaning column itself. OpenSees does not apply stiffness proportional damping to zero length elements (such as isolation element). In order to apply damping to only certain elements, the Rayleigh command is used in combination with the region command.

As described in the previous section, the stiffness of the elastic frame elements has been modified. As explained in Ibarra and Krawinkler (2005) and Zareian et al. (2010), the stiffness proportional damping coefficient that is used with these elements must also be modified. As the stiffness of the elastic elements was made “ $(n+1)/n$ ” times greater than the stiffness of the actual frame member, the stiffness proportional damping coefficient of these elements must also be made “ $(n+1)/n$ ” times greater than the traditional stiffness proportional damping coefficient.

### *6.4.4. Transient Integration Scheme*

The structure is analyzed under gravity loads which are equal to self weighting of the frame, before the dynamic analysis is conducted. The gravity loads are applied using a load-controlled static analysis with 10 steps. For the dynamic analysis, the structure is subjected to the different acceleration time histories recorded from shake table testing program. To apply the ground motion to the structure, the uniform excitation pattern is used. To execute the dynamic analysis, the analyze command is used with the specified number of analysis steps and the time step of the analysis. The time step used in the analysis should be less than or equal to the time step of the input ground motion.

The common numerical integration methods like Newmark method was not used in this study since the engaging stiff elements at the time of the impact excites high frequencies responses leading to divergence in the response. The alternative integration schemes like Hilber et al. (1977) were employed to overcome this problem. The Hilber-Hughes-Taylor (HHT) method (1977) (also called  $\alpha$ -method) is an extension to the Newmark method. With the HHT method it is possible to introduce numerical dissipation without degrading the order of accuracy. The HHT method uses the same finite difference formulas as the Newmark method with fixed  $\gamma$  and  $\beta$  ( $\gamma = 3/2 - \alpha, \beta = (2 - \alpha)^2 / 4$ ). In the HHT method, the same Newmark approximations are used:

$$U_{t+\Delta t} = U_t + \Delta t \dot{U}_t + [(0.5 - \beta) \Delta t^2] \ddot{U}_t + [\beta \Delta t^2] \ddot{U}_{t+\Delta t} \quad (6-31)$$

$$\dot{U}_{t+\Delta t} = \dot{U}_t + \Delta t \ddot{U}_t + [(1 - \gamma) \Delta t] \ddot{U}_t + [\gamma \Delta t] \ddot{U}_{t+\Delta t} \quad (6-32)$$

but the time-discrete momentum equation is modified:

$$R_{t+\alpha\Delta t} = F_{t+\Delta t}^{ext} - M \ddot{U}_{t+\Delta t} - C \dot{U}_{t+\alpha\Delta t} - F^{int}(U_{t+\alpha\Delta t}) \quad (6-33)$$

where the displacements and velocities at the intermediate point are given by:

$$U_{t+\alpha\Delta t} = (1 - \alpha)U_t + \alpha U_{t+\Delta t} \quad (6-34)$$

$$\dot{U}_{t+\alpha\Delta t} = (1 - \alpha)\dot{U}_t + \alpha \dot{U}_{t+\Delta t} \quad (6-35)$$

Following the methods for Newmark method, linearization of the nonlinear momentum equation results in the following linear equations:

$$K_{t+\Delta t}^* dU_{t+\Delta t}^{i+1} = R_{t+\Delta t}^i \quad (6-36)$$

Where

$$R_{t+\Delta t}^i = F_{t+\Delta t}^{ext} - M\ddot{U}_{t+\Delta t}^{i-1} - C\dot{U}_{t+\alpha\Delta t}^{i-1} - F^{int}(U_{t+\alpha\Delta t}^{i-1}) \quad (6-37)$$

The linear equations are used to solve for  $U_{t+\alpha\Delta t}$ ,  $\dot{U}_{t+\alpha\Delta t}$ ,  $\ddot{U}_{t+\Delta t}$ .

For  $\alpha = 1$  the method reduces to the Newmark method. Decreasing  $\alpha$  means increasing the numerical damping. This damping is low for low-frequency modes and high for the high-frequency modes. It should be noted that  $\alpha$  in this document is defined differently that in the paper (Hilber et al. 1977),  $\alpha = (1 + \alpha_{HHT})$ .

## 6.5. Numerical Simulation Results

The results for numerical simulation of the experimental test setup are shown in this section. The results are shown in three categories of fixed base model, base isolated model without moat wall, and base isolated model with moat wall. It should be noted that the input motion for each numerical simulation is given from accelerometers installed on shake table not the true motion. As discussed earlier there is a difference between applied motion to shake table (true motion or target motion) and recorded acceleration from shake table (achieved motion) due to fidelity of the actuators and dynamic system of the shake table. In this numerical study, the achieved motion was applied to the finite element model in order to compare results with the shake table models and also calibrate the required parameter in proposed elements.

### 6.5.1. Fixed Base Model

The first series of experimental testing was conducted on a fixed base model. The numerical simulation of the fixed base model was conducted in order to calibrate the properties of the superstructure. A robust numerical model for superstructure is essential when the results of impact tests are compared with the proposed impact element. Since the IMRF model was not

replaced between applying different levels of ground motions GM15-2 and GM16-2, a cumulative damage was imposed to the structure which makes numerical simulation more difficult. To overcome this problem a consecutive input motion was made from recorded acceleration from each test and about 10 sec zero acceleration was added between each two records to allow any free vibration to decay. In this way, the effect of cumulative damage could be captured. The sequence of applying the different motions is shown in Tables 4-8 and 4-9.

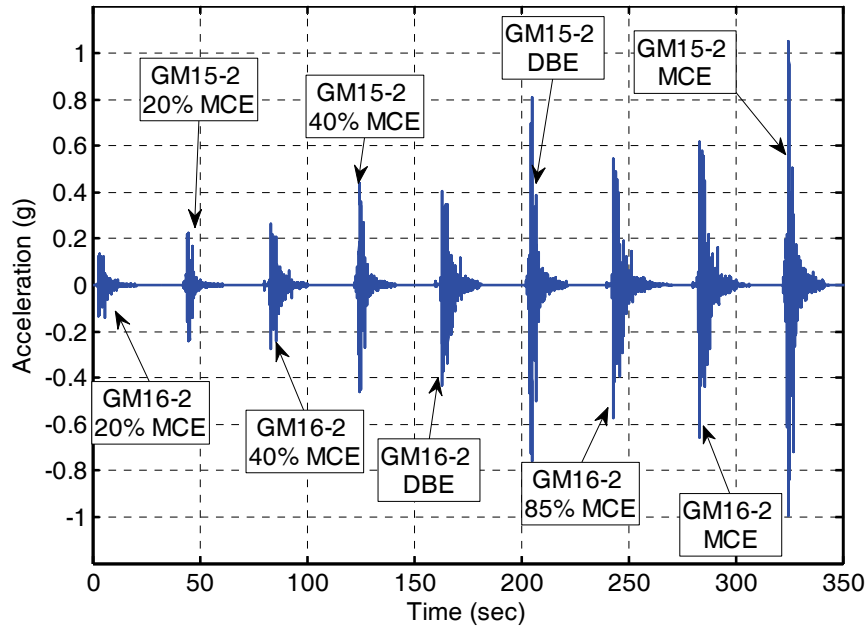


**Figure 6-11 Sequence of applied ground motion on fixed base model**

Figure 6-11 shows the motions applied on the fixed base model including the sequence of changing the motions and also increasing the amplitude. Record GM15-2 was applied in 4 amplitudes of 20, 40, 67, and 100% MCE scaled motion while record GM16-2 was also applied at 85% MCE level. In total, the fixed base model was exposed to 9 ground motions that are shown in Figure 6-11.

Figure 6-12 shows the story drift ratio for all three levels of the superstructure under the nine input motions. The numerical simulation shows good agreement with experimental results for lower level of input motions. As the amplitude of the input motions is increased, more discrepancy is shown in results leading to 10% error in residual drift of first and third floor by

the end of the simulation. The peak SDR was well simulated in most of the input motions except in third floor under GM16-2 record at MCE level leading to 25% error.

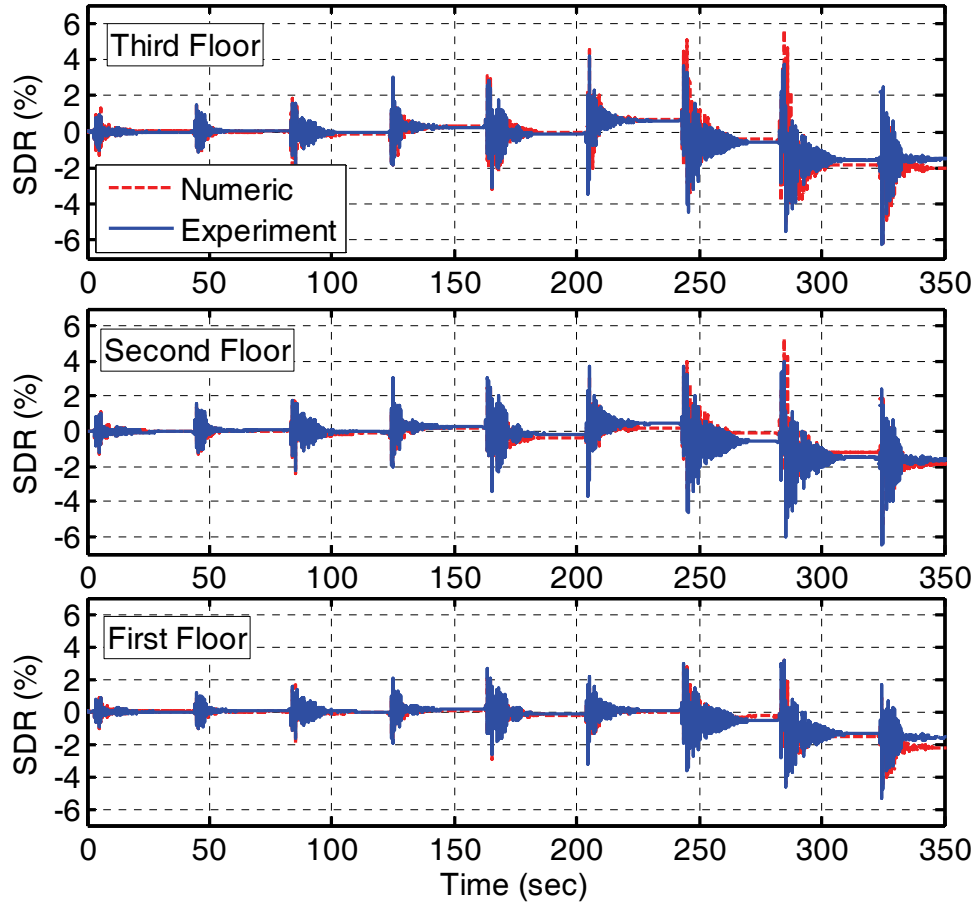


**Figure 6-12 Story drift ratio (SDR) for fixed base model.**

In general, using the material model proposed by Lignos et al. (2011) results in acceptable numerical simulation of plasticity in moment frames undergoing large drift and also continues damage.

Figure 6-13 compares the absolute acceleration response for each level of fixed base model. The numerical simulation of acceleration shows higher frequency response in comparison to experimental results, which could be due to errors in modeling of damping in the numerical simulation. In general 10 to 20% error in acceleration response was seen in all records.

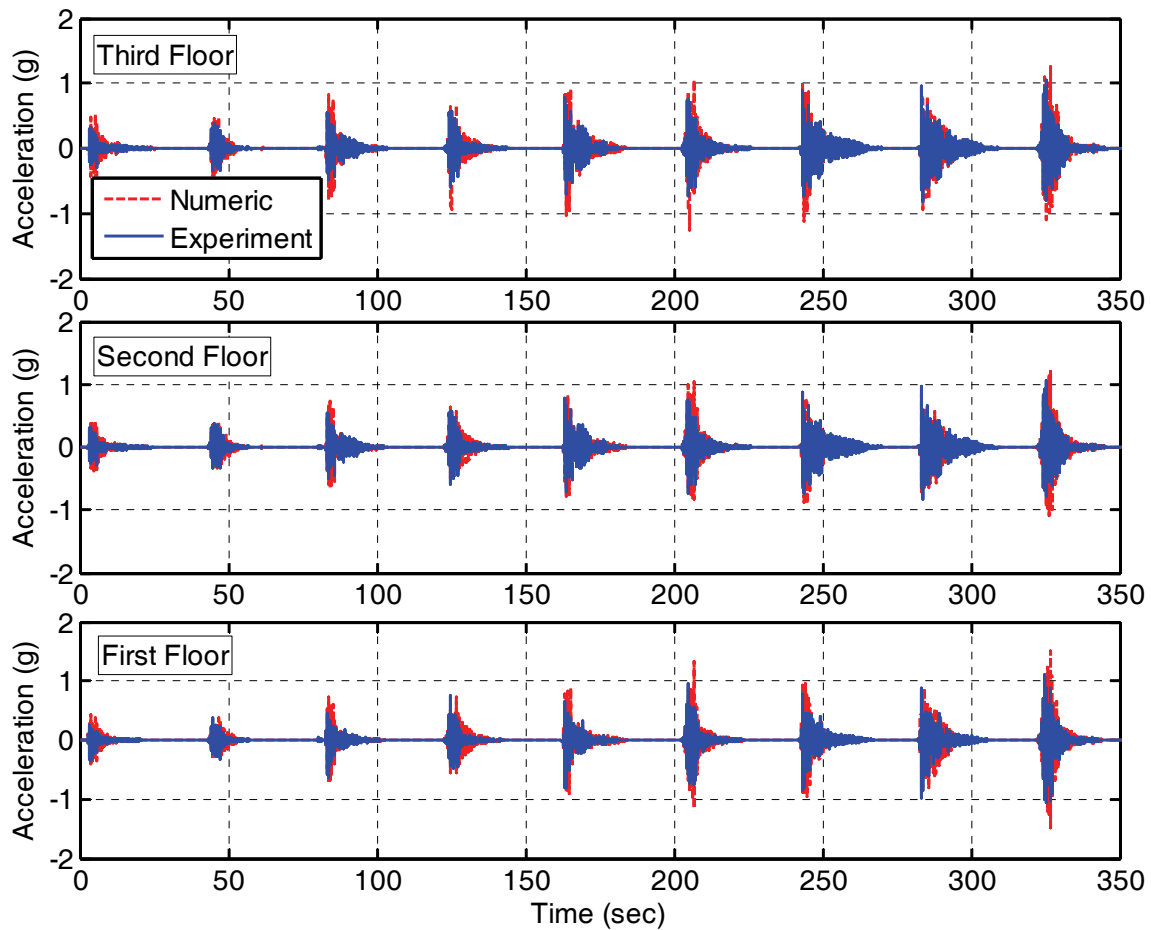


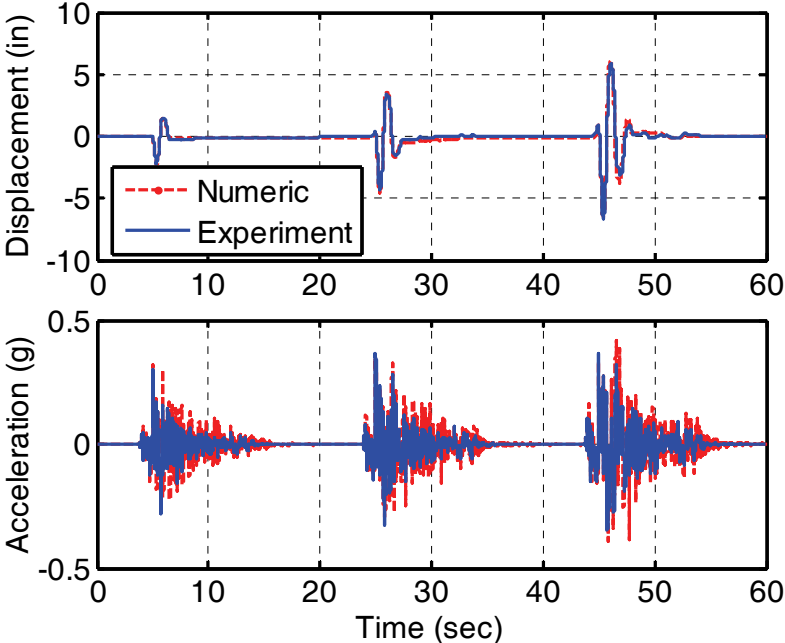
**Figure 6-13 Absolute acceleration response for fixed base model.**

### 6.5.2. Base Isolated Model without Moat Wall

The experimental program continued by changing the IMRF scaled model due to damage imposed during fixed base testing and adding the friction pendulum bearings at the base level. The single friction pendulum bearing was modeled using the corresponding element in OpenSees in which uplift behavior is considered by assigning non-tension material to axial coordinates. In this element P-Delta moments are entirely transferred to the concave sliding surface.

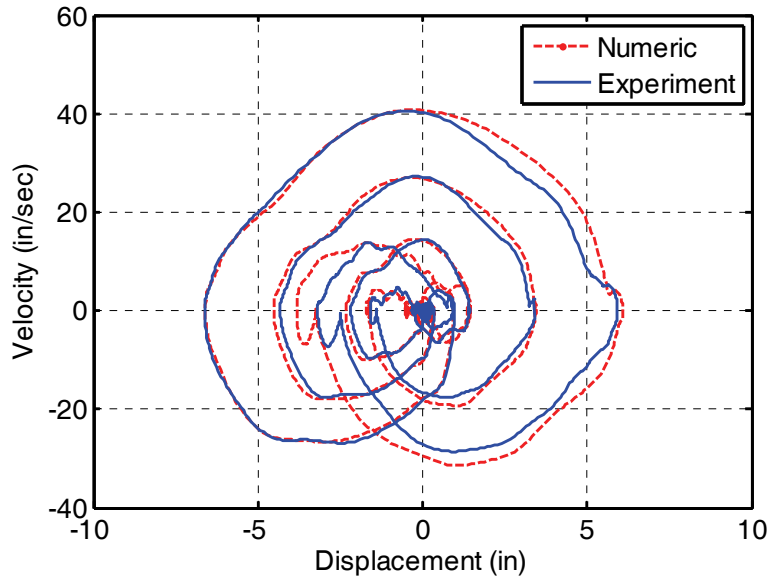
The numerical simulation in this step is aimed to calibrate the properties of single friction isolator under different amplitude excitation. As mentioned in section 4-7, five ground motions scaled to three different amplitudes of 40%, 67% and 100% MCE level were applied to base isolated structure. The results for GM17-1 input motion is shown in this section. Figure 6-14

shows the base level displacement and acceleration of base isolated model under GM17-1 input motion which induces the largest displacements in the base isolated model. This figure shows that numerical model could simulate the base level displacement well, although effect of higher frequencies excitation is obvious in acceleration likely due to errors in modeling damping.

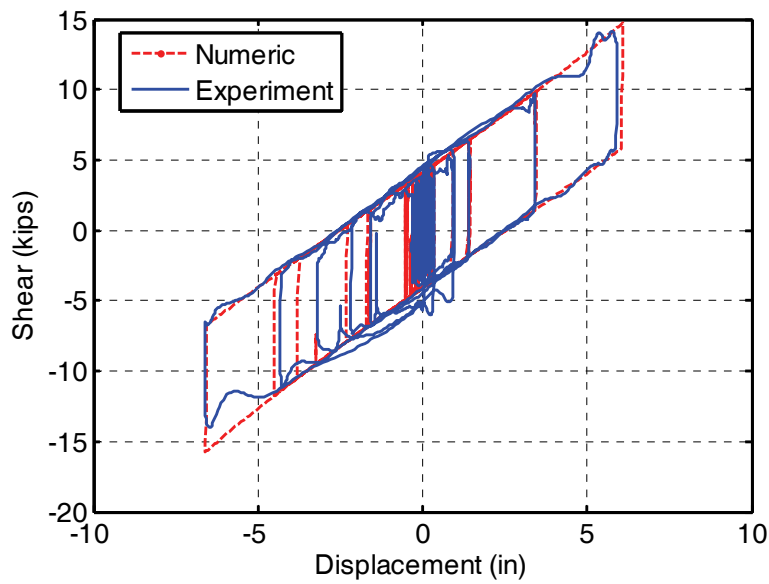


**Figure 6-14 Base level displacement and acceleration for base isolated model for GM17-1.**

Figure 6-15 and Figure 6-16 show the base level velocity versus displacement and total isolators hysteresis behavior, respectively. The base velocity obtained from numerical simulation shows good agreement with experimental results. The experimental velocity is obtained by integrating the acceleration at the base. The total isolators hysteresis was calculated by adding the shear force recorded in each load cell under isolators in experiment.



**Figure 6-15 Base level velocity versus displacement under GM17-1.**



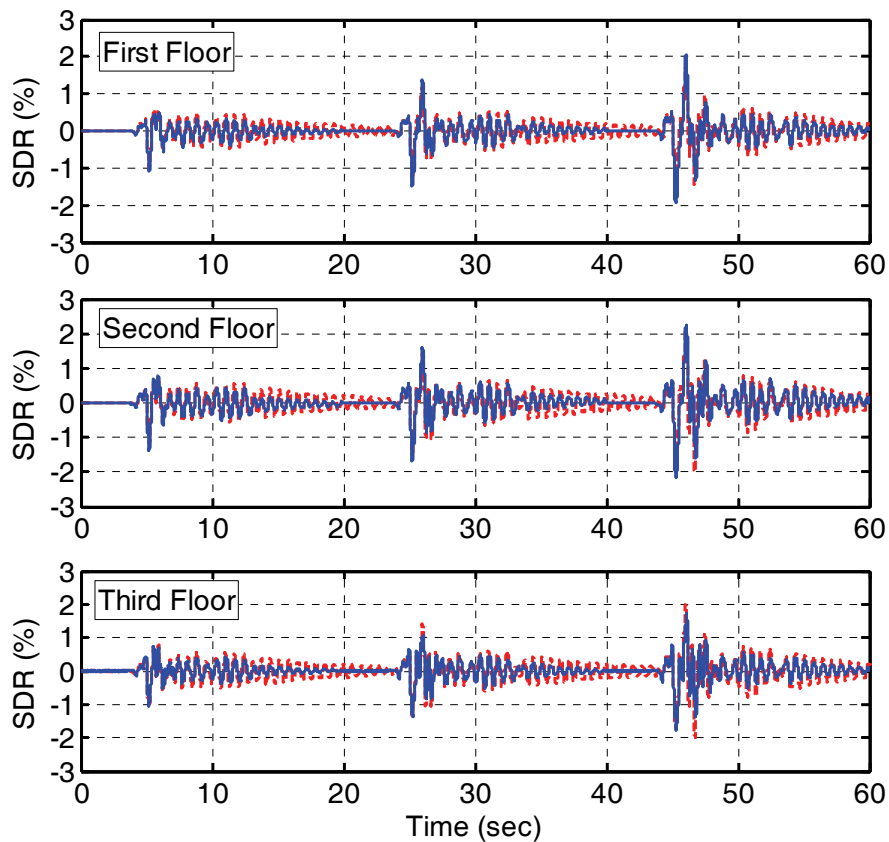
**Figure 6-16 Total isolators hysteresis under GM17-1.**

Figure 6-17 compares the story drift ratio obtained from experimental testing program and numerical simulation under three different amplitudes of GM17-1 input motion. Maximum SDR of about 2.1% obtained in the second floor of the frame under MCE level resulted in minor

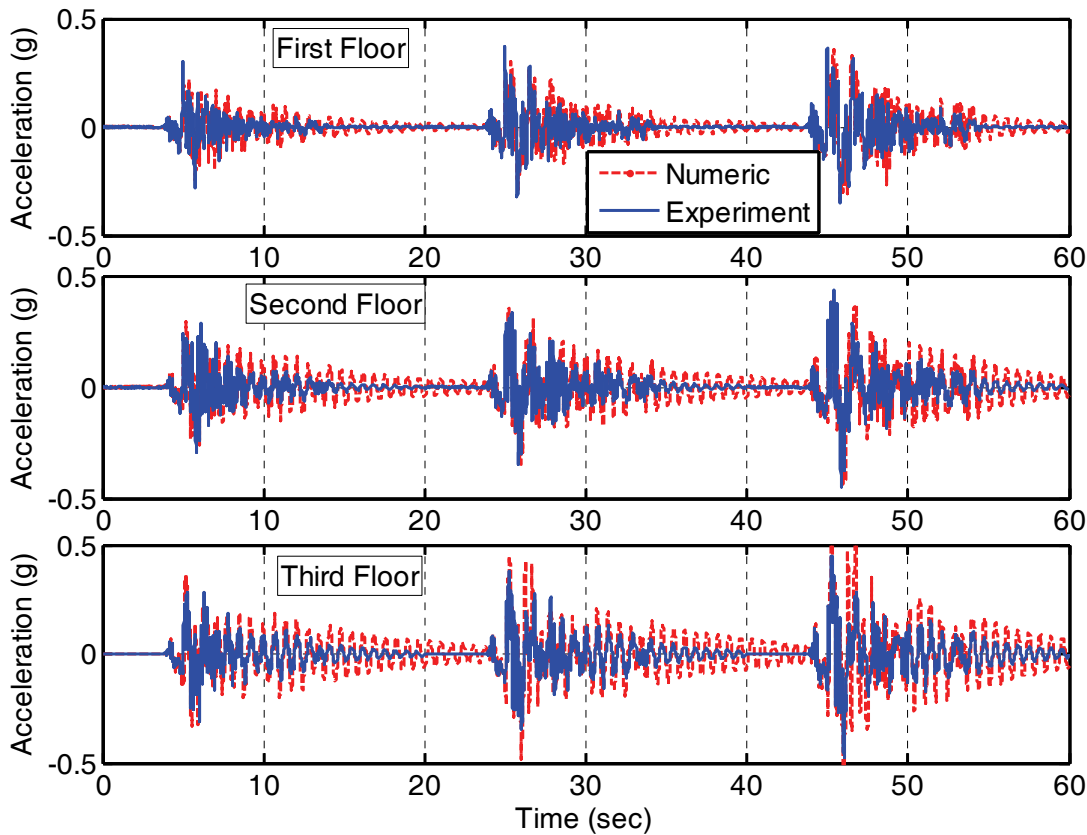
yielding in structure. Overall, the numerical simulation shows a good agreement with experimental testing.

Figure 6-18 shows each floor's acceleration for the same input motion. The effect of damping in acceleration is less apparent here due to the fact that higher frequencies are filtered out by isolator elements at the base level.

In general it can be seen that numerical model of the superstructure IMRF and base isolation system can capture essential characteristics of the experimental model under different levels of input motion. It is important to have a reliable numerical model of the experimental structural model without moat wall in order to compare the response capture from experimental impact testing and numerical simulation using the proposed impact element.



**Figure 6-17 Story drift ratio for base isolated model under GM17-1.**



**Figure 6-18 Absolute acceleration response for base isolated model under GM17-1.**

### 6.5.3. Base Isolated Model with Moat Wall

The impact tests were conducted using different records for different wall types and different gap displacement. The experimental results for record GM17-1 are compared to numerical simulation of the test setup including the proposed impact element. The proposed impact model was used to simulate the moat wall behavior. The moat wall model parameters are presented in sections 6.3.4 and 6.3.5. The results obtained from experiments are compared with the numerical model, focusing on the prediction of the impact force and superstructure response.

Figure 6-19 compares the experimental and numerical simulation results for the west 2 in. concrete wall impact force under GM17-1 record. The local deformation and global vibration response phases are clearly shown in this figure. The first peak in the impact force is mainly due to local deformation of two bodies at the contact point, followed by a longer duration contact force and larger displacement mainly influenced by the dynamic properties of the wall as well as

the applied ground motion. It can be seen that the concrete wall shows relatively low resistance after the first phase of the impact, mainly from compression of soil behind the wall since the concrete wall formed a plastic hinge at its base. Note that the time in Figure 6-19 is a pseudo time shifted so that in all cases, initiation of impact occurs at the origin to provide a better comparison.

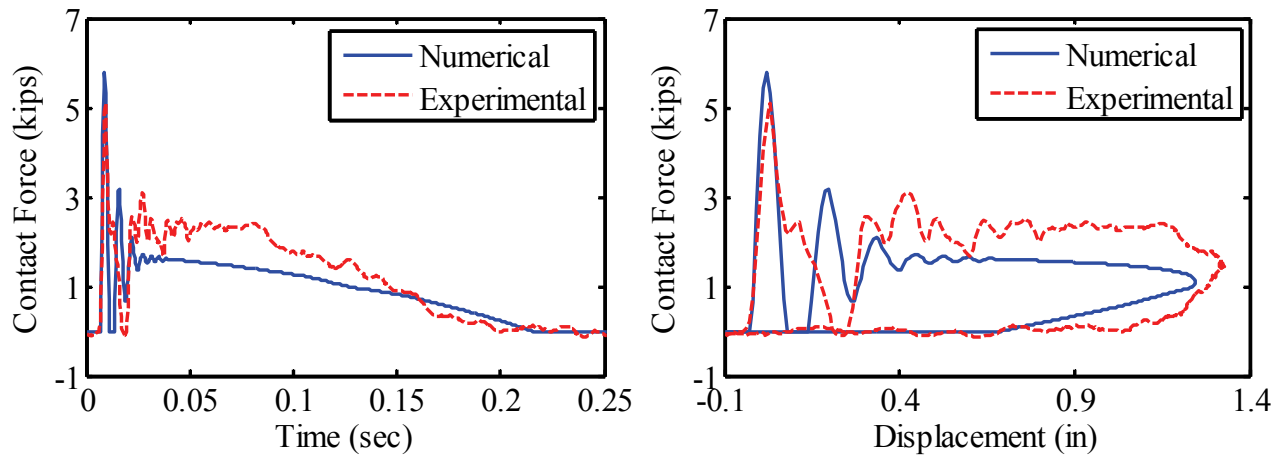


**Figure 6-19 Impact force for 2 in. concrete wall installed at 6 in. gap distance: (a) Impact force versus contact time, (b) Impact force versus penetration displacement.**

The experimental test was repeated by rotating the concrete walls (4 in front wall and 2 in back wall) followed by a new set of concrete walls with 6 in front wall thickness and 4 in back wall thickness. The parameters for the proposed impact element for different type of moat walls are summarized in Table 6-1. All the parameters in this table are calculated from physical properties of moat walls except the damping ratio,  $\xi$ , which is calibrated from experimental results that clearly show over-damped response. This behavior of the moat wall was expected due to large plastic deformation in moat wall and compression of loose soil backfill.

Figure 6-20 and Figure 6-21 show the impact force result for the 4 in. concrete wall installed at 6 in. gap distance and 6 in. concrete wall installed at 4 in. gap distance, respectively. The comparison of the impact force recorded in experimental simulations and the proposed impact element with parameters determined based on physical properties of the moat wall are in very good agreement.

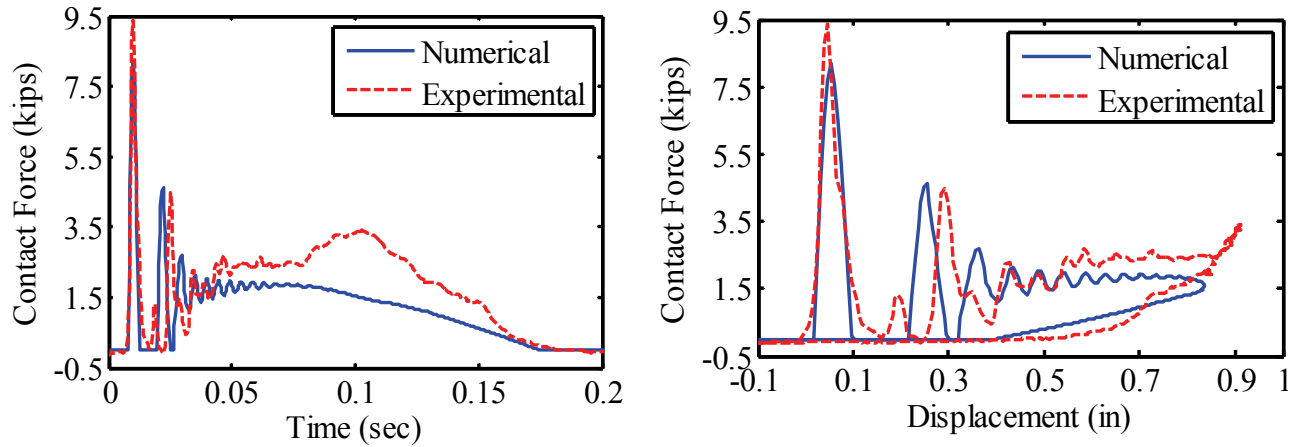


**Figure 6-20 Impact force for 4 in. concrete wall installed at 6 in. gap distance: (a) Impact force versus contact time, (b) Impact force versus penetration displacement.**

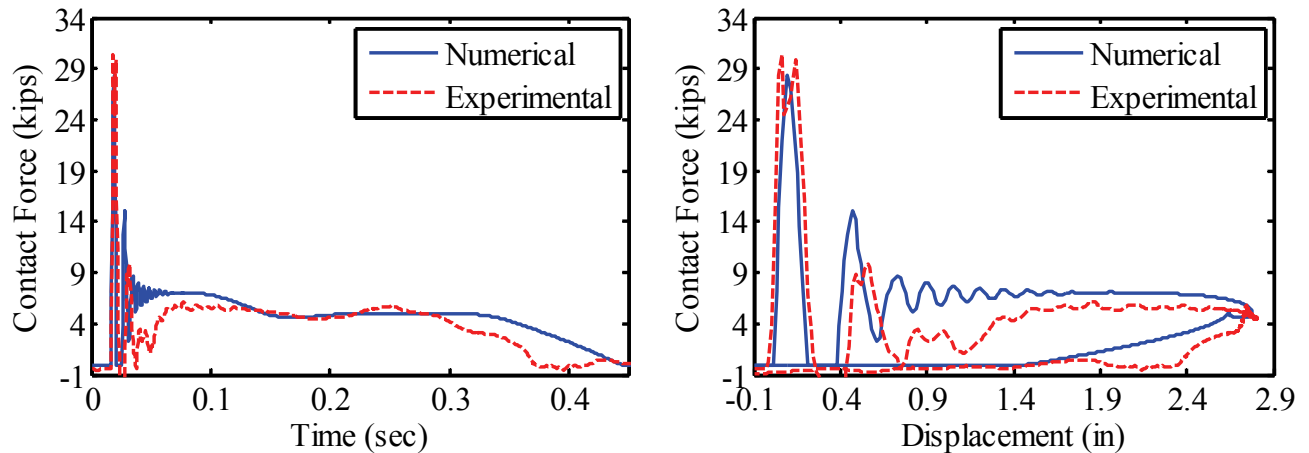


**Figure 6-21 Impact force for 6 in. concrete wall installed at 4 in. gap distance: (a) Impact force versus contact time, (b) Impact force versus penetration displacement.**

The relatively rigid steel triangle wall was installed at a 4 and 6 in. gap distance from the isolated structure to examine a wider range of moat wall stiffness values. Four 20 in. long rods were used to attach the steel wall to the shake table platform. Initial experiments indicated rocking of the steel wall, thus the bolted connection was reinforced with a 2 in. linear weld to prevent slip and uplift at the base of the steel wall. The corresponding mass,  $M$ , and stiffness,  $K$ , are shown in Table 6-1. The damping ratio in this table is obtained from calibrating the numerical analysis with the proposed impact element against experimental results. Figure 6-22 and Figure 6-23 show the impact force for steel moat wall installed at 4 and 6 in gap distance, respectively.

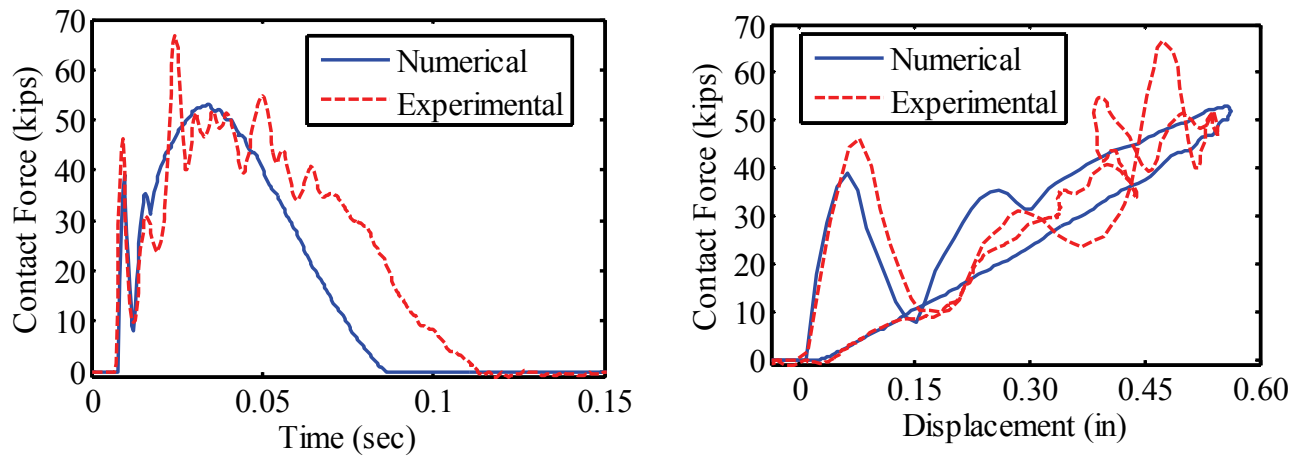


**Figure 6-22 Impact force for steel wall installed at 4 in. gap distance: (a) Impact force versus contact time, (b) Impact force versus penetration displacement.**

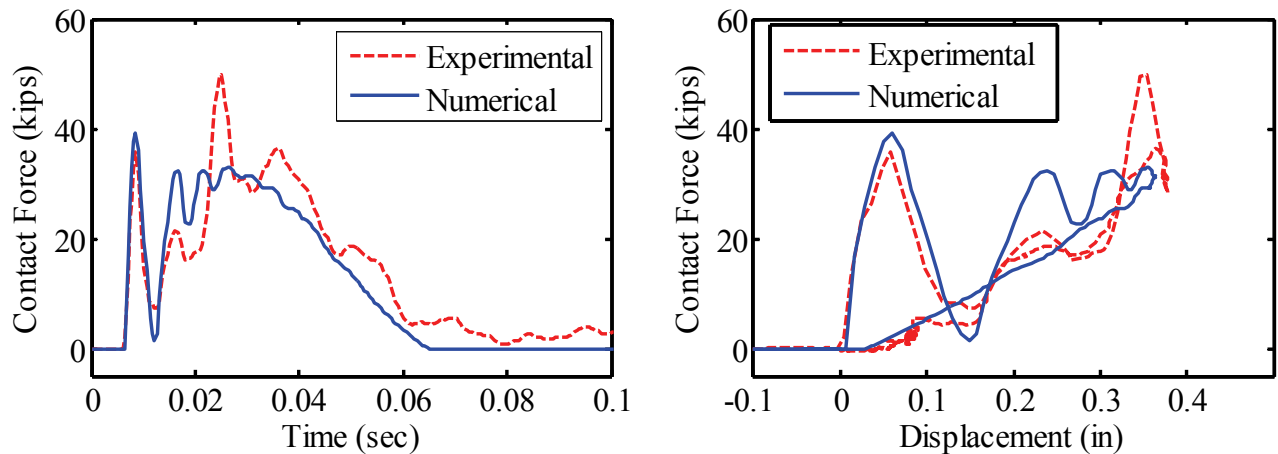


**Figure 6-23 Impact force for steel wall installed at 6 in. gap distance: (a) Impact force versus contact time, (b) Impact force versus penetration displacement.**

The numerical simulation of impact force was validated by comparison to experimental results for different wall types and gap distances. It was shown that the proposed simplified impact element could capture essential characteristics of structural impact.

The superstructure response for the steel moat walls installed at 4 in. gap distance are presented here to demonstrate that the numerical model including the proposed impact element can capture

the impact force as well as the superstructure response. Figure 6-24 shows the base plate velocity versus displacement obtained from shake table test and the corresponding numerical simulation. It can be seen that numerical displacement and velocity are in good agreement with experimental results during contact with moat walls (beyond  $\pm 4$  in).

Superstructure acceleration and story drift ratios are plotted in Figure 6-25. The first impact to the west wall (negative displacement) and the second impact to the east wall (positive displacement) occurred at time 1.71 and 2.28 second, respectively. The acceleration spiked in all levels at the instances of the impact in comparison to the case without moat walls. The peak acceleration increased by 430, 270, and 214% in the first, second, and third story, respectively, and this increase is captured in the numerical model within 8% error.

In terms of story drift ratio, the third story shows maximum amplification compared to the case without impact. The story drift ratio is amplified from 1.7% to 5% at the third level when the steel moat wall was installed at 4 in. gap, leading to considerable yielding and permanent residual drift in frame model. Although the second impact occurred at a higher velocity, the larger increase in drift ratio occurred following the first impact, indicating that the effect of the impact on superstructure response is largely dependent on the state of the superstructure at the instance of impact. In this case, the first impact occurred just before the peak negative superstructure displacement. The first impact pushed the structure to a larger peak displacement while the second impact did not occur near the superstructure peak displacement response. Figure 6-25 also show that numerical model including the proposed impact element can reproduce the seismic response of base isolated structure impacting against a moat wall.

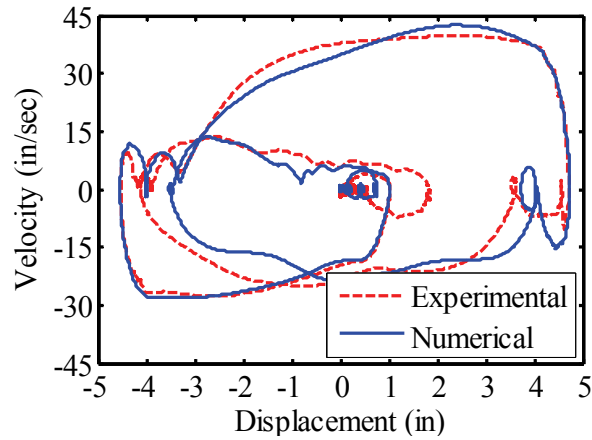


**Figure 6-24 Base level velocity versus displacement for steel wall installed at 4 in gap distance.**

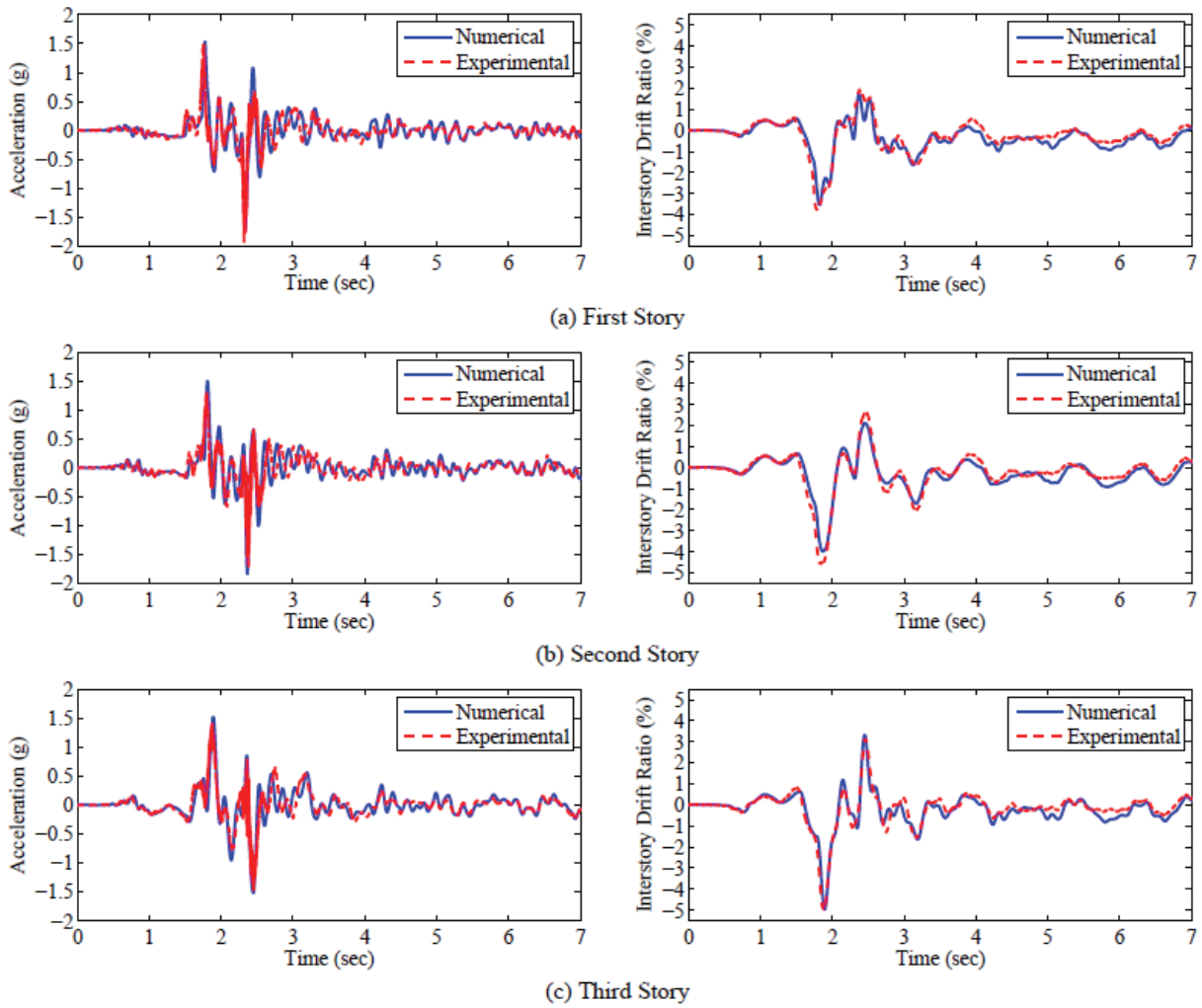


**Figure 6-25 Superstructure acceleration and story drift ratio.**

## 6.6. Sensitivity Analysis

A sensitivity analysis was conducted on the proposed impact model parameters to examine the effects of uncertainty in assigned values on the simulated structural response. The Hertz stiffness ( $K_h$ ), restitution coefficient ( $e$ ), rotational spring stiffness ( $K_\theta$ ) and damping ratio ( $\xi$ ) are considered here. Changes in these four parameters over a range of [-50%, +50%] of their base value was examined for resulting peak displacements and acceleration response of the building. Each separate parameter was varied one at the time, and the response of the structure was compared with corresponding results using base values. The base values are obtained from the procedure explained in section 3 of this paper and presented in Table 6-1.

Defining the relative response change as the absolute response divided by response to base value parameters leads to the diagrams shown in Figure 6-26 for the case of the 6 in concrete wall installed at a 4 in gap distance under GM17-1 motion. Figure 6-26 (a) and (b) show the sensitivity of the four parameters on the base level peak acceleration and displacement, respectively. It can be seen that the two local parameters (Hertz stiffness and restitution coefficient) have the most effect on base level acceleration resulting in maximum 17% response change in comparison with base values for a 50% change in model parameter values. Figure 6-26 (c) and (d) show changes in average of peak acceleration and drift for the three superstructure levels due to changes in these four parameters. The two moat wall parameters (spring stiffness and damping ratio) have the most effect on the superstructure response and base level displacement. The maximum change in superstructure response is less than 7% due to 50% change in rotational spring stiffness or damping ratio. The same level of sensitivity was obtained for other types of moat walls and under different gap distances. The sensitivity analysis shows that the simplified impact model is reliable considering uncertainty in assigning parameter values.

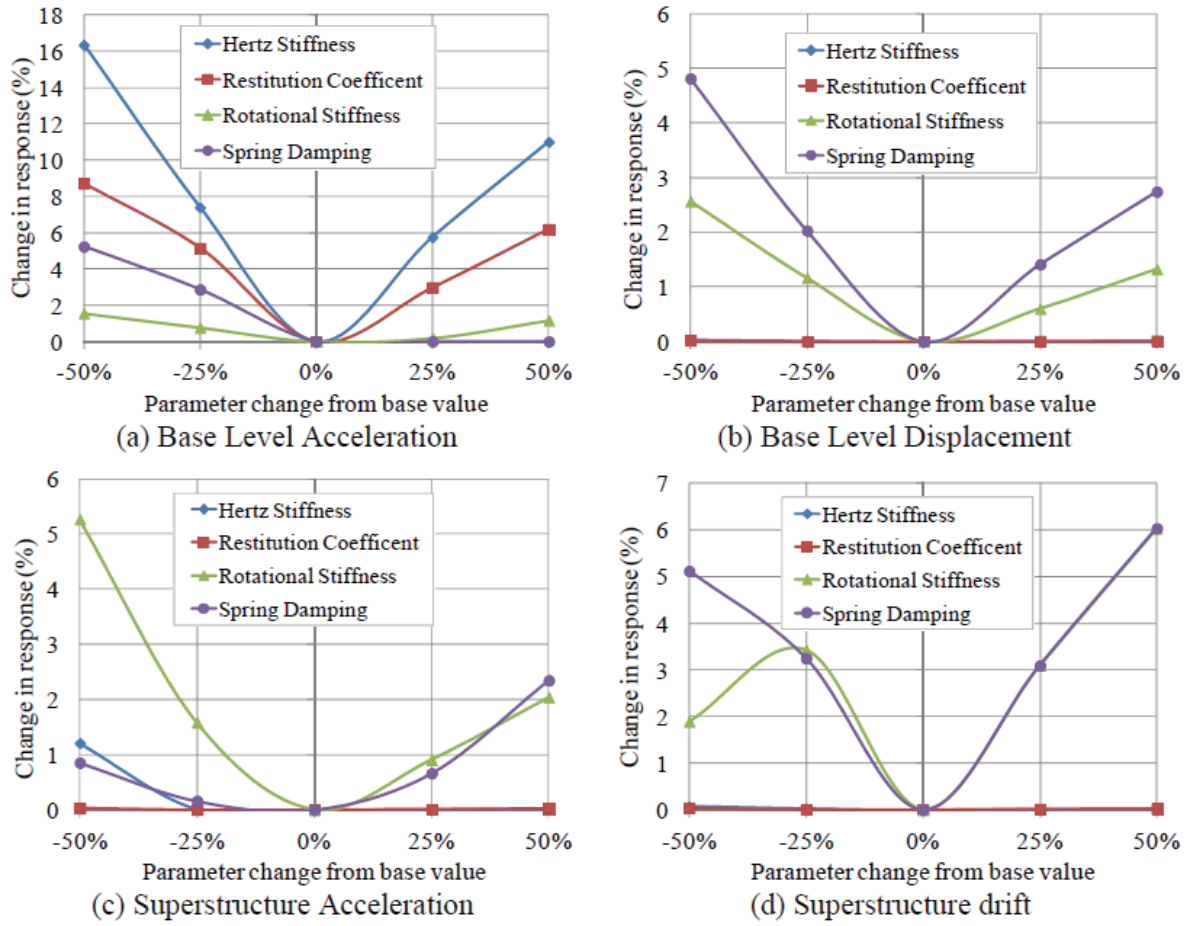


**Figure 6-26 Effect of changing impact model parameters on structural response.**

## **SECTION 7**

### **POUNDING IN THREE DIMENSIONAL BASE ISOLATED BUILDINGS**

#### **7.1. Introduction**

The experimental study and numerical studies previously presented were conducted on a 2-dimensional (2D) framed model due to complexity of the impact phenomena and limitations of the test setup. The experimental results were used to understand the structural impact phenomena and also the effect of pounding at the base level on response of the scaled model superstructure. The 2D numerical study led to a new unidirectional impact element to include effect of both local and vibration aspects of structural impact. While the proposed impact model could capture the essential behavior of structural impact in a 2D frame collision, the extension of the proposed model to a more general 3-Dimensional (3D) element is essential for dynamic analysis of more realistic buildings models.

The proposed impact element in Section 6 was extended to a 3D impact element to capture the collision between the base level of a 3D base isolated building to a moat wall. The response of 3-story IMRF and OCBF prototype models presented in Section 3 is examined considering impact to a surrounding moat wall at the base level by implementing the proposed impact element to finite element models of the buildings. The effect of pounding to moat wall in both prototype buildings were investigated by comparing the superstructure response with and without presence of the moat wall. These studies provide critical information for the design of base isolated buildings, particularly the moat wall clearance and its potential effect on the superstructure response.

#### **7.2. 3D Moat Wall Model**

The moat wall model presented in Section 6 was able to capture the nonlinearity in moat wall as well as the soil back fill by considering equivalent stiffness for an assumed displacement. A more generic moat wall model is presented in this section to be used in 3D numerical studies. For this purpose a single beam element is combined with a nonlinear spring in series to simulate the concrete moat wall and soil back fill. The single beam element can represent a certain wall width and also can capture nonlinearity in the wall behavior. The height of the beam element can be set

to the height of the wall. In common structural finite element software such as SAP2000 or OpenSees a beam element can be defined by assigning a section properties and end nodes. Nonlinearity in sections of the beam element can be defined using either uniaxial fibers with a finite length or concentrated plastic hinges.

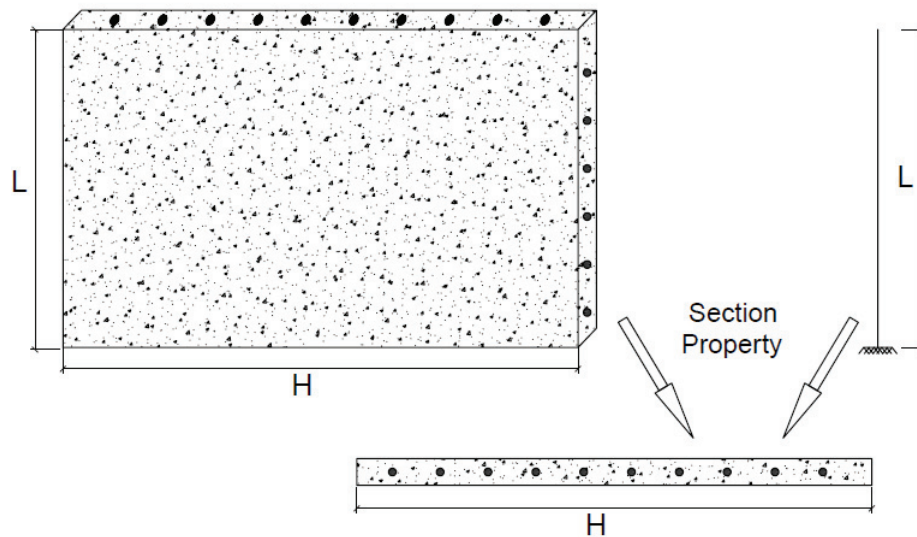


**Figure 7-1 Moat wall model using beam element**

As shown in Figure 7-1, the 2-node beam element model using fiber section can represent a solid concrete moat wall specifying the locations of steel rebars explicitly. Different material can be assigned to steel rebar and concrete. Defining fiber sections in 3D beam element model leads to include in and out of plane stiffness and also torsion stiffness in numeric study. Each beam element can represent a certain length of the wall ( $H$ ) and can be connected to each other using an interaction element. The behavior of these internal elements will be described later.

### *7.2.1. Soil Backfill*

Nonlinear response of bridge abutment and soil backfill has been studied experimentally and numerically (Shamsabadi et al. (2007), Faraji et al. (2001), Siddharthan et al. (1998), and Gadre et al. (1998)). The nonlinear force-displacement capacity of the bridge abutment in a seismic event is developed mainly from the mobilized passive pressure behind the abutment back wall.

Earth pressure theories have been developed based on different assumptions and methods to predict lateral soil-abutment capacity. In this study, the modified hyperbolic abutment-backfill stress-strain behavior (LSH) was selected since it shows good agreement with various experimental studies and it is easy to implement in numerically. A hyperbolic force-displacement (HFD) relationship (Figure 7-2) was developed by Shamsabadi et al. (2007) as a function of three parameters including average abutment stiffness, a maximum backfill capacity, and a maximum displacement that can be used by structural engineers. The HFD tool is found to be a good fit with many experimental test data and all curves calculated by the LSH model. The three HFD parameters are derived directly from the experimental data. The HFD model is found to be a practical, powerful, and versatile tool for seismic bridge design that can be used by structural and geotechnical engineers (Shamsabadi et al. 2007).

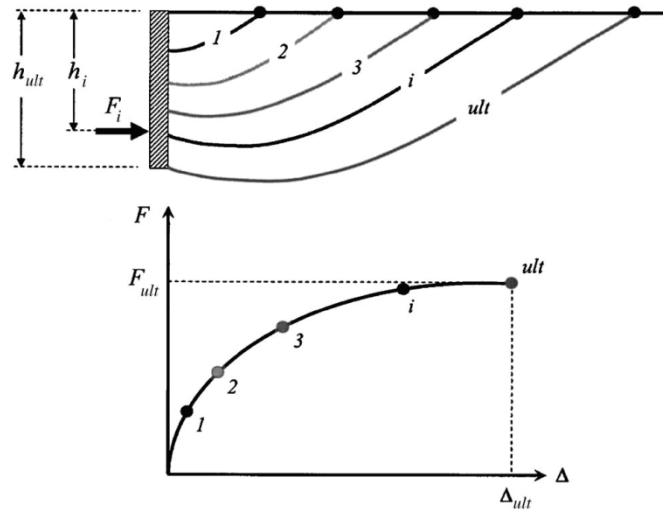


**Figure 7-2 Logarithmic-Spiral passive wedge and corresponding force-displacement relationship (Shamsabadi et al. (2007))**

The HFD force-displacement relationship is shown below:

$$F(y) = \frac{y}{A + By} \quad (7-1)$$

The constants A and B can be calculated by

$$A = \frac{y_{max}}{2Ky_{max} - F_{ult}} \quad (7-2)$$

$$B = \frac{2(Ky_{max} - F_{ult})}{F_{ult}(2Ky_{max} - F_{ult})} \quad (7-3)$$

Where average soil stiffness ( $K$ ) and the maximum abutment force ( $F_{ult}$ ) developed at a maximum displacement ( $y_{max}$ ) are shown in Figure 7-3.

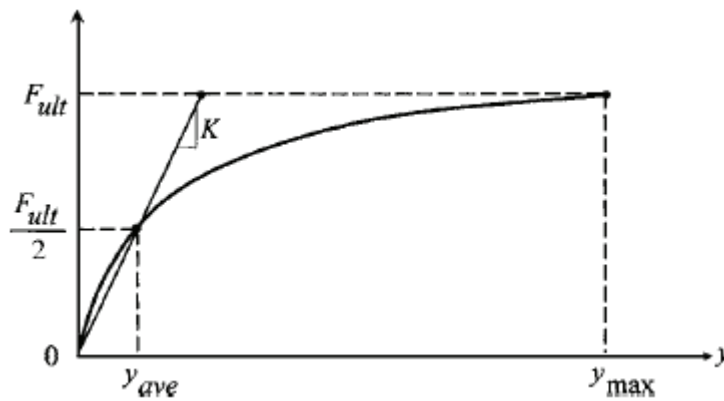


**Figure 7-3 Hyperbolic force-displacement parameters (Shamsabadi et al. (2007))**

The Equation 7-1 was originally generated for a common abutment bridge height which is equal to 3.28 ft. Shamsabadi et al. (2010) modified the original equation to a more generic equation in order to consider the variable wall heights. They also recommended different sets of required parameters for this equation based on various numerical and experimental studies. Since the prototype models were assumed to be located in Los Angeles, UCLA's silty sand soil was assumed for soil backfill in moat walls. The final equation for UCLA's silty sand backfill is

$$F(y) = \frac{71.5y}{\frac{H}{3.28} + 4.75y} \left( \frac{H}{3.28} \right)^{1.56} \quad y \leq 0.05H \quad (7-4)$$

This equation represents the soil resistant force for wall width of 1 ft. Parameter H is the height of the wall in ft and  $y$  is the wall displacement in inches. The Equation 7-4 should be multiplied by the width of the wall to compute the lateral force from soil backfill.

*7.2.2. Local Impact Element*

To simulate both phases of impact, the moat wall element should be combined with an element to capture local aspects of pounding. This element simulates the local deformations at the contact point dependent mainly on material properties of two objects, which can be defined by a Hertz damped model. A bilinear spring to represent the Hertz damped model has been implemented in OpenSees (McKenna et al. 2000) as well as other structural simulation software. This element was described in section 6.

Figure 7-4 shows the proposed moat wall element. This system includes a beam element to model the concrete moat wall with a concentrated or distributed plastic hinge at its end, a nonlinear spring in the back end to represent soil back fill and a nonlinear spring in front to simulate local deformations at the contact point. Equation 7-4 can be used to model the soil spring for a given moat wall width.

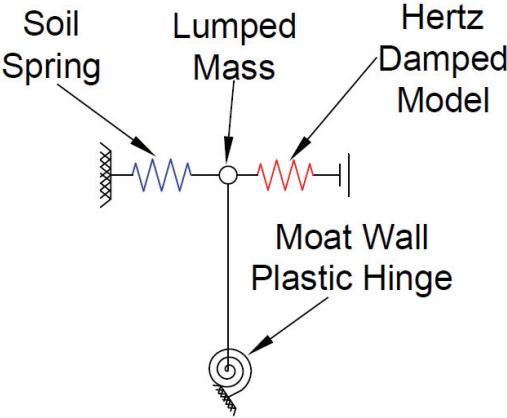


**Figure 7-4 Side view of moat wall element**

*7.2.3. Internal Shear Elements*

The moat wall model shown in Figure 7-4 can be used for collision between a point at the base level of the superstructure and a point on the moat wall with specific length and fixed boundary

condition at the bottom. This element can be replicated at a given distance to represent continuous walls along the base level of the superstructure. Figure 7-5 shows the plan view of real continuous moat wall around the base level of the IMRF structure and the simulated moat wall model using the element in Figure 7-4. The spacing between these moat wall elements could be set to bay span of the superstructure to align the end of column elements with moat wall elements.

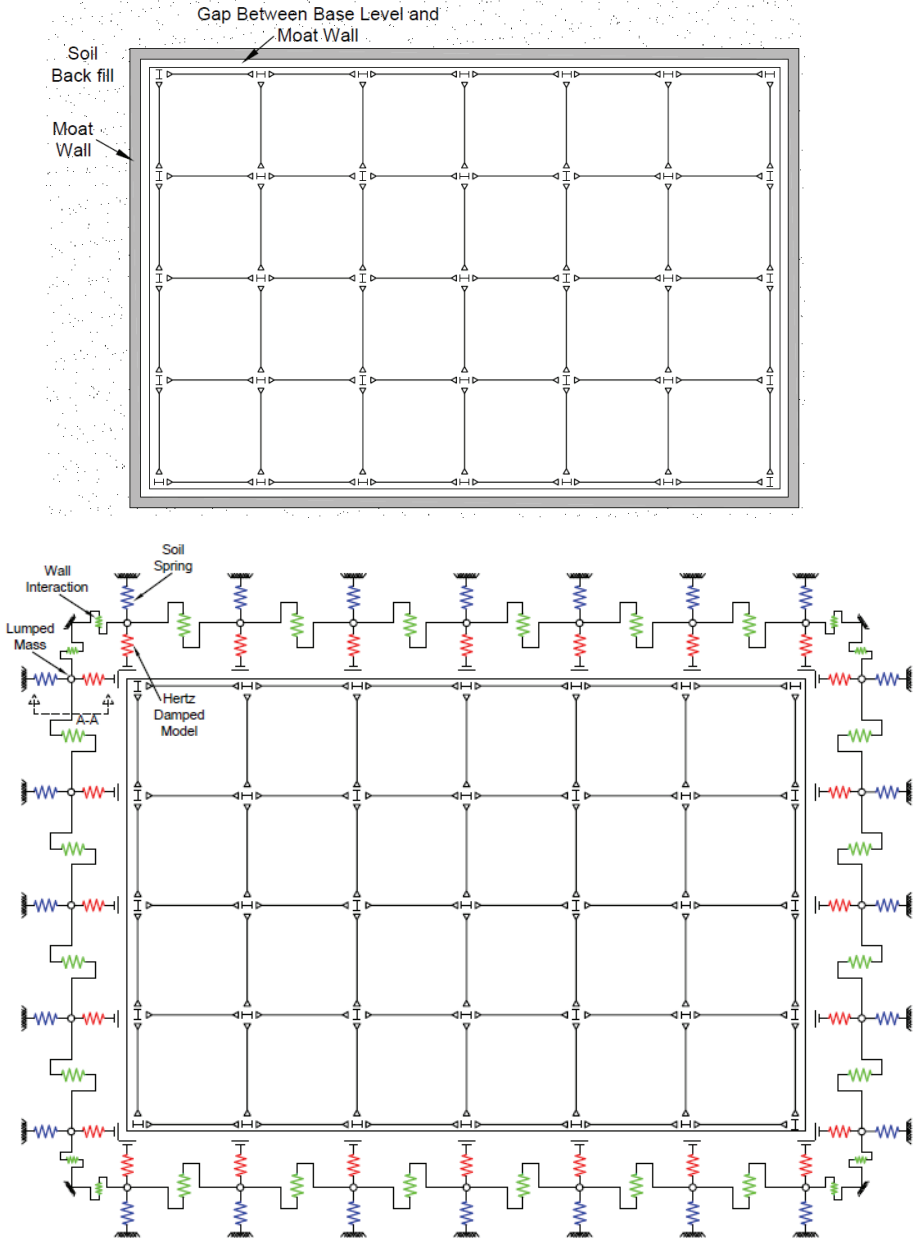


**Figure 7-5 Plan view of the prototype model a) Continues moat wall and soil backfill b) District moat wall model**

The single moat wall elements in Figure 7-4 should be connected using interactional elements to represent continuous moat wall behavior. These internal elements are shown in Figure 7-5(b) and have been defined here based on finite element analysis. Figure 7-6 shows different contact situations between the superstructure base level and one side of the moat wall. Figure 7-6 (a) shows undeformed position, in the left figure the outer rectangular represents moat wall and inner rectangular represents base level of the superstructure. In the figure to the right, continuous moat wall is replaced by a set of moat wall spring and internal elements.

Figure 7-6 (b) shows a structure under unidirectional excitation with all points of the base level on one side in contact with the moat wall springs. In this case, all the moat wall components (including local impact element, moat wall element, and soil backfill) will be engaged but only the two outer internal elements that connect two end moat walls to the fixed point are engaged. It should be mentioned that corner nodes are assumed to be fixed with the partial flexibility in these nodes neglected. The other internal elements do not deform since the relative lateral deformation in moat wall elements are zero. This situation is not very common due to eccentricities in the structure that result in torsional movement of the base level. In this case, a corner point of the base level first touches the moat wall and pushes back this point (Figure 7-6 (c)). Placing a moat wall element at the corner point results in engaging primarily this element through direct contact. The internal element between the corner wall element and the adjacent element is engaged since the base level is not yet in contact with the second wall element and there is a relative displacement between these two wall elements (Figure 7-6(c)). Pushing the moat wall further leads to pounding with the second wall element (Figure 7-6(d)). This would result in engaging the next internal element and so on.

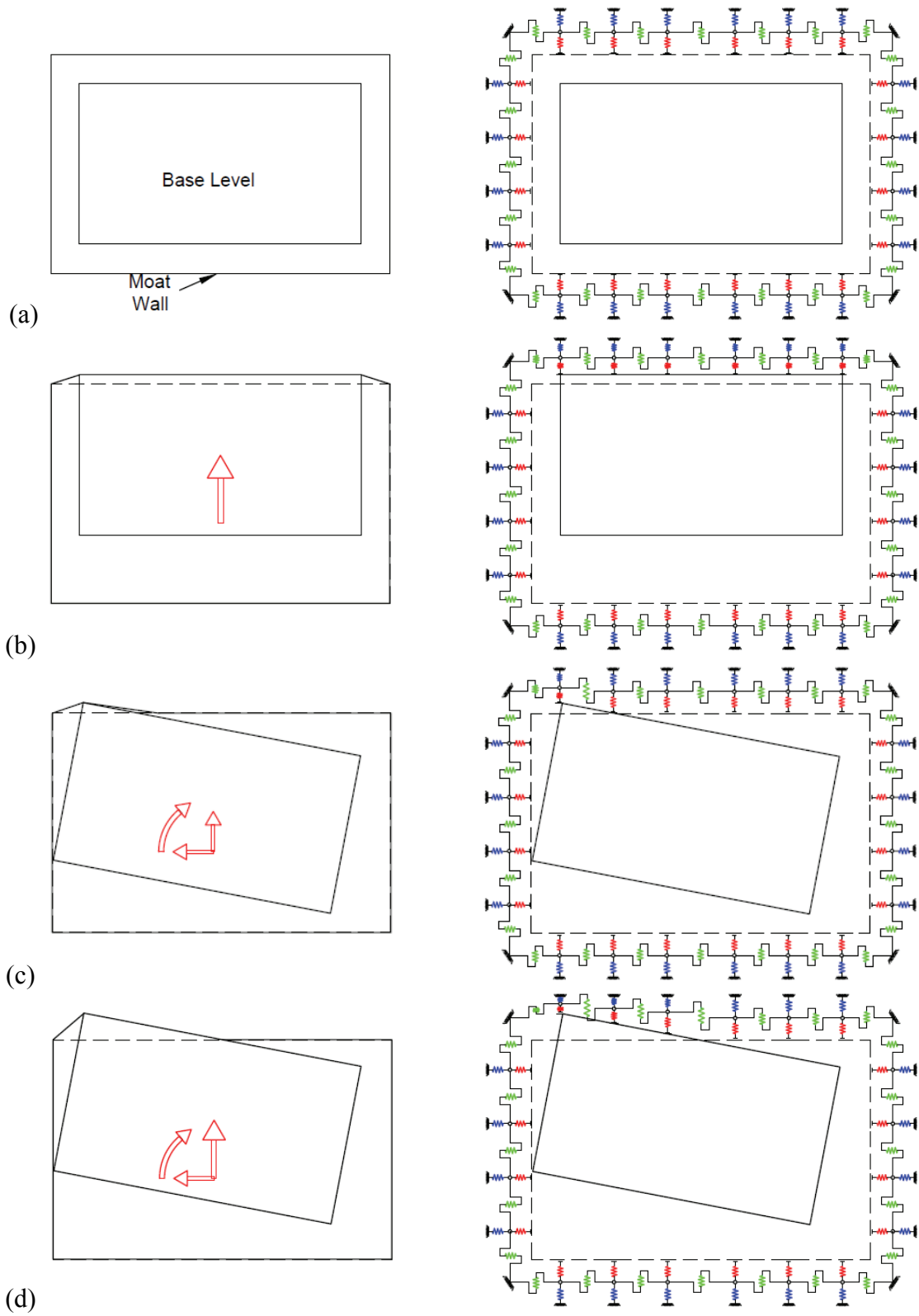


**Figure 7-6 Different Contact scenarios between Base Level and Moat Wall**

The internal elements have to be defined in such a way that they represent the continuous moat wall behavior. For this matter a finite element study was conducted using ABAQUS software. An 8-node brick element was assigned to 360 in. width by 120 in. height concrete wall. Reduced integration method applying hourglass control was selected for this element. Concrete damaged plasticity was assigned to these elements. The concrete damaged plasticity model is based on the assumption of isotropic damage and is designed for applications in which the concrete is subjected to arbitrary loading conditions, including cyclic loading. The model takes into consideration the degradation of the elastic stiffness induced by plastic straining both in tension and compression. It also accounts for stiffness recovery effects under cyclic loading.

Beam elements were assigned to represent rebars embedded in solid concrete. Bilinear material was defined based on yielding strength in steel rebars and assigned to these beam elements. The rebar elements were tied to concrete elements in order to simulate interaction of the rebar and concrete in moat wall.

First a 360 in width by 120 in height moat wall was built and fixed at its end to represent a cantilever column (Figure 7-7). Top line of the wall was pushed using explicit displacement integration method. The pace of applying displacement was reduced to a very small number to prevent exciting the inertia in shear force. Explicit integration scheme was selected over implicit one due to difficulty of convergence in implicit integration. On the other hand, fiber section described in page 149 was assigned to a beam element in OpenSees to compare the response of the cantilever wall in OpenSees and ABAQUS. Figure 7-8 shows that OpenSees can simulate the behavior of cantilever wall adequately. First crack strength ( $\approx 39$  kips) and rebar yielding ( $\approx 60$  kips) are in agreement with traditional concrete design calculations. This figure shows that modeling moat wall in OpenSees could be reasonably accurate in comparison with ABAQUS detailed finite element results. The difference between ABAQUS and OpenSees results in small displacements is due to fact that in ABAQUS modeling only 4 elements were assumed along the thickness of the wall which leads to sudden drop once each row of concrete elements reaching its tension capacity. On the other hand since large number of fibers were used in OpenSees this transition between tension failure of concrete and yielding point of rebars would happen more smoothly.

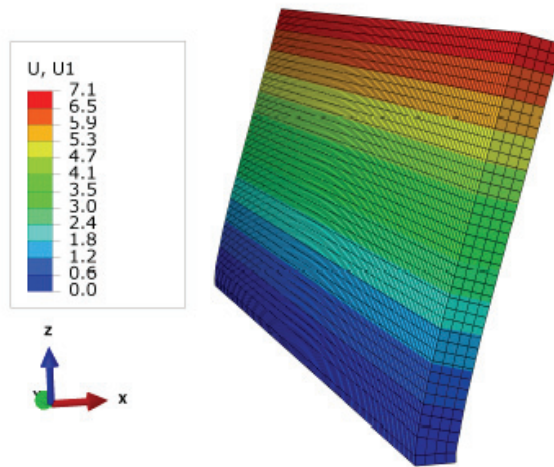


**Figure 7-7 Single wall pushover in ABAQUS**

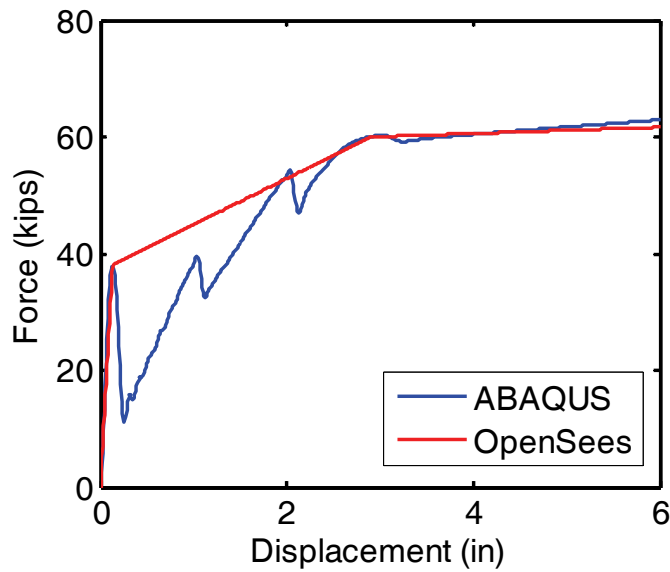


**Figure 7-8 Comparison of behavior of a cantilever wall in OpenSees and ABAQUS**

After conducting the benchmark test for a single cantilever wall and verifying the results obtained in OpenSees with ABAQUS, a continuous moat wall modeled in ABAQUS with the same height and 2160 in width (total wall length for one side of the frame) and fixed boundary condition in all sides. A middle 360 in part of the wall was pushed (Figure 7-9) in order to see the effect of continuous wall on pushover curve and to calibrate the internal shear springs in Figure 7-5.

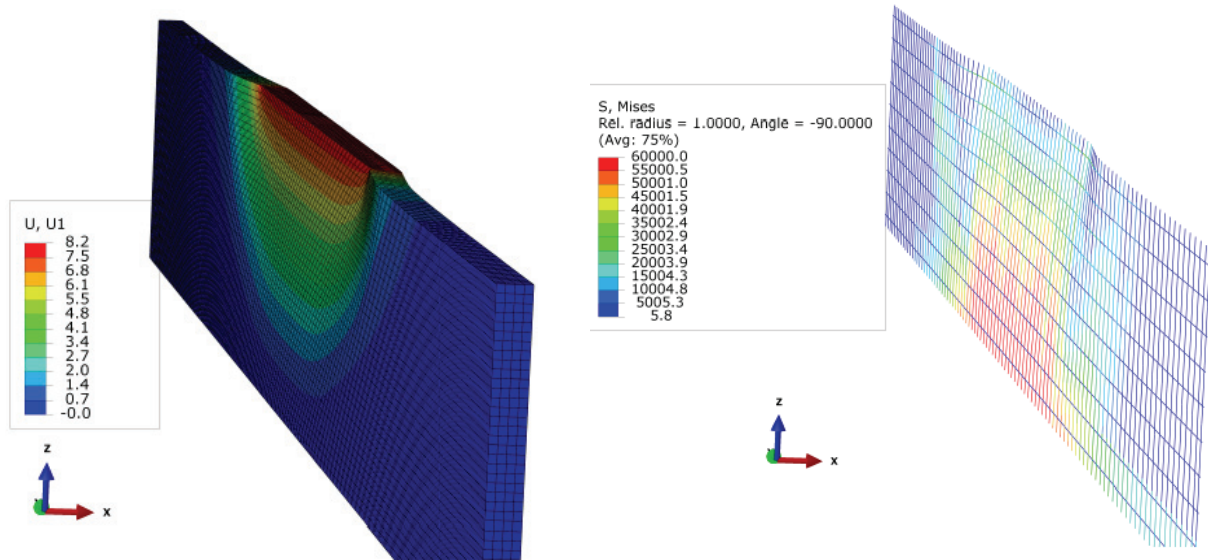


**Figure 7-9 Pushing on center of continuous moat wall: deformations and rebar stress**

From Figure 7-9 it can be concluded that for a continuous moat wall being pushed in a center section, the dominant behavior is still bending of the vertical rebars, thus the wall can be modeled as a single wall with a modified width (around 2 times the real wall width since the strength and stiffness calculated for small displacements of this wall in Figure 7-10 is almost two times the results obtained in Figure 7-8). The pushover force versus top of the wall displacement was plotted in Figure 7-10. The results obtained from ABAQUS analysis for the continuous moat wall subtracted from the single cantilever moat wall (Figure 7-8) was used to calibrate the internal shear springs between cantilever moat walls. The calculated behavior was assigned to internal shear springs and the moat wall shown in Figure 7-9 was modeled in OpenSees using 6 single cantilever moat walls connected with this internal shear spring and the middle section was pushed. The comparison of the pushover force obtained in OpenSees and ABAQUS is shown in Figure 7-10. It can be seen that using single cantilever moat wall connected by shear spring can represent the behavior of continuous moat wall modeled detailed using finite elements.

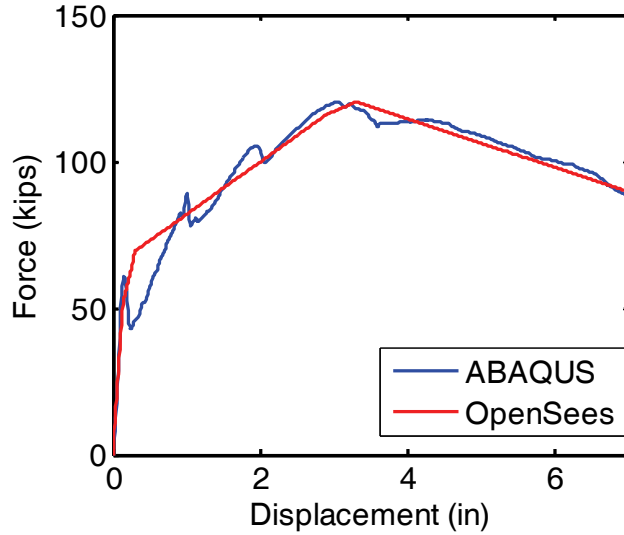


**Figure 7-10 Pushover of continuous moat wall (middle section)**

The same procedure was repeated for a corner portion of the moat wall where it is mostly that the first contact between the moat wall and base level occurs (Figure 7-11). The corner portion of the wall is more brittle with yielding in horizontal rebars connected the end of the wall dominating the response. In this case, the pushover curve obtained from ABAQUS compared with a single cantilever moat wall was used to calibrate the corner shear springs. The six cantilever moat walls in OpenSees connected to each other using internal shear springs and also the two outer walls are connected to a fix point using a corner shear spring. The corner moat wall was modeled in OpenSees using the calibrated spring with the resulting pushover force versus displacement compared to the full ABAQUS model in Figure 7-12.

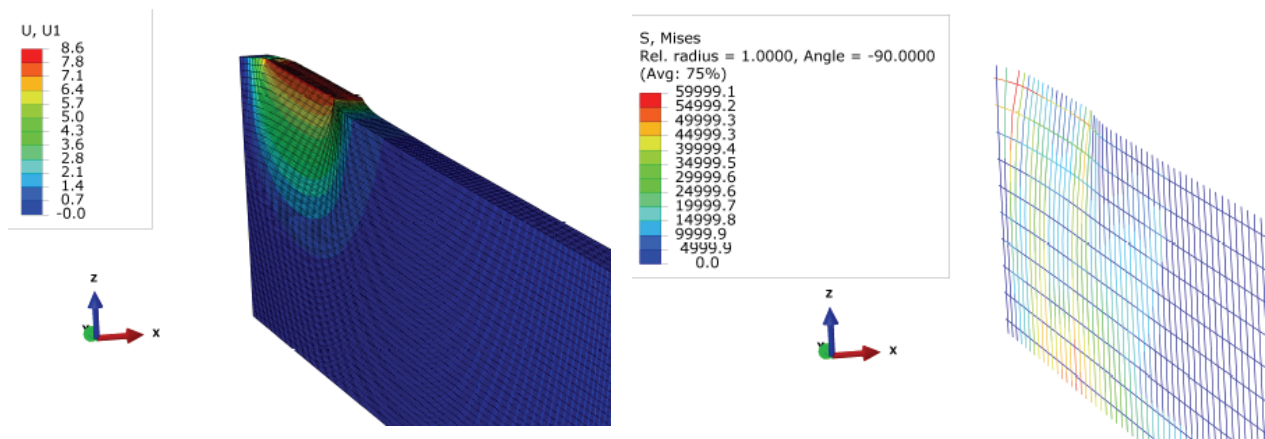


**Figure 7-11 Pushing continuous moat wall (corner section) and rebar stress**

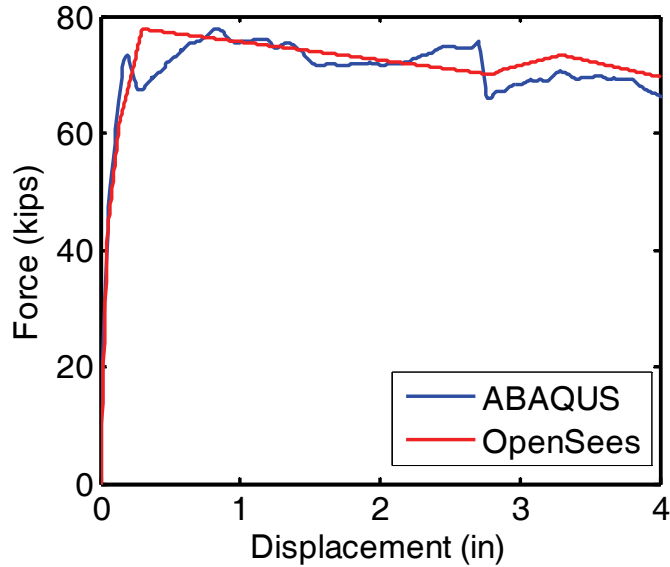


**Figure 7-12 Pushover of continuous moat wall (corner section)**

In summary it can be concluded that using single cantilever column representing wall sections connected using internal shear spring to each other and to a fixed point at corners could simulate a continuous moat wall behavior during contact between moat wall and base level adequately.

### 7.3. Base Isolated IMRF Building

The numerical assumptions for 3D modeling of the prototype IMRF model which was described in Section 3 are presented here. A detailed 3D numerical models of IMRF building was developed in OpenSees by Sayani et al. (2011) and modified here to consider the moat wall effect. The following description for 3D model is summarized from Sayani et al. (2011). Although the building is symmetric about both axes, the mass centers were shifted by 5% of the longest plan dimension in both directions to account for accidental torsion (ASCE 2005). Equivalent mass and rotational inertia were lumped at the center of mass. Slab action was accounted for through a rigid diaphragm constraint, except at the base level, where slabs were modeled with shell elements to enhance the rigidity of the model against local isolator uplift.

Energy dissipation was added to the superstructure using stiffness proportional damping calibrated to give 2.5% damping at its respective first mode frequencies. Stiffness proportional damping was selected since Rayleigh damping has been observed to artificially suppress the first

mode of an isolated building even compared with a rigid structure approximation (Ryan et al. 2008). Tangent stiffness proportional damping rather than initial stiffness proportional damping was selected to prevent the damping forces from becoming unrealistically large compared with the element forces after the superstructure yields.

### *7.3.1. Plastic Hinges*

All columns and moment-resisting beams were modeled using force-based nonlinear beam-column elements that combine finite length “plastic hinge” regions at the element ends with an interior elastic region (Scott et al. 2006). The columns were modeled using fiber sections that inherently account for moment-axial force interaction at each analysis step, whereas stress resultant models were chosen for the moment-resisting beam elements. The steel stress-strain and moment-curvature relationships were modified to include strength and stiffness degradation using Lignos et al. (2011) model (Bilin model). Lignos et al. (2011) tested a large number of beam section under cyclic loading and proposed equations to calculate the degradation parameters for different beam section. They proposed these parameters for moment-chord rotation behavior for each section. Assigning moment-curvature relationships for beam elements in which axial force plays insignificant role is adequately reasonable. Unlike beam elements, column section experienced a large axial force especially under large deformations. For this reason, fiber sections were selected to properly account for the effects of axial load on moment strength of the columns.

In order to consider the effect of strength degradation for column section, the following procedure was conducted to modify the Bilin model proposed by Lignos et al. (2011) for stress-strain relationship. First, moment-rotation response of each column section was developed using parameters proposed by Lignos et al. (2011) and assigning these values to a zero length section for a cyclic pushover. Then, a fiber section for the same column geometry was generated with the Bilin model assigned to each fiber element as stress-strain behavior. The required parameters for the fiber section using Bilin model was calibrated based on comparing these two responses for a given displacement history. Figure 7-13 compares the zero length section response with fiber section element for moment frame column section W14x176. This figure shows that Bilin model in OpenSees (McKenna et al. 2000) can be used as stress-strain behavior and assigned to

fiber section as material to consider both moment-axial force interaction and also strength and stiffness degradation simultaneously.

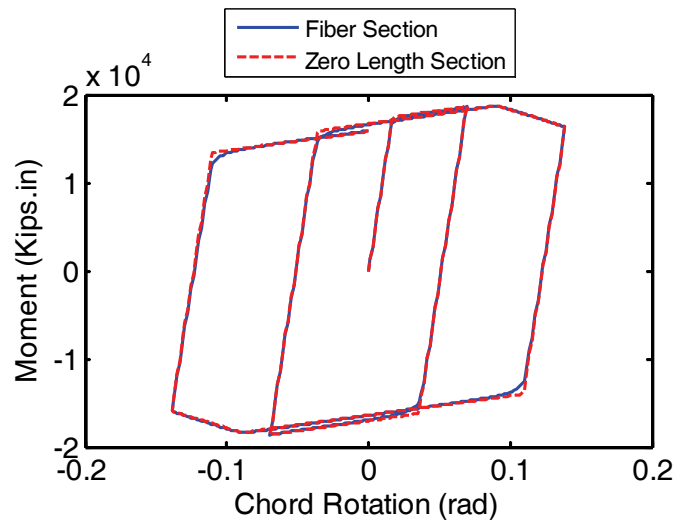


**Figure 7-13 Cyclic behavior of column section W 14x176**

Table 7-1 shows the required parameters for fiber section definition considering degradation effects. The parameters for zero length sections were calculated using equations presented in (Lignos et al. 2011). These parameters are shown in Figure 7-14. The parameters for fiber sections are calibrated from the procedure described here.

**Table 7-1 Modified Bilin model parameters for fiber section.**

Parameter	Zero Length Section			Parameter	Fiber Section		
	W14x176	W14x109	W12x53		W14x176	W14x109	W12x53
$M_y$ (kips.in)	17600	10560	4290	$F_y$ (ksi)	55.0	55.0	55.0
$M_c/M_y$	1.10	1.10	1.10	$\alpha$	0.006	0.006	0.006
$K_{initial}$	infinity	infinity	infinity	$K_{initial}$	29000	29000	29000
$\lambda$	4.9	2.2	1.5	$\lambda$	2.5	1.1	0.7
$\theta_p$	0.074	0.064	0.069	$\epsilon_p$	0.034	0.031	0.033
$\theta_{pc}$	0.322	0.191	0.170	$\epsilon_{pc}$	0.13	0.08	0.07

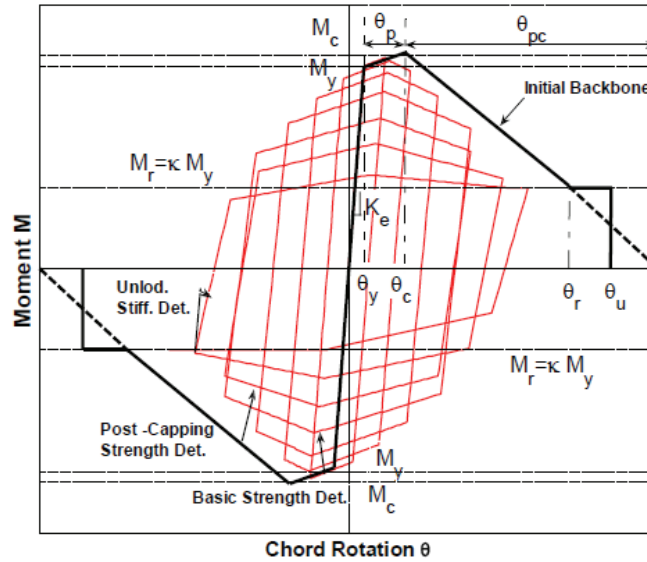


**Figure 7-14 Modified Ibarra Krawinkler deterioration model (Lignos et al. 2011)**

This procedure was used to include deterioration and degradation in columns as well as in beam sections. The effect of including deterioration in beam and columns section will be shown in section 8 where pushover curve for the frame in both cases were compared.

### 7.3.2. Panel Zone Flexibility

As mentioned in Section 6 of this report, considering effect of panel zone flexibility in modeling of the moment resistant frames are vital in estimating lateral deformations (Gupta et al. 1999). The panel zones were modeled using a trilinear hysteretic behavior described in (Gupta et al. 1999).

### 7.3.3. Isolator Model

Isolators were modeled independently, one beneath each column, using a combination of elements to realize a composite force deformation in each direction that could represent either elastomeric or friction pendulum devices. An elastic column element and an elastic-perfectly plastic spring were assembled in parallel to obtain the composite bilinear lateral force-deformation behavior shown in Figure 7-15(b). The characteristic yield strength  $Q$ , post yield stiffness  $k_b$ , and yield displacement  $u_y$  of the isolators determine the lateral force-deformation relation. Assuming  $u_y$  0.4 in,  $Q$  and  $k_b$  were determined by matching the secant stiffness  $k_M$  and

hysteretic energy dissipated to the equivalent period  $T_M$  (3.1 s) and damping ratio  $\beta_M$  (15:8%) at the MCE displacement  $D_M$  (24.3 in.).

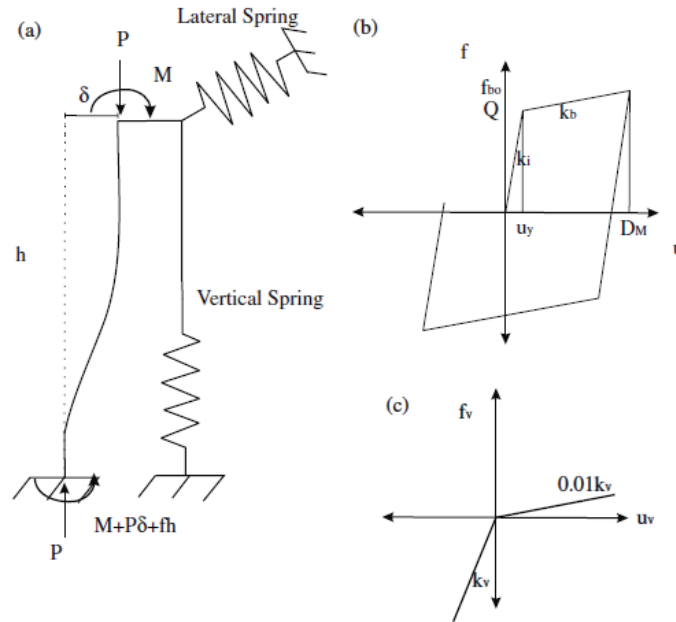


**Figure 7-15 (a) Isolator model; (b) Lateral force-deformation; (c) Vertical force-deformation in the isolation devices (Sayani et al. 2011)**

The elastic plastic spring, with stiffness  $k_i$ - $k_b$  and yield strength  $Q$ , is a bidirectionally coupled element with a circular yield surface that exhibits identical resistance in any direction in the  $x$ - $y$  plane. The column allows transfer of the approximate moments that arise attributable to the lateral deformation of the isolator. For the column element,  $EI$  was selected to obtain a lateral stiffness  $k_b$ , and the effective height  $h'$  was selected such that the moment in the element  $f h'$  equals the moment  $fh+P\delta$  in the isolator at the design displacement. Likewise, the composite vertical force-deformation behavior was built from the axial stiffness of the column element acting in parallel with a compression-only vertical spring. The compressive stiffness  $k_v$  of the isolators was computed assuming a vertical frequency of 10 Hz. Since typical bearings have no or low resistance to tension, the tensile stiffness was assumed to be 1% of the value of the compressive stiffness, and  $EA$  for the column element was calibrated to a stiffness of  $0.01k_v$ . The energy dissipation is provided by hysteresis in the lateral directions and 5% viscous damping in the vertical direction at 10 Hz.

## 7.4. Base Isolated OCBF Building

The numerical assumptions for 3D modeling of the prototype OCBF model described in Section 3 are presented here. A detailed 3D numerical models of OCBF building was developed in OpenSees by Erduran et al. (2011) and modified here to consider the moat wall effect. The general modeling assumptions for IMRF building was applied to the OCBF model as well, however, the OCBF model required brace elements as described next.

### 7.4.1. Brace Elements

Multiple nonlinear beam–column elements were strung together to physically simulate the inelastic buckling behavior in braces. A single brace using two force-based nonlinear beam–column elements with fiber sections and three numerical integration points along the length of the element was selected. An initial camber of 0.1% of the brace length was applied at the brace midpoint to initiate buckling (Figure 7-16). This modeling is based on the recommendations of Uriz et al. (2008). Based on the beam–column dimensions and likely connection geometry, the braces were modeled with an effective length of  $0.7L$ , where  $L$  is the full diagonal length between beam–column intersection centerlines. This reduction in effective length increases the overall stiffness of the frame and the critical buckling load of the members, contributing to frame overstrength relative to the design assumptions. The connection region was modeled by a rigid frame element followed by a ‘gusset’ frame element with the actual cross-section dimensions of the gusset plate and a length of  $2t$ , where  $t$  is the thickness of the gusset plate (Figure 7-16). The gusset element is very flexible practically simulating a pin connection in the out-of-plane direction. The resultant simulated cyclic force–deformation of a representative brace is shown in Figure 7-16(c).

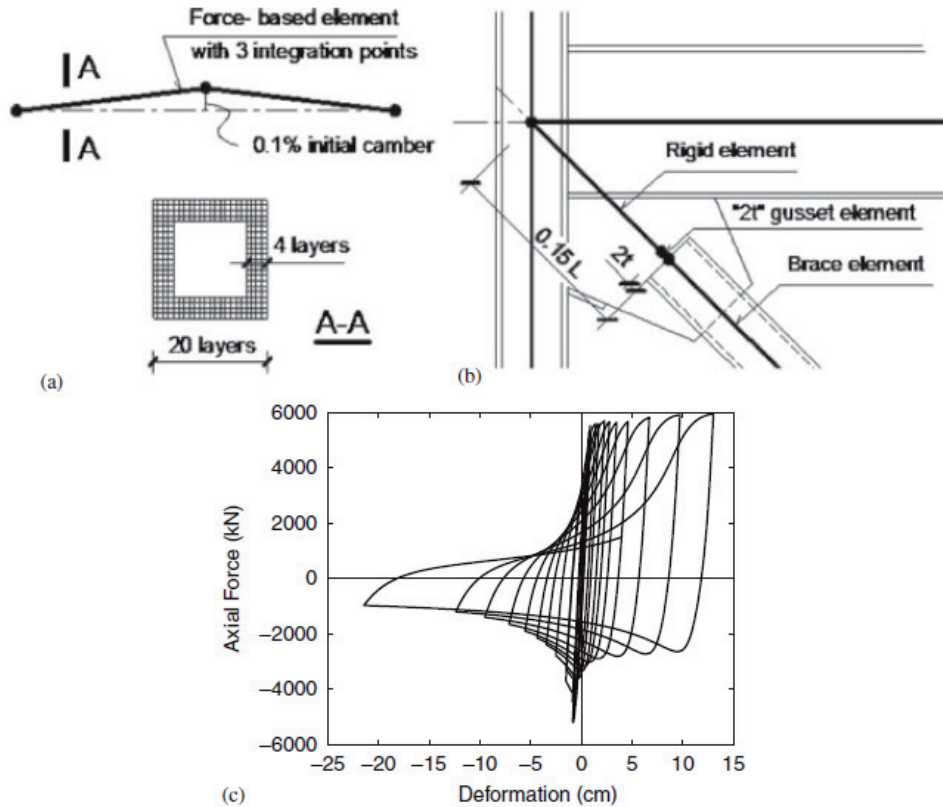


**Figure 7-16 (a) Brace model using two nonlinear frame elements with initial camber; (b) connection geometry and modeling details; and (c) Cyclic axial force–deformation relationship for a representative brace element (Erduran et al. 2011)**

### 7.5. Response of IMRF and OCBF models in MCE Event (2/50 year)

The performance of the two prototype base isolated models was examined under the ground motion set described in Section 3 with and without moat walls. The moat wall gap distance was set to 30 in., which is approximately equal to  $D_{TM}$  specified by ASCE (2005) based on a static design procedure. The actual design value of the gap distance may vary depending on the results of dynamic analysis of the building but can be no less than  $0.8 D_{TM}$ . All the ground motions described in Section 3 were scaled to MCE level for the period range of 0 to 3 sec. Two horizontal components of each ground motion were applied on the frame simultaneously. First, detailed response of the OCBF model with moat wall under one extreme ground motion (GM9) is shown for purpose of describing 3D moat wall behavior and then the envelope results under 20 ground motions for both models are discussed.

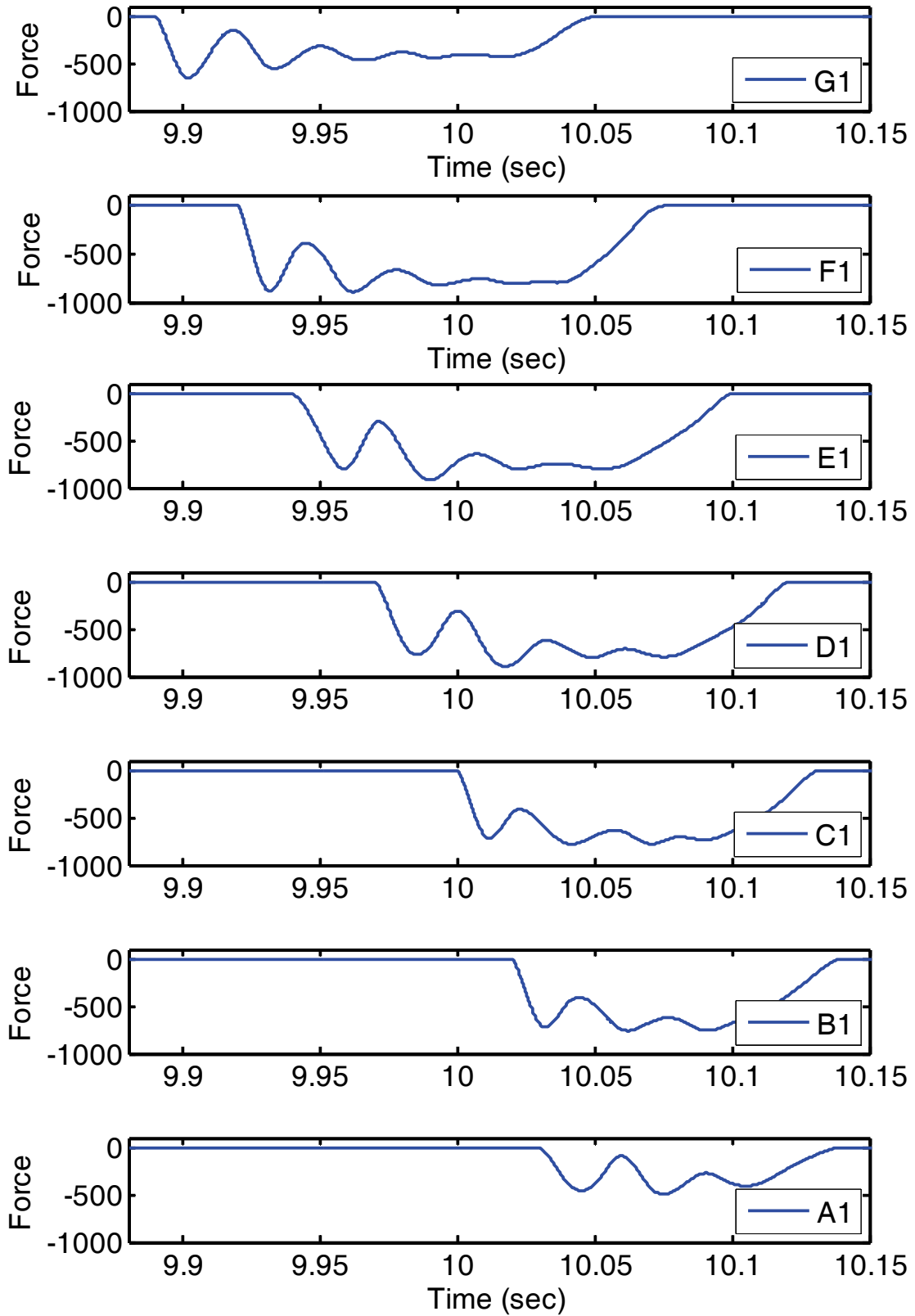
### *7.5.1. Detailed Response of OCBF Model under Input Motion GM9*

Response of the OCBF model under ground motion GM9 is shown here to describe the behavior of new impact element in 3D analysis and also explaining how pounding to moat wall would affect the response of superstructure. The envelope response of both models under all of the ground motions will be examined in next section.

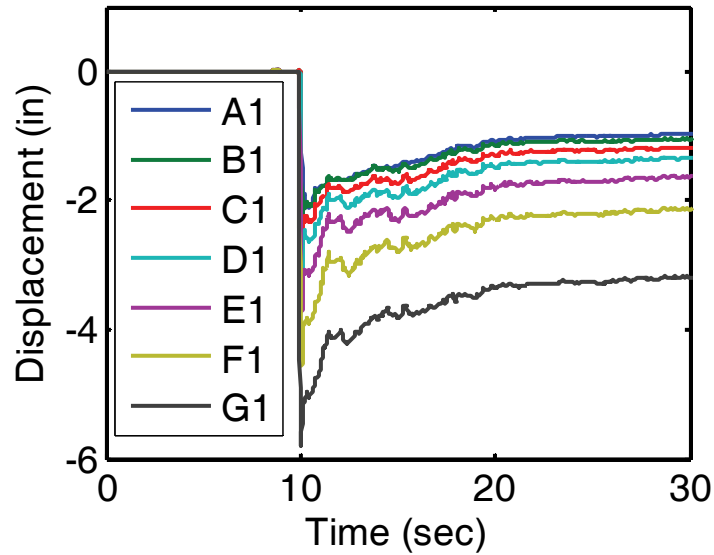
As mentioned earlier both components of the ground motion were applied simultaneously on the model in x- and y-direction (corresponding to long and short direction of the model, respectively). The base isolated model starts moving in two directions without contacting any displacement restrainer up to time 9.89 sec when first contact occurs at corner G1 (refer to right bottom corner of base level, Figure 3-2 in section 3). This pounding leads to generating force in impact element and also soil backfill resulting pushing back the moat wall. Continuing pushing back the moat wall results in engaging the other impact elements in line 1 (bottom x-direction in Figure 3-2) and generating force in these elements. Figure 7-17 shows the impact force in the 7 elements in this row. The time of rising of force verifies that contact between base level and moat wall started at point G1 propagating to point A1. Impact force in this figure is always negative showing that impact element acts only in compression.

The shape of impact force versus time is very similar to those obtained from experimental testing with concrete walls for small scale. The first peak in this force is due to dynamic oscillation of impact element while the whole trend is following the soil backfill response (hyperbolic nonlinearity).

Figure 7-18 shows the moat wall displacement in line 1 due to impact force. As mentioned, point G1 is moved more than other corner point A1. All the points show residual deformation verifying plastic deformation in moat wall and soil backfill which is source of damping for impact force in Figure 7-17.

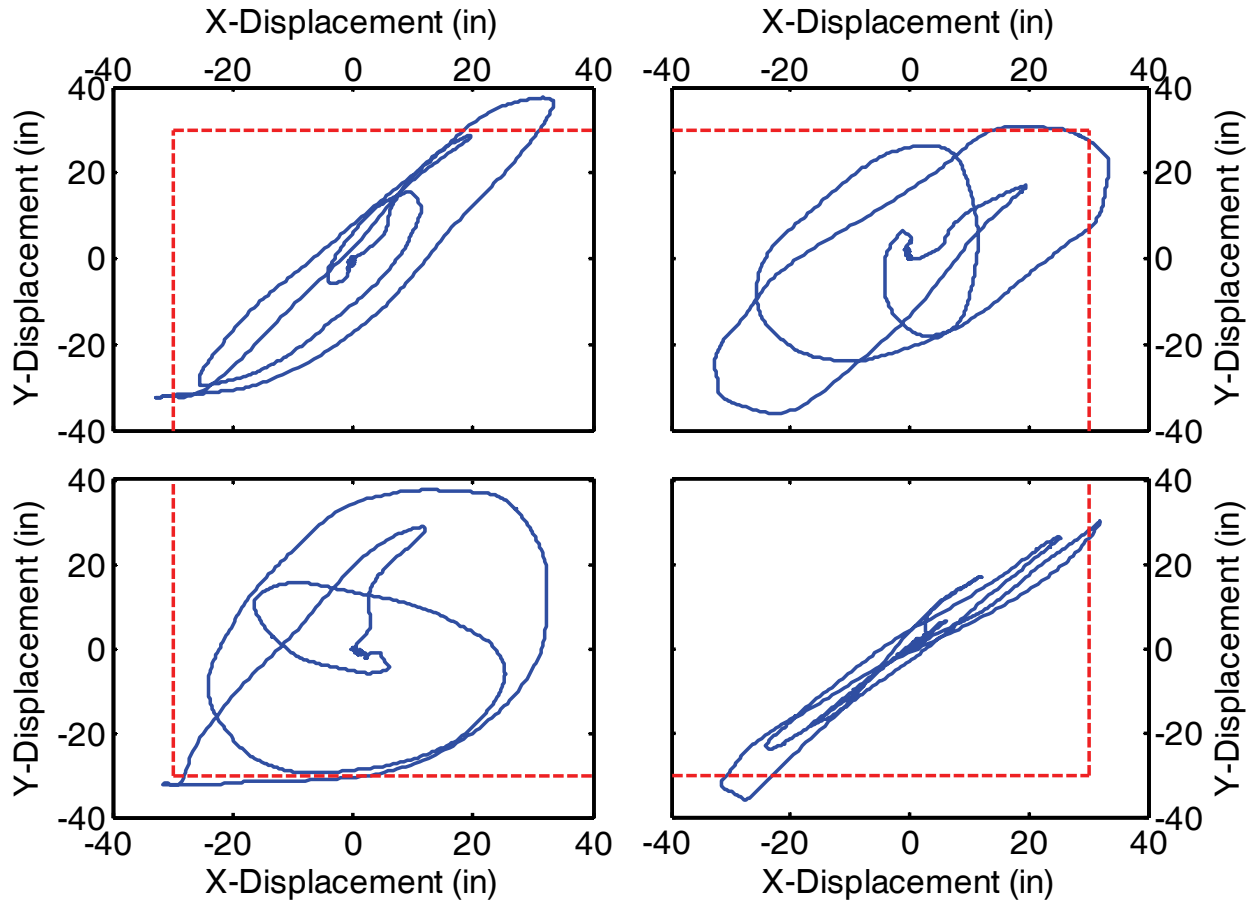


**Figure 7-17 Impact force in line 1 for OCBF model under GM9.**



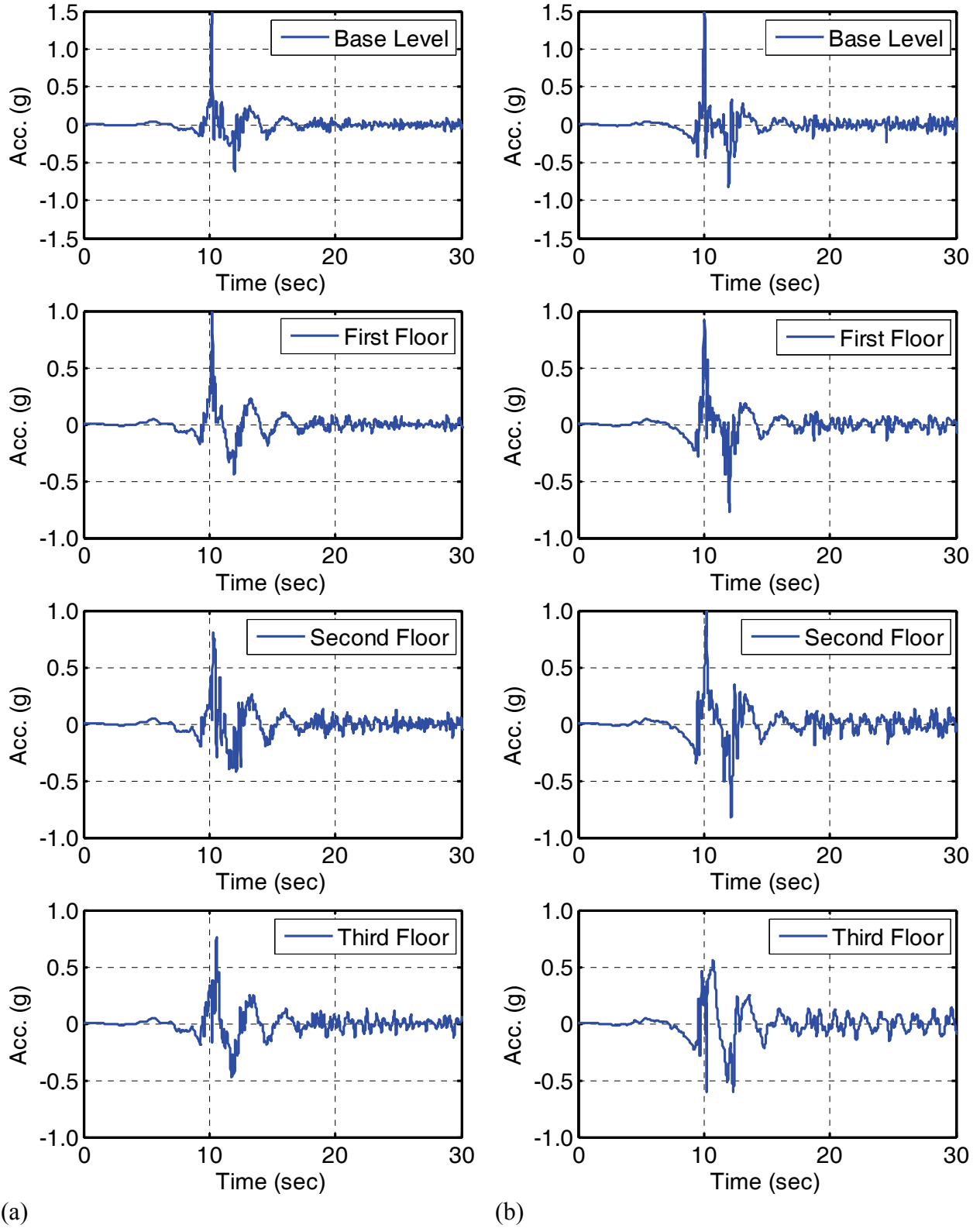
**Figure 7-18 Moat wall displacement in line 1 for OCBF model under GM9.**

The base level of isolated model is detached from moat wall in line 1 at time 10.15 sec which makes total contact duration of less than 0.5 sec. The base level continues moving in plane due to input motion resulting in pounding to moat wall in other directions. Figure 7-19 shows 4 corners of the base level displacement in X and Y direction. The moat walls are shown in this figure with dashed line. This figure shows the number of pounding at each corner and also the power of impact can be estimated by distance that base level moves beyond the gap distance. For example it can be concluded that impact force in Y direction at point A5 will be higher than force obtained from point G5 in the same direction since displacement beyond moat wall gap distance is larger at point A5 than G5.



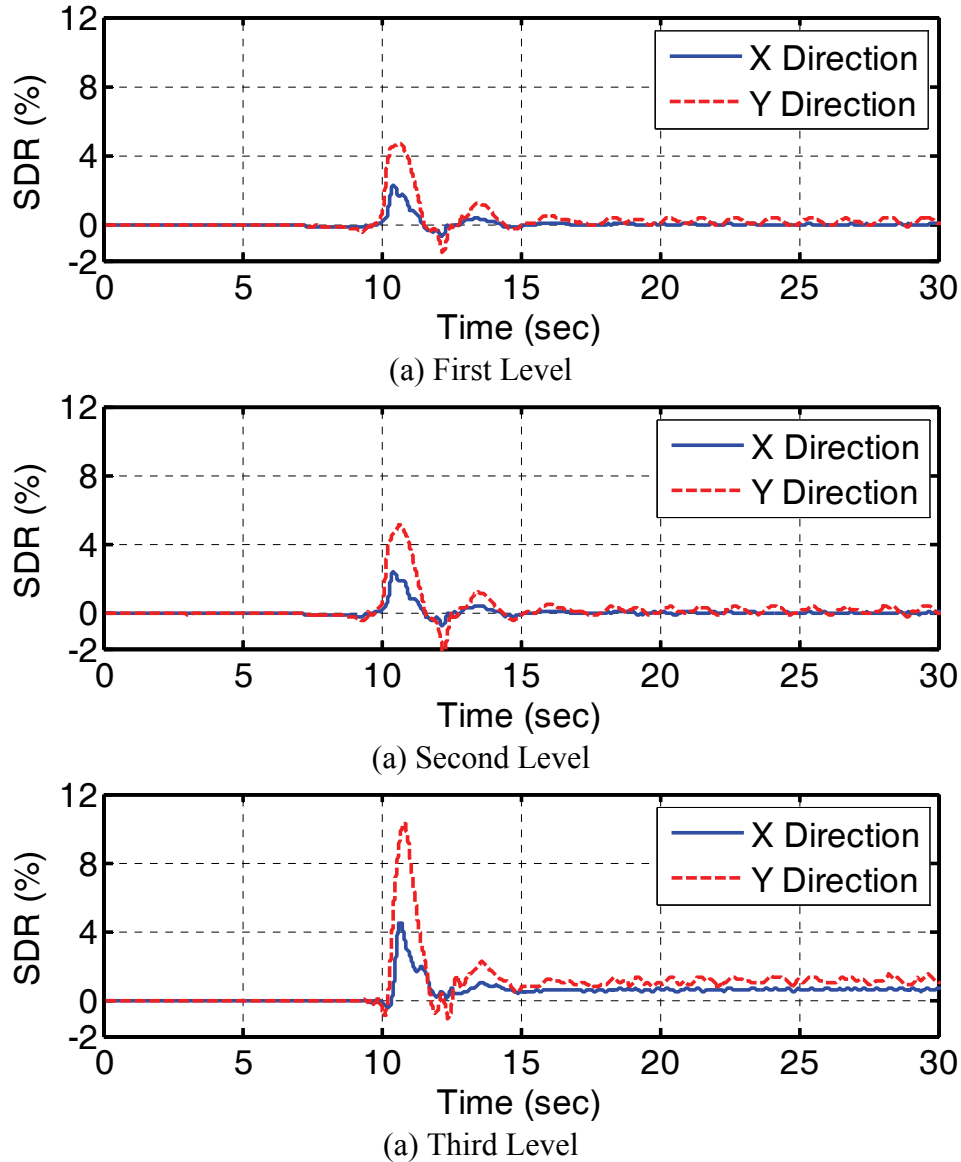
**Figure 7-19 Displacement of 4 corners of the base level for OCBF model under GM9.**

Pounding to moat wall would affect the acceleration and displacement response of the structure. Figure 7-20 shows the acceleration time history of each level of the structure under input motion GM9. Acceleration was recorded at master node at each level. Master node is defined at the node that total mass of that level is assigned to. This node is shifted from geometry center of the level by 5% of maximum plane dimension to include accidental eccentricity. It can be seen that acceleration is increased suddenly at the time of impact. This increase is more apparent at lower level than upper floors. This finding is in agree with experimental results in which increase in acceleration was more noticeable at lower level close to pounding point.



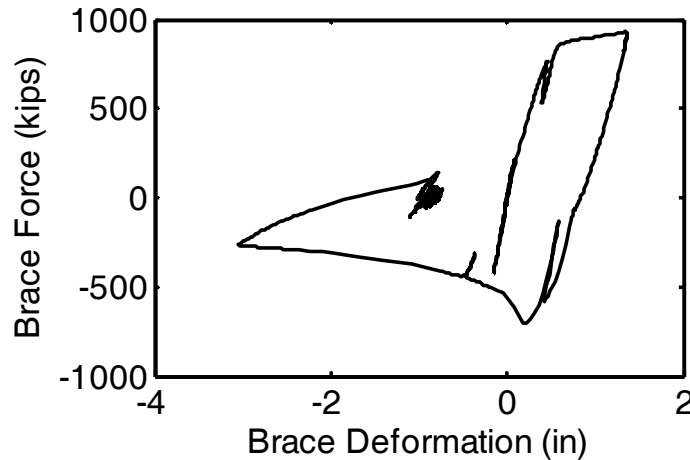
**Figure 7-20 Acceleration response for OCBF model (a) X direction (b) Y direction.**

Figure 7-21 shows the story drift ratio of OCBF model under input motion GM9. This figure shows that maximum SDR for OCBF frame is about 10% which shows almost 600% increase in compare with the case without moat wall. Increasing in SDR is one of the consequences of impact to moat walls which was obtained in experiment testing as well. The increase in SDR due to impact to moat wall is more significant in upper floors based on both experimental and numerical investigation.



**Figure 7-21 Story drift ratio for OCBF model under GM9.**

Large drift ratio in OCBF model is always accompanied by buckling in braces. Figure 7-22 shows the force deformation for second floor brace. Yielding in tension and also buckling of the brace in compression force is clear in this figure. Buckling in the brace yields to large deformation (up to 6 time of yielding deformation) in brace.



**Figure 7-22 Second floor brace force-deformation of OCBF model under GM9.**

### 7.5.2. Base Isolated IMRF Model

To examine the effect of impact to moat walls on the IMRF model, the behavior of the base isolated IMRF model with no moat wall was first studied under 20 ground motions at MCE level. Figure 7-23 shows the maximum base level master node and corner nodes in X and Y directions for each ground motion. The reference gap distance from ASCE 7-05 is shown by the dashed line (30 in.). It can be seen that only 5 ground motions induce master node displacements larger than 30 in. while 8 ground motions induce corner displacement more than the specified gap distance. The average (median in parentheses) of base level master node displacement is equal to 18.9 in (16.4 in) and 21.9 in (21.5 in) for X and Y directions, respectively. This parameter for corner nodes is equal to 21.7 in (19.5 in) and 26.3 in (25.2 in) for X and Y direction, respectively. It should be noted that master node and corner node average displacement is less than the estimated value ( $D_M$ ,  $D_{TM}$ ) based on static analysis. This analysis demonstrates that scaling ground motions to a specific target spectrum does not guarantee producing average displacement in dynamic analysis as it is highly dependent on the ground motions selected. The difference between code based estimated values propose for required

minimum gap distance for moat walls, and average maximum displacement of corner nodes under dynamic analysis to scaled ground motions offers some level of conservatism in an average sense to base isolated structures. More importantly, there may be a few ground motions which can exceed this average leading to pounding in isolated structures.

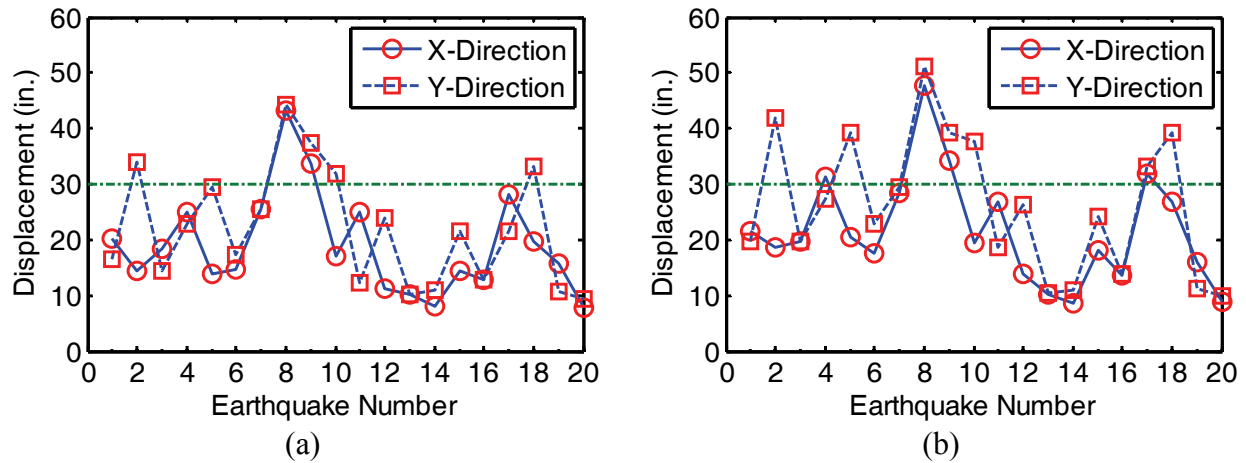


**Figure 7-23 (a) Base level master node displacement and (b) Base level corner node displacement for IMRF model without moat wall**

Installing the moat walls at 30 in gap distance ( $D_{TM}$ ) and repeating the dynamic analysis leads to pounding at the base level of the IMRF model to moat walls for those ground motions exceeding the clearance. The maximum impact force generated at impact is shown in Figure 7-24 for each earthquake record considered. The impact force reported is the maximum of total impact force generated on one side of the moat wall to the structure base level.

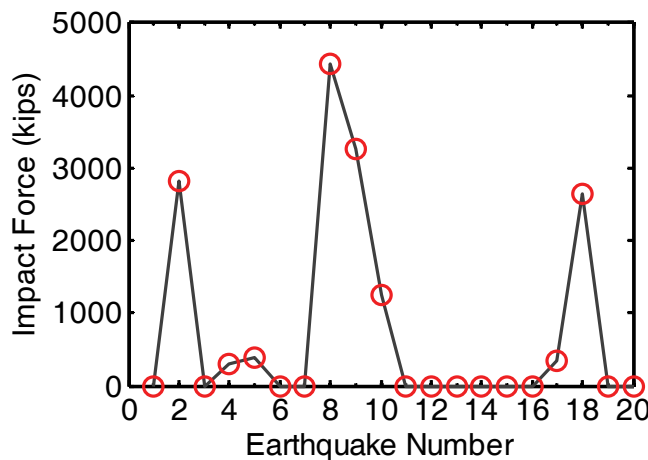


**Figure 7-24 Maximum impact force generated at IMRF model**

This figure also shows the occurrence of impact for each ground motion. As expected from Figure 7-23(b), only 8 ground motions induced pounding in the IMRF model considering corner displacements. The earthquakes with impact force equal to zero did not hit the moat walls at the base level. Figure 7-25 shows the base level displacement for the case that moat walls are installed at 30 in gap distance. When compared to Fig 1-17, this figure shows that large displacement in the isolation level were prevented by pounding to the moat walls, although in some cases the base level still moved beyond the gap distance by pushing back the wall and soil backfill. The maximum displacement beyond the gap distance was reduced to 6 in form 22 in for GM8. This large reduction in displacement correlates to the large impact force shown in Figure 7-24 for GM8.

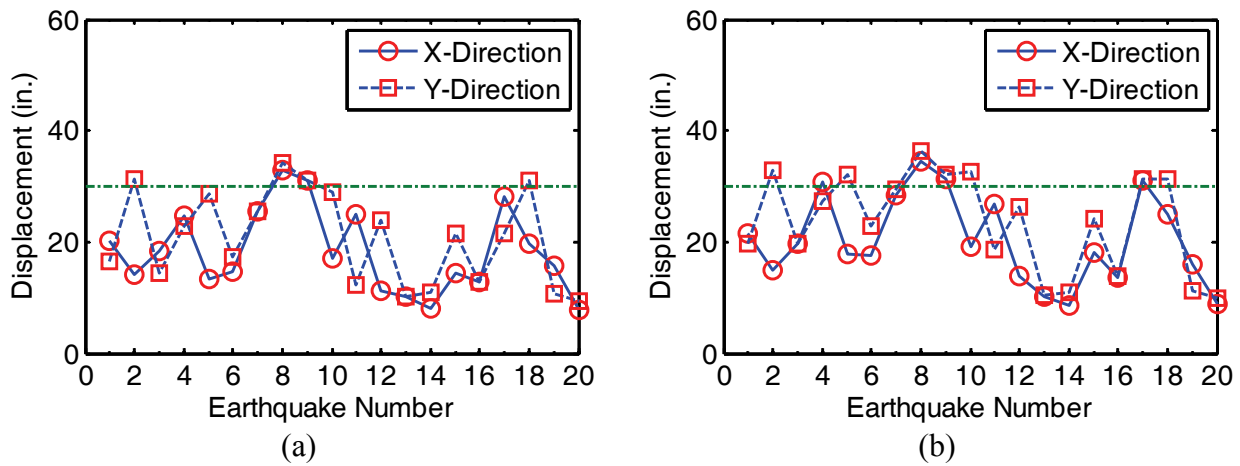


**Figure 7-25 (a) Base level master node displacement (b) Base level corner node displacement for IMRF model with wall**

Figure 7-26 shows the maximum vector summation acceleration for the master node in each floor and compares the results of the two cases with and without moat wall. It is obvious that results would be the same for the ground motions not inducing pounding to the moat wall. The acceleration is amplified in all levels of the structure due to moat wall pounding. The amplification factor decreases for higher story levels as observed in the experiments. The maximum acceleration amplification occurs at the base level, which is approximately equal to 6 for GM8. It should be mentioned that the results are presented for the master node at each floor, which is distant from location of impact (at the center of the mass in each level). The

acceleration presented in this figure represents the average acceleration for each floor. Acceleration amplification is expected to be higher for the nodes closer to impact region.

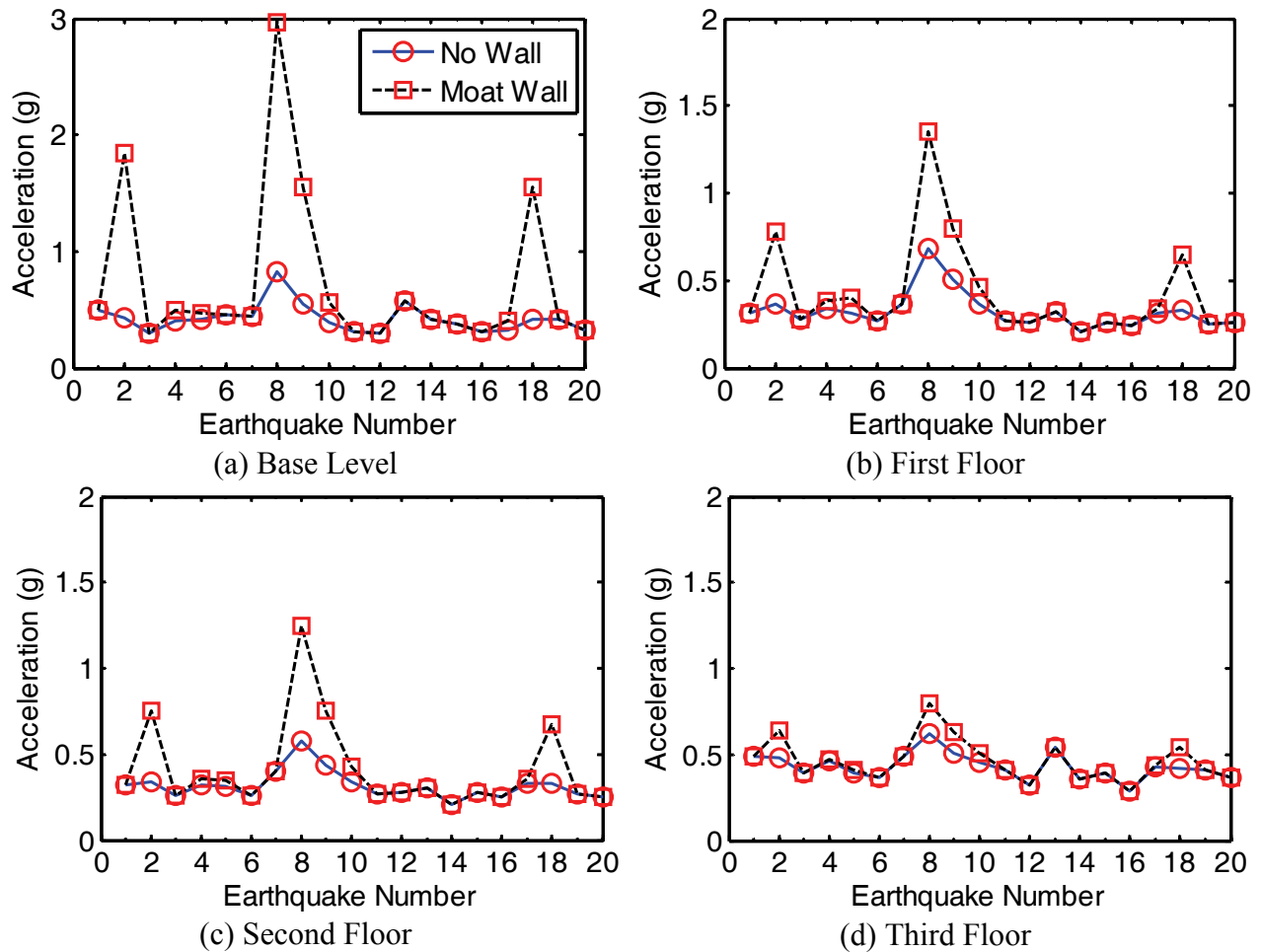


**Figure 7-26 Maximum master node acceleration of IMRF model**

Story drift ratio was evaluated separately in each direction as the maximum at any of the four corners of the building and is shown in Figure 7-28. Large SDR is obtained for the two records of GM8 and GM9 even for the case without moat wall. Defining 5% as SDR collapse criteria as suggested in (FEMA 1997) indicates that the base isolated structure without moat walls can potentially collapse under these two ground motions at MCE level. Two ground motions also induce large displacement at the isolation level resulting in unusual superstructure behavior. Sayani et al. (2011) examined carefully the behavior of the structure for these two records. This large displacement demand at the base level could be explained by looking at the average

displacement spectrum of the 20 ground motions and discrepancy between the SRSS displacement and these two outlier records at the period of the isolation system (3.1 sec). Figure 7-27 shows 5% damped SRSS x and y-component displacement spectra for the 20 ground motions. The differences between GM8 and GM9 displacement spectra and the mean 20 ground motions are obvious in this figure. Also, considering Figure 7-23, one can conclude that records GM8 and GM9 are the only ground motions that induce large displacement in both directions, unlike the other ground motions which have one weak component that compensates the other strong component. Looking into the time history response for GM8 reveals that the peak base displacements in both directions occur approximately at the same time, resulting in large vector summation of displacement. These results in high shear force simultaneously applied to the superstructure in both directions, leading to large drift ratios.

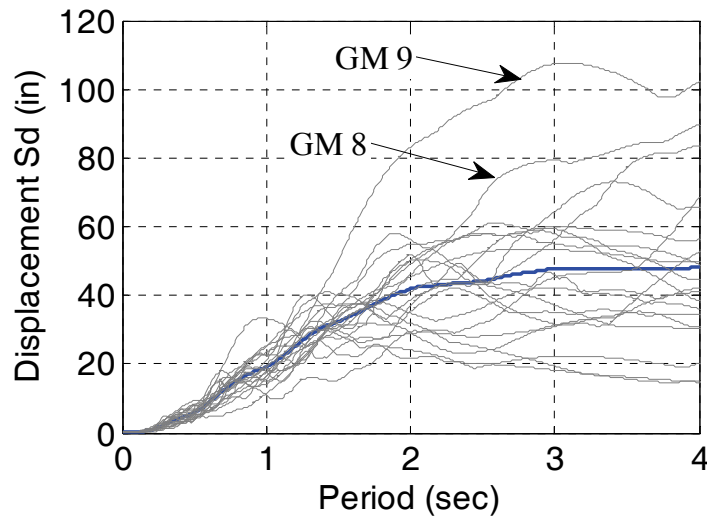


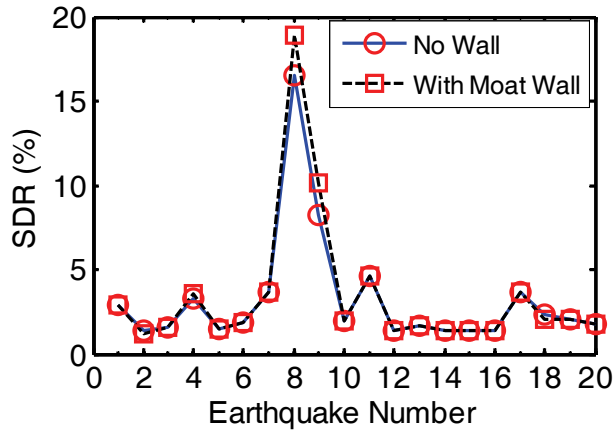
**Figure 7-27 SRSS of x and y-component displacement spectra for 20 ground motions**

The amplification in SDR is approximately distributed equally in all levels of the frame in each direction. The SDR was increased for two ground motion GM8 and GM9 in both directions of X and Y showing that for these two records impact occurred in both directions. Unlike, for two records of GM2 and GM18, pounding and thus amplification only occurred in the Y direction. For the other ground motions inducing pounding (GM4, 5, 10, and 17) the increase in drift ratio is insignificant and not clearly evident in this figure.

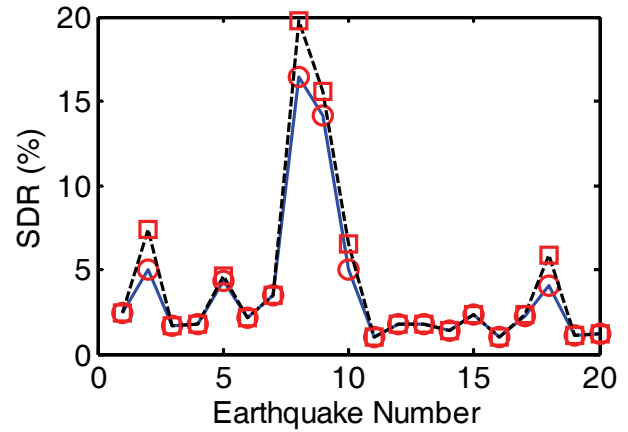
Plastic rotation demands were evaluated as the maximum over all pertinent elements at all levels. Figure 7-29 shows the maximum plastic rotation of beam and column element in IMRF model. As was expected from SDR comparison with and without moat wall analysis, the plastic hinge was not changed significantly. Regardless of the two extreme motions (GM8 and GM9), yielding is persistent because the IMRF has little reserve capacity.

Sayani et al. (2011) compared the response of the base isolated IMRF without moat wall with fixed base SMRF. They reported that for the design event, median story drift demands in the isolated IMRF are reduced on the order of 33–50% relative to the conventional SMRF, which is small compared with expectations set by previous studies. Although comparative studies often assume comparable natural periods, in this study, the IMRF without isolators is substantially more flexible than the conventional SMRF. Furthermore, the effective isolation period ( $T_D = 2.77$  s) exceeds the superstructure natural period ( $T = 1.4$  s) by less than a factor of 2 at the design displacement. Although the benefits of seismic isolation are reported in many studies, story drift reduction is not as significant here compared with ideal applications because of the moment frame flexibility. Therefore, significant structural participation in the first mode, leading to moderate story drift demands, is not surprising.

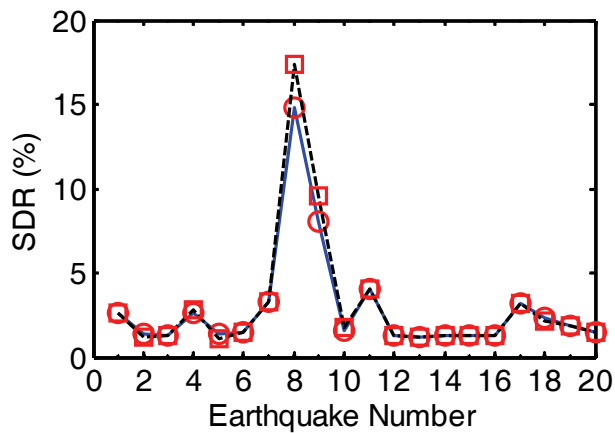
Sayani et al. (2011) compared the base isolated IMRF and fixed base SMRF response under design event (DBE) ground motions and concluded that although a minimally code-compliant IMRF design meets typical performance objectives for the design event, a more robust design is advisable if the response in a stronger earthquake is important. This conclusion becomes more vital by considering the effect of pounding of base isolated building to a moat wall for large displacements. Although pounding to a moat wall limits large displacements in the isolators, impact forces generated at the contact surface leads to increasing story drift ratios and acceleration in all levels of the structure.



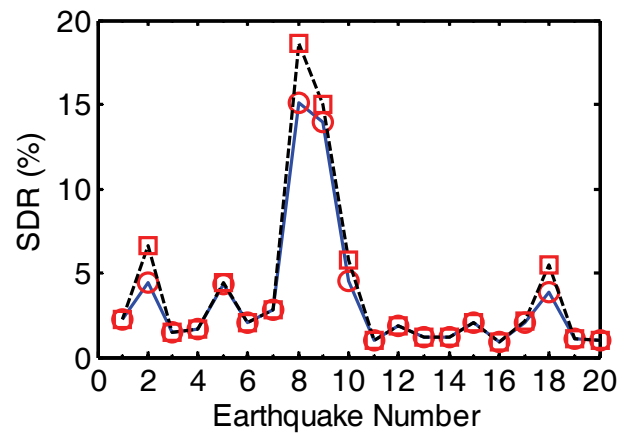
(a) Third Floor X Direction



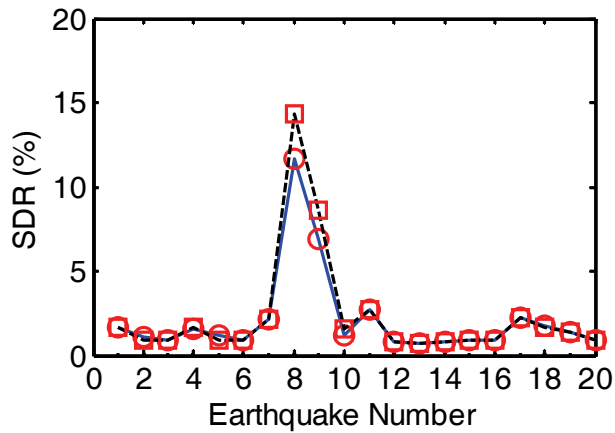
(b) Third Floor Y Direction



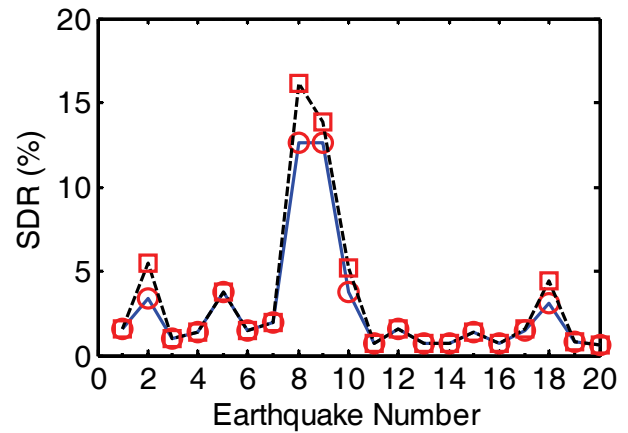
(c) Second Floor X Direction



(d) Second Floor Y Direction



(e) First Floor X Direction



(f) First Floor Y Direction

**Figure 7-28 Maximum story drift ratio (SDR) of IMRF model**

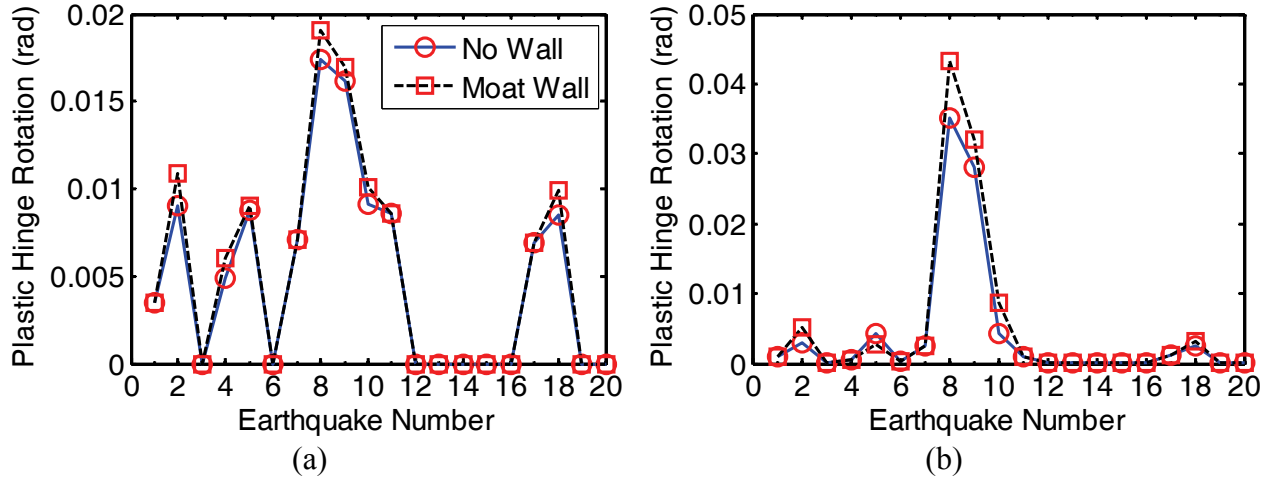
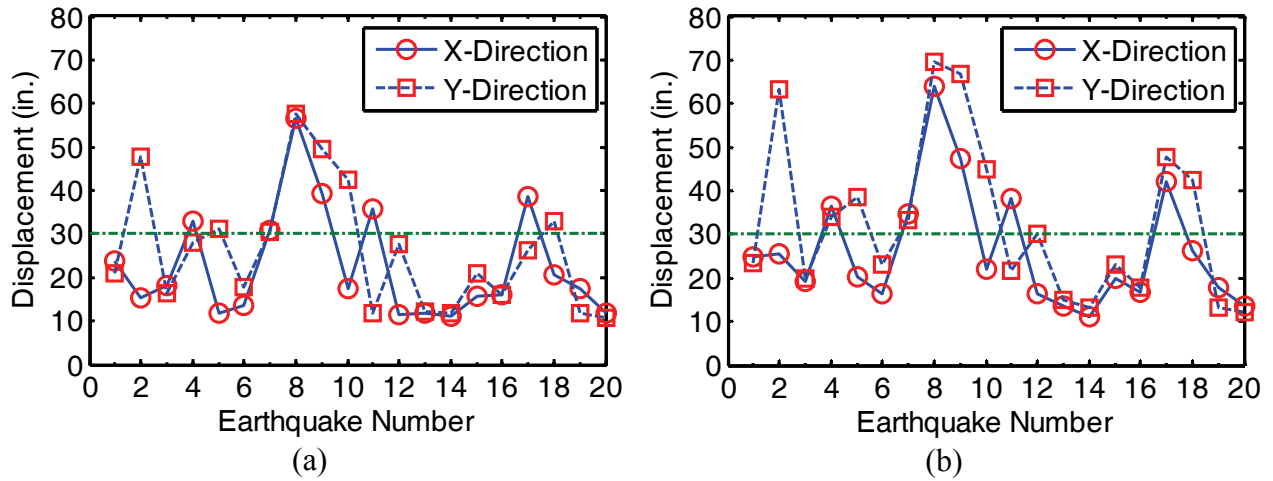


**Figure 7-29 Maximum plastic rotation of (a) Beam elements (b) Column elements of IMRF model**

### 7.5.3. Base Isolated OCBF Model

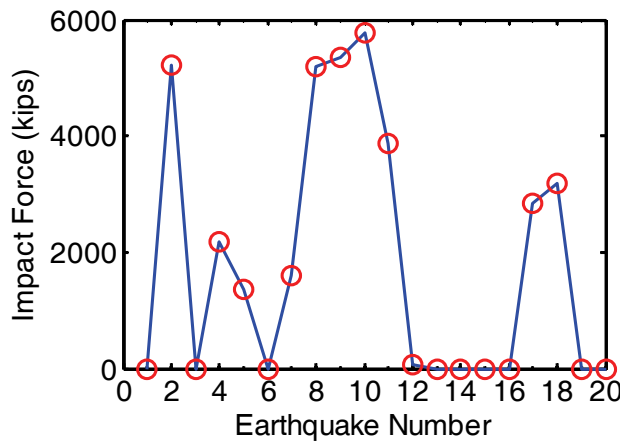
The response of base isolated OCBF model under 20 scaled ground motions was investigated in the presence of moat walls. The response of base isolated OCBF model would be of interest since unlike the IMRF model the superstructure is very stiff and adding base isolation leads to a period elongation of approximately 6. To examine the effects of impact to moat walls on OCBF superstructures, first the behavior of the base isolated OCBF model with no moat wall was studied under 20 ground motions at MCE level. Figure 7-30 shows the maximum base level master node and corner nodes in X and Y direction for each ground motion. The average (median in parentheses) of base level master node displacement is equal to 22.5 in (17.4 in) and 26.2 in (23.7 in) for X and Y direction, respectively. This value for corner node displacement is equal to 26.4 in (21.1 in) and 32.7 in (26.8 in) for X and Y direction, respectively. Comparing the base level displacement in OCBF and IMRF models reveals that the average (and also median) displacement in OCBF model is higher than IMRF building. Although the isolator period in both frames is very close, the base level displacement in OCBF is closer to those obtained from single degree of freedom analysis using displacement spectrum. This can be explained by considering flexibility in IMRF superstructure. The base isolated IMRF has a very flexible superstructure ( $T = 1.5$  sec) leading to high first mode participation in dynamic analysis, while base isolated OCBF has a very stiff superstructure ( $T=0.40$  sec) that behaves like a rigid mass on top of the isolation

system. In other words, the flexibility and deformations in the superstructure reduce the displacement demands on the isolation system.



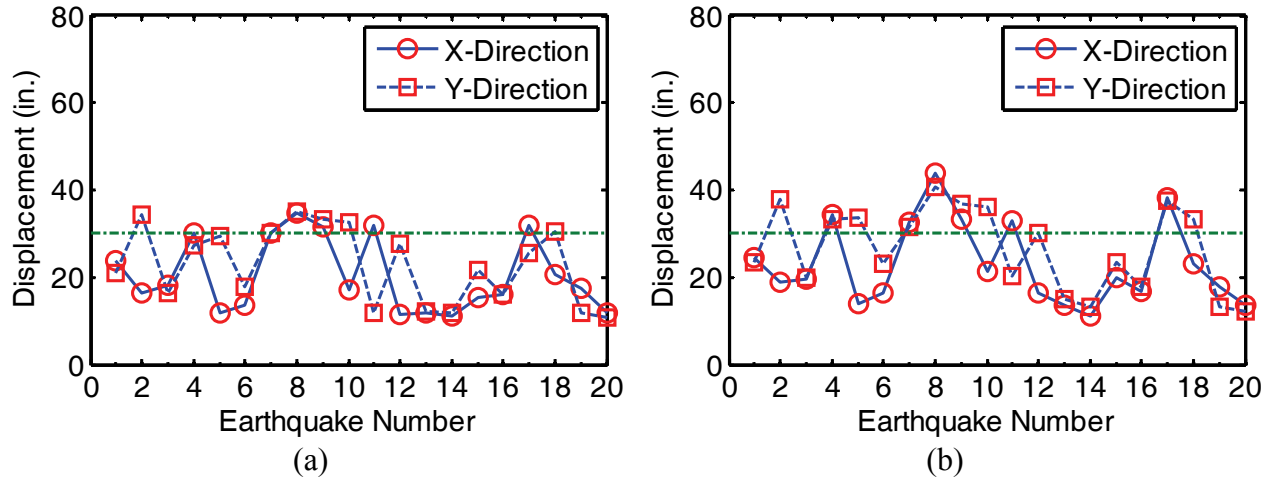
**Figure 7-30 (a) Base level master node displacement (b) Base level corner node displacement for OCBF model without moat wall**

Figure 7-30 shows that 11 ground motions lead to moat wall pounding at least in one direction. The maximum displacement beyond the gap distance for OCBF frame is obtained from EQ8 which is equal to approximately 40 in. Installing the moat wall at 30 in gap distance leads to the impact force shown in Figure 7-31.



**Figure 7-31 Maximum impact force generated at OCBF model**

Figure 7-32 shows the base level displacement for the case with moat walls installed at 30 in gap distance. This figure shows that installing moat wall at 30 in gap distance prevents large displacement at base level and bounds it to maximum 45 in for corner node under EQ8.



**Figure 7-32 (a) Base level master node displacement (b) Base level corner node displacement for OCBF model with wall**

The maximum total acceleration for the OCBF model was recorded at each level master node. The total mass for each floor was assigned to the master node of that level. Figure 7-33 compares maximum acceleration for each level for the two cases with and without moat wall. As expected from experimental tests and also results from the IMRF model, the acceleration increased because of impact to moat walls in all levels, although this amplification decays with distance from the source of impact (first floor). The average acceleration increased 140% for the base level of OCBF model while the third floor shows 26% increase for average acceleration.

Figure 7-34 shows the maximum SDR obtained considering corner nodes in both horizontal directions for OCBF model. The performance of base isolated OCBF without moat walls is good. The maximum SDR for all levels remain less than 2% except under GM8 that shows large SDR.

Installing moat walls at 30 in gap distance leads to increase in SDR for all levels of the model. This amplification in response is more obvious in upper levels. The average SDR increase is 400% in third level as a result of pounding to moat walls. This unacceptable response of the base isolated OCBF model is verified by investigating the number of braces buckled under each

ground motion for the two cases with and without moat walls. It should be recalled that there are 16, 8, and 8 braces in the first, second, and third level of OCBF model, respectively. Figure 7-35 shows the number of buckled braces for each level separately. It can be seen that brace buckling is observed in only 1 of 20 ground motions (GM8) when the moat wall is not included, but braces buckle in 6 of 20 ground motions because of pounding to moat walls. Buckling of the braces results in increasing the SDR at that level.

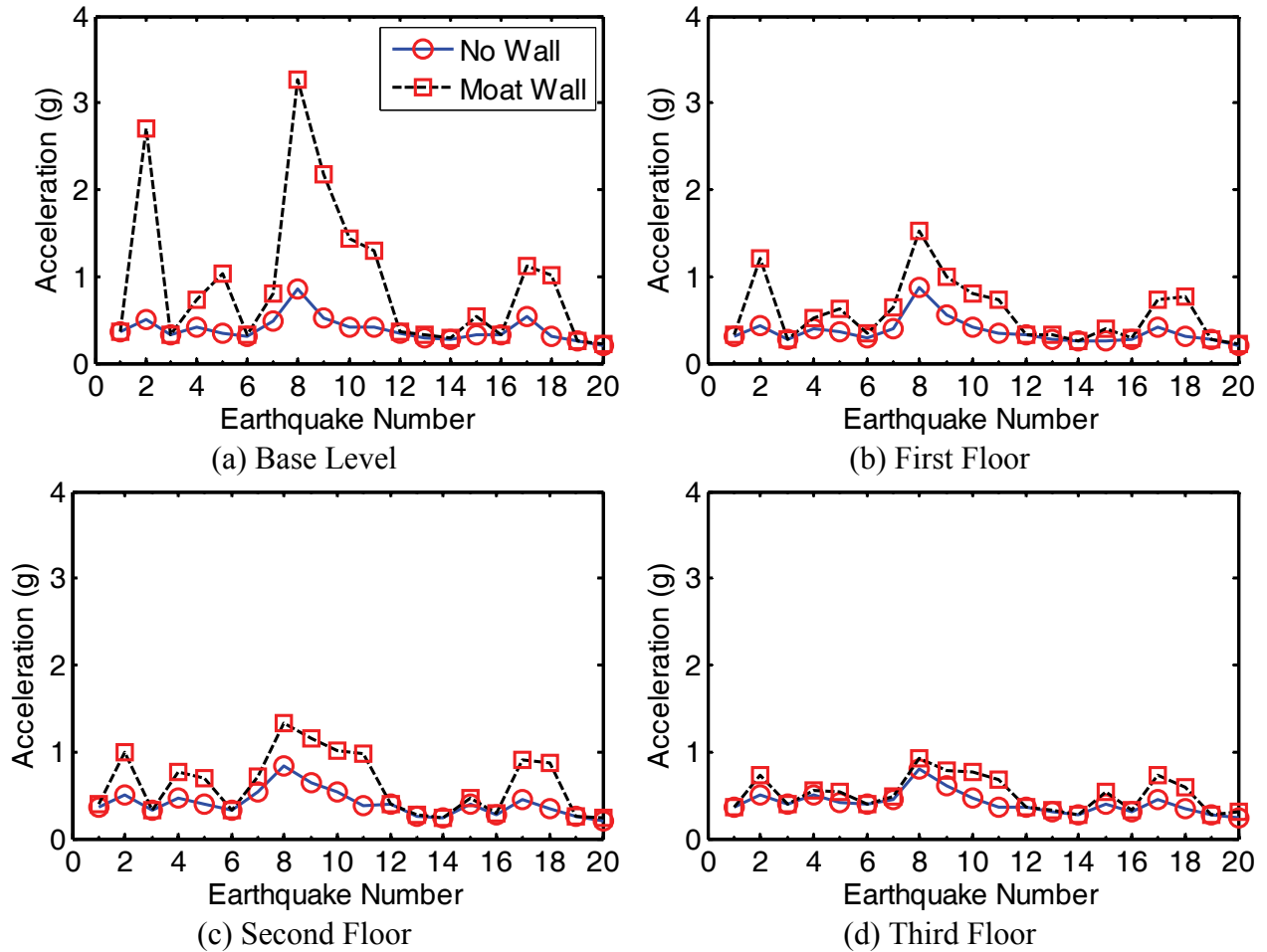
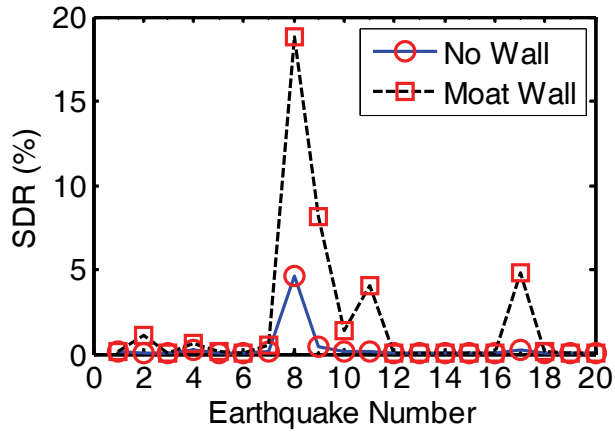
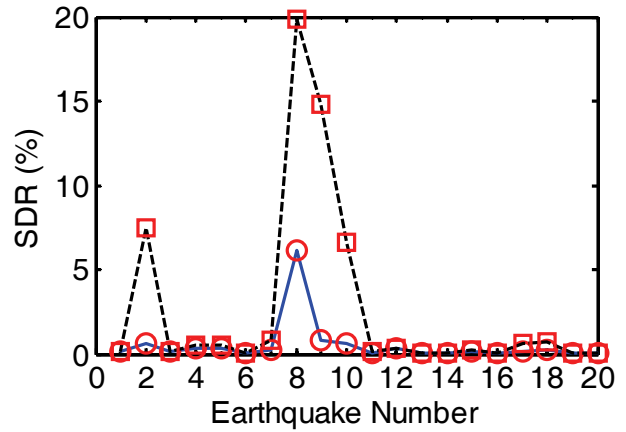


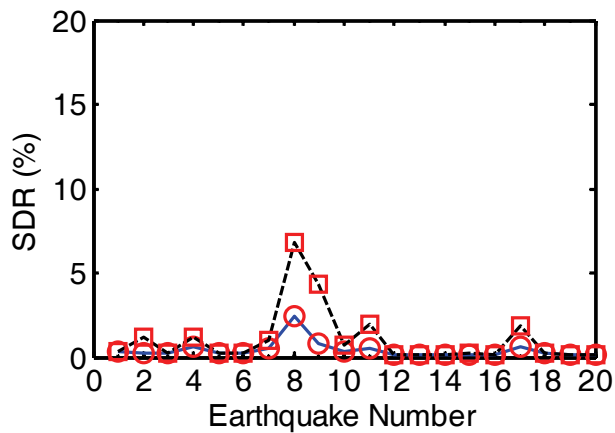
**Figure 7-33 Maximum master node acceleration of OCBF model.**



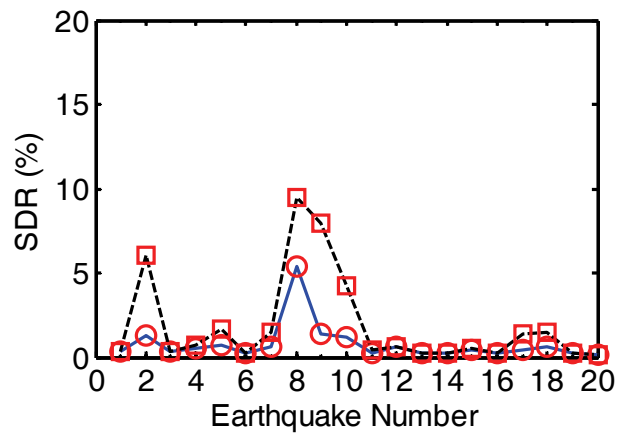
(a) Third Floor X Direction



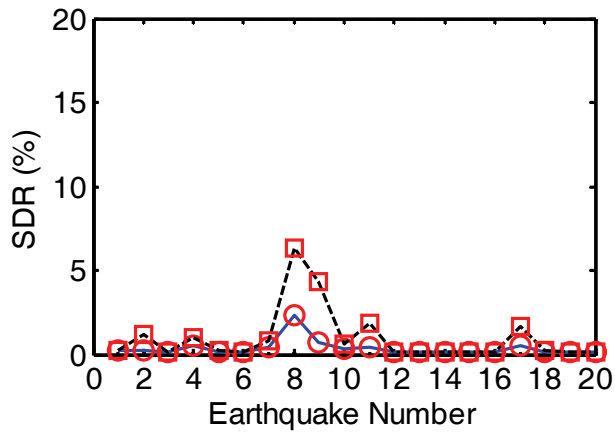
(b) Third Floor Y Direction



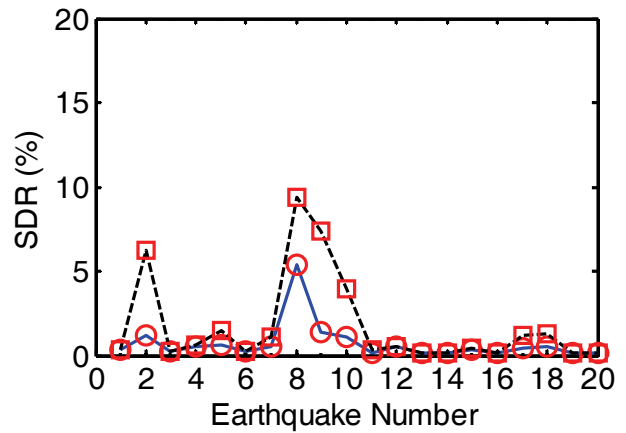
(c) Second Floor X Direction



(d) Second Floor Y Direction



(e) First Floor X Direction



(f) First Floor Y Direction

**Figure 7-34 Maximum story drift ratio (SDR) of OCBF model**

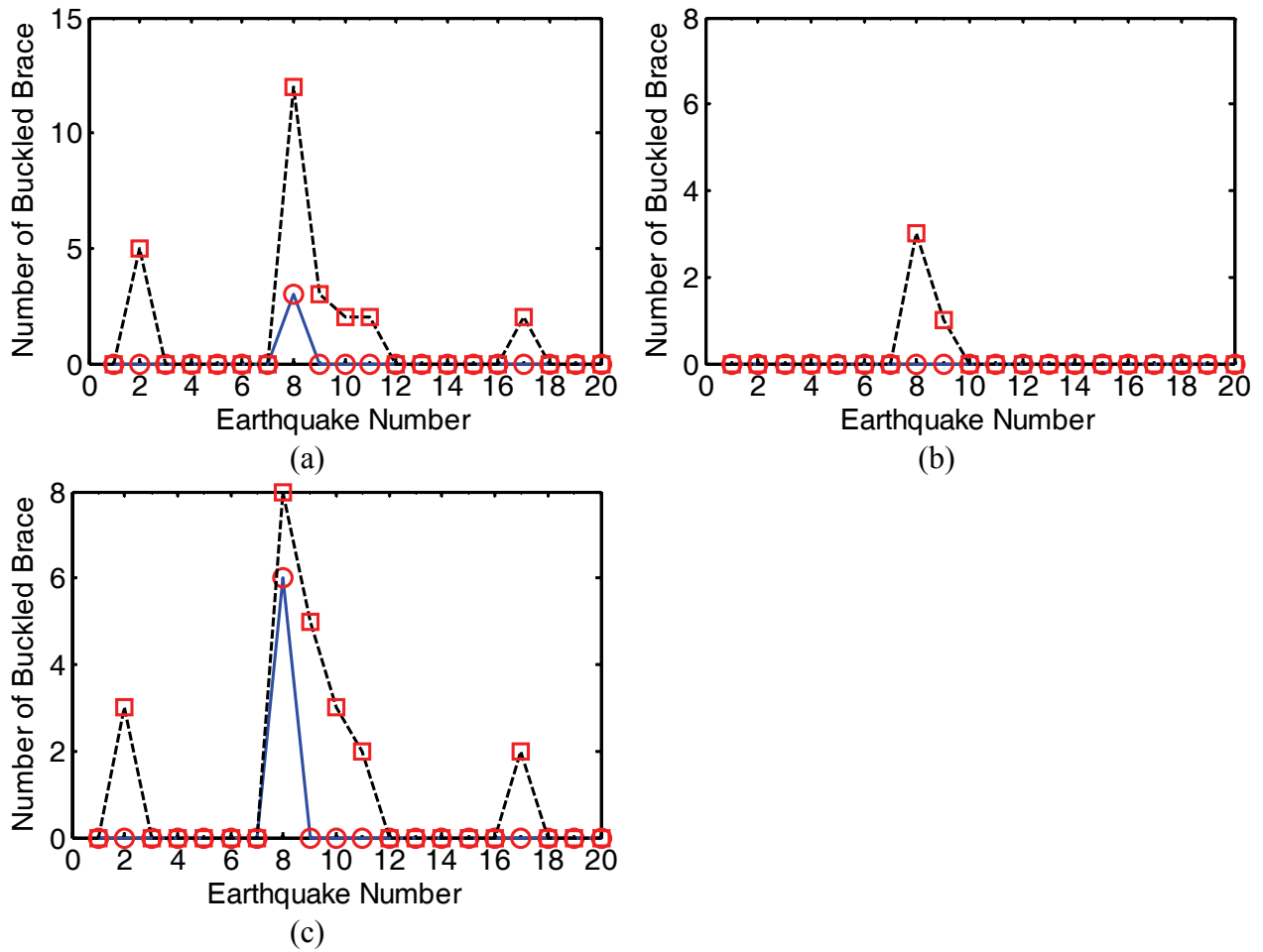


**Figure 7-35 Number of buckled braces (a) First floor (b) Second floor (c) Third floor of OCBF model**

Plastic hinge rotation at the end of beams and columns are shown in Figure 7-36. Plastic hinges were formed only under GM8 without moat walls, while significant plastic hinge rotation was observed under most of ground motions inducing pounding to moat walls. The average beam and column plastic rotation increased 900% and 800% because of pounding to moat wall.

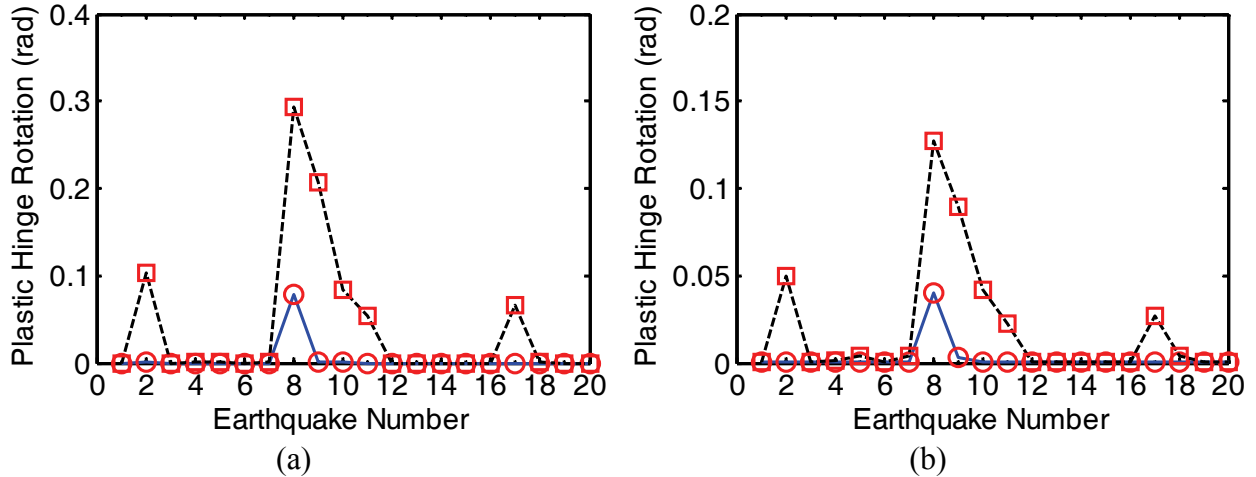


**Figure 7-36 Maximum plastic rotation of (a) Beam elements (b) Column elements of OCBF model**

#### 7.5.4. Base Isolated IMRF and OCBF Comparison

Both base isolated IMRF and OCBF models were designed for the same hazard level and location although the IMRF model was designed for response modification factor of 1.67 and the OCBF model was designed for  $R=1$ . A higher  $R$  for IMRF model resulted in a more flexible superstructure in comparison with the OCBF. The superstructure first mode period for the IMRF and OCBF models are 1.4 and 0.4 sec. The isolation system was designed for approximately the same period and damping ratio for both systems (3.1 sec and 15% at MCE level). This leads to period shifting factor of 2.1 and 7.75 for IMRF and OCBF models, respectively. Larger period shifting is desirable based on base isolated design philosophy for further reduce seismic design forces.

The following results were concluded for the case that the moat wall was not modeled in dynamic analysis under 20 ground motions scaled to MCE level. The  $R=1$  design with overstrength has been shown to keep the isolated OCBF nearly elastic and prevent buckling of the braces. Median story drifts remain small and floor accelerations are held within about 0.5g although PGA is on the order of 1g to 1.5g. Braces do not appear to buckle (except one case), and only small plastic rotations develop. The observed overstrength of the OCBF helps to maintain solid performance of the structural system in MCE event.

On the other hand, the IMRF model was damaged even without moat walls. Although the isolation system is very effective in limiting total floor accelerations to levels well below the PGA, large story drift ratios were recorded specially for outlier ground motions. Although the design objectives for the isolated IMRF have been basically met (Sayani et al. 2011), for the design event (10/50 year), the flexibility of the moment frame leads to significant structural participation in the first modes of the isolated IMRF and larger relative story drifts compared with the idealized (stiff) structural systems at MCE level.

Higher participation of the first mode of the IMRF model resulted in reducing maximum base level displacement demand in comparison with equivalent single degree analysis. Stiff behavior of the OCBF model leads to larger displacement at base level resulting in stronger pounding to moat walls.

Installing the moat wall at 30 in. gap distance (equal to  $D_{TM}$  for both models) resulted in pounding of base level to moat walls in 8 and 11 ground motion for IMRF and OCBF models. Since the average base level displacement for both models calculated by dynamic analysis under 20 ground motions scaled to MCE spectrum is less than  $D_{TM}$  calculated by static design procedure, using 30 in gap distance (equal to  $D_{TM}$  for both models) is reasonable. The average impact force generated is equal to 2000 and 3300 kips for ground motions inducing pounding in IMRF and OCBF, respectively.

Seismic responses, when sampled over many motions, are widely accepted to follow a lognormal statistical distribution. As such, the median and dispersion of the lognormal data, defined as

$$\mu = \exp \left[ \frac{\sum_{i=1}^n \ln x_i}{n} \right], \quad \zeta = \left[ \frac{\sum_{i=1}^n (\ln x_i - \ln \mu)^2}{n - 1} \right]^{1/2} \quad (7-5)$$

are generally used to describe the central tendencies and variability of the response quantities for different ground motion sets. The median plus one standard deviation, or 84 percentile values, were computed as  $\mu \cdot \exp(\zeta)$ .

Median and 84% of story drift ratio and acceleration for both IMRF and OCBF models are shown in Figure 7-37 and Figure 7-38. Story drift ratio was evaluated as the maximum drift among the four corners of the building. These parameters are compared for the two cases with and without moat wall to show the effect of pounding.

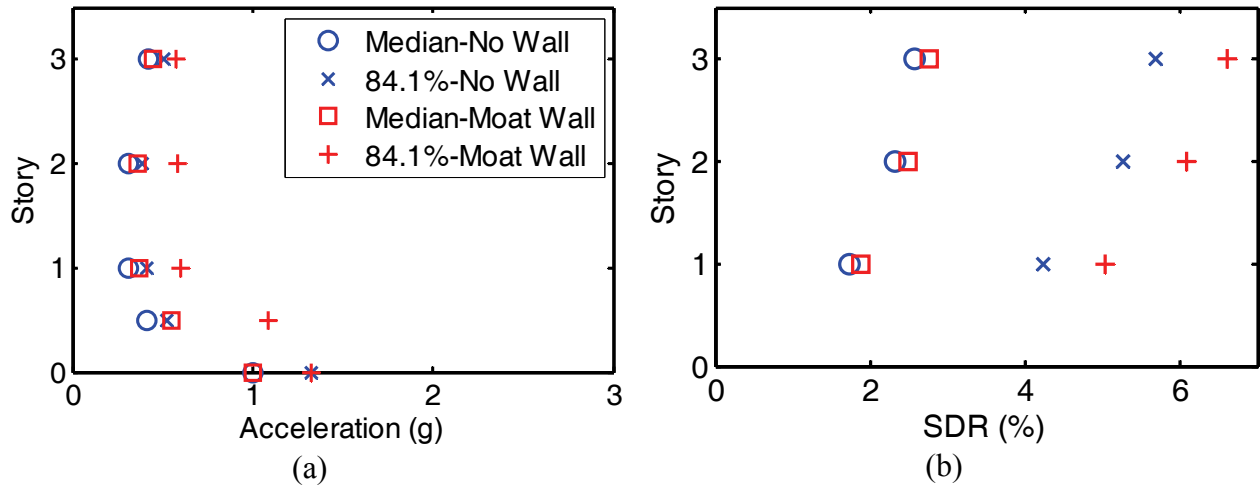


**Figure 7-37 Median and 84% of (a) Acceleration (b) SDR for IMRF model under 20 ground motions**

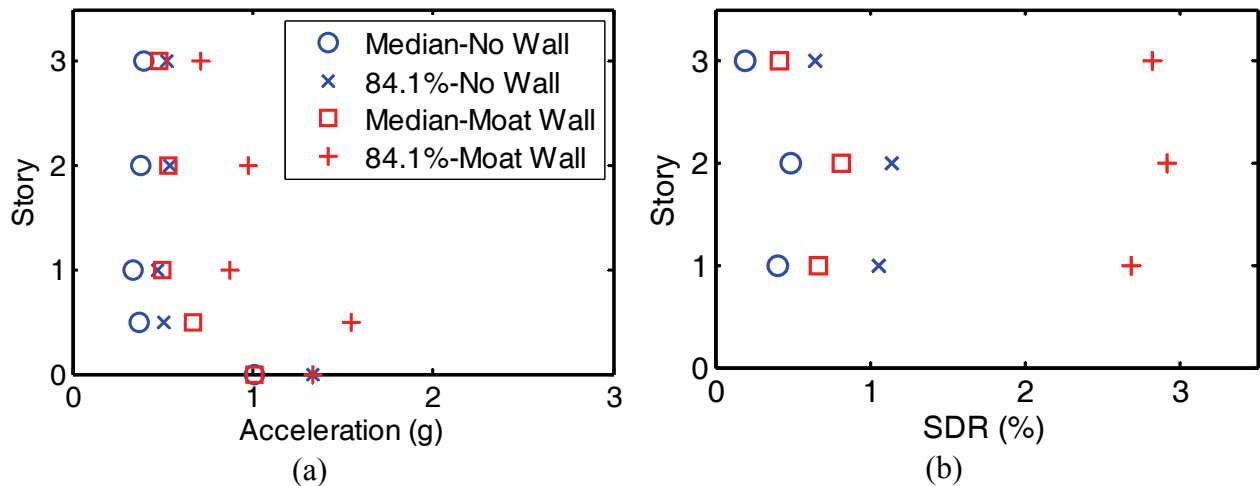


**Figure 7-38 Median and 84% of (a) Acceleration (b) SDR for OCBF model under 20 ground motions**

Both frames show that the median floor accelerations are held within about 0.5g without moat walls although median PGA is on the order of 1g. Pounding to moat walls increases the acceleration in all levels especially in lower levels. The median floor acceleration does not show

significant increase although 84% value shows 200% increase in base level and approximately 80% increase in floor levels. The average value remains the same because of the fact that in many ground motions no pounding occurs but 84% value increases a lot since the ground motions pounding to moat wall contribute a significant deviation from the average.

Large median and 84% SDR in IMRF model for the case without moat wall verifies the effects of the flexible superstructure. The 84% value SDR in IMRF model is almost 2-3 times larger than median value showing the effect of outliers (GM8 and GM9). Unlike the IMRF model, OCBF model shows very stiff behavior. The median SDR value is on the order of 0.5 to 0.9% with smaller dispersion. Pounding to moat walls increases SDR in all levels especially in upper floors. The effect of pounding on median SDR is more clear for OCBF model because of the fact that 11 out of 20 ground motions induce pounding to moat walls in OCBF model while 8 out of 20 ground motions pound in the IMRF model. The flexible superstructure of the IMRF model leads to large SDR even in cases without moat walls. When the moat walls are added, the SDR increases only slightly, but as a percentage it is less significant compared to the OCBF. A larger increase in SDR response for the OCBF frame is obtained that is likely due to the larger number of ground motions inducing pounding, stiffer and non-ductile superstructure frame. Stiff superstructure in OCBF frame also results in larger displacement demand at the base level inducing stronger pounding to moat walls in compare to IMRF model.

As expected, larger dispersions are obtained in both acceleration and SDR for the cases with pounding in comparison with the case without moat walls. This shows that the response of the models worsens for the case of pounding to moat walls, inducing sudden increased accelerations and drifts.

As mentioned earlier two ground motions (GM8 and GM9) induced very large displacement at the isolation level, resulting in unusual superstructure behavior. This large displacement demand at the base level, which is more than twice as the median displacement demand in the other 18 ground motions resulted in large uncertainty in the average superstructure response of the 20 ground motions and discrepancy between the median and 84% response. The response of these two motions was removed from the statistical study to have more reliable median and 84% response without consideration of these outliers. The median and 84% response of both the

IMRF and OCBF models are re-plotted in Figure 7-39 and Figure 7-40 removing the response of 2 ground motions GM8 and GM9.

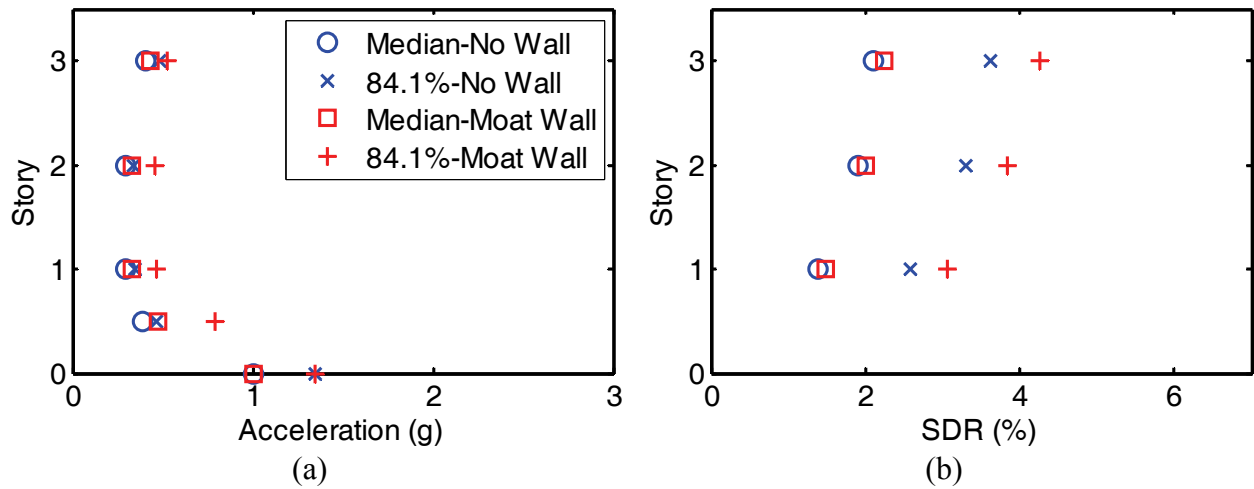


**Figure 7-39 Median and 84% of (a) Acceleration (b) SDR for IMRF model under 18 ground motions**

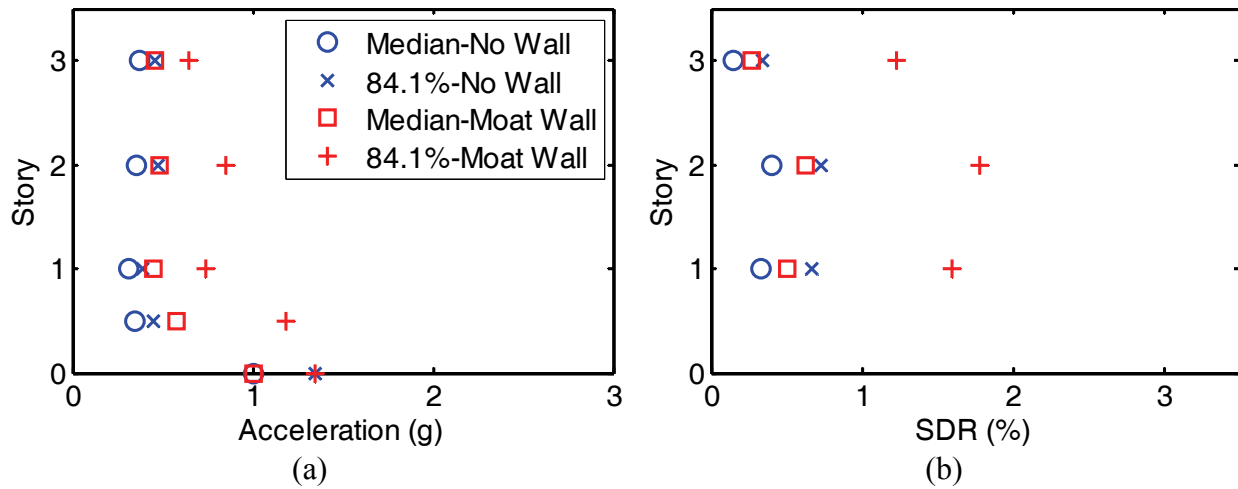


**Figure 7-40 Median and 84% of (a) Acceleration (b) SDR for OCBF model under 18 ground motions**

Removing the 2 outlier ground motions from statistical studies results in decreasing the median and 84% of both acceleration and SDR in both cases with and without moat wall. The differences between the median and 84% response was also reduced.

In summary, the response of a minimally code-compliant IMRF without considering potential impact to moat walls is not satisfying at MCE event and pounding to moat walls worsen this

situation. A more robust design is advisable for this model if the response in a rarer earthquake is important. One suggestion in this regard could be designing a stiffer superstructure which leads to larger period shifting by considering the base isolation system or decreasing R factor to design for higher base shear. Although the response of the isolated OCBF is favorable compared with the IMRF for the case without moat walls, wherein the median demands for story drifts are substantially lower than those of the IMRF, pounding to moat walls make a significant change in this behavior resulting in large median SDR with huge dispersions. Brace buckling and significant inelastic response were observed in all the motions inducing pounding to moat walls. One might conclude that pounding to moat walls worsens the response of both frames in terms of both acceleration and SDR, although this effect is worse for stiff OCBF frame.

## **SECTION 8**

### **COLLAPSE EVALUATION OF SEISMICALLY ISOLATED STRUCTURE CONSIDERING POUNDING TO A MOAT WALL**

#### **8.1. Introduction**

The 3D prototype building model described in Section 3 was further investigated under extreme ground motions considering the potential for impact to a moat wall. The response of the base isolated model with and without moat wall was compared to evaluate the effects of impact on the collapse capacity of the structure for ground motions of increasing intensity. However, the response of the model due to impact to the moat wall is under influence of the ground motions intensity and moat wall gap distance. A series of collapse studies using the fragility curve concept was conducted for both prototype models and for various gap distances.

In order to assess the behavior and collapse capacity of base isolated structures considering pounding to a moat wall, the Methodology proposed in FEMA P695 (FEMA 2009b) was implemented. This Methodology uses Incremental Dynamic Analysis (IDA) (Vamvatsikos et al. 2002) to estimate the median collapse spectral acceleration and then computes the probability of collapse at MCE level. The average of this probability should be less than 10% for a set of archetype models and less than 20% for each archetype model.

The objective of this section is to evaluate the collapse probability of the base isolated models used in this study and also investigate the effect of moat wall gap distance on the probability of collapse for base isolated structures. The adequacy of minimum moat wall gap distance required by ASCE 7-05 is investigated. For this purpose, the numerical models developed in section 7 were used and the ground motion set presented in FEMA P695 was replaced by the ground motion set described in Section 3.

#### **8.2. Background Study and Objectives**

Chapter 10 in FEMA P695 examines the collapse probability of base isolated structures. In this study, 2D models of 4-story reinforced concrete structures designed for various base shear and ductility demand and different moat wall gap distance were developed and the collapse capacity was investigated. Although different archetypes for superstructure models were investigated,

only one moat wall model type was used consisting of 5 bilinear springs to capture the nonlinear impact forces. Figure 8-1 shows the moat wall force-displacement model used in the FEMA P695 (FEMA 2009b) case study. Gap spring properties are defined relative to the strength of the superstructure such that the moat wall force is equal to the strength of the superstructure,  $V_{max}$ , at approximately 4 inches of moat wall displacement. No detailed information on the development of the proposed moat wall model was reported, but it does include some key features such as nonlinear behavior for impact and energy loss during pounding. However, the lack of background, particularly experimental validation, for the proposed moat wall model serves as motivation to re-examine moat wall impact behavior using the model proposed in this report. An important aspect to consider in the FEMA P695 model is that no capping force was defined for the moat wall resistance, which leads to the transfer of increasingly large force to the structure for increasing earthquake intensities.

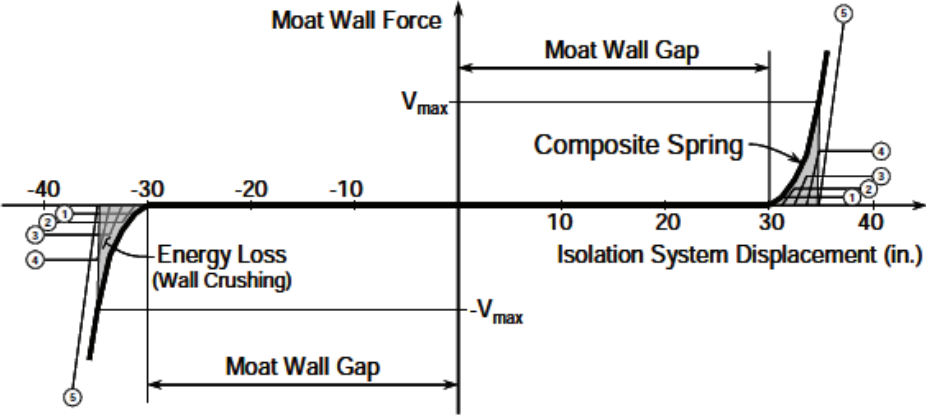


**Figure 8-1 Moat wall force displacement model used in FEMA P695 case study (FEMA 2009b).**

Another important issue to mention is that the FEMA P695 case study was conducted on 2D models. As shown in section 7, many of the ground motions that led to pounding initiate at corner points of the base level due to torsion. This shows the importance of considering 3D modeling for improved accuracy. In addition, the moat wall model proposed here considers the effects of bending failure in moat wall as well as effect of soil backfill.

In summary, this section is intended to assess the validity of current design requirement for moat wall gap distance of base isolated structures utilizing the Methodology proposed in FEMA P695 with the moat wall model proposed in this report. It is important to mention that this study is not intended to modify or propose a new response modification factors for base isolated structures as is intended in FEMA P695 since only a limited number of buildings models and gap distance combinations are examined.

### **8.3. Scope of the Collapse Evaluation Methodology Proposed by FEMA P695**

The Methodology proposed in FEMA P695 for collapse evaluation of a single model is summarized and simplified in this study. Although the Methodology proposed in FEMA P695 is intended to quantify the building system performance and response parameters for use in seismic design, it can also be used to evaluate the probability of collapse for a given building model as it is implemented here.

The Methodology for a given building model includes the following steps:

1- Develop model: In this step, a numerical model for the given building is developed consisting of a detailed finite element model suitable for nonlinear time history analysis. Numerical models should directly simulate all significant deterioration modes that can contribute to the collapse behavior. Typically, this is accomplished through structural component models that simulate stiffness, strength, and inelastic deformation under reverse cyclic loading. In cases where it is not possible to directly simulate all significant deterioration modes contributing to collapse, non-simulated collapse modes can be indirectly evaluated using alternative limit state checks on structural response quantities measured in the analyses.

2- Analyze model: Collapse assessment can be performed using both nonlinear static (pushover) and nonlinear dynamic (response history) analysis procedures. The nonlinear response is evaluated for a set of pre-defined ground motions that are used for collapse assessment of all systems. The ground motion set includes 22 ground motion record pairs from sites located greater than or equal to 10 km from fault rupture, referred to as the “Far-Field” record set. It is important to mention that this Methodology is different from IDA analysis in the sense that there is no need to conduct full IDA analysis in order to plot fragility curve and the median collapse

capacity,  $\hat{S}_{CT}$ , is the only parameter needed from IDA analysis. The median collapse capacity,  $\hat{S}_{CT}$ , is defined as the minimum ground motion intensity that leads to the collapse of the model under half of the ground motions. These two methods are also different in terms of scaling the ground motions. While IDA (Vamvatsikos et al. 2002) requires scaling each ground motion pair with a unique scaling factor to match spectral acceleration at a specific period (i.e. first mode period) to a target response spectra, the Methodology requires that normalized ground motion set to be scaled with one scaling factor to match the median of the ground motion set to a target spectra at the specified period.

3- Evaluate performance: The results from nonlinear static analyses and nonlinear dynamic analyses are used to evaluate the acceptability of the calculated collapse margin ratio (CMR), which is the ratio of the ground motion intensity that causes median collapse,  $\hat{S}_{CT}$ , to the MCE ground motion intensity defined by the building code,  $S_{MT}$ . CMR obtained from numerical analysis is adjusted by a Spectral Shape Factor (SSF) to include the effect of spectral shape of the applied ground motions. The SSF depends on fundamental period and period-based ductility,  $\mu_T$ , of the model. Acceptability is measured by comparing the adjusted collapse margin ratio (ACMR) to acceptable values that depend on the quality of information used to define the system, total system uncertainty, and established limits on acceptable probabilities of collapse.

In this Methodology, it is suggested that the probability of collapse due to Maximum Considered Earthquake (MCE) ground motions be limited to 10%. Each performance group (including different archetypical of the model) is required to meet this collapse probability limit, on average, recognizing that some individual archetypes could have collapse probabilities that exceed this value. A limit of twice that value, or 20%, is suggested as a criterion for evaluating the acceptability of potential “outliers” within a performance group.

#### **8.4. Approach and Assumptions**

The important assumptions and approach to apply the Methodology on the prototype structure is described in this subsection.

#### 8.4.1. Ground Motion Set

The ground motion set presented in Section 3 and also used in section 7 is replaced by the Far Field ground motion set presented in FEMA P695 since many of the adjusting factors proposed in the FEMA P695 was calculated based on this set. The Far-Field record set includes twenty-two component pairs of horizontal ground motions from sites located greater than or equal to 10 km from fault rupture (Table 8-1). Actual earthquake records are used, in contrast with artificial or synthetic records, recognizing that regional variation of ground motions would not be addressed. The ground motions were selected from the PEER NGA database based on source magnitude, source type, site conditions, and source distance. Figure 8-2 shows the median of the 2 components for each of the 22 pairs of unscaled and un-normalized ground motion acceleration spectra and also the overall median of all 44 records.

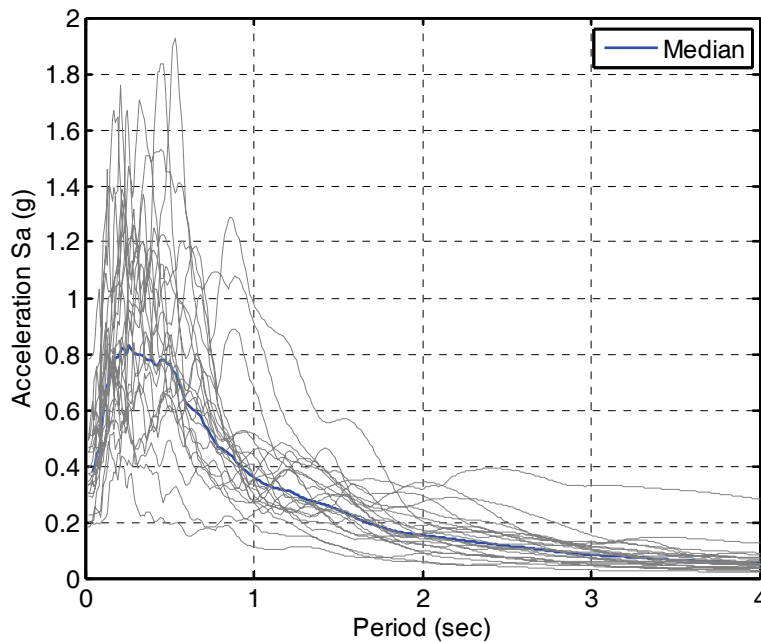


**Figure 8-2 The 22 unscaled ground motions spectra and median spectrum**

**Table 8-1 Ground motion set for collapse assessment (from FEMA P695)**

EQ Index	EQ ID	PEER-NGA Rec. Num.	Event Information				Site Information			
			Mag.	Year	Event	Fault Type	Station Name	Vs_30 (m/s)	Campbell Distance (km)	
1	12011	953	6.7	1994	Northridge	Blind thrust	Beverly Hills - 14145 Mulhol	356	17.2	
2	12012	960	6.7	1994	Northridge	Blind thrust	Canyon Country - W Lost Cany	309	12.4	
3	12041	1602	7.1	1999	Duzce, Turkey	Strike-slip	Bolu	326	12.4	
4	12052	1787	7.1	1999	Hector Mine	Strike-slip	Hector	685	12.0	
5	12061	169	6.5	1979	Imperial Valley	Strike-slip	Delta	275	22.5	
6	12062	174	6.5	1979	Imperial Valley	Strike-slip	El Centro Array #11	196	13.5	
7	12071	1111	6.9	1995	Kobe, Japan	Strike-slip	Nishi-Akashi	609	25.2	
8	12072	1116	6.9	1995	Kobe, Japan	Strike-slip	Shin-Osaka	256	28.5	
9	12081	1158	7.5	1999	Kocaeli, Turkey	Strike-slip	Duzce	276	15.4	
10	12082	1148	7.5	1999	Kocaeli, Turkey	Strike-slip	Arcelik	523	13.5	
11	12091	900	7.3	1992	Landers	Strike-slip	Yermo Fire Station	354	23.8	

**Table 8-1 Continued, Ground motion set for collapse assessment (from FEMA P695)**

EQ Index	EQ ID	PEER-NGA Rec. Num.	Event Information				Site Information			
			Mag.	Year	Event	Fault Type	Station Name	Vs_30 (m/s)	Campbell Distance (km)	
12	12092	848	7.3	1992	Landers	Strike-slip	Coolwater	271	20.0	
13	12101	752	6.9	1989	Loma Prieta	Strike-slip	Capitola	289	35.5	
14	12102	767	6.9	1989	Loma Prieta	Strike-slip	Gilroy Array #3	350	12.8	
15	12111	1633	7.4	1990	Manjil, Iran	Strike-slip	Abbar	724	13.0	
16	12121	721	6.5	1987	Superstition Hills	Strike-slip	El Centro Imp. Co. Cent	192	18.5	
17	12122	725	6.5	1987	Superstition Hills	Strike-slip	Poe Road (temp)	208	11.7	
18	12132	829	7.0	1992	Cape Mendocino	Thrust	Rio Dell Overpass - FF	312	14.3	
19	12141	1244	7.6	1999	Chi-Chi, Taiwan	Thrust	CHY101	259	15.5	
20	12142	1485	7.6	1999	Chi-Chi, Taiwan	Thrust	TCU045	705	26.8	
21	12151	68	6.6	1971	San Fernando	Thrust	LA - Hollywood Stor FF	316	25.9	
22	12171	125	6.5	1976	Friuli, Italy	Thrust	Tolmezzo	425	15.8	

Scaling of ground motion records is a necessary for nonlinear dynamic analysis since few, if any, available unscaled records are strong enough to collapse modern buildings. The scaling process of the Methodology includes two parts:

1- Normalization of Records: Each individual record is normalized by their respective peak ground velocity (geometric mean of PGV of the two components). In this step, the two components of each record are multiplied by a single normalization factor equal to the median PGV of all records in set divided by the PGV of the each record itself. Normalization by peak ground velocity is a simple way to remove unwarranted variability between records due to inherent differences in event magnitude, distance to source, source type and site conditions, while still maintaining the inherent unpredictable (i.e., record-to-record) variability necessary for accurately predicting collapse fragility (FEMA 2009b).

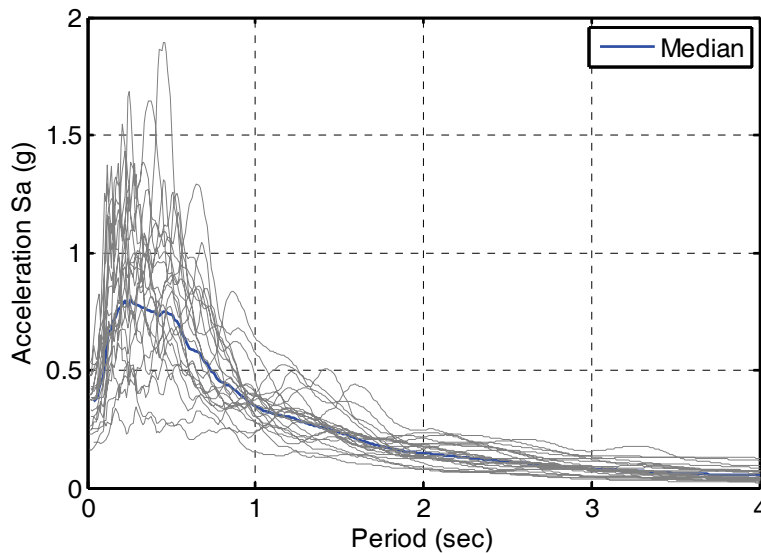


**Figure 8-3 Ground motion spectra and median spectrum for 22 normalized records**

2- Scaling of Record Set: In this step the whole record set is scaled up or down in amplitude such that 50 percent of the ground motions lead to collapse. This approach is used to determine the median collapse capacity,  $\hat{S}_{CT}$ , of the model. Figure 8-4 shows the normalized ground motion set scaled to MCE spectrum at fundamental period of the model (i.e.  $T_m = 3.1$  sec).

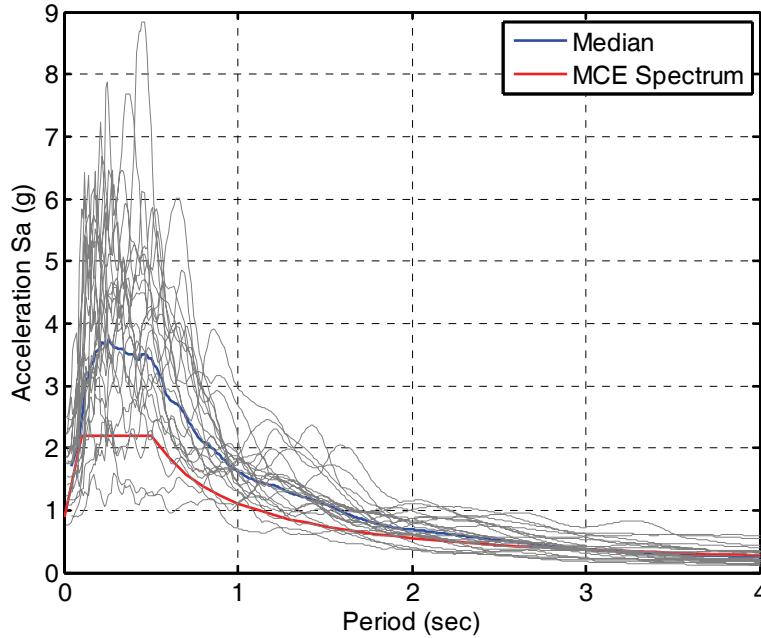


**Figure 8-4 The normalized 22 ground motion spectra scaled to MCE spectrum**

#### 8.4.2. MCE Spectrum

The CMR is defined as the ratio of  $\hat{S}_{CT}$  to  $S_{MT}$  where  $S_{MT}$  is the MCE spectral acceleration at fundamental period of the model. This ratio should be adjusted by the Spectral Shape Factor (SSF) dependent on the properties of the model, characteristics of the ground motions and also the site and hazard level of interest. As mentioned in section 3 of this report, the prototype model was designed for occupancy category II and importance factor  $I = 1.0$  according to ASCE 7-05(ASCE 2005). The building was designed for a Los Angeles, California location (34.50 N, 118.2 W) on stiff soil (site class D with reference shear wave velocity of 180 to 360 m/s). The mapped spectral accelerations for this location are  $S_s = 2.2$  g for short periods and  $S_1 = 0.74$  g for a 1-s period. However, for seismic design loading, the Methodology defines MCE and DBE ground motions for structures in Seismic Design Categories (SDC) B, C, and D specified by Section 11.7.2 of ASCE7-05. For these SDCs, maximum and minimum ground motions are defined based on the respective upper-bound and lower-bound values of MCE and DBE spectral acceleration, as given in Table 11.6-1 of ASCE7-05, for short-period response, and in Table 11.6-2 of ASCE7-05, for 1-second response. Maximum values of spectral acceleration for SDC D in FEMA P695 ( $S_s = 1.5$  g and  $S_1 = 0.60$  g) are based on the effective boundary between deterministic (near-source) and probabilistic regions of MCE ground motions, as defined in

Section 21.2 of ASCE7-05. The Methodology purposely excludes SDC D structures at deterministic (near-source) sites defined by 1-second spectral acceleration equal to or greater than 0.60 g, although Section 11.6 of ASCE7-05 defines SDC D structures as having 1-second spectral acceleration values as high as 0.75 g. Figure 8-5 shows the difference in MCE spectrum that the prototype model is designed for and SDC D<sub>max</sub> for FEMA P695. The MCE spectrum that the prototype model is designed for is approximately 1.25 times larger than the MCE SDC D<sub>max</sub> of FEMA P695.

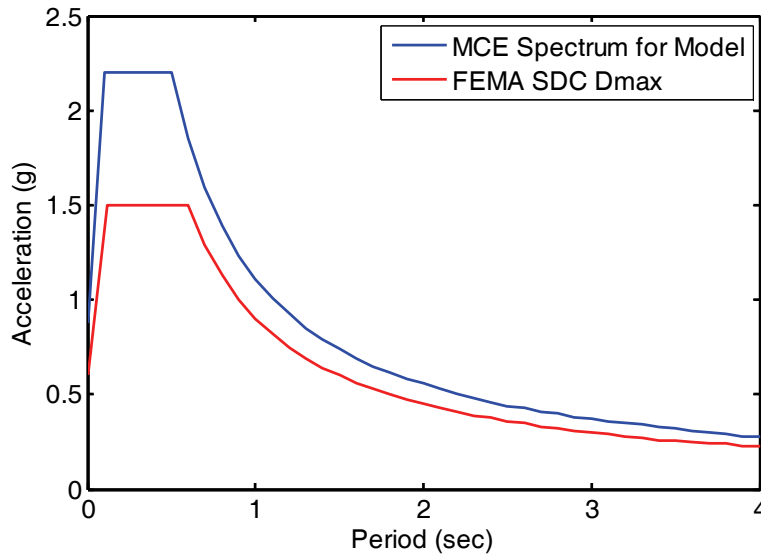


**Figure 8-5 MCE spectrum for model site location and FEMA SDC Dmax**

The MCE spectrum is important in essence of scaling the ground motions and also to calculate the SSF value in order to adjust the calculated CMR. This factor is calculated from (Equation B-4, (FEMA 2009b)):

$$SSF = \exp [\beta_1(\bar{\epsilon}_0 - \bar{\epsilon}(T)_{records})] \quad (8-1)$$

where  $\bar{\epsilon}_0$  is the expected epsilon dependent on both site and hazard level of interest. Epsilon,  $\epsilon$ , is defined as the number of logarithmic standard deviations between the observed spectral value and the median prediction from an attenuation function. Table B-1 in FEMA P695 shows the value of  $\bar{\epsilon}_0$  for different seismic design categories and also various hazard levels. The

Methodology reasons that since the average median collapse capacity is roughly twice the MCE, therefore the ground motion hazard level that should be used in establishing the  $\bar{\epsilon}_0$  should have spectral acceleration demand that is twice (or more) of the 2% in 50 year demand (MCE). The Methodology proposed the value for  $\bar{\epsilon}_0$  1.0 for SDC B/C, 1.5 for SDC D, and 1.2 for SDC E which are the values for hazard level of 0.5% in 50 year demand.

However as mentioned before, the SDC D in FEMA P695 is different from the spectrum that the prototype model was designed for in this study. In this study, the value for  $\bar{\epsilon}_0$  was selected equal to 1.7 which is the average of  $\bar{\epsilon}_0(1)$  for a hazard level of 0.5% in 50 year demand over 58 zip codes in area of Los Angeles where the prototype model is located.

In Equation 8-1  $\bar{\epsilon}(T)_{records}$  is for the Far-Field record set and is equal to

$$\bar{\epsilon}(T)_{records} = 0.6(1.5 - T) \quad (8-2)$$

where  $0.0 < \bar{\epsilon}(T)_{records} \leq 0.6$  and T is code-defined fundamental period of the structure.  $\beta_1$  in Equation 8-1 is calculated from Equation B-3 in FEMA P695:

$$\beta_1 = 0.14(\mu_T - 1)^{0.42} \quad (8-3)$$

where  $\mu_T$  is period-based ductility and defined as the ratio of the ultimate displacement at roof to effective yield roof displacement.

#### 8.4.3. Period-based Ductility

Period-based ductility,  $\mu_T$ , is an important parameter to calculate adjusting parameters in the Methodology. As defined before period-based ductility is equal to ratio of the ultimate displacement at roof to effective yield roof displacement.

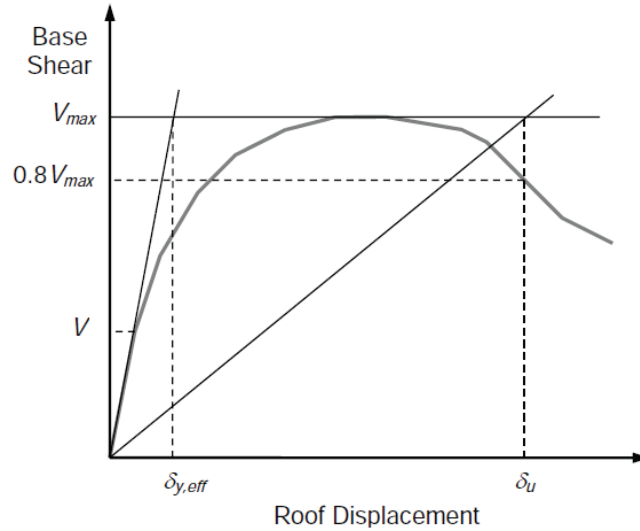


**Figure 8-6 Idealized nonlinear static pushover curve (FEMA 2009b)**

As shown in Figure 8-6  $\mu_T$  should be calculated from static pushover analysis as the ratio of  $\delta_u$  to  $\delta_{y,eff}$  which the later one can be calculated from Equation 10-6 of FEMA P695 for base isolated buildings:

$$\delta_{y,eff} = C_0 \frac{V_{max}}{W} \left[ \frac{g}{4\pi^2} \right] \max(T, T_1)^2 \quad (8-4)$$

where  $C_0$  relates the SDOF displacement to the roof displacement according to ASCE/SEI 41-06 section 3.3.3.3;  $V_{max}/W$  is shown in Figure 8-6 and is equal to maximum base shear normalized by building weight,  $T$  is code defined fundamental period of building and  $T_1$  is the undamaged fundamental period of the structural mode computed using eigenvalue analysis.

#### 8.4.4. Total System Collapse Uncertainty

The total system collapse uncertainty is an important factor to evaluate the probability of collapse at the MCE. The total uncertainty of the collapse system is calculated by combining the four identified sources including record-to-record, design, test data, and modeling uncertainties (Equation 7-5 FEMA P695).

$$\beta_{TOT} = \sqrt{\beta_{RTR}^2 + \beta_{DR}^2 + \beta_{TD}^2 + \beta_{MDL}^2} \quad (8-5)$$

The total uncertainty influences the shape of the collapse fragility curve. The larger  $\beta_{TOT}$  the flatter the fragility curve obtained. Each part of the total uncertainty factor is described below:

#### 8.4.4.1. Record-to-Record Uncertainty (RTR)

Record-to-record uncertainty is due to variability in the response of model to different ground motion records. This uncertainty can be shown from IDA curve of the model. Although the value for this parameter can be calculated from a complete IDA and plotted fragility curve, the Methodology recommends a range of 0.35 to 0.45 for various building types. The value of RTR can be calculated from:

$$\beta_{RTR} = 0.1 + 0.1\mu_T \leq 0.4 \quad (8-6)$$

#### 8.4.4.2. Design Requirements Uncertainty (DR)

Design requirements uncertainty ( $\beta_{DR}$ ) is a parameter to include the uncertainty of completeness and robustness of the design requirements. The isolated model designed in this study is assigned (A) superior ( $\beta_{DR} = 0.1$ ) for design requirements since it complies with all requirements in ASCE7-05 chapter 17.

#### 8.4.4.3. Test Data Uncertainty (TD)

Test data-related uncertainty is quantified in terms of the availability and also quality. The component behavior of the superstructure (plastic hinge behavior and brace buckling behavior) was calibrated from a wealth of test data (Uriz et al. 2008; Lignos et al. 2011) and is rated (B) good ( $\beta_{TD} = 0.2$ ). ASCE/SEI 7-05 requires prototype testing of isolator units for the purpose of establishing and validating the design properties of the isolation system and verifying stability for MCE response. These tests are specific to the isolation system installed in a particular

building, and follow detailed requirements for force-deflection response outlined in the design requirements. As a result, there is substantially smaller uncertainty related to the test data in an isolated system than the superstructure.

#### 8.4.4.4. Modeling Uncertainty (MDL)

The capability of the analysis model in capturing the full range of structural response characteristics of the model is quantified by modeling uncertainty parameter. The superstructure modeling is rated A because of effort put in detailed modeling of the beams, columns, braces and also connections elements, although modeling of the isolation system would be rated as good, B, due to lack of modeling of changes in properties under cyclic deformation such as softening and damping loss due to heat effects. Overall, modeling uncertainty is rated good, B,  $\beta_{MDL} = 0.2$  for the sake of conservatism.

#### 8.4.5. 3-Dimensional Analysis

For 3-dimensional models as applied here, the Methodology proposed in FEMA P695 requires to apply the twenty-two record pairs twice to each model, once with the ground motion records oriented along one principal direction, and then again with the records rotated 90 degrees. The case that leads to smaller collapse intensity from each set of analysis of one pair ground motion should be considered to calculate the median collapse intensity.

The Methodology also recommends the median collapse intensity obtained from 3D analysis should be multiplied by a factor of 1.2 to achieve parity with the two dimensional analyses. This procedure was followed in the analysis presented in Section 8.5.

#### 8.4.6. Collapse Criteria

As mentioned earlier, simulated collapse mechanisms were considered explicitly in the numerical study using material models with capping strength, negative stiffness after reaching capping strength, and degradation in strength and stiffness at both levels of distributed and concentrated plastic hinges. Although detailed modeling of structural components was implemented here, 5% and 2% maximum story drift ratio was selected as collapse criteria for

IMRF and OCBF models, respectively. These criteria were selected base on Table 2-4 of FEMA 273 (FEMA 1997) in which 5% and 2% drift ratio is recommended as the collapse prevention limit for moment and braced frames, respectively.

## **8.5. Collapse Assessment**

### *8.5.1. IMRF Model*

The Methodology described earlier in this section was utilized to assess collapse probability of a base isolated IMRF model. The same 3D finite element numerical model and moat wall element described in Section 7 was used in this section for purpose of static pushover and also nonlinear dynamic analysis. Various moat wall gap distances were examined to evaluate the effect of this design parameter on probability of collapse of base isolated IMRF building pounding a moat wall.

#### 8.5.1.1. Static Pushover Analysis

A static pushover analysis of the prototype model was conducted to calculate the maximum shear strength and also period based ductility. The static pushover analysis was conducted on both fixed base (superstructure) and isolated base model.

Figure 8-7 shows the static nonlinear pushover curve of the IMRF superstructure while the structure is fixed at its base. Nonlinear static analysis of the fixed-base structure was conducted using a lateral loads pattern prescribed by Equation 12.8-13 of ASCE 7-05 based on the first mode shape. These figures show that the maximum shear strength of the IMRF superstructure is roughly about 0.22% of the weight followed by negative stiffness (i.e. at maximum shear strength) after approximately 22 in (5% drift ratio) roof displacement.

The effective yielding displacement  $\delta_{y,eff}$  was calculated for both directions of the IMRF model as roughly equal to 6.0 which leads to a period-base ductility around 11 for IMRF model in both directions.

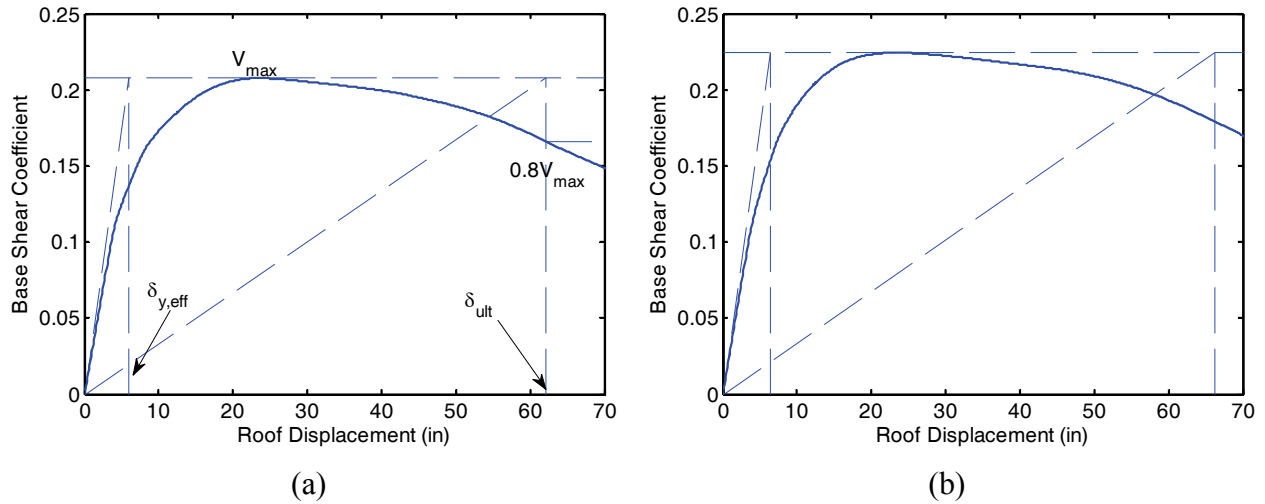


**Figure 8-7 Nonlinear static pushover curve for fixed-base IMRF in (a) X direction (b) Y direction**

FEMA P695 suggests calculating the period-base ductility of base-isolated structures from pushover analysis considering the bearings. Figure 8-8 shows the pushover curve of the base-isolated IMRF model in X and Y direction.

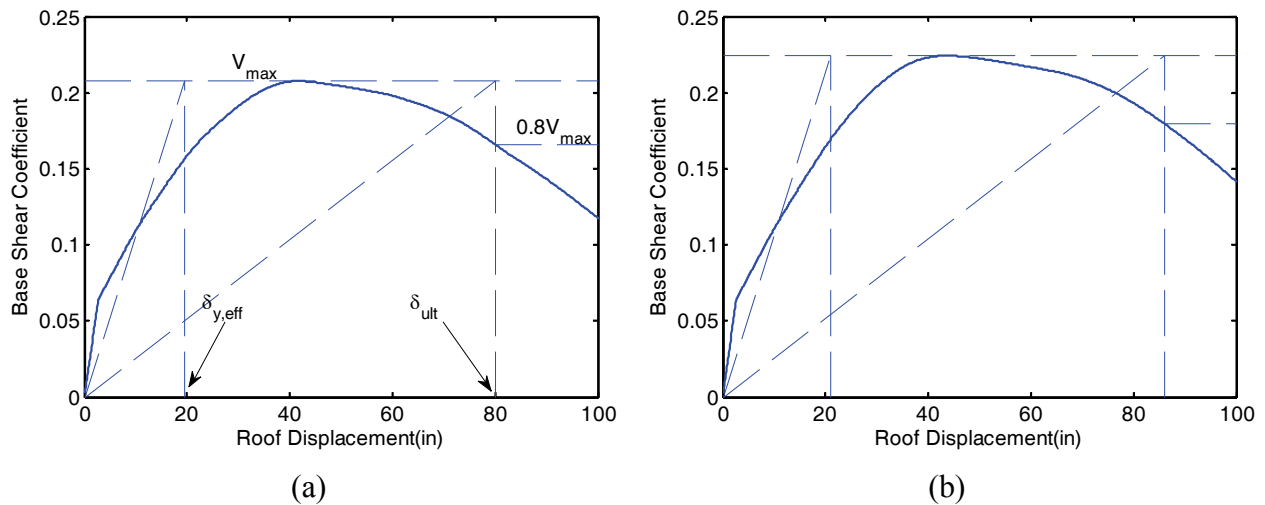


**Figure 8-8 Nonlinear static pushover curve for base-isolated IMRF in (a) X direction and (b) Y direction**

The effective yield displacement was calculated using Equation 8-4. The fundamental period of the base-isolated structure is defined as the effective isolation period at MCE level ( $T_M$ ) which is equal to 3.1. The yield displacement,  $\delta_{y,eff}$ , was calculated for both directions as roughly equal

to 20 in., which leads to period-base ductility of 4 for the base-isolated model in both directions. The period-based ductility values obtained in this study are relatively large due to the flexibility of IMRF superstructure.

It is important to mention that moat walls are not modeled in pushover analysis since a sudden increase in stiffness associated with the moat wall is inconsistent with the assumptions used in developing the relationship between  $\mu_T$  and  $SSF$  (FEMA 2009b). Also, Figure 8-8 shows that 5% roof drift (27 in roof displacement) is slightly larger than the displacement at which the maximum strength of the building occurs in both directions. This verifies that 5% maximum story drift ratio considered as collapse criteria for IMRF model is rational.

#### 8.5.1.2. Collapse Assessment Parameters

Once the period-based ductility is calculated, spectral shape factor ( $SSF$ ) can be calculated using Equations 8-1 substituting  $\bar{\epsilon}(T)_{records} = 0$  and  $\beta_1 = 0.225$  from Equations 8-2 and 8-3, respectively. Substituting  $\bar{\epsilon}_0 = 1.7$  in Equation 8-1 leads to  $SSF$  1.47 for the base isolated model. It should be noted that this value is slightly higher than the value proposed in table 7-1b of FEMA P695 for corresponding  $\mu_T$  and fundamental period, which is equal to 1.4. This difference is because of the target epsilon used for this table. Table 7-1b of FEMA P695 which is for SDC  $D_{max}$ , calculated base on  $\bar{\epsilon}_0 = 1.5$ . The spectral shape factor 1.47 calculated here for this study is based on target epsilon of 1.7. The calculated  $SSF$  will be used to adjust median collapse intensity from incremental dynamic analysis.

The total uncertainty,  $\beta_{TOT}$ , associated with collapse must be assessed in order to compare the  $ACMR$  to the acceptance criteria. The base isolated IMRF model was assigned ratings of (B) Good for modeling, (B) Good for test data, and (A) Superior for design requirements. Record-to-record uncertainty,  $\beta_{RTR}$ , could be calculated using Equation 8-6 equal to 0.4. In total, for the 3-story base isolated IMRF model examined here, the total collapse uncertainty of 0.5 was calculated using Equation 8-5.

### 8.5.1.3. Nonlinear Dynamic Analysis

In this part, the results of incremental dynamic analysis of the 3D model are shown. Although the Methodology in FEMA P695 just requires calculation of median collapse intensity, a full IDA was conducted here to produce fragility curve for other response quantities such as floor acceleration. The Far-Field ground motion set described earlier was scaled to match the median spectral acceleration to various acceleration intensities. Although the probability of collapse at acceleration intensities less than MCE level is negligible, the starting intensity was set to less than 0.1 of MCE level in order to investigate the behavior of the base-isolated system at different hazard levels. As mentioned earlier, IDA was conducted twice for each ground motion to find the minimum collapse probability for 2 directions of each ground motion pair. First, all of the ground motions component 1 and 2 were applied in x- and y-direction respectively. The ground motion components were switched in the next step. The minimum collapse intensity obtained from two sets of analysis was considered in IDA curve.

IDA curves are plotted for maximum direction of IMRF model in Figure 8-9 for different moat wall gap distances. The y-axis in this figure and for other IDA curves in this section is a scale factor relative to the MCE spectrum intensity at period  $T_M$  ( $S_a = 0.36$ ), such that an intensity scale factor of 1 represents the MCE intensity at the fundamental period of the model.

The IDA curves presented correspond to the direction of each ground motion pair resulting in smaller collapse intensity. It can be observed that by including the effects of moat wall impact and decreasing the moat wall gap distance leads to larger drift ratios at lower intensity scale factors, particularly for the ground motions with the larger scale factors. These figures shows that median collapse intensity should decreased by decreasing the moat wall gap distance for the IMRF model.

For each case, the collapse fragility curve was developed by calculating the probability of exceeding 5% SDR for a given intensity scale factor. Figure 8-10 shows the fragility curves for the IMRF model with different moat wall configurations. It should be mentioned that these fragility curves are obtained from IDA results not from procedures proposed in FEMA P695. For

the FEMA P695 Methodology, only median collapse intensity is needed which is equal to intensity scale factor corresponding to probability of collapse of 0.5.

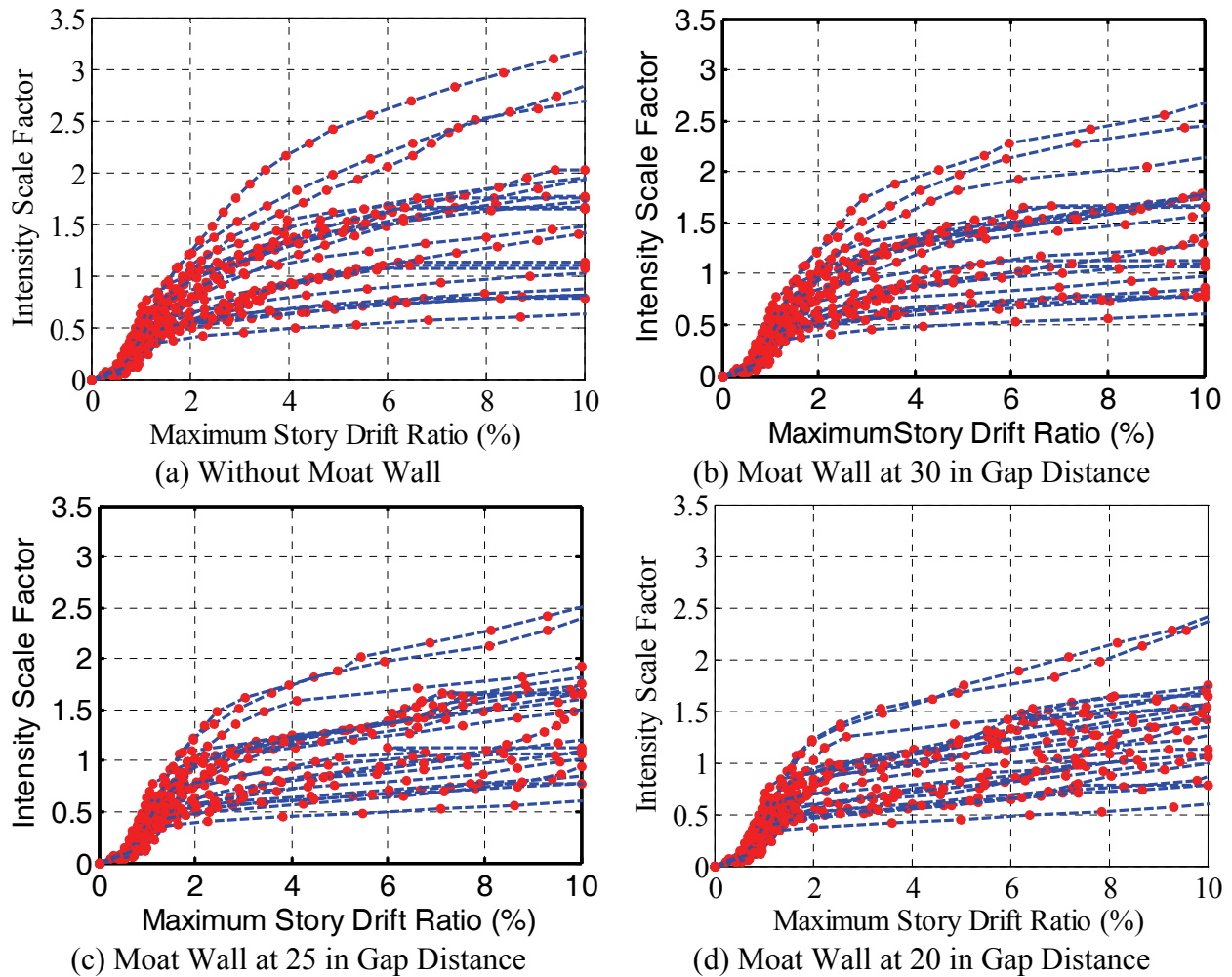
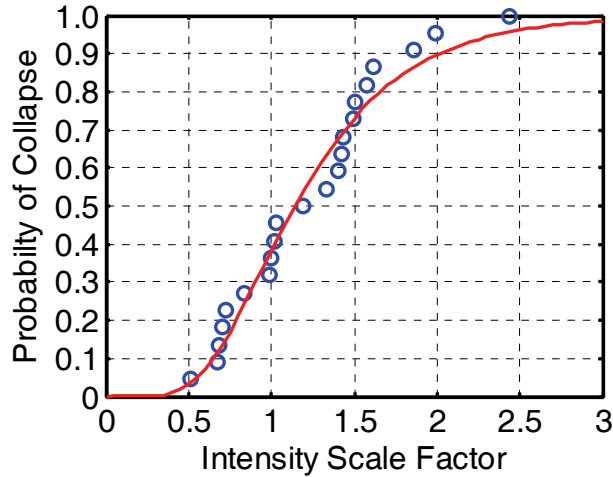


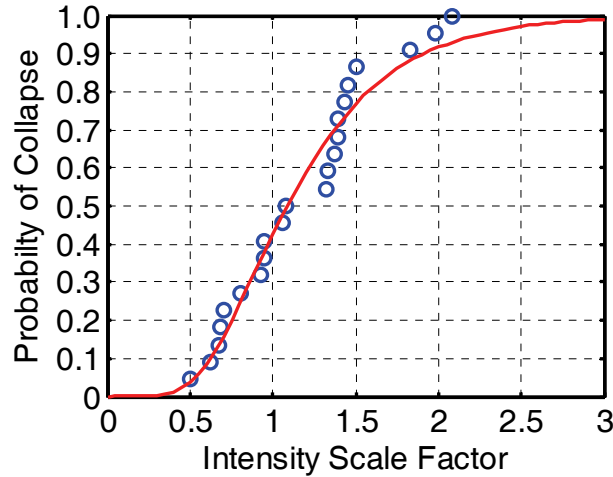
**Figure 8-9 IDA curve for maximum direction of IMRF model and different moat wall situations**

In collapse fragility curves, the probability at intensity scale factor equal to 1 shows the probability of collapse at MCE level, although the Methodology in FEMA P695 justifies this number by adjusting the median collapse intensity and considering uncertainty of design and modeling.

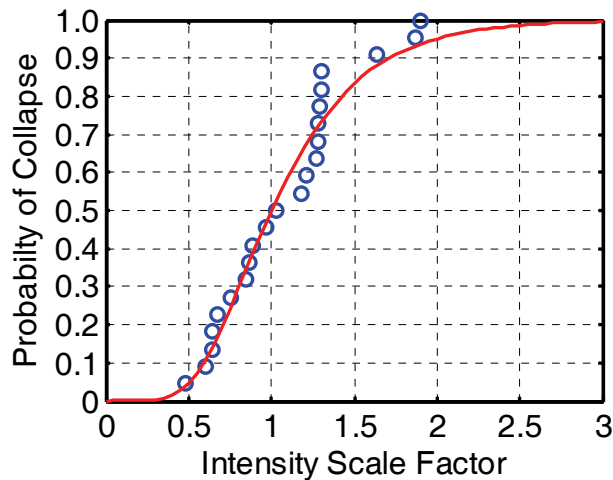
It should be noted that since the fragility curves were plotted based on MCE intensity scale factor, there is no need to divide the intensity at probability of 0.5 by intensity at MCE to calculate the CMR. The CMR was calculated for each case and reported in Table 8-2.



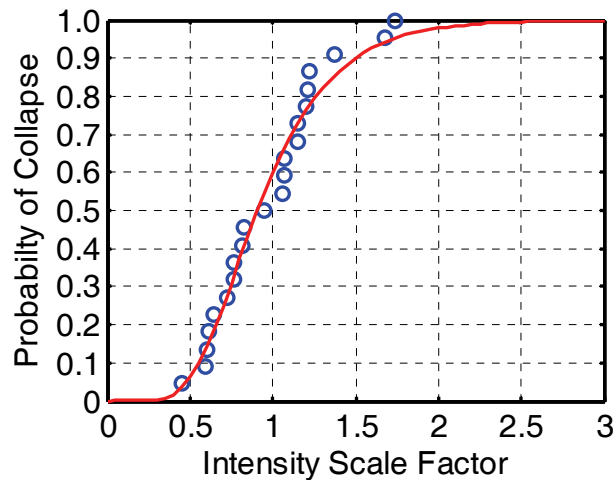
(a) Without Moat Wall



(b) Moat Wall at 30 in Gap Distance



(c) Moat Wall at 25 in Gap Distance



(d) Moat Wall at 20 in Gap Distance

**Figure 8-10 Collapse fragility curve for IMRF model from IDA**

**Table 8-2 Collapse margin ratio for IMRF models**

Gap Size (in)	Collapse Margin Ratio ( <i>CMR</i> )	Variance ( $\beta$ )	Collapse probability at MCE (%)
Without wall	1.14	0.44	40
30	1.08	0.43	44
25	1.00	0.42	50
20	0.91	0.39	60

The *CMR* calculated for each case should be multiplied by adjusting factors to include the effect of 3D analysis (1.2) and also spectral shape of ground motions (1.47) previously described. The

adjusted CMR (ACMR) is calculated and modified fragility curves were plotted with corrected median and  $\beta_{TOT}$  equal to 0.5.

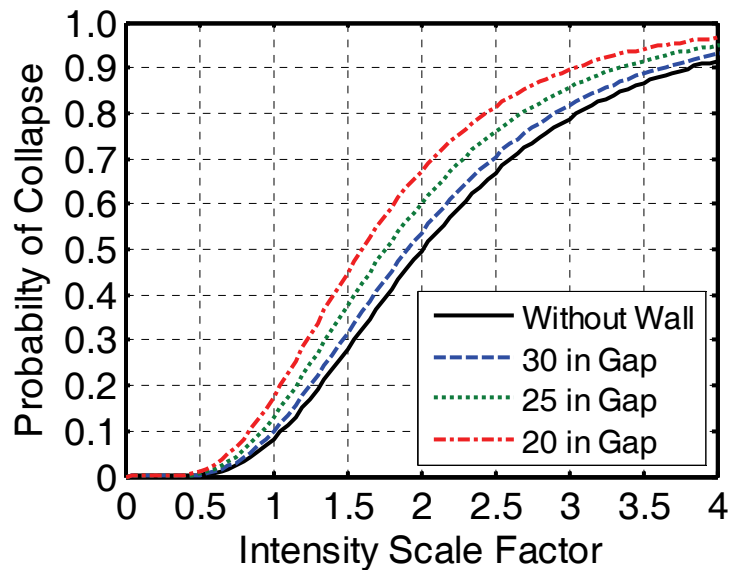


**Figure 8-11 Adjusted collapse fragility curve for 3D IMRF model**

Figure 8-11 shows the adjusted fragility curve for base-isolated IMRF model for different moat wall configurations in the maximum direction. The probability of collapse at intensity scale factor of 1 (corresponding to MCE level) is considered as the criterion for collapse assessment. The acceptable probability of collapse at MCE intensity is equal to 10% for average of a set of archetypes with maximum of 20% for individual models (outliers). The probability of collapse for the base-isolated model without moat wall examined in this study turned out 8.1%, which is slightly less than the acceptable value for average of archetypes.

Considering pounding to moat walls in base isolated buildings can lead to an increase in the probability of collapse at MCE level shaking. The probability of collapse for different moat wall configurations is listed in Table 8-3. Decreasing the moat wall gap distance resulted in increasing the adjusted collapse probability at the MCE event. The probability of collapse for the case that the moat wall is installed at 20 in. gap (65% of required displacement by ASCE7-05) distance is twice as the probability of collapse for the case without moat wall, although both of them are below the 20% limit for outliers. The results obtained here for the IMRF model are in agreement with findings in Section 11 of FEMA P695 in which the probability of collapse for base isolated

moment frame buildings with sufficient strength and ductility were observed to be relatively insensitive to the size of the gap distance.

**Table 8-3 Adjusted collapse margin ratio for IMRF models**

Gap Size (in)	Adjusted Collapse Margin Ratio ( <i>ACMR</i> )	Collapse probability at MCE (%)
Without wall	2.01	8.1
30	1.91	9.7
25	1.76	12.9
20	1.60	17.4

### 8.5.2. OCBF Model

The procedure described for the IMRF model was repeated for the OCBF model to investigate the behavior of base isolated structure with stiff braced frame as superstructure. As stated in Section 7, OSBF and IMRF models are different in terms of superstructure flexibility and this resulted in different behavior under extreme ground motions. In this section the probability of collapse of a stiff OCBF frame is investigated for different moat wall configurations.

#### 8.5.2.1. Static Pushover Analysis

A static pushover analysis of the prototype model was conducted to calculate the maximum shear strength and also period based ductility. The static pushover analysis was conducted on both fixed base (superstructure) and isolated base models. The pushover analysis resulted in identical response for both directions of the OCBF model since the lateral resistant system in both directions is exactly the same in this model. The pushover curve for fixed base and base isolated models are shown in Figure 8-12.

The fixed base OCBF frame shows very stiff behavior at the beginning up to the point that braces in the second floor buckle under compression forces when the base shear is equal to 40% of the total mass of the frame (including mass of base level, 7087 kips). The braces in third floor buckle right after the second floor, resulting in a drop in base shear to 25% of total mass. After this point, increasing the lateral forces leads to increasing the drift in two upper floors and results in forming plastic hinges in columns and beams of these levels. Braces in the first floor did not

buckle even for large roof displacement. The maximum base shear was achieved before buckling in the second floor at roof displacement equal to 1 in.

The approximate equation for fundamental period of OCBF frames given in Equation 12.8-7 of ASCE 7-05 leads to a larger period (0.48 sec) in comparison to the actual fundamental period of the frame obtained from eigenvalue analysis (0.39 sec). Using a larger period (0.48 sec) in Equation 8-4 leads to an effective yield displacement of 1.0 in. The ultimate displacement for the fixed base frame was selected based on 20% base shear drop after maximum base shear which is equal to 2.9 in. roof displacement. The period base ductility for fixed base OCBF frame is calculated equal to 2.9, which is substantially smaller than the period base ductility of the IMRF model.

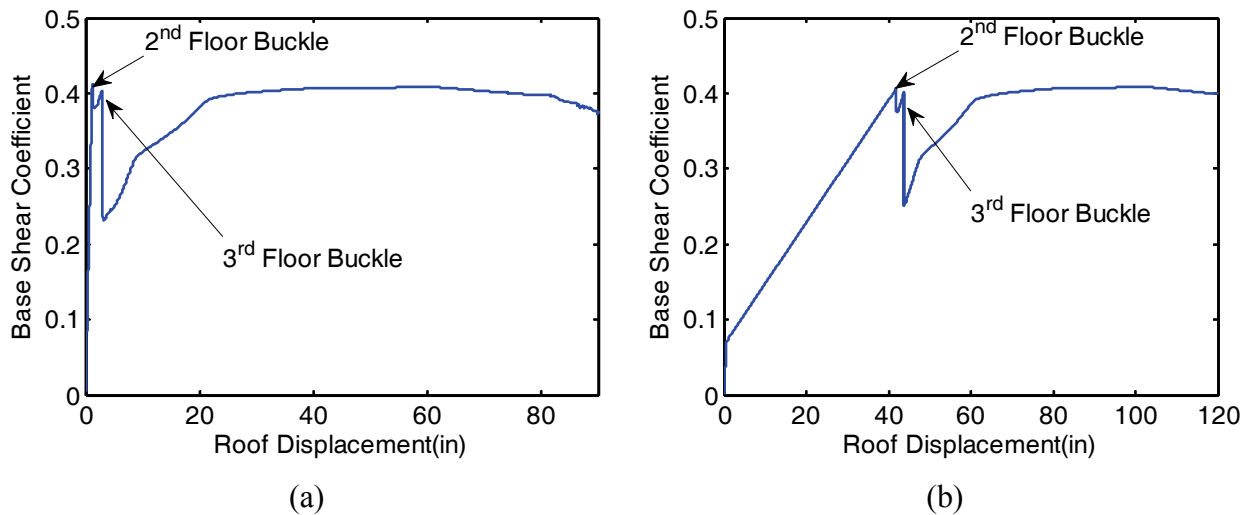


**Figure 8-12 Nonlinear static pushover curve for (a) Fixed base (b) Base isolated OCBF model**

The effective yield displacement for the base isolated OCBF model was calculated as 38 in. using Equation 8-4. The fundamental period for base-isolated structure is defined as effective isolation period at MCE level ( $T_M$ ) which is equal to 3.1. The period-base ductility was calculated as 1.15 for base-isolated OCBF model. The period-based ductility values obtained for OCBF model are relatively small due to the brittle behavior of the superstructure after brace buckling.

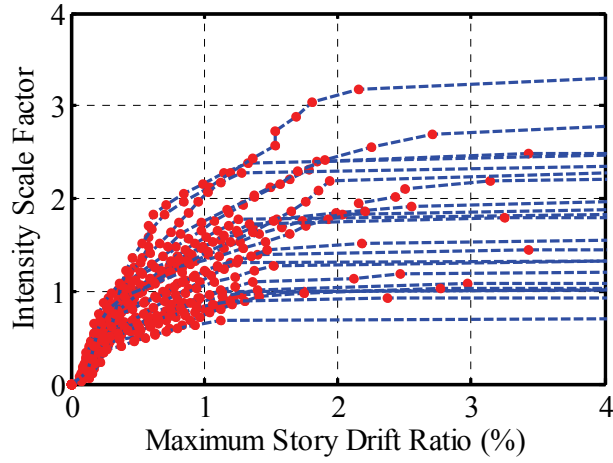
### 8.5.2.2. Collapse Assessment Parameters

Once the period-based ductility is calculated, spectral shape factor (SSF) can be calculated using Equations 8-1 substituting  $\bar{\epsilon}(T)_{records} = 0$  and  $\beta_1 = 0.063$  from Equations 8-2 and 8-3, respectively. Substituting  $\bar{\epsilon}_0 = 1.7$  and these parameters in Equation 8-1 leads to SSF 1.12 for base isolated OCBF model. The calculated SSF will be used to adjust median collapse intensity from incremental dynamic analysis.

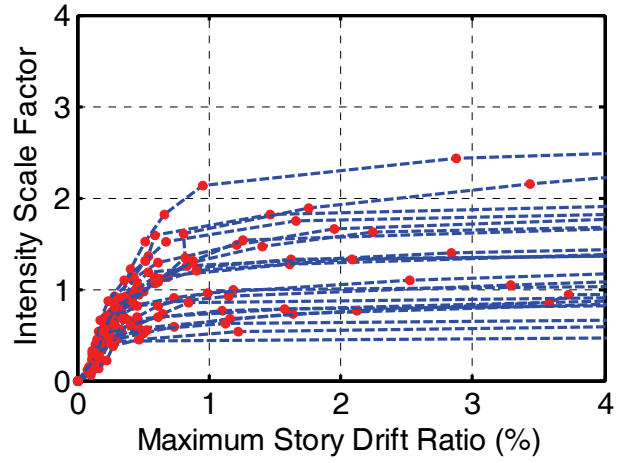
The total uncertainty,  $\beta_{TOT}$ , was calculated using associated uncertainties for: modeling rating of (B) Good, test data of (B) Good, design requirements of (A) Superior. Record-to-record uncertainty,  $\beta_{RTR}$ , could be calculated using Equation 8-6 equal to 0.22. In total, for the 3-story base isolated OCBF model examined in this report, the total collapse uncertainty of 0.37 was calculated using Equation 8-5.

### 8.5.2.3. Nonlinear Dynamic Analysis

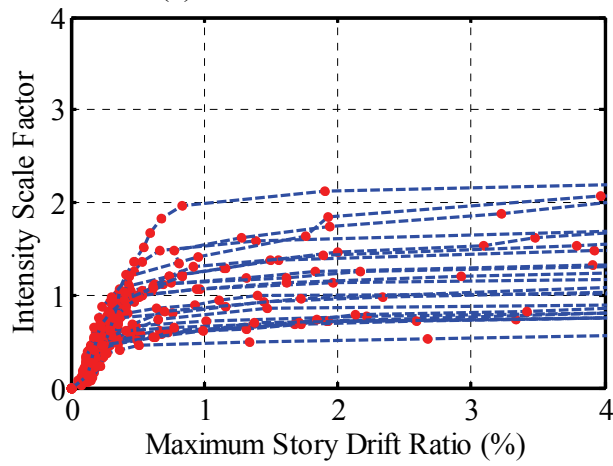
In this part, the results of incremental dynamic analysis of the 3D base isolated OCBF model are shown. Full IDA was conducted on base isolated OCBF model with different moat wall configurations (No moat wall and also with moat wall installed at 20, 25, 30, and 35 in gap distance) to produce fragility curve for this stiff brittle braced frame. The same far-field ground motion set used for IMRF model was scaled to match the median spectral acceleration to various acceleration intensities. IDA curves are plotted in Figure 8-13 for maximum direction of OCBF model for different moat wall gap distances.



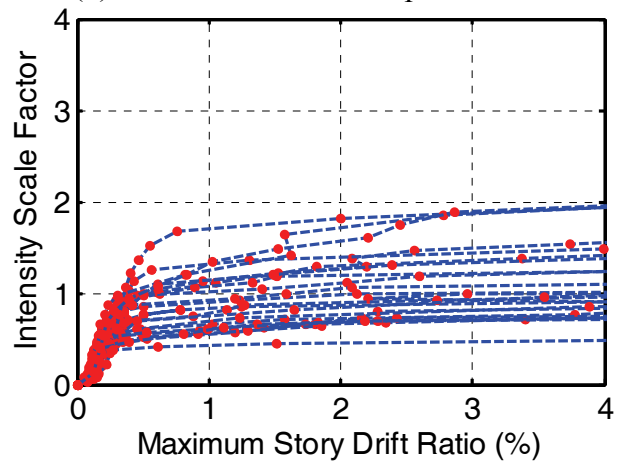
(a) Without Moat Wall



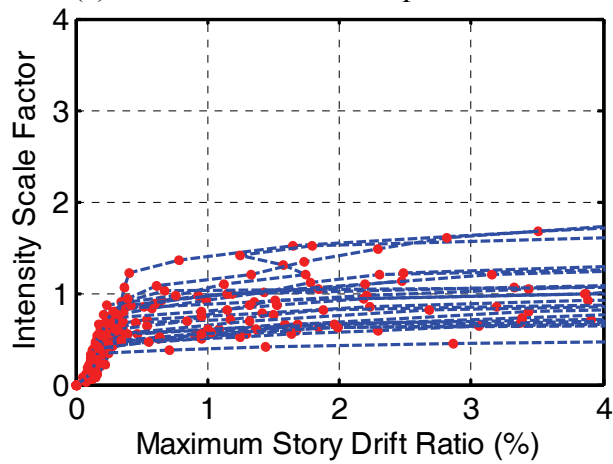
(b) Moat Wall at 35 in Gap Distance



(c) Moat Wall at 30 in Gap Distance



(d) Moat Wall at 25 in Gap Distance



(e) Moat Wall at 20 in Gap Distance

**Figure 8-13 IDA curve for maximum direction of OCBF model and different moat wall situations**

The IDA curve was developed for maximum direction considering the direction of each ground motion pair leading to smaller collapse intensity. It can be seen that by adding moat wall and decreasing the moat wall gap distance leads to flattening the IDA curve showing the fact that larger drift ratios are obtained at lower intensity scale factors. This figure shows that by decreasing the moat wall gap distance, more ground motions induce pounding to moat wall at lower intensities.

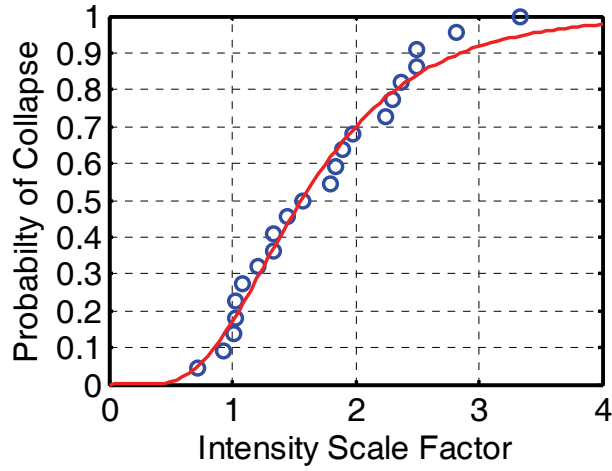
For each case, the collapse fragility curve was developed by calculating probability of exceedance to 2% SDR for a given intensity scale factor. Figure 8-14 shows the fragility curves for OCBF model for different moat wall configurations. It should be mentioned that these fragility curves are obtained from IDA results not from procedure proposed in FEMA P695. For the FEMA P695 Methodology, only median collapse intensity is needed.

It should be noted that since the fragility curves were plotted based on MCE intensity scale factor, there is no need to divide the intensity at probability of 0.5 by intensity at MCE to calculate the CMR. The CMR was calculated for each case and reported in Table 8-4.

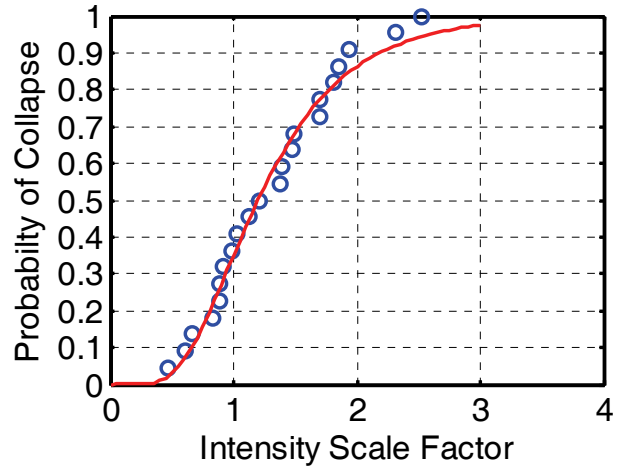
**Table 8-4 Collapse margin ratio for OCBF models**

Gap Size (in)	Collapse Margin Ratio ( <i>CMR</i> )	Variance ( $\beta$ )	Collapse probability at MCE (%)
Without wall	1.56	0.47	17
35	1.20	0.47	35
30	1.13	0.43	38
25	1.05	0.41	44
20	0.96	0.35	54

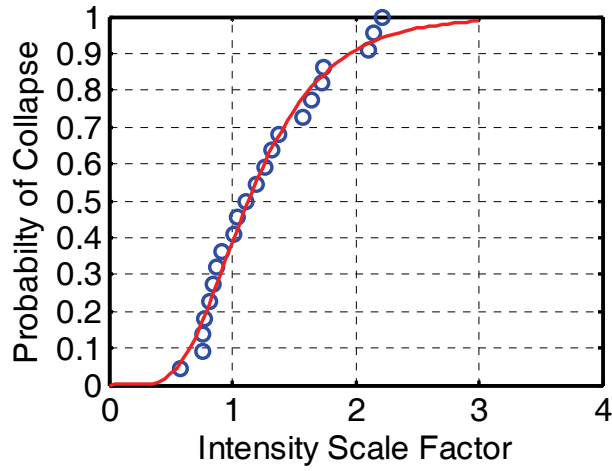
The CMR calculated for each case should be multiplied by adjusting factors to include the effect of 3D analysis (1.2) and also spectral shape of ground motions (1.12) described before. The adjusted CMR (ACMR) is calculated and modified fragility curves were plotted with corrected median and  $\beta_{TOT}$  equal to 0.37.



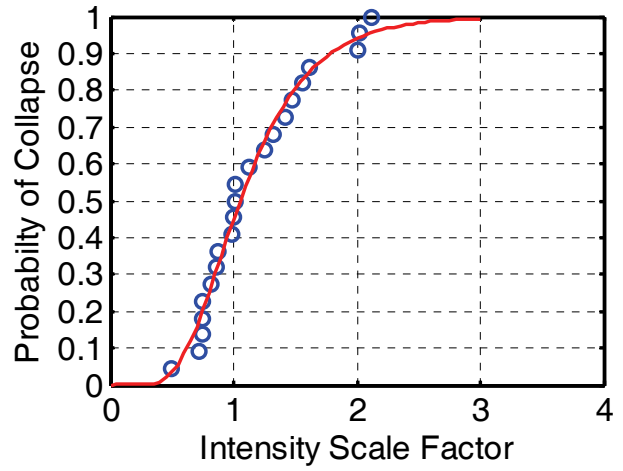
(a) Without Moat Wall



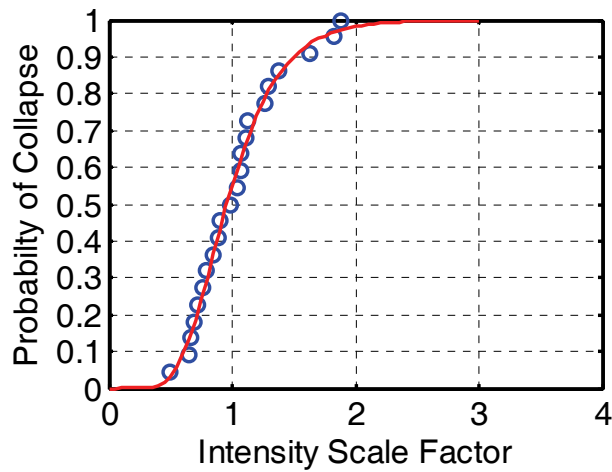
(b) Moat Wall at 35 in Gap Distance



(c) Moat Wall at 30 in Gap Distance



(d) Moat Wall at 25 in Gap Distance



(e) Moat Wall at 20 in Gap Distance

**Figure 8-14 Collapse fragility curve for OCBF model from IDA**

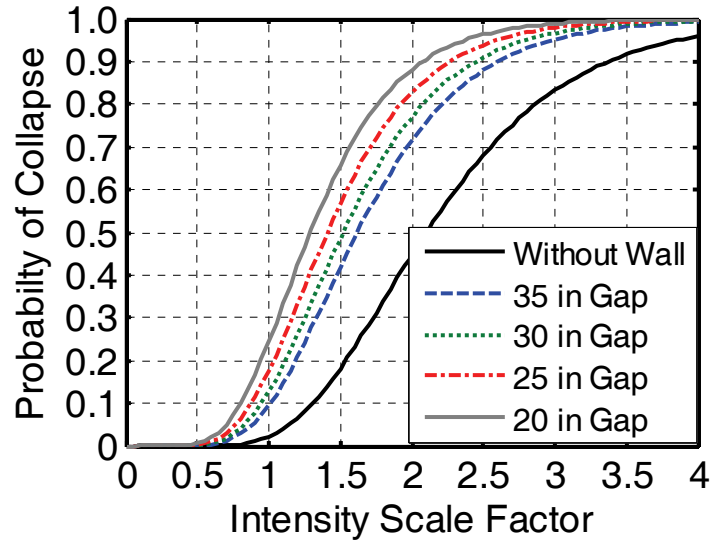


**Figure 8-15 Adjusted collapse fragility curve for base isolated OCBF model**

Figure 8-15 shows the adjusted fragility curve for the base-isolated OCBF model for different moat wall configurations in the maximum response direction. The probability of collapse at intensity scale factor of 1 (corresponding to MCE level) is considered as the criterion for collapse assessment. The acceptable probability of collapse at MCE intensity is equal to 10% for average of a set of archetypes with maximum of 20% for individual models (outliers). The probability of collapse for base-isolated OCBF model without moat wall in this study turned out to be 2.2% which is substantially less than accepted value for average of archetypes. This verifies the results obtained in Section 7 for OCBF frame, which suggested that the response of base isolated stiff OCBF frames without moat wall is promising.

Considering pounding to moat wall in base isolated model leads to increasing the probability of collapse at MCE event. The probability of collapse for different moat wall configuration is listed in Table 8-5. Decreasing the moat wall gap distance also resulted in increasing the adjusted collapse probability at MCE event. The probability of collapse for the case that moat wall is installed at 20 in gap (65% of required displacement by ASCE7-05) distance is ten times as the probability of collapse for the case without moat wall. The results obtained here for OCBF model show that the probability of collapse for base isolated OCBF frame with moat wall installed at required displacement by ASCE 7-05 (30 in gap distance) is greater than the acceptable criterion of 10%. Increasing the moat wall gap distance to 35 in gap distance (approximately 16%

increase) resulted in dropping the probability of collapse to 9.6% which is only slightly better than the acceptable criterion by FEMA P695.

**Table 8-5 Adjusted collapse margin ratio for OCBF models**

Gap Size (in)	Adjusted Collapse Margin Ratio ( <i>ACMR</i> )	Collapse probability at MCE (%)
Without wall	2.10	2.2
35	1.62	9.6
30	1.52	12.9
25	1.41	17.6
20	1.29	24.6

### 8.6. Base Isolated IMRF and OCBF Models Comparison

The Methodology proposed in FEMA P695 was utilized to assess collapse probability of the two prototype base isolated IMRF and OCBF models. Although both models were designed for the same location and hazard level, the dynamic properties of the superstructures are significantly different. The fixed base fundamental period of OCBF frame is 0.39 sec while IMRF model shows flexible behavior with period of 1.4 sec. The isolation system was designed for approximately the same period and damping ratio for both systems (3.1 sec and 15% at MCE level). This leads to period shifting factor of 2.1 and 7.75 for IMRF and OCBF models, respectively. Larger period shifting is desirable based on base isolated design philosophy.

The IMRF model was designed for a response modification factor of  $R=1.67$  while the OCBF frame was designed for  $R=1$ . This results in maximum base shear coefficient of 0.41 and 0.22 for IMRF and OCBF model in pushover analysis, respectively. Period based ductility, which is a parameter representing period elongation in frame at collapse, was calculated to 4.0 and 1.15 for IMRF and OCBF models, respectively. In general, it can be concluded that OCBF frame shows stiffer and more brittle behavior in comparison with the IMRF model.

Figure 8-16 shows the ratio of *ACMR* to acceptable *ACMR* for 10% probability of collapse for both models. It can be seen that OCBF model without moat walls shows more conservative margins in comparison to IMRF model which is slightly higher than accepted ratio. However, considering moat walls in collapse evaluation analysis changes these margin ratios. Installing the moat wall at 30 in. gap distance equal to total maximum displacement of base isolated model and

is minimum required gap distance by ASCE7-05 results in dropping the ACMR for OCBF frame below the accepted ratio, but it is still slightly over the accepted value for IMRF model. This verifies that pounding to moat wall at required gap distance by ASCE7-05 results in acceptable probability of collapse (less than 10%) for flexible and ductile IMRF model. Unlike the IMRF model, the OCBF frame shows a notable drop in collapse margin ratio because of pounding to moat wall at 30 in gap distance and requires increasing gap distance to 35 in to have acceptable collapse probability. Increasing the minimum gap distance for the OCBF model requires extra caution regarding design of base isolation devices to make sure that isolators can reach to this displacement without any local failure.

The gap distances below the 30 in. leads to decreasing the collapse margin ratio below the accepted number. The trend for decreasing of ACMR is similar for both models and shows 20% drop because of reducing the gap distance to 20 in gap distance (67% of required gap distance by ASCE7-05).

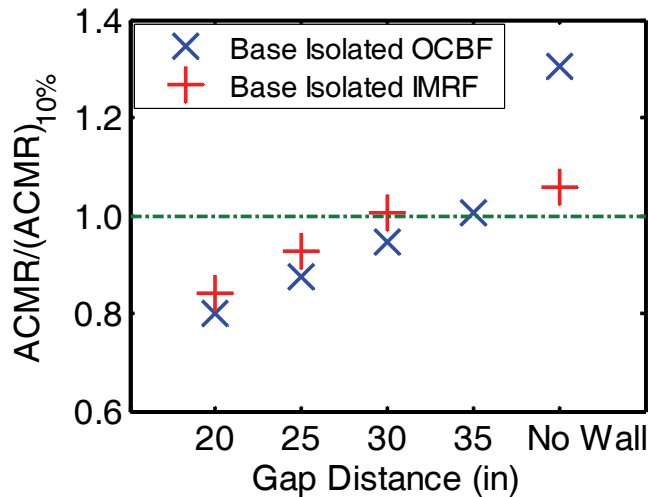


**Figure 8-16 Ratio of adjusted collapse margin ratio (ACMR) to accepted ACMR for 10% probability of collapse**

## **SECTION 9**

### **SUMMARY AND CONCLUSION**

A typical base isolated building design requires a clear space in the basement in which the building is free to move sideways without hitting the surrounding walls. This space is commonly referred to as the "moat". Structural design codes such as the International Building Code (ICC 2006) and ASCE 7-05 (ASCE 2005) require the minimum moat wall distance equal to maximum displacement of the base isolated structure under maximum considerable earthquake ( $D_{TM}$ ) although the superstructure is designed for design basis earthquake (DBE). Despite the cautious regulation for moat wall gap distance, pounding of base isolated building to moat wall has been reported in previous earthquakes and can be expected for future extreme earthquakes.

The pounding problem between adjacent buildings structures and highway bridge segments has been a major cause of seismic damage, even collapse, of civil infrastructures during earthquakes in the past several decades. Pounding incidences between fixed-supported buildings due to strong earthquakes motivated relevant research, which led to seismic-code reforms in order to mitigate the risks from poundings of adjacent fixed base structures. However, very limited research work has been carried out for poundings of seismically isolated buildings, which exhibit quite different dynamic characteristics from fixed base buildings.

This study investigated the pounding phenomenon in base isolated buildings from both experimental and analytical perspectives by conducting shake table pounding experiments, determining effective ways to model impact to moat walls and evaluating the adequacy of code specified gap distance of moat walls. The goal of this study was to determine the effect of pounding on the global response of base isolated buildings through conducting realistic experimental testing and the development of reliable analytical models for moat wall pounding. For the first time, a series of shake table experiments were conducted on base isolated buildings against moat walls of various stiffness and set at various distance in order to investigate the effects on superstructure response. The experimental results led to the development of a new impact element for moat walls and a comprehensive comparative study of base isolated building considering pounding to moat walls.

Two 3-story base isolated buildings were designed by professional engineers for studies carried out as part of the NEES TIPS project. The intermediate moment resistant frame (IMRF) structure has a fundamental period of 1.4 sec while ordinary concentric braced (OCBF) model is much stiffer with fundamental period of 0.39 sec under fixed base conditions. By implementing the seismic isolation system both structural systems experience an increasing of the fundamental period to 3.1 sec. The total maximum displacement for both base isolated models which are located at highest seismic zone in the United States, are approximately equal to 30 in.

The base isolated IMRF model was selected for the experimental program due to availability of scaled members and simplicity in fabrication. The test program consists of shake table testing of a quarter-scale model representative of the three-story IMRF using the NEES equipment site at the Structural Engineering and Earthquake Simulation Laboratory (SEESL) at the University at Buffalo. The principal objective of these experiments was to generate experimental data for base isolated building pounding a moat wall, specifically the impact force and the superstructure response. This data is subsequently used to validate the numerical models of structural pounding. These experiments generated a unique data set on structural pounding including the behavior of a base isolated building impacting different types of moat wall installed at different gap distance.

The shake table testing occurred in three phases. The first stage examined the response of fixed-base three-story IMRF model. The data generated in this phase was used to validate a numerical model of the IMRF and also examined the response of superstructure in the inelastic range. In the second phase, isolation devices were installed at the base level of the IMRF model and the response of base isolated model was examined under different levels of ground motion. The third and last phase of the testing examine the response of the base isolated three-story IMRF including pounding to a moat wall. For this purpose, different types of moat walls were installed at various gap distances relative to base level of isolated model and different ground motions were applied to capture the variation in response with moat wall stiffness and impact velocity. The conclusions based on experimental observations are as follows:

1. The pounding experiments indicate that the contact forces generated during pounding can induce yielding in the superstructure and amplify the response acceleration at all stories

of the building. The response amplification and damage depends on the gap distance, moat wall properties, and impact velocity.

2. Acceleration response in the superstructure increased almost uniformly at all stories, except for the larger amplification at the base level where pounding occurred. The acceleration amplification captured by instrumentation consisted of rigid body motion and also internal wave propagation in the steel plates, in addition to potential excitation of the instrument itself.
3. Peak story drift ratios increased uniformly at all stories for softer pounding experiments with more flexible walls or lower impact velocities. As the pounding forces increased, increased drifts were observed throughout the structure with substantially larger amplifications in upper floors. Although peak story drift ratios obtained in pounding experiments shows moderate yielding in the superstructure, larger drifts were observed for the same structure under fixed base condition.
4. In a collision between the base level of an isolated structure and a moat wall as observed in the experiments, contact between two objects consists of two phases: the first local material indentation phase followed by the second global dynamic response phase. The contact forces generated are dependent on geometry and material properties at the point of contact for the first phase and global dynamic characteristic of two objects in the second phase. Test results show that the response of the isolated superstructure is more sensitive to the longer duration dynamic global phase, dependent on the properties of the wall.

To better understand the consequences of impact on the superstructure, a 2 dimensional (2D) impact element considering moat wall flexibility was proposed based on impact theory and observations during experimental simulations. It was demonstrated that numerical simulations using the proposed impact element can capture the dominant characteristics of the contact force observed in experiments of base isolated buildings impacting various moat wall configurations including concrete walls with soil backfill and rigid steel walls. The contact force is dependent on impact velocity, geometry and material properties at the contact surface, as well as the global dynamic characteristic of the moat wall. The required parameters in this impact element are

derived based on mechanics-based models considering material properties and geometric measurements of the experimental setup. The conclusions based on proposed impact element and comparisons with experimental results are as follows:

5. A new impact element was proposed to simulate the effects of the two impact phases. The required equations to determine model parameters were derived for a generic moat wall considering nonlinear response in the moat wall and soil backfill. The numerical simulation of impact force was validated by comparison to experimental results for different wall types and gap distances.
6. The experimental and numerical simulation of impact force for different moat wall types show that soil backfill and formation of a plastic hinge at the moat wall base contribute significantly towards damping the impact energy.
7. Sensitivity analysis conducted show that the maximum change in superstructure response is less than 7% due to a 50% change in impact model parameters. These studies demonstrate that the simplified impact model can provide reasonable results considering uncertainty in assigning model parameters.

The proposed 2D impact element was extended to a 3D impact element to capture the collision between the base level of a 3D base isolated building to a moat wall. The response of 3-story IMRF and OCBF prototype models were examined considering impact to a surrounding moat wall at the base level by implementing the proposed impact element to finite element models of the buildings. The effect of pounding to moat wall in both prototype buildings were investigated by comparing the superstructure response with and without presence of the moat wall under 20 ground motions from the NEES TIPS project scaled to MCE event. This study provided critical information for the design of base isolated buildings, particularly the moat wall clearance and its potential effect on the superstructure response.

8. Response of a minimally code-compliant IMRF based isolated structure without considering pounding to moat walls does not satisfying at MCE event. Large story drift ratio and yielding occurs in the building at this level of shaking. Pounding to moat walls worsen this situation for the IMRF model. A more robust design is necessary for this

model to improve its performance in a rare earthquake. One suggestion in this regard could be designing a stiffer superstructure which leads to larger period shifting by considering the base isolation system or decreasing R factor to design for higher base shear.

9. Although the response of the isolated OCBF is better compared with the IMRF for the case without moat walls, wherein the median demands for story drifts are substantially lower than those of the IMRF, pounding to moat walls makes a significant change in this behavior resulting in large median SDR with huge dispersions. Brace buckling and significant inelastic response were observed in all the motions inducing pounding to moat walls.
10. It can be concluded that pounding to moat walls worsens the response of both frames in terms of both acceleration and SDR, although this effect is worse for stiff OCBF frame.

A series of collapse studies using the fragility curve concept was conducted for both prototype models and for various gap distances. The objective of this study was to evaluate the collapse probability of the base isolated models used in this study and also investigate the effect of moat wall gap distance on the probability of collapse for base isolated structures. For this purpose the Methodology presented in FEMA P695 was utilized resulting in following conclusion:

11. The OCBF model without moat wall shows more conservative collapse probability (2%) in comparison to the IMRF model (8.1%) which is slightly below the accepted ratio (10%). Considering moat wall in collapse evaluation analysis changes these margin ratios. Installing moat wall at 30 in gap distance which is equal to total maximum displacement of base isolated model and is minimum required gap distance by ASCE7-05 results in increasing the probability of collapse for OCBF frame to 12.9% but it is still slightly less than the accepted value for the IMRF model (9.7%).
12. These studies verify that pounding to moat wall at required gap distance by ASCE7-05 result in acceptable probability of collapse for flexible and ductile IMRF model. However, the OCBF frame shows a notable drop in collapse margin ratio because of pounding to moat wall at 30 in gap distance and requires a gap distance of 35 in. to have acceptable collapse probability.

13. The gap distances below the 30 in lead to decreasing the collapse margin ratio below the accepted number for both models. The trend for increasing of collapse probability is similar for both models and shows 20% increase for reducing the gap distance to 20 in (67% of required gap distance by ASCE7-05).

The present study could be complemented with additional research in the following areas:

- Large scale experimental shake table testing of 3D base isolated buildings to study the effects of pounding. This testing program should include moat walls in all directions and at least two horizontal components of ground motion should be applied simultaneously.
- More base isolated archetypes should be examined for pounding to moat walls and evaluated based on the reference gap distance by ASCE 7-05 and the requirement for minimum moat wall distance should be modified based on the results obtained in this study, if necessary.
- The efficacy of pounding reduction devices such as shock absorbers and additional dampers between superstructure segments needs to be examined using analytical methods and validated using experimental techniques.

## SECTION 10

### REFERENCES

- American Institute of Steel Construction (AISC). (2005). Seismic provisions for structural steel buildings, AISC 341-05. Chicago, IL.
- Anagnostopoulos, S. A. and Spiliopoulos, K. V. (1992). "An Investigation of Earthquake Induced Pounding between Adjacent Buildings." *Earthquake Engineering & Structural Dynamics* **21**(4): 289-302.
- Anderson, E. and Mahin, S. A. (1998). Displacement-based design of seismically isolated bridges. Proc. of the Sixth U.S. National Conference on Earthquake Engineering. Oakland, California.
- Arnold, C. (2009). "Seismic Safety of the Building Envelope." *National Institute of Building Science*.
- American Society of Civil Engineers (ASCE). (2005). Minimum Design Loads for Buildings And Other Structures. SEI/ASCE 7-05.
- Bracci, J. M., Reinhorn, A. M. and Mander, J. B. (1992). "Seismic Resistance of Reinforced Concrete Frame Structures Designed Only for Gravity Loads: Part I - Design and Properties of a One-third Scale Model Structure." *Technical Report: NCEER-92-0027*, National Center for Earthquake Engineering Research, State University of New York at Buffalo, Buffalo, NY, USA.
- Chau, K. T., Wei, X. X., Guo, X. and Shen, C. Y. (2003). "Experimental and theoretical simulations of seismic poundings between two adjacent structures." *Earthquake Engineering & Structural Dynamics* **32**(4): 537-554.
- Chiou, B., Darragh, R., Gregor, N. and Silva, W. (2008). "NGA Project Strong-Motion Database." *Earthquake Spectra* **24**(1): 23-44.
- Chopra, A. K. and Goel, R. K. (2000). "Evaluation of NSP to estimate seismic deformation: SDF systems." *Journal of Structural Engineering-Asce* **126**(4): 482-490.
- Constantinou, M. C., Kalpakidis, I., Filiatrault, A. and Lay, R. A. E. (2011). "LRFD-Based Analysis and Design Procedures for Bridge Bearings and Seismic Isolators." *Technical*

- Report: MCEER-11-0004*, Multidisciplinary Center for Earthquake Engineering Research, Buffalo, NY.
- Constantinou, M. C., Whittaker, A. S., Kalpakidis, Y., Fenz, D. M. and Warn, G. P. (2007). "Performance of Seismic Isolation Hardware under Service and Seismic Loading." *Technical Report: MCEER-07-0012*, Multidisciplinary Center for Earthquake Engineering Research, Buffalo, NY.
- DesRoches, R. and Fenves, G. L. (1997). "New Design and Analysis Procedures for Intermediate Hinges in Multiple Frame Bridges." *Technical Report: Report No. UCB/EERC-97/12*, Earthquake Engineering Research Center, University of California, Berkeley.
- Dicleli, M. and Buddaram, S. (2007). "Comprehensive evaluation of equivalent linear analysis method for seismic-isolated structures represented by sdof systems." *Engineering Structures* **29**(8): 1653-1663.
- Earthquake Engineering Research Institute (EERI) (1995a). "Northridge Earthquake Reconnaissance Report." Earthquake Engineering Research Institute.
- Earthquake Engineering Research Institute (EERI) (1995b). "The Hyogo-Ken Nanbu Earthquake Reconnaissance Report." Earthquake Engineering Research Institute.
- Earthquake Engineering Research Institute (EERI) (2000). "1999 Kocaeli, Turkey, Earthquake Reconnaissance Report." Earthquake Engineering Research Institute.
- Earthquake Engineering Research Institute (EERI) (2001). "1999 Chi-Chi, Taiwan, Earthquake Reconnaissance Report." Earthquake Engineering Research Institute.
- Erduran, E., Dao, N. D. and Ryan, K. L. (2011). "Comparative response assessment of minimally compliant low-rise conventional and base-isolated steel frames." *Earthquake Engineering & Structural Dynamics* **40**(10): 1123-1141.
- Fajfar, P. (1999). "Capacity spectrum method based on inelastic demand spectra." *Earthquake Engineering & Structural Dynamics* **28**(9): 979-993.
- Faraji, S., Ting, J. M., Crovo, D. S. and Ernst, H. (2001). "Nonlinear analysis of integral bridges: Finite-element model." *Journal of Geotechnical and Geoenvironmental Engineering* **127**(5): 454-461.
- Federal Emergency Management Agency (FEMA). (1997). NEHRP GUIDELINES FOR THE SEISMIC REHABILITATION OF BUILDINGS. FEMA 273, Washington, DC.

- Federal Emergency Management Agency (FEMA). (2000a). State of the art report on systems performance of steel moment frames subjected to earthquake ground shaking. FEMA 355-C, Washington, DC.
- Federal Emergency Management Agency (FEMA). (2000b). State of the art report on connection performance. FEMA 355-D, Washington, DC.
- Federal Emergency Management Agency (FEMA). (2000c). Recommended Seismic Design Criteria for New Steel Moment-Frame Buildings. FEMA 350, Washington, DC.
- Federal Emergency Management Agency (FEMA). (2009a). Guidelines for Seismic Performance Assessment of Buildings. Washington, DC.
- Federal Emergency Management Agency (FEMA). (2009b). Quantification of building seismic performance factors. FEMA P695, Washington, DC.
- Filiatrault, A., Wagner, P. and Cherry, S. (1995). "Analytical Prediction of Experimental Building Pounding." *Earthquake Engineering & Structural Dynamics* **24**(8): 1131-1154.
- Franchin, P., Monti, G. and Pinto, P. E. (2001). "On the accuracy of simplified methods for the analysis of isolated bridges." *Earthquake Engineering & Structural Dynamics* **30**(3): 363-382.
- Frankel, A. D., Mueller, C. S., Barnhard, T. P., Leyendecker, E. V., Wesson, R. L., Harmsen, S. C., Klein, F. W., Perkins, D. M., Dickman, N. C., Hanson, S. L. and Hopper, M. G. (2000). "USGS National Seismic Hazard Maps." *Earthquake Spectra* **16**(1): 1-19.
- Gadre, A. and Dobry, R. (1998). "Lateral cyclic loading centrifuge tests on square embedded footing." *Journal of Geotechnical and Geoenvironmental Engineering* **124**(11): 1128-1138.
- Gavin, H. P. and Nigbor, R. L. (2012). Performance of the Base-Isolated Christchurch Women's Hospital in the September 4, 2010, Darfield Earthquake and the February 22, 2011, Christchurch Earthquake. 20th Analysis and Computation Specialty Conference: 554-563.
- Gavin, H. P. and Wilkinson, G. (2010). "Preliminary observations of the effects of the 2010 darfield earthquake on the base-isolated christchurch women's hospital." *Bulletin of the New Zealand Society for Earthquake Engineering* **43**(4): 360-367.
- Goldsmith, W. (2001). Impact: the Theory and Physical Behavior of Colliding Solids. New York, Dover Publication.

- Guo, A. X., Li, Z. J., Li, H. and Ou, J. P. (2009). "Experimental and analytical study on pounding reduction of base-isolated highway bridges using MR dampers." *Earthquake Engineering & Structural Dynamics* **38**(11): 1307-1333.
- Gupta, A. and Krawinkler, H. (1999). "Seismic demands for performance evaluation of steel moment resisting frame structures." *Technical Report: 132*, John A. Blume Earthquake Engineering Center, Dep. of Civil Engineering, Stanford University.
- Hilber, H. M., Hughes, T. J. R. and Taylor, R. L. (1977). "Improved Numerical Dissipation for Time Integration Algorithms in Structural Dynamics." *Earthquake Engineering & Structural Dynamics* **5**(3): 283-292.
- Hunt, K. H. and Crossley, F. R. E. (1975). "Coefficient of Restitution Interpreted as Damping in Vibroimpact." *Journal of Applied Mechanics-Transactions of the Asme* **42**(2): 440-445.
- Ibarra, L. F. and Krawinkler, H. (2005). "Global collapse of frame structures under seismic excitation." *Technical Report: 152*, John A. Blume Earthquake Engineering Center, Dep. of Civil Engineering, Stanford University.
- International Code Council (ICC). (2006). International Building Code (IBC). Falls Church, VA.
- Jankowski, R. (2007). "Theoretical and experimental assessment of parameters for the non-linear viscoelastic model of structural pounding." *Journal of Theoretical and Applied Mechanics* **45**(4): 931-942.
- Jankowski, R. (2010). "Experimental study on earthquake-induced pounding between structural elements made of different building materials." *Earthquake Engineering & Structural Dynamics* **39**(3): 343-354.
- Jankowski, R., Wilde, K. and Fujino, Y. (1998). "Pounding of superstructure segments in isolated elevated bridge during earthquakes." *Earthquake Engineering & Structural Dynamics* **27**(5): 487-502.
- Komodromos, P., Polycarpou, P. C., Papaloizou, L. and Phocas, M. C. (2007). "Response of seismically isolated buildings considering poundings." *Earthquake Engineering & Structural Dynamics* **36**(12): 1605-1622.
- Kusumastuti, D., Reinhorn, A. M. and Rutenberg, A. (2005). "A versatile experimentation model for study of structures near collapse." *Technical Report: MCEER-0002*, Multidisciplinary Center for Earthquake Engineering Research, Buffalo, NY.

- Lankarani, H. M. and Nikraves, P. E. (1990). "A Contact Force Model with Hysteresis Damping for Impact Analysis of Multibody Systems." *Journal of Mechanical Design* **112**(3): 369-376.
- Lignos, D. G. and Krawinkler, H. (2011). "Deterioration Modeling of Steel Components in Support of Collapse Prediction of Steel Moment Frames under Earthquake Loading." *Journal of Structural Engineering* **137**(11): 1291-1302.
- Luco, J. E., Ozcelik, O. and Conte, J. P. (2010). "Acceleration Tracking Performance of the UCSD-NEES Shake Table." *Journal of Structural Engineering-Asce* **136**(5): 481-490.
- Maison, B. F. and Kasai, K. (1992). "Dynamics of Pounding When 2 Buildings Collide." *Earthquake Engineering & Structural Dynamics* **21**(9): 771-786.
- Malhotra, P. K. (1997). "Dynamics of seismic impacts in base-isolated buildings." *Earthquake Engineering & Structural Dynamics* **26**(8): 797-813.
- Malhotra, P. K. (1998). "Dynamics of seismic pounding at expansion joints of concrete bridges." *Journal of Engineering Mechanics (ASCE)* **124**(7): 794-802.
- Marhefka, D. W. and Orin, D. E. (1999). "A compliant contact model with nonlinear damping for simulation of robotic systems." *Ieee Transactions on Systems Man and Cybernetics Part a-Systems and Humans* **29**(6): 566-572.
- Matsagar, V. A. and Jangid, R. S. (2003). "Seismic response of base-isolated structures during impact with adjacent structures." *Engineering Structures* **25**(10): 1311-1323.
- McKenna, F., Fenves, G. and Scott, M. (2000). "Open System for Earthquake Engineering Simulation (OpenSees)." *University of California, Berkeley, CA*.
- Mosqueda, G., Whittaker, A. S., Fenves, G. L. and Mahin, S. A. (2004). "Experimental and Analytical Studies of The Friction Pendulum System for the Seismic Protection of Simple Bridges." *Technical Report: UCB/EERC 2001-01*, University of California, Berkeley, Berkeley, CA, USA.
- Muthukumar, S. (2003). A Contact Element Approach with Hysteresis Damping for the Analysis and Design of Pounding in Bridges. PhD, Georgia Institute of Technology.
- Muthukumar, S. and DesRoches, R. (2006). "A Hertz contact model with non-linear damping for pounding simulation." *Earthquake Engineering & Structural Dynamics* **35**(7): 811-828.
- Nagarajaiah, S. and Sun, X. H. (2001). "Base-isolated FCC building: Impact response in Northridge earthquake." *Journal of Structural Engineering (ASCE)* **127**(9): 1063-1075.

- Nakashima, M., Mahin, S. A., Furukawa, S. and Becker, T. C. (2010). Comparison of US and Japanese Codes and Practices for Seismically Isolated Buildings. Structures Congress 2010: 2330-2338.
- Nowak, R. F., Kusner, D. A., Larson, R. L. and Thoen, B. K. (2000). Utilizing modern digital signal processing for improvement of shaking table performance. Proc. of 12th WCEE. Aukland.
- Pant, D. R. and Wijeyewickrema, A. C. (2012). "Structural performance of a base-isolated reinforced concrete building subjected to seismic pounding." *Earthquake Engineering & Structural Dynamics* **41**(12): 1709-1716.
- Papadrakakis, M., Mouzakis, H., Plevris, N. and Bitzarakis, S. (1991). "A Lagrange Multiplier Solution Method for Pounding of Buildings during Earthquakes." *Earthquake Engineering & Structural Dynamics* **20**(11): 981-998.
- Priestley, M. J. N., Calvi, G. M. and Seible, F. (1996). Seismic design and retrofit of bridges. New York [u.a., Wiley.
- Rosenblueth, E. (1986). "The Mexican Earthquake - a Firsthand Report." *Civil Engineering* **56**(1): 38-40.
- Ryan, K. L., Mahin, S. A. and Mosqueda, G. (2008). Introduction to NEES TIPS: Tools for Isolation and Protective Systems. Structures Congress 2008: 1-16.
- Ryan, K. L. and Polanco, J. (2008). "Problems with Rayleigh Damping in Base-Isolated Buildings." *Journal of Structural Engineering-Asce* **134**(11): 1780-1784.
- Sato, E., Furukawa, S., Kakehi, A. and Nakashima, M. (2011). "Full-scale shaking table test for examination of safety and functionality of base-isolated medical facilities." *Earthquake Engineering & Structural Dynamics* **40**(13): 1435-1453.
- Sayani, P. J., Erduran, E. and Ryan, K. L. (2011). "Comparative response assessment of minimally compliant low-rise base-isolated and conventional steel moment-resisting frame buildings." *Journal of Structural Engineering* **137**(10): 1118-1131.
- Scott, M. H. and Fenves, G. L. (2006). "Plastic hinge integration methods for force-based beam-column elements." *Journal of Structural Engineering* **132**: 244.
- Scott, R. F. (1973). Earthquake-Induced Earth Pressures on Retaining Walls. 5th World Conference on Earthquake Engineering. Rome, Italy. **2**: 1560-1569.

- Shakal, A., Huang, M., Darragh, R., Cao, T., Sherburne, R., Malhotra, P., Cramer, C., R., S., Graizer, V., Maldonado, G., Petersen, C. and Wampole, J. (1994). "CSMIP Strong-Motion Records from the Northridge, California Earthquake of January 17, 1994." *Technical Report: OSMS. 94-07*, California Strong Motion Instrumentation Program, Division of Mines and Geology, Sacramento, CA.
- Shamsabadi, A., Khalili-Tehrani, P., Stewart, J. P. and Taciroglu, E. (2010). "Validated Simulation Models for Lateral Response of Bridge Abutments with Typical Backfills." *Journal of Bridge Engineering* **15**(3): 302-311.
- Shamsabadi, A., Rollins, K. M. and Kapuskar, M. (2007). "Nonlinear soil-abutment-bridge structure interaction for seismic performance-based design." *Journal of Geotechnical and Geoenvironmental Engineering* **133**(6): 707-720.
- Siddharthan, R. V. and El-Gamal, M. (1998). "Permanent rotational deformation of dry cohesionless slopes under seismic excitations." *Liquefaction, Differential Settlement, and Foundation Engineering*(1633): 45-50.
- Somerville, P., Anderson, D., Sun, J., Punyamurthula, S. and Smith, N. (1998). Generation of ground motion time histories for performance-based seismic engineering. 6th U.S. National Conf. of Earthquake Engineering. Seattle, Washington.
- Sun, H., Li, B., Bi, K., Chouw, N., Butterworth, J. W. and Hao, H. (2011). Shake table test of a three-span bridge model. Ninth Pacific Conference on Earthquake Engineering Building an Earthquake-Resilient Society. Auckland, New Zealand.
- Tsai, H. C. (1997). "Dynamic analysis of base-isolated shear beams bumping against stops." *Earthquake Engineering & Structural Dynamics* **26**(5): 515-528.
- Uriz, P., Filippou, F. C. and Mahin, S. A. (2008). "Model for cyclic inelastic buckling of steel braces." *Journal of Structural Engineering-Asce* **134**(4): 619-628.
- Vamvatsikos, D. and Cornell, C. A. (2002). "Incremental dynamic analysis." *Earthquake Engineering & Structural Dynamics* **31**(3): 491-514.
- Vlassis, A. G., Maragakis, E. and Saiidi, M. (2001). "Update on analytical and experimental research on bridge restrainers." *Design of Structures*(1770): 132-138.
- Wolf, J. P. and Skrikerud, P. E. (1980). "Mutual Pounding of Adjacent Structures during Earthquakes." *Nuclear Engineering and Design* **57**(2): 253-275.

- Ye, K., Li, L. and Zhu, H. P. (2009). "A note on the Hertz contact model with nonlinear damping for pounding simulation." *Earthquake Engineering & Structural Dynamics* **38**(9): 1135-1142.
- Zareian, F. and Medina, R. A. (2010). "A practical method for proper modeling of structural damping in inelastic plane structural systems." *Computers & Structures* **88**(1-2): 45-53.

## MCEER Technical Reports

MCEER publishes technical reports on a variety of subjects written by authors funded through MCEER. These reports are available from both MCEER Publications and the National Technical Information Service (NTIS). Requests for reports should be directed to MCEER Publications, MCEER, University at Buffalo, State University of New York, 133A Ketter Hall, Buffalo, New York 14260. Reports can also be requested through NTIS, P.O. Box 1425, Springfield, Virginia 22151. NTIS accession numbers are shown in parenthesis, if available.

- NCEER-87-0001 "First-Year Program in Research, Education and Technology Transfer," 3/5/87, (PB88-134275, A04, MF-A01).
- NCEER-87-0002 "Experimental Evaluation of Instantaneous Optimal Algorithms for Structural Control," by R.C. Lin, T.T. Soong and A.M. Reinhorn, 4/20/87, (PB88-134341, A04, MF-A01).
- NCEER-87-0003 "Experimentation Using the Earthquake Simulation Facilities at University at Buffalo," by A.M. Reinhorn and R.L. Ketter, not available.
- NCEER-87-0004 "The System Characteristics and Performance of a Shaking Table," by J.S. Hwang, K.C. Chang and G.C. Lee, 6/1/87, (PB88-134259, A03, MF-A01). This report is available only through NTIS (see address given above).
- NCEER-87-0005 "A Finite Element Formulation for Nonlinear Viscoplastic Material Using a Q Model," by O. Gyebe and G. Dasgupta, 11/2/87, (PB88-213764, A08, MF-A01).
- NCEER-87-0006 "Symbolic Manipulation Program (SMP) - Algebraic Codes for Two and Three Dimensional Finite Element Formulations," by X. Lee and G. Dasgupta, 11/9/87, (PB88-218522, A05, MF-A01).
- NCEER-87-0007 "Instantaneous Optimal Control Laws for Tall Buildings Under Seismic Excitations," by J.N. Yang, A. Akbarpour and P. Ghaemmaghami, 6/10/87, (PB88-134333, A06, MF-A01). This report is only available through NTIS (see address given above).
- NCEER-87-0008 "IDARC: Inelastic Damage Analysis of Reinforced Concrete Frame - Shear-Wall Structures," by Y.J. Park, A.M. Reinhorn and S.K. Kunnath, 7/20/87, (PB88-134325, A09, MF-A01). This report is only available through NTIS (see address given above).
- NCEER-87-0009 "Liquefaction Potential for New York State: A Preliminary Report on Sites in Manhattan and Buffalo," by M. Budhu, V. Vijayakumar, R.F. Giese and L. Baumgras, 8/31/87, (PB88-163704, A03, MF-A01). This report is available only through NTIS (see address given above).
- NCEER-87-0010 "Vertical and Torsional Vibration of Foundations in Inhomogeneous Media," by A.S. Veletsos and K.W. Dotson, 6/1/87, (PB88-134291, A03, MF-A01). This report is only available through NTIS (see address given above).
- NCEER-87-0011 "Seismic Probabilistic Risk Assessment and Seismic Margins Studies for Nuclear Power Plants," by Howard H.M. Hwang, 6/15/87, (PB88-134267, A03, MF-A01). This report is only available through NTIS (see address given above).
- NCEER-87-0012 "Parametric Studies of Frequency Response of Secondary Systems Under Ground-Acceleration Excitations," by Y. Yong and Y.K. Lin, 6/10/87, (PB88-134309, A03, MF-A01). This report is only available through NTIS (see address given above).
- NCEER-87-0013 "Frequency Response of Secondary Systems Under Seismic Excitation," by J.A. HoLung, J. Cai and Y.K. Lin, 7/31/87, (PB88-134317, A05, MF-A01). This report is only available through NTIS (see address given above).
- NCEER-87-0014 "Modelling Earthquake Ground Motions in Seismically Active Regions Using Parametric Time Series Methods," by G.W. Ellis and A.S. Cakmak, 8/25/87, (PB88-134283, A08, MF-A01). This report is only available through NTIS (see address given above).
- NCEER-87-0015 "Detection and Assessment of Seismic Structural Damage," by E. DiPasquale and A.S. Cakmak, 8/25/87, (PB88-163712, A05, MF-A01). This report is only available through NTIS (see address given above).

- NCEER-87-0016 "Pipeline Experiment at Parkfield, California," by J. Isenberg and E. Richardson, 9/15/87, (PB88-163720, A03, MF-A01). This report is available only through NTIS (see address given above).
- NCEER-87-0017 "Digital Simulation of Seismic Ground Motion," by M. Shinozuka, G. Deodatis and T. Harada, 8/31/87, (PB88-155197, A04, MF-A01). This report is available only through NTIS (see address given above).
- NCEER-87-0018 "Practical Considerations for Structural Control: System Uncertainty, System Time Delay and Truncation of Small Control Forces," J.N. Yang and A. Akbarpour, 8/10/87, (PB88-163738, A08, MF-A01). This report is only available through NTIS (see address given above).
- NCEER-87-0019 "Modal Analysis of Nonclassically Damped Structural Systems Using Canonical Transformation," by J.N. Yang, S. Sarkani and F.X. Long, 9/27/87, (PB88-187851, A04, MF-A01).
- NCEER-87-0020 "A Nonstationary Solution in Random Vibration Theory," by J.R. Red-Horse and P.D. Spanos, 11/3/87, (PB88-163746, A03, MF-A01).
- NCEER-87-0021 "Horizontal Impedances for Radially Inhomogeneous Viscoelastic Soil Layers," by A.S. Veletsos and K.W. Dotson, 10/15/87, (PB88-150859, A04, MF-A01).
- NCEER-87-0022 "Seismic Damage Assessment of Reinforced Concrete Members," by Y.S. Chung, C. Meyer and M. Shinozuka, 10/9/87, (PB88-150867, A05, MF-A01). This report is available only through NTIS (see address given above).
- NCEER-87-0023 "Active Structural Control in Civil Engineering," by T.T. Soong, 11/11/87, (PB88-187778, A03, MF-A01).
- NCEER-87-0024 "Vertical and Torsional Impedances for Radially Inhomogeneous Viscoelastic Soil Layers," by K.W. Dotson and A.S. Veletsos, 12/87, (PB88-187786, A03, MF-A01).
- NCEER-87-0025 "Proceedings from the Symposium on Seismic Hazards, Ground Motions, Soil-Liquefaction and Engineering Practice in Eastern North America," October 20-22, 1987, edited by K.H. Jacob, 12/87, (PB88-188115, A23, MF-A01). This report is available only through NTIS (see address given above).
- NCEER-87-0026 "Report on the Whittier-Narrows, California, Earthquake of October 1, 1987," by J. Pantelic and A. Reinhorn, 11/87, (PB88-187752, A03, MF-A01). This report is available only through NTIS (see address given above).
- NCEER-87-0027 "Design of a Modular Program for Transient Nonlinear Analysis of Large 3-D Building Structures," by S. Srivastav and J.F. Abel, 12/30/87, (PB88-187950, A05, MF-A01). This report is only available through NTIS (see address given above).
- NCEER-87-0028 "Second-Year Program in Research, Education and Technology Transfer," 3/8/88, (PB88-219480, A04, MF-A01).
- NCEER-88-0001 "Workshop on Seismic Computer Analysis and Design of Buildings With Interactive Graphics," by W. McGuire, J.F. Abel and C.H. Conley, 1/18/88, (PB88-187760, A03, MF-A01). This report is only available through NTIS (see address given above).
- NCEER-88-0002 "Optimal Control of Nonlinear Flexible Structures," by J.N. Yang, F.X. Long and D. Wong, 1/22/88, (PB88-213772, A06, MF-A01).
- NCEER-88-0003 "Substructuring Techniques in the Time Domain for Primary-Secondary Structural Systems," by G.D. Manolis and G. Juhn, 2/10/88, (PB88-213780, A04, MF-A01).
- NCEER-88-0004 "Iterative Seismic Analysis of Primary-Secondary Systems," by A. Singhal, L.D. Lutes and P.D. Spanos, 2/23/88, (PB88-213798, A04, MF-A01).
- NCEER-88-0005 "Stochastic Finite Element Expansion for Random Media," by P.D. Spanos and R. Ghanem, 3/14/88, (PB88-213806, A03, MF-A01).

- NCEER-88-0006 "Combining Structural Optimization and Structural Control," by F.Y. Cheng and C.P. Pantelides, 1/10/88, (PB88-213814, A05, MF-A01).
- NCEER-88-0007 "Seismic Performance Assessment of Code-Designed Structures," by H.H-M. Hwang, J-W. Jaw and H-J. Shau, 3/20/88, (PB88-219423, A04, MF-A01). This report is only available through NTIS (see address given above).
- NCEER-88-0008 "Reliability Analysis of Code-Designed Structures Under Natural Hazards," by H.H-M. Hwang, H. Ushiba and M. Shinozuka, 2/29/88, (PB88-229471, A07, MF-A01). This report is only available through NTIS (see address given above).
- NCEER-88-0009 "Seismic Fragility Analysis of Shear Wall Structures," by J-W Jaw and H.H-M. Hwang, 4/30/88, (PB89-102867, A04, MF-A01).
- NCEER-88-0010 "Base Isolation of a Multi-Story Building Under a Harmonic Ground Motion - A Comparison of Performances of Various Systems," by F-G Fan, G. Ahmadi and I.G. Tadjbakhsh, 5/18/88, (PB89-122238, A06, MF-A01). This report is only available through NTIS (see address given above).
- NCEER-88-0011 "Seismic Floor Response Spectra for a Combined System by Green's Functions," by F.M. Lavelle, L.A. Bergman and P.D. Spanos, 5/1/88, (PB89-102875, A03, MF-A01).
- NCEER-88-0012 "A New Solution Technique for Randomly Excited Hysteretic Structures," by G.Q. Cai and Y.K. Lin, 5/16/88, (PB89-102883, A03, MF-A01).
- NCEER-88-0013 "A Study of Radiation Damping and Soil-Structure Interaction Effects in the Centrifuge," by K. Weissman, supervised by J.H. Prevost, 5/24/88, (PB89-144703, A06, MF-A01).
- NCEER-88-0014 "Parameter Identification and Implementation of a Kinematic Plasticity Model for Frictional Soils," by J.H. Prevost and D.V. Griffiths, not available.
- NCEER-88-0015 "Two- and Three- Dimensional Dynamic Finite Element Analyses of the Long Valley Dam," by D.V. Griffiths and J.H. Prevost, 6/17/88, (PB89-144711, A04, MF-A01).
- NCEER-88-0016 "Damage Assessment of Reinforced Concrete Structures in Eastern United States," by A.M. Reinhorn, M.J. Seidel, S.K. Kunnath and Y.J. Park, 6/15/88, (PB89-122220, A04, MF-A01). This report is only available through NTIS (see address given above).
- NCEER-88-0017 "Dynamic Compliance of Vertically Loaded Strip Foundations in Multilayered Viscoelastic Soils," by S. Ahmad and A.S.M. Israil, 6/17/88, (PB89-102891, A04, MF-A01).
- NCEER-88-0018 "An Experimental Study of Seismic Structural Response With Added Viscoelastic Dampers," by R.C. Lin, Z. Liang, T.T. Soong and R.H. Zhang, 6/30/88, (PB89-122212, A05, MF-A01). This report is available only through NTIS (see address given above).
- NCEER-88-0019 "Experimental Investigation of Primary - Secondary System Interaction," by G.D. Manolis, G. Juhn and A.M. Reinhorn, 5/27/88, (PB89-122204, A04, MF-A01).
- NCEER-88-0020 "A Response Spectrum Approach For Analysis of Nonclassically Damped Structures," by J.N. Yang, S. Sarkani and F.X. Long, 4/22/88, (PB89-102909, A04, MF-A01).
- NCEER-88-0021 "Seismic Interaction of Structures and Soils: Stochastic Approach," by A.S. Veletsos and A.M. Prasad, 7/21/88, (PB89-122196, A04, MF-A01). This report is only available through NTIS (see address given above).
- NCEER-88-0022 "Identification of the Serviceability Limit State and Detection of Seismic Structural Damage," by E. DiPasquale and A.S. Cakmak, 6/15/88, (PB89-122188, A05, MF-A01). This report is available only through NTIS (see address given above).
- NCEER-88-0023 "Multi-Hazard Risk Analysis: Case of a Simple Offshore Structure," by B.K. Bhartia and E.H. Vanmarcke, 7/21/88, (PB89-145213, A05, MF-A01).

- NCEER-88-0024 "Automated Seismic Design of Reinforced Concrete Buildings," by Y.S. Chung, C. Meyer and M. Shinozuka, 7/5/88, (PB89-122170, A06, MF-A01). This report is available only through NTIS (see address given above).
- NCEER-88-0025 "Experimental Study of Active Control of MDOF Structures Under Seismic Excitations," by L.L. Chung, R.C. Lin, T.T. Soong and A.M. Reinhorn, 7/10/88, (PB89-122600, A04, MF-A01).
- NCEER-88-0026 "Earthquake Simulation Tests of a Low-Rise Metal Structure," by J.S. Hwang, K.C. Chang, G.C. Lee and R.L. Ketter, 8/1/88, (PB89-102917, A04, MF-A01).
- NCEER-88-0027 "Systems Study of Urban Response and Reconstruction Due to Catastrophic Earthquakes," by F. Kozin and H.K. Zhou, 9/22/88, (PB90-162348, A04, MF-A01).
- NCEER-88-0028 "Seismic Fragility Analysis of Plane Frame Structures," by H.H-M. Hwang and Y.K. Low, 7/31/88, (PB89-131445, A06, MF-A01).
- NCEER-88-0029 "Response Analysis of Stochastic Structures," by A. Kardara, C. Bucher and M. Shinozuka, 9/22/88, (PB89-174429, A04, MF-A01).
- NCEER-88-0030 "Nonnormal Accelerations Due to Yielding in a Primary Structure," by D.C.K. Chen and L.D. Lutes, 9/19/88, (PB89-131437, A04, MF-A01).
- NCEER-88-0031 "Design Approaches for Soil-Structure Interaction," by A.S. Veletsos, A.M. Prasad and Y. Tang, 12/30/88, (PB89-174437, A03, MF-A01). This report is available only through NTIS (see address given above).
- NCEER-88-0032 "A Re-evaluation of Design Spectra for Seismic Damage Control," by C.J. Turkstra and A.G. Tallin, 11/7/88, (PB89-145221, A05, MF-A01).
- NCEER-88-0033 "The Behavior and Design of Noncontact Lap Splices Subjected to Repeated Inelastic Tensile Loading," by V.E. Sagan, P. Gergely and R.N. White, 12/8/88, (PB89-163737, A08, MF-A01).
- NCEER-88-0034 "Seismic Response of Pile Foundations," by S.M. Mamoon, P.K. Banerjee and S. Ahmad, 11/1/88, (PB89-145239, A04, MF-A01).
- NCEER-88-0035 "Modeling of R/C Building Structures With Flexible Floor Diaphragms (IDARC2)," by A.M. Reinhorn, S.K. Kunnath and N. Panahshahi, 9/7/88, (PB89-207153, A07, MF-A01).
- NCEER-88-0036 "Solution of the Dam-Reservoir Interaction Problem Using a Combination of FEM, BEM with Particular Integrals, Modal Analysis, and Substructuring," by C-S. Tsai, G.C. Lee and R.L. Ketter, 12/31/88, (PB89-207146, A04, MF-A01).
- NCEER-88-0037 "Optimal Placement of Actuators for Structural Control," by F.Y. Cheng and C.P. Pantelides, 8/15/88, (PB89-162846, A05, MF-A01).
- NCEER-88-0038 "Teflon Bearings in Aseismic Base Isolation: Experimental Studies and Mathematical Modeling," by A. Mokha, M.C. Constantinou and A.M. Reinhorn, 12/5/88, (PB89-218457, A10, MF-A01). This report is available only through NTIS (see address given above).
- NCEER-88-0039 "Seismic Behavior of Flat Slab High-Rise Buildings in the New York City Area," by P. Weidlinger and M. Ettouney, 10/15/88, (PB90-145681, A04, MF-A01).
- NCEER-88-0040 "Evaluation of the Earthquake Resistance of Existing Buildings in New York City," by P. Weidlinger and M. Ettouney, 10/15/88, not available.
- NCEER-88-0041 "Small-Scale Modeling Techniques for Reinforced Concrete Structures Subjected to Seismic Loads," by W. Kim, A. El-Attar and R.N. White, 11/22/88, (PB89-189625, A05, MF-A01).
- NCEER-88-0042 "Modeling Strong Ground Motion from Multiple Event Earthquakes," by G.W. Ellis and A.S. Cakmak, 10/15/88, (PB89-174445, A03, MF-A01).

- NCEER-88-0043 "Nonstationary Models of Seismic Ground Acceleration," by M. Grigoriu, S.E. Ruiz and E. Rosenblueth, 7/15/88, (PB89-189617, A04, MF-A01).
- NCEER-88-0044 "SARCF User's Guide: Seismic Analysis of Reinforced Concrete Frames," by Y.S. Chung, C. Meyer and M. Shinozuka, 11/9/88, (PB89-174452, A08, MF-A01).
- NCEER-88-0045 "First Expert Panel Meeting on Disaster Research and Planning," edited by J. Pantelic and J. Stoyke, 9/15/88, (PB89-174460, A05, MF-A01).
- NCEER-88-0046 "Preliminary Studies of the Effect of Degrading Infill Walls on the Nonlinear Seismic Response of Steel Frames," by C.Z. Chrysostomou, P. Gergely and J.F. Abel, 12/19/88, (PB89-208383, A05, MF-A01).
- NCEER-88-0047 "Reinforced Concrete Frame Component Testing Facility - Design, Construction, Instrumentation and Operation," by S.P. Pessiki, C. Conley, T. Bond, P. Gergely and R.N. White, 12/16/88, (PB89-174478, A04, MF-A01).
- NCEER-89-0001 "Effects of Protective Cushion and Soil Compliancy on the Response of Equipment Within a Seismically Excited Building," by J.A. HoLung, 2/16/89, (PB89-207179, A04, MF-A01).
- NCEER-89-0002 "Statistical Evaluation of Response Modification Factors for Reinforced Concrete Structures," by H.H-M. Hwang and J-W. Jaw, 2/17/89, (PB89-207187, A05, MF-A01).
- NCEER-89-0003 "Hysteretic Columns Under Random Excitation," by G-Q. Cai and Y.K. Lin, 1/9/89, (PB89-196513, A03, MF-A01).
- NCEER-89-0004 "Experimental Study of 'Elephant Foot Bulge' Instability of Thin-Walled Metal Tanks," by Z-H. Jia and R.L. Ketter, 2/22/89, (PB89-207195, A03, MF-A01).
- NCEER-89-0005 "Experiment on Performance of Buried Pipelines Across San Andreas Fault," by J. Isenberg, E. Richardson and T.D. O'Rourke, 3/10/89, (PB89-218440, A04, MF-A01). This report is available only through NTIS (see address given above).
- NCEER-89-0006 "A Knowledge-Based Approach to Structural Design of Earthquake-Resistant Buildings," by M. Subramani, P. Gergely, C.H. Conley, J.F. Abel and A.H. Zaghaw, 1/15/89, (PB89-218465, A06, MF-A01).
- NCEER-89-0007 "Liquefaction Hazards and Their Effects on Buried Pipelines," by T.D. O'Rourke and P.A. Lane, 2/1/89, (PB89-218481, A09, MF-A01).
- NCEER-89-0008 "Fundamentals of System Identification in Structural Dynamics," by H. Imai, C-B. Yun, O. Maruyama and M. Shinozuka, 1/26/89, (PB89-207211, A04, MF-A01).
- NCEER-89-0009 "Effects of the 1985 Michoacan Earthquake on Water Systems and Other Buried Lifelines in Mexico," by A.G. Ayala and M.J. O'Rourke, 3/8/89, (PB89-207229, A06, MF-A01).
- NCEER-89-R010 "NCEER Bibliography of Earthquake Education Materials," by K.E.K. Ross, Second Revision, 9/1/89, (PB90-125352, A05, MF-A01). This report is replaced by NCEER-92-0018.
- NCEER-89-0011 "Inelastic Three-Dimensional Response Analysis of Reinforced Concrete Building Structures (IDARC-3D), Part I - Modeling," by S.K. Kunnath and A.M. Reinhorn, 4/17/89, (PB90-114612, A07, MF-A01). This report is available only through NTIS (see address given above).
- NCEER-89-0012 "Recommended Modifications to ATC-14," by C.D. Poland and J.O. Malley, 4/12/89, (PB90-108648, A15, MF-A01).
- NCEER-89-0013 "Repair and Strengthening of Beam-to-Column Connections Subjected to Earthquake Loading," by M. Corazao and A.J. Durrani, 2/28/89, (PB90-109885, A06, MF-A01).
- NCEER-89-0014 "Program EXKAL2 for Identification of Structural Dynamic Systems," by O. Maruyama, C-B. Yun, M. Hoshiya and M. Shinozuka, 5/19/89, (PB90-109877, A09, MF-A01).

- NCEER-89-0015 "Response of Frames With Bolted Semi-Rigid Connections, Part I - Experimental Study and Analytical Predictions," by P.J. DiCorso, A.M. Reinhorn, J.R. Dickerson, J.B. Radzimirski and W.L. Harper, 6/1/89, not available.
- NCEER-89-0016 "ARMA Monte Carlo Simulation in Probabilistic Structural Analysis," by P.D. Spanos and M.P. Mignolet, 7/10/89, (PB90-109893, A03, MF-A01).
- NCEER-89-P017 "Preliminary Proceedings from the Conference on Disaster Preparedness - The Place of Earthquake Education in Our Schools," Edited by K.E.K. Ross, 6/23/89, (PB90-108606, A03, MF-A01).
- NCEER-89-0017 "Proceedings from the Conference on Disaster Preparedness - The Place of Earthquake Education in Our Schools," Edited by K.E.K. Ross, 12/31/89, (PB90-207895, A012, MF-A02). This report is available only through NTIS (see address given above).
- NCEER-89-0018 "Multidimensional Models of Hysteretic Material Behavior for Vibration Analysis of Shape Memory Energy Absorbing Devices, by E.J. Graesser and F.A. Cozzarelli, 6/7/89, (PB90-164146, A04, MF-A01).
- NCEER-89-0019 "Nonlinear Dynamic Analysis of Three-Dimensional Base Isolated Structures (3D-BASIS)," by S. Nagarajaiah, A.M. Reinhorn and M.C. Constantinou, 8/3/89, (PB90-161936, A06, MF-A01). This report has been replaced by NCEER-93-0011.
- NCEER-89-0020 "Structural Control Considering Time-Rate of Control Forces and Control Rate Constraints," by F.Y. Cheng and C.P. Pantelides, 8/3/89, (PB90-120445, A04, MF-A01).
- NCEER-89-0021 "Subsurface Conditions of Memphis and Shelby County," by K.W. Ng, T-S. Chang and H-H.M. Hwang, 7/26/89, (PB90-120437, A03, MF-A01).
- NCEER-89-0022 "Seismic Wave Propagation Effects on Straight Jointed Buried Pipelines," by K. Elhmadi and M.J. O'Rourke, 8/24/89, (PB90-162322, A10, MF-A02).
- NCEER-89-0023 "Workshop on Serviceability Analysis of Water Delivery Systems," edited by M. Grigoriu, 3/6/89, (PB90-127424, A03, MF-A01).
- NCEER-89-0024 "Shaking Table Study of a 1/5 Scale Steel Frame Composed of Tapered Members," by K.C. Chang, J.S. Hwang and G.C. Lee, 9/18/89, (PB90-160169, A04, MF-A01).
- NCEER-89-0025 "DYNA1D: A Computer Program for Nonlinear Seismic Site Response Analysis - Technical Documentation," by Jean H. Prevost, 9/14/89, (PB90-161944, A07, MF-A01). This report is available only through NTIS (see address given above).
- NCEER-89-0026 "1:4 Scale Model Studies of Active Tendon Systems and Active Mass Dampers for Aseismic Protection," by A.M. Reinhorn, T.T. Soong, R.C. Lin, Y.P. Yang, Y. Fukao, H. Abe and M. Nakai, 9/15/89, (PB90-173246, A10, MF-A02). This report is available only through NTIS (see address given above).
- NCEER-89-0027 "Scattering of Waves by Inclusions in a Nonhomogeneous Elastic Half Space Solved by Boundary Element Methods," by P.K. Hadley, A. Askar and A.S. Cakmak, 6/15/89, (PB90-145699, A07, MF-A01).
- NCEER-89-0028 "Statistical Evaluation of Deflection Amplification Factors for Reinforced Concrete Structures," by H.H.M. Hwang, J-W. Jaw and A.L. Ch'ng, 8/31/89, (PB90-164633, A05, MF-A01).
- NCEER-89-0029 "Bedrock Accelerations in Memphis Area Due to Large New Madrid Earthquakes," by H.H.M. Hwang, C.H.S. Chen and G. Yu, 11/7/89, (PB90-162330, A04, MF-A01).
- NCEER-89-0030 "Seismic Behavior and Response Sensitivity of Secondary Structural Systems," by Y.Q. Chen and T.T. Soong, 10/23/89, (PB90-164658, A08, MF-A01).
- NCEER-89-0031 "Random Vibration and Reliability Analysis of Primary-Secondary Structural Systems," by Y. Ibrahim, M. Grigoriu and T.T. Soong, 11/10/89, (PB90-161951, A04, MF-A01).

- NCEER-89-0032 "Proceedings from the Second U.S. - Japan Workshop on Liquefaction, Large Ground Deformation and Their Effects on Lifelines, September 26-29, 1989," Edited by T.D. O'Rourke and M. Hamada, 12/1/89, (PB90-209388, A22, MF-A03).
- NCEER-89-0033 "Deterministic Model for Seismic Damage Evaluation of Reinforced Concrete Structures," by J.M. Bracci, A.M. Reinhorn, J.B. Mander and S.K. Kunnath, 9/27/89, (PB91-108803, A06, MF-A01).
- NCEER-89-0034 "On the Relation Between Local and Global Damage Indices," by E. DiPasquale and A.S. Cakmak, 8/15/89, (PB90-173865, A05, MF-A01).
- NCEER-89-0035 "Cyclic Undrained Behavior of Nonplastic and Low Plasticity Silts," by A.J. Walker and H.E. Stewart, 7/26/89, (PB90-183518, A10, MF-A01).
- NCEER-89-0036 "Liquefaction Potential of Surficial Deposits in the City of Buffalo, New York," by M. Budhu, R. Giese and L. Baumgrass, 1/17/89, (PB90-208455, A04, MF-A01).
- NCEER-89-0037 "A Deterministic Assessment of Effects of Ground Motion Incoherence," by A.S. Veletsos and Y. Tang, 7/15/89, (PB90-164294, A03, MF-A01).
- NCEER-89-0038 "Workshop on Ground Motion Parameters for Seismic Hazard Mapping," July 17-18, 1989, edited by R.V. Whitman, 12/1/89, (PB90-173923, A04, MF-A01).
- NCEER-89-0039 "Seismic Effects on Elevated Transit Lines of the New York City Transit Authority," by C.J. Costantino, C.A. Miller and E. Heymsfield, 12/26/89, (PB90-207887, A06, MF-A01).
- NCEER-89-0040 "Centrifugal Modeling of Dynamic Soil-Structure Interaction," by K. Weissman, Supervised by J.H. Prevost, 5/10/89, (PB90-207879, A07, MF-A01).
- NCEER-89-0041 "Linearized Identification of Buildings With Cores for Seismic Vulnerability Assessment," by I-K. Ho and A.E. Aktan, 11/1/89, (PB90-251943, A07, MF-A01).
- NCEER-90-0001 "Geotechnical and Lifeline Aspects of the October 17, 1989 Loma Prieta Earthquake in San Francisco," by T.D. O'Rourke, H.E. Stewart, F.T. Blackburn and T.S. Dickerman, 1/90, (PB90-208596, A05, MF-A01).
- NCEER-90-0002 "Nonnormal Secondary Response Due to Yielding in a Primary Structure," by D.C.K. Chen and L.D. Lutes, 2/28/90, (PB90-251976, A07, MF-A01).
- NCEER-90-0003 "Earthquake Education Materials for Grades K-12," by K.E.K. Ross, 4/16/90, (PB91-251984, A05, MF-A05). This report has been replaced by NCEER-92-0018.
- NCEER-90-0004 "Catalog of Strong Motion Stations in Eastern North America," by R.W. Busby, 4/3/90, (PB90-251984, A05, MF-A01).
- NCEER-90-0005 "NCEER Strong-Motion Data Base: A User Manual for the GeoBase Release (Version 1.0 for the Sun3)," by P. Friberg and K. Jacob, 3/31/90 (PB90-258062, A04, MF-A01).
- NCEER-90-0006 "Seismic Hazard Along a Crude Oil Pipeline in the Event of an 1811-1812 Type New Madrid Earthquake," by H.H.M. Hwang and C-H.S. Chen, 4/16/90, (PB90-258054, A04, MF-A01).
- NCEER-90-0007 "Site-Specific Response Spectra for Memphis Sheahan Pumping Station," by H.H.M. Hwang and C.S. Lee, 5/15/90, (PB91-108811, A05, MF-A01).
- NCEER-90-0008 "Pilot Study on Seismic Vulnerability of Crude Oil Transmission Systems," by T. Ariman, R. Dobry, M. Grigoriu, F. Kozin, M. O'Rourke, T. O'Rourke and M. Shinozuka, 5/25/90, (PB91-108837, A06, MF-A01).
- NCEER-90-0009 "A Program to Generate Site Dependent Time Histories: EQGEN," by G.W. Ellis, M. Srinivasan and A.S. Cakmak, 1/30/90, (PB91-108829, A04, MF-A01).
- NCEER-90-0010 "Active Isolation for Seismic Protection of Operating Rooms," by M.E. Talbott, Supervised by M. Shinozuka, 6/8/9, (PB91-110205, A05, MF-A01).

- NCEER-90-0011 "Program LINEARID for Identification of Linear Structural Dynamic Systems," by C-B. Yun and M. Shinozuka, 6/25/90, (PB91-110312, A08, MF-A01).
- NCEER-90-0012 "Two-Dimensional Two-Phase Elasto-Plastic Seismic Response of Earth Dams," by A.N. Yiagos, Supervised by J.H. Prevost, 6/20/90, (PB91-110197, A13, MF-A02).
- NCEER-90-0013 "Secondary Systems in Base-Isolated Structures: Experimental Investigation, Stochastic Response and Stochastic Sensitivity," by G.D. Manolis, G. Juhn, M.C. Constantinou and A.M. Reinhorn, 7/1/90, (PB91-110320, A08, MF-A01).
- NCEER-90-0014 "Seismic Behavior of Lightly-Reinforced Concrete Column and Beam-Column Joint Details," by S.P. Pessiki, C.H. Conley, P. Gergely and R.N. White, 8/22/90, (PB91-108795, A11, MF-A02).
- NCEER-90-0015 "Two Hybrid Control Systems for Building Structures Under Strong Earthquakes," by J.N. Yang and A. Daniellians, 6/29/90, (PB91-125393, A04, MF-A01).
- NCEER-90-0016 "Instantaneous Optimal Control with Acceleration and Velocity Feedback," by J.N. Yang and Z. Li, 6/29/90, (PB91-125401, A03, MF-A01).
- NCEER-90-0017 "Reconnaissance Report on the Northern Iran Earthquake of June 21, 1990," by M. Mehrain, 10/4/90, (PB91-125377, A03, MF-A01).
- NCEER-90-0018 "Evaluation of Liquefaction Potential in Memphis and Shelby County," by T.S. Chang, P.S. Tang, C.S. Lee and H. Hwang, 8/10/90, (PB91-125427, A09, MF-A01).
- NCEER-90-0019 "Experimental and Analytical Study of a Combined Sliding Disc Bearing and Helical Steel Spring Isolation System," by M.C. Constantinou, A.S. Mokha and A.M. Reinhorn, 10/4/90, (PB91-125385, A06, MF-A01). This report is available only through NTIS (see address given above).
- NCEER-90-0020 "Experimental Study and Analytical Prediction of Earthquake Response of a Sliding Isolation System with a Spherical Surface," by A.S. Mokha, M.C. Constantinou and A.M. Reinhorn, 10/11/90, (PB91-125419, A05, MF-A01).
- NCEER-90-0021 "Dynamic Interaction Factors for Floating Pile Groups," by G. Gazetas, K. Fan, A. Kaynia and E. Kausel, 9/10/90, (PB91-170381, A05, MF-A01).
- NCEER-90-0022 "Evaluation of Seismic Damage Indices for Reinforced Concrete Structures," by S. Rodriguez-Gomez and A.S. Cakmak, 9/30/90, PB91-171322, A06, MF-A01).
- NCEER-90-0023 "Study of Site Response at a Selected Memphis Site," by H. Desai, S. Ahmad, E.S. Gazetas and M.R. Oh, 10/11/90, (PB91-196857, A03, MF-A01).
- NCEER-90-0024 "A User's Guide to Strongmo: Version 1.0 of NCEER's Strong-Motion Data Access Tool for PCs and Terminals," by P.A. Friberg and C.A.T. Susch, 11/15/90, (PB91-171272, A03, MF-A01).
- NCEER-90-0025 "A Three-Dimensional Analytical Study of Spatial Variability of Seismic Ground Motions," by L-L. Hong and A.H.-S. Ang, 10/30/90, (PB91-170399, A09, MF-A01).
- NCEER-90-0026 "MUMOID User's Guide - A Program for the Identification of Modal Parameters," by S. Rodriguez-Gomez and E. DiPasquale, 9/30/90, (PB91-171298, A04, MF-A01).
- NCEER-90-0027 "SARCF-II User's Guide - Seismic Analysis of Reinforced Concrete Frames," by S. Rodriguez-Gomez, Y.S. Chung and C. Meyer, 9/30/90, (PB91-171280, A05, MF-A01).
- NCEER-90-0028 "Viscous Dampers: Testing, Modeling and Application in Vibration and Seismic Isolation," by N. Makris and M.C. Constantinou, 12/20/90 (PB91-190561, A06, MF-A01).
- NCEER-90-0029 "Soil Effects on Earthquake Ground Motions in the Memphis Area," by H. Hwang, C.S. Lee, K.W. Ng and T.S. Chang, 8/2/90, (PB91-190751, A05, MF-A01).

- NCEER-91-0001 "Proceedings from the Third Japan-U.S. Workshop on Earthquake Resistant Design of Lifeline Facilities and Countermeasures for Soil Liquefaction, December 17-19, 1990," edited by T.D. O'Rourke and M. Hamada, 2/1/91, (PB91-179259, A99, MF-A04).
- NCEER-91-0002 "Physical Space Solutions of Non-Proportionally Damped Systems," by M. Tong, Z. Liang and G.C. Lee, 1/15/91, (PB91-179242, A04, MF-A01).
- NCEER-91-0003 "Seismic Response of Single Piles and Pile Groups," by K. Fan and G. Gazetas, 1/10/91, (PB92-174994, A04, MF-A01).
- NCEER-91-0004 "Damping of Structures: Part 1 - Theory of Complex Damping," by Z. Liang and G. Lee, 10/10/91, (PB92-197235, A12, MF-A03).
- NCEER-91-0005 "3D-BASIS - Nonlinear Dynamic Analysis of Three Dimensional Base Isolated Structures: Part II," by S. Nagarajaiah, A.M. Reinhorn and M.C. Constantinou, 2/28/91, (PB91-190553, A07, MF-A01). This report has been replaced by NCEER-93-0011.
- NCEER-91-0006 "A Multidimensional Hysteretic Model for Plasticity Deforming Metals in Energy Absorbing Devices," by E.J. Graesser and F.A. Cozzarelli, 4/9/91, (PB92-108364, A04, MF-A01).
- NCEER-91-0007 "A Framework for Customizable Knowledge-Based Expert Systems with an Application to a KBES for Evaluating the Seismic Resistance of Existing Buildings," by E.G. Ibarra-Anaya and S.J. Fennes, 4/9/91, (PB91-210930, A08, MF-A01).
- NCEER-91-0008 "Nonlinear Analysis of Steel Frames with Semi-Rigid Connections Using the Capacity Spectrum Method," by G.G. Deierlein, S-H. Hsieh, Y-J. Shen and J.F. Abel, 7/2/91, (PB92-113828, A05, MF-A01).
- NCEER-91-0009 "Earthquake Education Materials for Grades K-12," by K.E.K. Ross, 4/30/91, (PB91-212142, A06, MF-A01). This report has been replaced by NCEER-92-0018.
- NCEER-91-0010 "Phase Wave Velocities and Displacement Phase Differences in a Harmonically Oscillating Pile," by N. Makris and G. Gazetas, 7/8/91, (PB92-108356, A04, MF-A01).
- NCEER-91-0011 "Dynamic Characteristics of a Full-Size Five-Story Steel Structure and a 2/5 Scale Model," by K.C. Chang, G.C. Yao, G.C. Lee, D.S. Hao and Y.C. Yeh," 7/2/91, (PB93-116648, A06, MF-A02).
- NCEER-91-0012 "Seismic Response of a 2/5 Scale Steel Structure with Added Viscoelastic Dampers," by K.C. Chang, T.T. Soong, S-T. Oh and M.L. Lai, 5/17/91, (PB92-110816, A05, MF-A01).
- NCEER-91-0013 "Earthquake Response of Retaining Walls; Full-Scale Testing and Computational Modeling," by S. Alampalli and A-W.M. Elgamal, 6/20/91, not available.
- NCEER-91-0014 "3D-BASIS-M: Nonlinear Dynamic Analysis of Multiple Building Base Isolated Structures," by P.C. Tsopelas, S. Nagarajaiah, M.C. Constantinou and A.M. Reinhorn, 5/28/91, (PB92-113885, A09, MF-A02).
- NCEER-91-0015 "Evaluation of SEAOC Design Requirements for Sliding Isolated Structures," by D. Theodossiou and M.C. Constantinou, 6/10/91, (PB92-114602, A11, MF-A03).
- NCEER-91-0016 "Closed-Loop Modal Testing of a 27-Story Reinforced Concrete Flat Plate-Core Building," by H.R. Somaprasad, T. Toksoy, H. Yoshiyuki and A.E. Aktan, 7/15/91, (PB92-129980, A07, MF-A02).
- NCEER-91-0017 "Shake Table Test of a 1/6 Scale Two-Story Lightly Reinforced Concrete Building," by A.G. El-Attar, R.N. White and P. Gergely, 2/28/91, (PB92-222447, A06, MF-A02).
- NCEER-91-0018 "Shake Table Test of a 1/8 Scale Three-Story Lightly Reinforced Concrete Building," by A.G. El-Attar, R.N. White and P. Gergely, 2/28/91, (PB93-116630, A08, MF-A02).
- NCEER-91-0019 "Transfer Functions for Rigid Rectangular Foundations," by A.S. Veletsos, A.M. Prasad and W.H. Wu, 7/31/91, not available.

- NCEER-91-0020 "Hybrid Control of Seismic-Excited Nonlinear and Inelastic Structural Systems," by J.N. Yang, Z. Li and A. Daniellians, 8/1/91, (PB92-143171, A06, MF-A02).
- NCEER-91-0021 "The NCEER-91 Earthquake Catalog: Improved Intensity-Based Magnitudes and Recurrence Relations for U.S. Earthquakes East of New Madrid," by L. Seeber and J.G. Armbruster, 8/28/91, (PB92-176742, A06, MF-A02).
- NCEER-91-0022 "Proceedings from the Implementation of Earthquake Planning and Education in Schools: The Need for Change - The Roles of the Changemakers," by K.E.K. Ross and F. Winslow, 7/23/91, (PB92-129998, A12, MF-A03).
- NCEER-91-0023 "A Study of Reliability-Based Criteria for Seismic Design of Reinforced Concrete Frame Buildings," by H.H.M. Hwang and H-M. Hsu, 8/10/91, (PB92-140235, A09, MF-A02).
- NCEER-91-0024 "Experimental Verification of a Number of Structural System Identification Algorithms," by R.G. Ghanem, H. Gavin and M. Shinozuka, 9/18/91, (PB92-176577, A18, MF-A04).
- NCEER-91-0025 "Probabilistic Evaluation of Liquefaction Potential," by H.H.M. Hwang and C.S. Lee," 11/25/91, (PB92-143429, A05, MF-A01).
- NCEER-91-0026 "Instantaneous Optimal Control for Linear, Nonlinear and Hysteretic Structures - Stable Controllers," by J.N. Yang and Z. Li, 11/15/91, (PB92-163807, A04, MF-A01).
- NCEER-91-0027 "Experimental and Theoretical Study of a Sliding Isolation System for Bridges," by M.C. Constantinou, A. Kartoum, A.M. Reinhorn and P. Bradford, 11/15/91, (PB92-176973, A10, MF-A03).
- NCEER-92-0001 "Case Studies of Liquefaction and Lifeline Performance During Past Earthquakes, Volume 1: Japanese Case Studies," Edited by M. Hamada and T. O'Rourke, 2/17/92, (PB92-197243, A18, MF-A04).
- NCEER-92-0002 "Case Studies of Liquefaction and Lifeline Performance During Past Earthquakes, Volume 2: United States Case Studies," Edited by T. O'Rourke and M. Hamada, 2/17/92, (PB92-197250, A20, MF-A04).
- NCEER-92-0003 "Issues in Earthquake Education," Edited by K. Ross, 2/3/92, (PB92-222389, A07, MF-A02).
- NCEER-92-0004 "Proceedings from the First U.S. - Japan Workshop on Earthquake Protective Systems for Bridges," Edited by I.G. Buckle, 2/4/92, (PB94-142239, A99, MF-A06).
- NCEER-92-0005 "Seismic Ground Motion from a Haskell-Type Source in a Multiple-Layered Half-Space," A.P. Theoharis, G. Deodatis and M. Shinozuka, 1/2/92, not available.
- NCEER-92-0006 "Proceedings from the Site Effects Workshop," Edited by R. Whitman, 2/29/92, (PB92-197201, A04, MF-A01).
- NCEER-92-0007 "Engineering Evaluation of Permanent Ground Deformations Due to Seismically-Induced Liquefaction," by M.H. Baziar, R. Dobry and A-W.M. Elgamal, 3/24/92, (PB92-222421, A13, MF-A03).
- NCEER-92-0008 "A Procedure for the Seismic Evaluation of Buildings in the Central and Eastern United States," by C.D. Poland and J.O. Malley, 4/2/92, (PB92-222439, A20, MF-A04).
- NCEER-92-0009 "Experimental and Analytical Study of a Hybrid Isolation System Using Friction Controllable Sliding Bearings," by M.Q. Feng, S. Fujii and M. Shinozuka, 5/15/92, (PB93-150282, A06, MF-A02).
- NCEER-92-0010 "Seismic Resistance of Slab-Column Connections in Existing Non-Ductile Flat-Plate Buildings," by A.J. Durrani and Y. Du, 5/18/92, (PB93-116812, A06, MF-A02).
- NCEER-92-0011 "The Hysteretic and Dynamic Behavior of Brick Masonry Walls Upgraded by Ferrocement Coatings Under Cyclic Loading and Strong Simulated Ground Motion," by H. Lee and S.P. Prawel, 5/11/92, not available.
- NCEER-92-0012 "Study of Wire Rope Systems for Seismic Protection of Equipment in Buildings," by G.F. Demetriades, M.C. Constantinou and A.M. Reinhorn, 5/20/92, (PB93-116655, A08, MF-A02).

- NCEER-92-0013 "Shape Memory Structural Dampers: Material Properties, Design and Seismic Testing," by P.R. Witting and F.A. Cozzarelli, 5/26/92, (PB93-116663, A05, MF-A01).
- NCEER-92-0014 "Longitudinal Permanent Ground Deformation Effects on Buried Continuous Pipelines," by M.J. O'Rourke, and C. Nordberg, 6/15/92, (PB93-116671, A08, MF-A02).
- NCEER-92-0015 "A Simulation Method for Stationary Gaussian Random Functions Based on the Sampling Theorem," by M. Grigoriu and S. Balopoulou, 6/11/92, (PB93-127496, A05, MF-A01).
- NCEER-92-0016 "Gravity-Load-Designed Reinforced Concrete Buildings: Seismic Evaluation of Existing Construction and Detailing Strategies for Improved Seismic Resistance," by G.W. Hoffmann, S.K. Kunnath, A.M. Reinhorn and J.B. Mander, 7/15/92, (PB94-142007, A08, MF-A02).
- NCEER-92-0017 "Observations on Water System and Pipeline Performance in the Limón Area of Costa Rica Due to the April 22, 1991 Earthquake," by M. O'Rourke and D. Ballantyne, 6/30/92, (PB93-126811, A06, MF-A02).
- NCEER-92-0018 "Fourth Edition of Earthquake Education Materials for Grades K-12," Edited by K.E.K. Ross, 8/10/92, (PB93-114023, A07, MF-A02).
- NCEER-92-0019 "Proceedings from the Fourth Japan-U.S. Workshop on Earthquake Resistant Design of Lifeline Facilities and Countermeasures for Soil Liquefaction," Edited by M. Hamada and T.D. O'Rourke, 8/12/92, (PB93-163939, A99, MF-E11).
- NCEER-92-0020 "Active Bracing System: A Full Scale Implementation of Active Control," by A.M. Reinhorn, T.T. Soong, R.C. Lin, M.A. Riley, Y.P. Wang, S. Aizawa and M. Higashino, 8/14/92, (PB93-127512, A06, MF-A02).
- NCEER-92-0021 "Empirical Analysis of Horizontal Ground Displacement Generated by Liquefaction-Induced Lateral Spreads," by S.F. Bartlett and T.L. Youd, 8/17/92, (PB93-188241, A06, MF-A02).
- NCEER-92-0022 "IDARC Version 3.0: Inelastic Damage Analysis of Reinforced Concrete Structures," by S.K. Kunnath, A.M. Reinhorn and R.F. Lobo, 8/31/92, (PB93-227502, A07, MF-A02).
- NCEER-92-0023 "A Semi-Empirical Analysis of Strong-Motion Peaks in Terms of Seismic Source, Propagation Path and Local Site Conditions, by M. Kamiyama, M.J. O'Rourke and R. Flores-Berrones, 9/9/92, (PB93-150266, A08, MF-A02).
- NCEER-92-0024 "Seismic Behavior of Reinforced Concrete Frame Structures with Nonductile Details, Part I: Summary of Experimental Findings of Full Scale Beam-Column Joint Tests," by A. Beres, R.N. White and P. Gergely, 9/30/92, (PB93-227783, A05, MF-A01).
- NCEER-92-0025 "Experimental Results of Repaired and Retrofitted Beam-Column Joint Tests in Lightly Reinforced Concrete Frame Buildings," by A. Beres, S. El-Borgi, R.N. White and P. Gergely, 10/29/92, (PB93-227791, A05, MF-A01).
- NCEER-92-0026 "A Generalization of Optimal Control Theory: Linear and Nonlinear Structures," by J.N. Yang, Z. Li and S. Vongchavalitkul, 11/2/92, (PB93-188621, A05, MF-A01).
- NCEER-92-0027 "Seismic Resistance of Reinforced Concrete Frame Structures Designed Only for Gravity Loads: Part I - Design and Properties of a One-Third Scale Model Structure," by J.M. Bracci, A.M. Reinhorn and J.B. Mander, 12/1/92, (PB94-104502, A08, MF-A02).
- NCEER-92-0028 "Seismic Resistance of Reinforced Concrete Frame Structures Designed Only for Gravity Loads: Part II - Experimental Performance of Subassemblages," by L.E. Aycaardi, J.B. Mander and A.M. Reinhorn, 12/1/92, (PB94-104510, A08, MF-A02).
- NCEER-92-0029 "Seismic Resistance of Reinforced Concrete Frame Structures Designed Only for Gravity Loads: Part III - Experimental Performance and Analytical Study of a Structural Model," by J.M. Bracci, A.M. Reinhorn and J.B. Mander, 12/1/92, (PB93-227528, A09, MF-A01).

- NCEER-92-0030 "Evaluation of Seismic Retrofit of Reinforced Concrete Frame Structures: Part I - Experimental Performance of Retrofitted Subassemblages," by D. Choudhuri, J.B. Mander and A.M. Reinhorn, 12/8/92, (PB93-198307, A07, MF-A02).
- NCEER-92-0031 "Evaluation of Seismic Retrofit of Reinforced Concrete Frame Structures: Part II - Experimental Performance and Analytical Study of a Retrofitted Structural Model," by J.M. Bracci, A.M. Reinhorn and J.B. Mander, 12/8/92, (PB93-198315, A09, MF-A03).
- NCEER-92-0032 "Experimental and Analytical Investigation of Seismic Response of Structures with Supplemental Fluid Viscous Dampers," by M.C. Constantinou and M.D. Symans, 12/21/92, (PB93-191435, A10, MF-A03). This report is available only through NTIS (see address given above).
- NCEER-92-0033 "Reconnaissance Report on the Cairo, Egypt Earthquake of October 12, 1992," by M. Khater, 12/23/92, (PB93-188621, A03, MF-A01).
- NCEER-92-0034 "Low-Level Dynamic Characteristics of Four Tall Flat-Plate Buildings in New York City," by H. Gavin, S. Yuan, J. Grossman, E. Pekelis and K. Jacob, 12/28/92, (PB93-188217, A07, MF-A02).
- NCEER-93-0001 "An Experimental Study on the Seismic Performance of Brick-Infilled Steel Frames With and Without Retrofit," by J.B. Mander, B. Nair, K. Wojtkowski and J. Ma, 1/29/93, (PB93-227510, A07, MF-A02).
- NCEER-93-0002 "Social Accounting for Disaster Preparedness and Recovery Planning," by S. Cole, E. Pantoja and V. Razak, 2/22/93, (PB94-142114, A12, MF-A03).
- NCEER-93-0003 "Assessment of 1991 NEHRP Provisions for Nonstructural Components and Recommended Revisions," by T.T. Soong, G. Chen, Z. Wu, R-H. Zhang and M. Grigoriu, 3/1/93, (PB93-188639, A06, MF-A02).
- NCEER-93-0004 "Evaluation of Static and Response Spectrum Analysis Procedures of SEAOC/UBC for Seismic Isolated Structures," by C.W. Winters and M.C. Constantinou, 3/23/93, (PB93-198299, A10, MF-A03).
- NCEER-93-0005 "Earthquakes in the Northeast - Are We Ignoring the Hazard? A Workshop on Earthquake Science and Safety for Educators," edited by K.E.K. Ross, 4/2/93, (PB94-103066, A09, MF-A02).
- NCEER-93-0006 "Inelastic Response of Reinforced Concrete Structures with Viscoelastic Braces," by R.F. Lobo, J.M. Bracci, K.L. Shen, A.M. Reinhorn and T.T. Soong, 4/5/93, (PB93-227486, A05, MF-A02).
- NCEER-93-0007 "Seismic Testing of Installation Methods for Computers and Data Processing Equipment," by K. Kosar, T.T. Soong, K.L. Shen, J.A. HoLung and Y.K. Lin, 4/12/93, (PB93-198299, A07, MF-A02).
- NCEER-93-0008 "Retrofit of Reinforced Concrete Frames Using Added Dampers," by A. Reinhorn, M. Constantinou and C. Li, not available.
- NCEER-93-0009 "Seismic Behavior and Design Guidelines for Steel Frame Structures with Added Viscoelastic Dampers," by K.C. Chang, M.L. Lai, T.T. Soong, D.S. Hao and Y.C. Yeh, 5/1/93, (PB94-141959, A07, MF-A02).
- NCEER-93-0010 "Seismic Performance of Shear-Critical Reinforced Concrete Bridge Piers," by J.B. Mander, S.M. Waheed, M.T.A. Chaudhary and S.S. Chen, 5/12/93, (PB93-227494, A08, MF-A02).
- NCEER-93-0011 "3D-BASIS-TABS: Computer Program for Nonlinear Dynamic Analysis of Three Dimensional Base Isolated Structures," by S. Nagarajaiah, C. Li, A.M. Reinhorn and M.C. Constantinou, 8/2/93, (PB94-141819, A09, MF-A02).
- NCEER-93-0012 "Effects of Hydrocarbon Spills from an Oil Pipeline Break on Ground Water," by O.J. Helweg and H.H.M. Hwang, 8/3/93, (PB94-141942, A06, MF-A02).
- NCEER-93-0013 "Simplified Procedures for Seismic Design of Nonstructural Components and Assessment of Current Code Provisions," by M.P. Singh, L.E. Suarez, E.E. Matheu and G.O. Maldonado, 8/4/93, (PB94-141827, A09, MF-A02).
- NCEER-93-0014 "An Energy Approach to Seismic Analysis and Design of Secondary Systems," by G. Chen and T.T. Soong, 8/6/93, (PB94-142767, A11, MF-A03).

- NCEER-93-0015 "Proceedings from School Sites: Becoming Prepared for Earthquakes - Commemorating the Third Anniversary of the Loma Prieta Earthquake," Edited by F.E. Winslow and K.E.K. Ross, 8/16/93, (PB94-154275, A16, MF-A02).
- NCEER-93-0016 "Reconnaissance Report of Damage to Historic Monuments in Cairo, Egypt Following the October 12, 1992 Dahshur Earthquake," by D. Sykora, D. Look, G. Croci, E. Karaesmen and E. Karaesmen, 8/19/93, (PB94-142221, A08, MF-A02).
- NCEER-93-0017 "The Island of Guam Earthquake of August 8, 1993," by S.W. Swan and S.K. Harris, 9/30/93, (PB94-141843, A04, MF-A01).
- NCEER-93-0018 "Engineering Aspects of the October 12, 1992 Egyptian Earthquake," by A.W. Elgamal, M. Amer, K. Adalier and A. Abul-Fadl, 10/7/93, (PB94-141983, A05, MF-A01).
- NCEER-93-0019 "Development of an Earthquake Motion Simulator and its Application in Dynamic Centrifuge Testing," by I. Krstelj, Supervised by J.H. Prevost, 10/23/93, (PB94-181773, A-10, MF-A03).
- NCEER-93-0020 "NCEER-Taisei Corporation Research Program on Sliding Seismic Isolation Systems for Bridges: Experimental and Analytical Study of a Friction Pendulum System (FPS)," by M.C. Constantinou, P. Tsopelas, Y-S. Kim and S. Okamoto, 11/1/93, (PB94-142775, A08, MF-A02).
- NCEER-93-0021 "Finite Element Modeling of Elastomeric Seismic Isolation Bearings," by L.J. Billings, Supervised by R. Shepherd, 11/8/93, not available.
- NCEER-93-0022 "Seismic Vulnerability of Equipment in Critical Facilities: Life-Safety and Operational Consequences," by K. Porter, G.S. Johnson, M.M. Zadeh, C. Scawthorn and S. Eder, 11/24/93, (PB94-181765, A16, MF-A03).
- NCEER-93-0023 "Hokkaido Nansei-oki, Japan Earthquake of July 12, 1993, by P.I. Yanev and C.R. Scawthorn, 12/23/93, (PB94-181500, A07, MF-A01).
- NCEER-94-0001 "An Evaluation of Seismic Serviceability of Water Supply Networks with Application to the San Francisco Auxiliary Water Supply System," by I. Markov, Supervised by M. Grigoriu and T. O'Rourke, 1/21/94, (PB94-204013, A07, MF-A02).
- NCEER-94-0002 "NCEER-Taisei Corporation Research Program on Sliding Seismic Isolation Systems for Bridges: Experimental and Analytical Study of Systems Consisting of Sliding Bearings, Rubber Restoring Force Devices and Fluid Dampers," Volumes I and II, by P. Tsopelas, S. Okamoto, M.C. Constantinou, D. Ozaki and S. Fujii, 2/4/94, (PB94-181740, A09, MF-A02 and PB94-181757, A12, MF-A03).
- NCEER-94-0003 "A Markov Model for Local and Global Damage Indices in Seismic Analysis," by S. Rahman and M. Grigoriu, 2/18/94, (PB94-206000, A12, MF-A03).
- NCEER-94-0004 "Proceedings from the NCEER Workshop on Seismic Response of Masonry Infills," edited by D.P. Abrams, 3/1/94, (PB94-180783, A07, MF-A02).
- NCEER-94-0005 "The Northridge, California Earthquake of January 17, 1994: General Reconnaissance Report," edited by J.D. Goltz, 3/11/94, (PB94-193943, A10, MF-A03).
- NCEER-94-0006 "Seismic Energy Based Fatigue Damage Analysis of Bridge Columns: Part I - Evaluation of Seismic Capacity," by G.A. Chang and J.B. Mander, 3/14/94, (PB94-219185, A11, MF-A03).
- NCEER-94-0007 "Seismic Isolation of Multi-Story Frame Structures Using Spherical Sliding Isolation Systems," by T.M. Al-Hussaini, V.A. Zayas and M.C. Constantinou, 3/17/94, (PB94-193745, A09, MF-A02).
- NCEER-94-0008 "The Northridge, California Earthquake of January 17, 1994: Performance of Highway Bridges," edited by I.G. Buckle, 3/24/94, (PB94-193851, A06, MF-A02).
- NCEER-94-0009 "Proceedings of the Third U.S.-Japan Workshop on Earthquake Protective Systems for Bridges," edited by I.G. Buckle and I. Friedland, 3/31/94, (PB94-195815, A99, MF-A06).

- NCEER-94-0010 "3D-BASIS-ME: Computer Program for Nonlinear Dynamic Analysis of Seismically Isolated Single and Multiple Structures and Liquid Storage Tanks," by P.C. Tsopelas, M.C. Constantinou and A.M. Reinhorn, 4/12/94, (PB94-204922, A09, MF-A02).
- NCEER-94-0011 "The Northridge, California Earthquake of January 17, 1994: Performance of Gas Transmission Pipelines," by T.D. O'Rourke and M.C. Palmer, 5/16/94, (PB94-204989, A05, MF-A01).
- NCEER-94-0012 "Feasibility Study of Replacement Procedures and Earthquake Performance Related to Gas Transmission Pipelines," by T.D. O'Rourke and M.C. Palmer, 5/25/94, (PB94-206638, A09, MF-A02).
- NCEER-94-0013 "Seismic Energy Based Fatigue Damage Analysis of Bridge Columns: Part II - Evaluation of Seismic Demand," by G.A. Chang and J.B. Mander, 6/1/94, (PB95-18106, A08, MF-A02).
- NCEER-94-0014 "NCEER-Taisei Corporation Research Program on Sliding Seismic Isolation Systems for Bridges: Experimental and Analytical Study of a System Consisting of Sliding Bearings and Fluid Restoring Force/Damping Devices," by P. Tsopelas and M.C. Constantinou, 6/13/94, (PB94-219144, A10, MF-A03).
- NCEER-94-0015 "Generation of Hazard-Consistent Fragility Curves for Seismic Loss Estimation Studies," by H. Hwang and J-R. Huo, 6/14/94, (PB95-181996, A09, MF-A02).
- NCEER-94-0016 "Seismic Study of Building Frames with Added Energy-Absorbing Devices," by W.S. Pong, C.S. Tsai and G.C. Lee, 6/20/94, (PB94-219136, A10, A03).
- NCEER-94-0017 "Sliding Mode Control for Seismic-Excited Linear and Nonlinear Civil Engineering Structures," by J. Yang, J. Wu, A. Agrawal and Z. Li, 6/21/94, (PB95-138483, A06, MF-A02).
- NCEER-94-0018 "3D-BASIS-TABS Version 2.0: Computer Program for Nonlinear Dynamic Analysis of Three Dimensional Base Isolated Structures," by A.M. Reinhorn, S. Nagarajaiah, M.C. Constantinou, P. Tsopelas and R. Li, 6/22/94, (PB95-182176, A08, MF-A02).
- NCEER-94-0019 "Proceedings of the International Workshop on Civil Infrastructure Systems: Application of Intelligent Systems and Advanced Materials on Bridge Systems," Edited by G.C. Lee and K.C. Chang, 7/18/94, (PB95-252474, A20, MF-A04).
- NCEER-94-0020 "Study of Seismic Isolation Systems for Computer Floors," by V. Lambrou and M.C. Constantinou, 7/19/94, (PB95-138533, A10, MF-A03).
- NCEER-94-0021 "Proceedings of the U.S.-Italian Workshop on Guidelines for Seismic Evaluation and Rehabilitation of Unreinforced Masonry Buildings," Edited by D.P. Abrams and G.M. Calvi, 7/20/94, (PB95-138749, A13, MF-A03).
- NCEER-94-0022 "NCEER-Taisei Corporation Research Program on Sliding Seismic Isolation Systems for Bridges: Experimental and Analytical Study of a System Consisting of Lubricated PTFE Sliding Bearings and Mild Steel Dampers," by P. Tsopelas and M.C. Constantinou, 7/22/94, (PB95-182184, A08, MF-A02).
- NCEER-94-0023 "Development of Reliability-Based Design Criteria for Buildings Under Seismic Load," by Y.K. Wen, H. Hwang and M. Shinozuka, 8/1/94, (PB95-211934, A08, MF-A02).
- NCEER-94-0024 "Experimental Verification of Acceleration Feedback Control Strategies for an Active Tendon System," by S.J. Dyke, B.F. Spencer, Jr., P. Quast, M.K. Sain, D.C. Kaspari, Jr. and T.T. Soong, 8/29/94, (PB95-212320, A05, MF-A01).
- NCEER-94-0025 "Seismic Retrofitting Manual for Highway Bridges," Edited by I.G. Buckle and I.F. Friedland, published by the Federal Highway Administration (PB95-212676, A15, MF-A03).
- NCEER-94-0026 "Proceedings from the Fifth U.S.-Japan Workshop on Earthquake Resistant Design of Lifeline Facilities and Countermeasures Against Soil Liquefaction," Edited by T.D. O'Rourke and M. Hamada, 11/7/94, (PB95-220802, A99, MF-E08).

- NCEER-95-0001 “Experimental and Analytical Investigation of Seismic Retrofit of Structures with Supplemental Damping: Part 1 - Fluid Viscous Damping Devices,” by A.M. Reinhorn, C. Li and M.C. Constantinou, 1/3/95, (PB95-266599, A09, MF-A02).
- NCEER-95-0002 “Experimental and Analytical Study of Low-Cycle Fatigue Behavior of Semi-Rigid Top-And-Seat Angle Connections,” by G. Pekcan, J.B. Mander and S.S. Chen, 1/5/95, (PB95-220042, A07, MF-A02).
- NCEER-95-0003 “NCEER-ATC Joint Study on Fragility of Buildings,” by T. Anagnos, C. Rojahn and A.S. Kiremidjian, 1/20/95, (PB95-220026, A06, MF-A02).
- NCEER-95-0004 “Nonlinear Control Algorithms for Peak Response Reduction,” by Z. Wu, T.T. Soong, V. Gattulli and R.C. Lin, 2/16/95, (PB95-220349, A05, MF-A01).
- NCEER-95-0005 “Pipeline Replacement Feasibility Study: A Methodology for Minimizing Seismic and Corrosion Risks to Underground Natural Gas Pipelines,” by R.T. Eguchi, H.A. Seligson and D.G. Honegger, 3/2/95, (PB95-252326, A06, MF-A02).
- NCEER-95-0006 “Evaluation of Seismic Performance of an 11-Story Frame Building During the 1994 Northridge Earthquake,” by F. Naeim, R. DiSulio, K. Benuska, A. Reinhorn and C. Li, not available.
- NCEER-95-0007 “Prioritization of Bridges for Seismic Retrofitting,” by N. Basöz and A.S. Kiremidjian, 4/24/95, (PB95-252300, A08, MF-A02).
- NCEER-95-0008 “Method for Developing Motion Damage Relationships for Reinforced Concrete Frames,” by A. Singhal and A.S. Kiremidjian, 5/11/95, (PB95-266607, A06, MF-A02).
- NCEER-95-0009 “Experimental and Analytical Investigation of Seismic Retrofit of Structures with Supplemental Damping: Part II - Friction Devices,” by C. Li and A.M. Reinhorn, 7/6/95, (PB96-128087, A11, MF-A03).
- NCEER-95-0010 “Experimental Performance and Analytical Study of a Non-Ductile Reinforced Concrete Frame Structure Retrofitted with Elastomeric Spring Dampers,” by G. Pekcan, J.B. Mander and S.S. Chen, 7/14/95, (PB96-137161, A08, MF-A02).
- NCEER-95-0011 “Development and Experimental Study of Semi-Active Fluid Damping Devices for Seismic Protection of Structures,” by M.D. Symans and M.C. Constantinou, 8/3/95, (PB96-136940, A23, MF-A04).
- NCEER-95-0012 “Real-Time Structural Parameter Modification (RSPM): Development of Innervated Structures,” by Z. Liang, M. Tong and G.C. Lee, 4/11/95, (PB96-137153, A06, MF-A01).
- NCEER-95-0013 “Experimental and Analytical Investigation of Seismic Retrofit of Structures with Supplemental Damping: Part III - Viscous Damping Walls,” by A.M. Reinhorn and C. Li, 10/1/95, (PB96-176409, A11, MF-A03).
- NCEER-95-0014 “Seismic Fragility Analysis of Equipment and Structures in a Memphis Electric Substation,” by J-R. Huo and H.H.M. Hwang, 8/10/95, (PB96-128087, A09, MF-A02).
- NCEER-95-0015 “The Hanshin-Awaji Earthquake of January 17, 1995: Performance of Lifelines,” Edited by M. Shinozuka, 11/3/95, (PB96-176383, A15, MF-A03).
- NCEER-95-0016 “Highway Culvert Performance During Earthquakes,” by T.L. Youd and C.J. Beckman, available as NCEER-96-0015.
- NCEER-95-0017 “The Hanshin-Awaji Earthquake of January 17, 1995: Performance of Highway Bridges,” Edited by I.G. Buckle, 12/1/95, not available.
- NCEER-95-0018 “Modeling of Masonry Infill Panels for Structural Analysis,” by A.M. Reinhorn, A. Madan, R.E. Valles, Y. Reichmann and J.B. Mander, 12/8/95, (PB97-110886, MF-A01, A06).
- NCEER-95-0019 “Optimal Polynomial Control for Linear and Nonlinear Structures,” by A.K. Agrawal and J.N. Yang, 12/11/95, (PB96-168737, A07, MF-A02).

- NCEER-95-0020 “Retrofit of Non-Ductile Reinforced Concrete Frames Using Friction Dampers,” by R.S. Rao, P. Gergely and R.N. White, 12/22/95, (PB97-133508, A10, MF-A02).
- NCEER-95-0021 “Parametric Results for Seismic Response of Pile-Supported Bridge Bents,” by G. Mylonakis, A. Nikolaou and G. Gazetas, 12/22/95, (PB97-100242, A12, MF-A03).
- NCEER-95-0022 “Kinematic Bending Moments in Seismically Stressed Piles,” by A. Nikolaou, G. Mylonakis and G. Gazetas, 12/23/95, (PB97-113914, MF-A03, A13).
- NCEER-96-0001 “Dynamic Response of Unreinforced Masonry Buildings with Flexible Diaphragms,” by A.C. Costley and D.P. Abrams, 10/10/96, (PB97-133573, MF-A03, A15).
- NCEER-96-0002 “State of the Art Review: Foundations and Retaining Structures,” by I. Po Lam, not available.
- NCEER-96-0003 “Ductility of Rectangular Reinforced Concrete Bridge Columns with Moderate Confinement,” by N. Wehbe, M. Saiidi, D. Sanders and B. Douglas, 11/7/96, (PB97-133557, A06, MF-A02).
- NCEER-96-0004 “Proceedings of the Long-Span Bridge Seismic Research Workshop,” edited by I.G. Buckle and I.M. Friedland, not available.
- NCEER-96-0005 “Establish Representative Pier Types for Comprehensive Study: Eastern United States,” by J. Kulicki and Z. Prucz, 5/28/96, (PB98-119217, A07, MF-A02).
- NCEER-96-0006 “Establish Representative Pier Types for Comprehensive Study: Western United States,” by R. Imbsen, R.A. Schamber and T.A. Osterkamp, 5/28/96, (PB98-118607, A07, MF-A02).
- NCEER-96-0007 “Nonlinear Control Techniques for Dynamical Systems with Uncertain Parameters,” by R.G. Ghanem and M.I. Bujakov, 5/27/96, (PB97-100259, A17, MF-A03).
- NCEER-96-0008 “Seismic Evaluation of a 30-Year Old Non-Ductile Highway Bridge Pier and Its Retrofit,” by J.B. Mander, B. Mahmoodzadegan, S. Bhadra and S.S. Chen, 5/31/96, (PB97-110902, MF-A03, A10).
- NCEER-96-0009 “Seismic Performance of a Model Reinforced Concrete Bridge Pier Before and After Retrofit,” by J.B. Mander, J.H. Kim and C.A. Ligozio, 5/31/96, (PB97-110910, MF-A02, A10).
- NCEER-96-0010 “IDARC2D Version 4.0: A Computer Program for the Inelastic Damage Analysis of Buildings,” by R.E. Valles, A.M. Reinhorn, S.K. Kunnath, C. Li and A. Madan, 6/3/96, (PB97-100234, A17, MF-A03).
- NCEER-96-0011 “Estimation of the Economic Impact of Multiple Lifeline Disruption: Memphis Light, Gas and Water Division Case Study,” by S.E. Chang, H.A. Seligson and R.T. Eguchi, 8/16/96, (PB97-133490, A11, MF-A03).
- NCEER-96-0012 “Proceedings from the Sixth Japan-U.S. Workshop on Earthquake Resistant Design of Lifeline Facilities and Countermeasures Against Soil Liquefaction, Edited by M. Hamada and T. O’Rourke, 9/11/96, (PB97-133581, A99, MF-A06).
- NCEER-96-0013 “Chemical Hazards, Mitigation and Preparedness in Areas of High Seismic Risk: A Methodology for Estimating the Risk of Post-Earthquake Hazardous Materials Release,” by H.A. Seligson, R.T. Eguchi, K.J. Tierney and K. Richmond, 11/7/96, (PB97-133565, MF-A02, A08).
- NCEER-96-0014 “Response of Steel Bridge Bearings to Reversed Cyclic Loading,” by J.B. Mander, D-K. Kim, S.S. Chen and G.J. Premus, 11/13/96, (PB97-140735, A12, MF-A03).
- NCEER-96-0015 “Highway Culvert Performance During Past Earthquakes,” by T.L. Youd and C.J. Beckman, 11/25/96, (PB97-133532, A06, MF-A01).
- NCEER-97-0001 “Evaluation, Prevention and Mitigation of Pounding Effects in Building Structures,” by R.E. Valles and A.M. Reinhorn, 2/20/97, (PB97-159552, A14, MF-A03).
- NCEER-97-0002 “Seismic Design Criteria for Bridges and Other Highway Structures,” by C. Rojahn, R. Mayes, D.G. Anderson, J. Clark, J.H. Hom, R.V. Nutt and M.J. O’Rourke, 4/30/97, (PB97-194658, A06, MF-A03).

- NCEER-97-0003 "Proceedings of the U.S.-Italian Workshop on Seismic Evaluation and Retrofit," Edited by D.P. Abrams and G.M. Calvi, 3/19/97, (PB97-194666, A13, MF-A03).
- NCEER-97-0004 "Investigation of Seismic Response of Buildings with Linear and Nonlinear Fluid Viscous Dampers," by A.A. Seleemah and M.C. Constantinou, 5/21/97, (PB98-109002, A15, MF-A03).
- NCEER-97-0005 "Proceedings of the Workshop on Earthquake Engineering Frontiers in Transportation Facilities," edited by G.C. Lee and I.M. Friedland, 8/29/97, (PB98-128911, A25, MR-A04).
- NCEER-97-0006 "Cumulative Seismic Damage of Reinforced Concrete Bridge Piers," by S.K. Kunnath, A. El-Bahy, A. Taylor and W. Stone, 9/2/97, (PB98-108814, A11, MF-A03).
- NCEER-97-0007 "Structural Details to Accommodate Seismic Movements of Highway Bridges and Retaining Walls," by R.A. Imbsen, R.A. Schamber, E. Thorkildsen, A. Kartoum, B.T. Martin, T.N. Rosser and J.M. Kulicki, 9/3/97, (PB98-108996, A09, MF-A02).
- NCEER-97-0008 "A Method for Earthquake Motion-Damage Relationships with Application to Reinforced Concrete Frames," by A. Singhal and A.S. Kiremidjian, 9/10/97, (PB98-108988, A13, MF-A03).
- NCEER-97-0009 "Seismic Analysis and Design of Bridge Abutments Considering Sliding and Rotation," by K. Fishman and R. Richards, Jr., 9/15/97, (PB98-108897, A06, MF-A02).
- NCEER-97-0010 "Proceedings of the FHWA/NCEER Workshop on the National Representation of Seismic Ground Motion for New and Existing Highway Facilities," edited by I.M. Friedland, M.S. Power and R.L. Mayes, 9/22/97, (PB98-128903, A21, MF-A04).
- NCEER-97-0011 "Seismic Analysis for Design or Retrofit of Gravity Bridge Abutments," by K.L. Fishman, R. Richards, Jr. and R.C. Divito, 10/2/97, (PB98-128937, A08, MF-A02).
- NCEER-97-0012 "Evaluation of Simplified Methods of Analysis for Yielding Structures," by P. Tsopelas, M.C. Constantinou, C.A. Kircher and A.S. Whittaker, 10/31/97, (PB98-128929, A10, MF-A03).
- NCEER-97-0013 "Seismic Design of Bridge Columns Based on Control and Repairability of Damage," by C-T. Cheng and J.B. Mander, 12/8/97, (PB98-144249, A11, MF-A03).
- NCEER-97-0014 "Seismic Resistance of Bridge Piers Based on Damage Avoidance Design," by J.B. Mander and C-T. Cheng, 12/10/97, (PB98-144223, A09, MF-A02).
- NCEER-97-0015 "Seismic Response of Nominally Symmetric Systems with Strength Uncertainty," by S. Balopoulou and M. Grigoriu, 12/23/97, (PB98-153422, A11, MF-A03).
- NCEER-97-0016 "Evaluation of Seismic Retrofit Methods for Reinforced Concrete Bridge Columns," by T.J. Wipf, F.W. Klaiber and F.M. Russo, 12/28/97, (PB98-144215, A12, MF-A03).
- NCEER-97-0017 "Seismic Fragility of Existing Conventional Reinforced Concrete Highway Bridges," by C.L. Mullen and A.S. Cakmak, 12/30/97, (PB98-153406, A08, MF-A02).
- NCEER-97-0018 "Loss Assessment of Memphis Buildings," edited by D.P. Abrams and M. Shinozuka, 12/31/97, (PB98-144231, A13, MF-A03).
- NCEER-97-0019 "Seismic Evaluation of Frames with Infill Walls Using Quasi-static Experiments," by K.M. Mosalam, R.N. White and P. Gergely, 12/31/97, (PB98-153455, A07, MF-A02).
- NCEER-97-0020 "Seismic Evaluation of Frames with Infill Walls Using Pseudo-dynamic Experiments," by K.M. Mosalam, R.N. White and P. Gergely, 12/31/97, (PB98-153430, A07, MF-A02).
- NCEER-97-0021 "Computational Strategies for Frames with Infill Walls: Discrete and Smeared Crack Analyses and Seismic Fragility," by K.M. Mosalam, R.N. White and P. Gergely, 12/31/97, (PB98-153414, A10, MF-A02).

- NCEER-97-0022 "Proceedings of the NCEER Workshop on Evaluation of Liquefaction Resistance of Soils," edited by T.L. Youd and I.M. Idriss, 12/31/97, (PB98-155617, A15, MF-A03).
- MCEER-98-0001 "Extraction of Nonlinear Hysteretic Properties of Seismically Isolated Bridges from Quick-Release Field Tests," by Q. Chen, B.M. Douglas, E.M. Maragakis and I.G. Buckle, 5/26/98, (PB99-118838, A06, MF-A01).
- MCEER-98-0002 "Methodologies for Evaluating the Importance of Highway Bridges," by A. Thomas, S. Eshenaur and J. Kulicki, 5/29/98, (PB99-118846, A10, MF-A02).
- MCEER-98-0003 "Capacity Design of Bridge Piers and the Analysis of Overstrength," by J.B. Mander, A. Dutta and P. Goel, 6/1/98, (PB99-118853, A09, MF-A02).
- MCEER-98-0004 "Evaluation of Bridge Damage Data from the Loma Prieta and Northridge, California Earthquakes," by N. Basoz and A. Kiremidjian, 6/2/98, (PB99-118861, A15, MF-A03).
- MCEER-98-0005 "Screening Guide for Rapid Assessment of Liquefaction Hazard at Highway Bridge Sites," by T. L. Youd, 6/16/98, (PB99-118879, A06, not available on microfiche).
- MCEER-98-0006 "Structural Steel and Steel/Concrete Interface Details for Bridges," by P. Ritchie, N. Kaulh and J. Kulicki, 7/13/98, (PB99-118945, A06, MF-A01).
- MCEER-98-0007 "Capacity Design and Fatigue Analysis of Confined Concrete Columns," by A. Dutta and J.B. Mander, 7/14/98, (PB99-118960, A14, MF-A03).
- MCEER-98-0008 "Proceedings of the Workshop on Performance Criteria for Telecommunication Services Under Earthquake Conditions," edited by A.J. Schiff, 7/15/98, (PB99-118952, A08, MF-A02).
- MCEER-98-0009 "Fatigue Analysis of Unconfined Concrete Columns," by J.B. Mander, A. Dutta and J.H. Kim, 9/12/98, (PB99-123655, A10, MF-A02).
- MCEER-98-0010 "Centrifuge Modeling of Cyclic Lateral Response of Pile-Cap Systems and Seat-Type Abutments in Dry Sands," by A.D. Gadre and R. Dobry, 10/2/98, (PB99-123606, A13, MF-A03).
- MCEER-98-0011 "IDARC-BRIDGE: A Computational Platform for Seismic Damage Assessment of Bridge Structures," by A.M. Reinhorn, V. Simeonov, G. Mylonakis and Y. Reichman, 10/2/98, (PB99-162919, A15, MF-A03).
- MCEER-98-0012 "Experimental Investigation of the Dynamic Response of Two Bridges Before and After Retrofitting with Elastomeric Bearings," by D.A. Wendichansky, S.S. Chen and J.B. Mander, 10/2/98, (PB99-162927, A15, MF-A03).
- MCEER-98-0013 "Design Procedures for Hinge Restrainers and Hinge Sear Width for Multiple-Frame Bridges," by R. Des Roches and G.L. Fenves, 11/3/98, (PB99-140477, A13, MF-A03).
- MCEER-98-0014 "Response Modification Factors for Seismically Isolated Bridges," by M.C. Constantinou and J.K. Quarshie, 11/3/98, (PB99-140485, A14, MF-A03).
- MCEER-98-0015 "Proceedings of the U.S.-Italy Workshop on Seismic Protective Systems for Bridges," edited by I.M. Friedland and M.C. Constantinou, 11/3/98, (PB2000-101711, A22, MF-A04).
- MCEER-98-0016 "Appropriate Seismic Reliability for Critical Equipment Systems: Recommendations Based on Regional Analysis of Financial and Life Loss," by K. Porter, C. Scawthorn, C. Taylor and N. Blais, 11/10/98, (PB99-157265, A08, MF-A02).
- MCEER-98-0017 "Proceedings of the U.S. Japan Joint Seminar on Civil Infrastructure Systems Research," edited by M. Shinozuka and A. Rose, 11/12/98, (PB99-156713, A16, MF-A03).
- MCEER-98-0018 "Modeling of Pile Footings and Drilled Shafts for Seismic Design," by I. PoLam, M. Kapuskar and D. Chaudhuri, 12/21/98, (PB99-157257, A09, MF-A02).

- MCEER-99-0001 "Seismic Evaluation of a Masonry Infilled Reinforced Concrete Frame by Pseudodynamic Testing," by S.G. Buonopane and R.N. White, 2/16/99, (PB99-162851, A09, MF-A02).
- MCEER-99-0002 "Response History Analysis of Structures with Seismic Isolation and Energy Dissipation Systems: Verification Examples for Program SAP2000," by J. Scheller and M.C. Constantinou, 2/22/99, (PB99-162869, A08, MF-A02).
- MCEER-99-0003 "Experimental Study on the Seismic Design and Retrofit of Bridge Columns Including Axial Load Effects," by A. Dutta, T. Kokorina and J.B. Mander, 2/22/99, (PB99-162877, A09, MF-A02).
- MCEER-99-0004 "Experimental Study of Bridge Elastomeric and Other Isolation and Energy Dissipation Systems with Emphasis on Uplift Prevention and High Velocity Near-source Seismic Excitation," by A. Kasalanati and M. C. Constantinou, 2/26/99, (PB99-162885, A12, MF-A03).
- MCEER-99-0005 "Truss Modeling of Reinforced Concrete Shear-flexure Behavior," by J.H. Kim and J.B. Mander, 3/8/99, (PB99-163693, A12, MF-A03).
- MCEER-99-0006 "Experimental Investigation and Computational Modeling of Seismic Response of a 1:4 Scale Model Steel Structure with a Load Balancing Supplemental Damping System," by G. Pekcan, J.B. Mander and S.S. Chen, 4/2/99, (PB99-162893, A11, MF-A03).
- MCEER-99-0007 "Effect of Vertical Ground Motions on the Structural Response of Highway Bridges," by M.R. Button, C.J. Cronin and R.L. Mayes, 4/10/99, (PB2000-101411, A10, MF-A03).
- MCEER-99-0008 "Seismic Reliability Assessment of Critical Facilities: A Handbook, Supporting Documentation, and Model Code Provisions," by G.S. Johnson, R.E. Sheppard, M.D. Quilici, S.J. Eder and C.R. Scawthorn, 4/12/99, (PB2000-101701, A18, MF-A04).
- MCEER-99-0009 "Impact Assessment of Selected MCEER Highway Project Research on the Seismic Design of Highway Structures," by C. Rojahn, R. Mayes, D.G. Anderson, J.H. Clark, D'Appolonia Engineering, S. Gloyd and R.V. Nutt, 4/14/99, (PB99-162901, A10, MF-A02).
- MCEER-99-0010 "Site Factors and Site Categories in Seismic Codes," by R. Dobry, R. Ramos and M.S. Power, 7/19/99, (PB2000-101705, A08, MF-A02).
- MCEER-99-0011 "Restrainer Design Procedures for Multi-Span Simply-Supported Bridges," by M.J. Randall, M. Saiidi, E. Maragakis and T. Isakovic, 7/20/99, (PB2000-101702, A10, MF-A02).
- MCEER-99-0012 "Property Modification Factors for Seismic Isolation Bearings," by M.C. Constantinou, P. Tsopelas, A. Kasalanati and E. Wolff, 7/20/99, (PB2000-103387, A11, MF-A03).
- MCEER-99-0013 "Critical Seismic Issues for Existing Steel Bridges," by P. Ritchie, N. Kauh and J. Kulicki, 7/20/99, (PB2000-101697, A09, MF-A02).
- MCEER-99-0014 "Nonstructural Damage Database," by A. Kao, T.T. Soong and A. Vender, 7/24/99, (PB2000-101407, A06, MF-A01).
- MCEER-99-0015 "Guide to Remedial Measures for Liquefaction Mitigation at Existing Highway Bridge Sites," by H.G. Cooke and J. K. Mitchell, 7/26/99, (PB2000-101703, A11, MF-A03).
- MCEER-99-0016 "Proceedings of the MCEER Workshop on Ground Motion Methodologies for the Eastern United States," edited by N. Abrahamson and A. Becker, 8/11/99, (PB2000-103385, A07, MF-A02).
- MCEER-99-0017 "Quindío, Colombia Earthquake of January 25, 1999: Reconnaissance Report," by A.P. Asfura and P.J. Flores, 10/4/99, (PB2000-106893, A06, MF-A01).
- MCEER-99-0018 "Hysteretic Models for Cyclic Behavior of Deteriorating Inelastic Structures," by M.V. Sivaselvan and A.M. Reinhorn, 11/5/99, (PB2000-103386, A08, MF-A02).

- MCEER-99-0019 "Proceedings of the 7<sup>th</sup> U.S.- Japan Workshop on Earthquake Resistant Design of Lifeline Facilities and Countermeasures Against Soil Liquefaction," edited by T.D. O'Rourke, J.P. Bardet and M. Hamada, 11/19/99, (PB2000-103354, A99, MF-A06).
- MCEER-99-0020 "Development of Measurement Capability for Micro-Vibration Evaluations with Application to Chip Fabrication Facilities," by G.C. Lee, Z. Liang, J.W. Song, J.D. Shen and W.C. Liu, 12/1/99, (PB2000-105993, A08, MF-A02).
- MCEER-99-0021 "Design and Retrofit Methodology for Building Structures with Supplemental Energy Dissipating Systems," by G. Pekcan, J.B. Mander and S.S. Chen, 12/31/99, (PB2000-105994, A11, MF-A03).
- MCEER-00-0001 "The Marmara, Turkey Earthquake of August 17, 1999: Reconnaissance Report," edited by C. Scawthorn; with major contributions by M. Bruneau, R. Eguchi, T. Holzer, G. Johnson, J. Mander, J. Mitchell, W. Mitchell, A. Papageorgiou, C. Scaethorn, and G. Webb, 3/23/00, (PB2000-106200, A11, MF-A03).
- MCEER-00-0002 "Proceedings of the MCEER Workshop for Seismic Hazard Mitigation of Health Care Facilities," edited by G.C. Lee, M. Ettouney, M. Grigoriu, J. Hauer and J. Nigg, 3/29/00, (PB2000-106892, A08, MF-A02).
- MCEER-00-0003 "The Chi-Chi, Taiwan Earthquake of September 21, 1999: Reconnaissance Report," edited by G.C. Lee and C.H. Loh, with major contributions by G.C. Lee, M. Bruneau, I.G. Buckle, S.E. Chang, P.J. Flores, T.D. O'Rourke, M. Shinozuka, T.T. Soong, C-H. Loh, K-C. Chang, Z-J. Chen, J-S. Hwang, M-L. Lin, G-Y. Liu, K-C. Tsai, G.C. Yao and C-L. Yen, 4/30/00, (PB2001-100980, A10, MF-A02).
- MCEER-00-0004 "Seismic Retrofit of End-Sway Frames of Steel Deck-Truss Bridges with a Supplemental Tendon System: Experimental and Analytical Investigation," by G. Pekcan, J.B. Mander and S.S. Chen, 7/1/00, (PB2001-100982, A10, MF-A02).
- MCEER-00-0005 "Sliding Fragility of Unrestrained Equipment in Critical Facilities," by W.H. Chong and T.T. Soong, 7/5/00, (PB2001-100983, A08, MF-A02).
- MCEER-00-0006 "Seismic Response of Reinforced Concrete Bridge Pier Walls in the Weak Direction," by N. Abo-Shadi, M. Saiidi and D. Sanders, 7/17/00, (PB2001-100981, A17, MF-A03).
- MCEER-00-0007 "Low-Cycle Fatigue Behavior of Longitudinal Reinforcement in Reinforced Concrete Bridge Columns," by J. Brown and S.K. Kunnath, 7/23/00, (PB2001-104392, A08, MF-A02).
- MCEER-00-0008 "Soil Structure Interaction of Bridges for Seismic Analysis," I. PoLam and H. Law, 9/25/00, (PB2001-105397, A08, MF-A02).
- MCEER-00-0009 "Proceedings of the First MCEER Workshop on Mitigation of Earthquake Disaster by Advanced Technologies (MEDAT-1), edited by M. Shinozuka, D.J. Inman and T.D. O'Rourke, 11/10/00, (PB2001-105399, A14, MF-A03).
- MCEER-00-0010 "Development and Evaluation of Simplified Procedures for Analysis and Design of Buildings with Passive Energy Dissipation Systems, Revision 01," by O.M. Ramirez, M.C. Constantinou, C.A. Kircher, A.S. Whittaker, M.W. Johnson, J.D. Gomez and C. Chrysostomou, 11/16/01, (PB2001-105523, A23, MF-A04).
- MCEER-00-0011 "Dynamic Soil-Foundation-Structure Interaction Analyses of Large Caissons," by C-Y. Chang, C-M. Mok, Z-L. Wang, R. Settgast, F. Waggoner, M.A. Ketchum, H.M. Gonnermann and C-C. Chin, 12/30/00, (PB2001-104373, A07, MF-A02).
- MCEER-00-0012 "Experimental Evaluation of Seismic Performance of Bridge Restrainers," by A.G. Vlassis, E.M. Maragakis and M. Saiid Saiidi, 12/30/00, (PB2001-104354, A09, MF-A02).
- MCEER-00-0013 "Effect of Spatial Variation of Ground Motion on Highway Structures," by M. Shinozuka, V. Saxena and G. Deodatis, 12/31/00, (PB2001-108755, A13, MF-A03).
- MCEER-00-0014 "A Risk-Based Methodology for Assessing the Seismic Performance of Highway Systems," by S.D. Werner, C.E. Taylor, J.E. Moore, II, J.S. Walton and S. Cho, 12/31/00, (PB2001-108756, A14, MF-A03).

- MCEER-01-0001 “Experimental Investigation of P-Delta Effects to Collapse During Earthquakes,” by D. Vian and M. Bruneau, 6/25/01, (PB2002-100534, A17, MF-A03).
- MCEER-01-0002 “Proceedings of the Second MCEER Workshop on Mitigation of Earthquake Disaster by Advanced Technologies (MEDAT-2),” edited by M. Bruneau and D.J. Inman, 7/23/01, (PB2002-100434, A16, MF-A03).
- MCEER-01-0003 “Sensitivity Analysis of Dynamic Systems Subjected to Seismic Loads,” by C. Roth and M. Grigoriu, 9/18/01, (PB2003-100884, A12, MF-A03).
- MCEER-01-0004 “Overcoming Obstacles to Implementing Earthquake Hazard Mitigation Policies: Stage 1 Report,” by D.J. Alesch and W.J. Petak, 12/17/01, (PB2002-107949, A07, MF-A02).
- MCEER-01-0005 “Updating Real-Time Earthquake Loss Estimates: Methods, Problems and Insights,” by C.E. Taylor, S.E. Chang and R.T. Eguchi, 12/17/01, (PB2002-107948, A05, MF-A01).
- MCEER-01-0006 “Experimental Investigation and Retrofit of Steel Pile Foundations and Pile Bents Under Cyclic Lateral Loadings,” by A. Shama, J. Mander, B. Blabac and S. Chen, 12/31/01, (PB2002-107950, A13, MF-A03).
- MCEER-02-0001 “Assessment of Performance of Bolu Viaduct in the 1999 Duzce Earthquake in Turkey” by P.C. Roussis, M.C. Constantinou, M. Erdik, E. Durukal and M. Dicleli, 5/8/02, (PB2003-100883, A08, MF-A02).
- MCEER-02-0002 “Seismic Behavior of Rail Counterweight Systems of Elevators in Buildings,” by M.P. Singh, Rildova and L.E. Suarez, 5/27/02. (PB2003-100882, A11, MF-A03).
- MCEER-02-0003 “Development of Analysis and Design Procedures for Spread Footings,” by G. Mylonakis, G. Gazetas, S. Nikolaou and A. Chauncey, 10/02/02, (PB2004-101636, A13, MF-A03, CD-A13).
- MCEER-02-0004 “Bare-Earth Algorithms for Use with SAR and LIDAR Digital Elevation Models,” by C.K. Huyck, R.T. Eguchi and B. Houshmand, 10/16/02, (PB2004-101637, A07, CD-A07).
- MCEER-02-0005 “Review of Energy Dissipation of Compression Members in Concentrically Braced Frames,” by K.Lee and M. Bruneau, 10/18/02, (PB2004-101638, A10, CD-A10).
- MCEER-03-0001 “Experimental Investigation of Light-Gauge Steel Plate Shear Walls for the Seismic Retrofit of Buildings” by J. Berman and M. Bruneau, 5/2/03, (PB2004-101622, A10, MF-A03, CD-A10).
- MCEER-03-0002 “Statistical Analysis of Fragility Curves,” by M. Shinozuka, M.Q. Feng, H. Kim, T. Uzawa and T. Ueda, 6/16/03, (PB2004-101849, A09, CD-A09).
- MCEER-03-0003 “Proceedings of the Eighth U.S.-Japan Workshop on Earthquake Resistant Design of Lifeline Facilities and Countermeasures Against Liquefaction,” edited by M. Hamada, J.P. Bardet and T.D. O’Rourke, 6/30/03, (PB2004-104386, A99, CD-A99).
- MCEER-03-0004 “Proceedings of the PRC-US Workshop on Seismic Analysis and Design of Special Bridges,” edited by L.C. Fan and G.C. Lee, 7/15/03, (PB2004-104387, A14, CD-A14).
- MCEER-03-0005 “Urban Disaster Recovery: A Framework and Simulation Model,” by S.B. Miles and S.E. Chang, 7/25/03, (PB2004-104388, A07, CD-A07).
- MCEER-03-0006 “Behavior of Underground Piping Joints Due to Static and Dynamic Loading,” by R.D. Meis, M. Maragakis and R. Siddharthan, 11/17/03, (PB2005-102194, A13, MF-A03, CD-A00).
- MCEER-04-0001 “Experimental Study of Seismic Isolation Systems with Emphasis on Secondary System Response and Verification of Accuracy of Dynamic Response History Analysis Methods,” by E. Wolff and M. Constantinou, 1/16/04 (PB2005-102195, A99, MF-E08, CD-A00).
- MCEER-04-0002 “Tension, Compression and Cyclic Testing of Engineered Cementitious Composite Materials,” by K. Kesner and S.L. Billington, 3/1/04, (PB2005-102196, A08, CD-A08).

- MCEER-04-0003 "Cyclic Testing of Braces Laterally Restrained by Steel Studs to Enhance Performance During Earthquakes," by O.C. Celik, J.W. Berman and M. Bruneau, 3/16/04, (PB2005-102197, A13, MF-A03, CD-A00).
- MCEER-04-0004 "Methodologies for Post Earthquake Building Damage Detection Using SAR and Optical Remote Sensing: Application to the August 17, 1999 Marmara, Turkey Earthquake," by C.K. Huyck, B.J. Adams, S. Cho, R.T. Eguchi, B. Mansouri and B. Houshmand, 6/15/04, (PB2005-104888, A10, CD-A00).
- MCEER-04-0005 "Nonlinear Structural Analysis Towards Collapse Simulation: A Dynamical Systems Approach," by M.V. Sivaselvan and A.M. Reinhorn, 6/16/04, (PB2005-104889, A11, MF-A03, CD-A00).
- MCEER-04-0006 "Proceedings of the Second PRC-US Workshop on Seismic Analysis and Design of Special Bridges," edited by G.C. Lee and L.C. Fan, 6/25/04, (PB2005-104890, A16, CD-A00).
- MCEER-04-0007 "Seismic Vulnerability Evaluation of Axially Loaded Steel Built-up Laced Members," by K. Lee and M. Bruneau, 6/30/04, (PB2005-104891, A16, CD-A00).
- MCEER-04-0008 "Evaluation of Accuracy of Simplified Methods of Analysis and Design of Buildings with Damping Systems for Near-Fault and for Soft-Soil Seismic Motions," by E.A. Pavlou and M.C. Constantinou, 8/16/04, (PB2005-104892, A08, MF-A02, CD-A00).
- MCEER-04-0009 "Assessment of Geotechnical Issues in Acute Care Facilities in California," by M. Lew, T.D. O'Rourke, R. Dobry and M. Koch, 9/15/04, (PB2005-104893, A08, CD-A00).
- MCEER-04-0010 "Scissor-Jack-Damper Energy Dissipation System," by A.N. Sigaher-Boyle and M.C. Constantinou, 12/1/04 (PB2005-108221).
- MCEER-04-0011 "Seismic Retrofit of Bridge Steel Truss Piers Using a Controlled Rocking Approach," by M. Pollino and M. Bruneau, 12/20/04 (PB2006-105795).
- MCEER-05-0001 "Experimental and Analytical Studies of Structures Seismically Isolated with an Uplift-Restraint Isolation System," by P.C. Roussis and M.C. Constantinou, 1/10/05 (PB2005-108222).
- MCEER-05-0002 "A Versatile Experimentation Model for Study of Structures Near Collapse Applied to Seismic Evaluation of Irregular Structures," by D. Kusumastuti, A.M. Reinhorn and A. Rutenberg, 3/31/05 (PB2006-101523).
- MCEER-05-0003 "Proceedings of the Third PRC-US Workshop on Seismic Analysis and Design of Special Bridges," edited by L.C. Fan and G.C. Lee, 4/20/05, (PB2006-105796).
- MCEER-05-0004 "Approaches for the Seismic Retrofit of Braced Steel Bridge Piers and Proof-of-Concept Testing of an Eccentrically Braced Frame with Tubular Link," by J.W. Berman and M. Bruneau, 4/21/05 (PB2006-101524).
- MCEER-05-0005 "Simulation of Strong Ground Motions for Seismic Fragility Evaluation of Nonstructural Components in Hospitals," by A. Wanitkorkul and A. Filiatrault, 5/26/05 (PB2006-500027).
- MCEER-05-0006 "Seismic Safety in California Hospitals: Assessing an Attempt to Accelerate the Replacement or Seismic Retrofit of Older Hospital Facilities," by D.J. Alesch, L.A. Arendt and W.J. Petak, 6/6/05 (PB2006-105794).
- MCEER-05-0007 "Development of Seismic Strengthening and Retrofit Strategies for Critical Facilities Using Engineered Cementitious Composite Materials," by K. Kesner and S.L. Billington, 8/29/05 (PB2006-111701).
- MCEER-05-0008 "Experimental and Analytical Studies of Base Isolation Systems for Seismic Protection of Power Transformers," by N. Murota, M.Q. Feng and G-Y. Liu, 9/30/05 (PB2006-111702).
- MCEER-05-0009 "3D-BASIS-ME-MB: Computer Program for Nonlinear Dynamic Analysis of Seismically Isolated Structures," by P.C. Tsopelas, P.C. Roussis, M.C. Constantinou, R. Buchanan and A.M. Reinhorn, 10/3/05 (PB2006-111703).
- MCEER-05-0010 "Steel Plate Shear Walls for Seismic Design and Retrofit of Building Structures," by D. Vian and M. Bruneau, 12/15/05 (PB2006-111704).

- MCEER-05-0011 "The Performance-Based Design Paradigm," by M.J. Astrella and A. Whittaker, 12/15/05 (PB2006-111705).
- MCEER-06-0001 "Seismic Fragility of Suspended Ceiling Systems," H. Badillo-Almaraz, A.S. Whittaker, A.M. Reinhorn and G.P. Cimellaro, 2/4/06 (PB2006-111706).
- MCEER-06-0002 "Multi-Dimensional Fragility of Structures," by G.P. Cimellaro, A.M. Reinhorn and M. Bruneau, 3/1/06 (PB2007-106974, A09, MF-A02, CD A00).
- MCEER-06-0003 "Built-Up Shear Links as Energy Dissipators for Seismic Protection of Bridges," by P. Dusicka, A.M. Itani and I.G. Buckle, 3/15/06 (PB2006-111708).
- MCEER-06-0004 "Analytical Investigation of the Structural Fuse Concept," by R.E. Vargas and M. Bruneau, 3/16/06 (PB2006-111709).
- MCEER-06-0005 "Experimental Investigation of the Structural Fuse Concept," by R.E. Vargas and M. Bruneau, 3/17/06 (PB2006-111710).
- MCEER-06-0006 "Further Development of Tubular Eccentrically Braced Frame Links for the Seismic Retrofit of Braced Steel Truss Bridge Piers," by J.W. Berman and M. Bruneau, 3/27/06 (PB2007-105147).
- MCEER-06-0007 "REDARS Validation Report," by S. Cho, C.K. Huyck, S. Ghosh and R.T. Eguchi, 8/8/06 (PB2007-106983).
- MCEER-06-0008 "Review of Current NDE Technologies for Post-Earthquake Assessment of Retrofitted Bridge Columns," by J.W. Song, Z. Liang and G.C. Lee, 8/21/06 (PB2007-106984).
- MCEER-06-0009 "Liquefaction Remediation in Silty Soils Using Dynamic Compaction and Stone Columns," by S. Thevanayagam, G.R. Martin, R. Nashed, T. Shenthan, T. Kanagalingam and N. Ecemis, 8/28/06 (PB2007-106985).
- MCEER-06-0010 "Conceptual Design and Experimental Investigation of Polymer Matrix Composite Infill Panels for Seismic Retrofitting," by W. Jung, M. Chiewanichakorn and A.J. Aref, 9/21/06 (PB2007-106986).
- MCEER-06-0011 "A Study of the Coupled Horizontal-Vertical Behavior of Elastomeric and Lead-Rubber Seismic Isolation Bearings," by G.P. Warn and A.S. Whittaker, 9/22/06 (PB2007-108679).
- MCEER-06-0012 "Proceedings of the Fourth PRC-US Workshop on Seismic Analysis and Design of Special Bridges: Advancing Bridge Technologies in Research, Design, Construction and Preservation," Edited by L.C. Fan, G.C. Lee and L. Ziang, 10/12/06 (PB2007-109042).
- MCEER-06-0013 "Cyclic Response and Low Cycle Fatigue Characteristics of Plate Steels," by P. Dusicka, A.M. Itani and I.G. Buckle, 11/1/06 (PB2007-106987).
- MCEER-06-0014 "Proceedings of the Second US-Taiwan Bridge Engineering Workshop," edited by W.P. Yen, J. Shen, J-Y. Chen and M. Wang, 11/15/06 (PB2008-500041).
- MCEER-06-0015 "User Manual and Technical Documentation for the REDARS<sup>TM</sup> Import Wizard," by S. Cho, S. Ghosh, C.K. Huyck and S.D. Werner, 11/30/06 (PB2007-114766).
- MCEER-06-0016 "Hazard Mitigation Strategy and Monitoring Technologies for Urban and Infrastructure Public Buildings: Proceedings of the China-US Workshops," edited by X.Y. Zhou, A.L. Zhang, G.C. Lee and M. Tong, 12/12/06 (PB2008-500018).
- MCEER-07-0001 "Static and Kinetic Coefficients of Friction for Rigid Blocks," by C. Kafali, S. Fathali, M. Grigoriu and A.S. Whittaker, 3/20/07 (PB2007-114767).
- MCEER-07-0002 "Hazard Mitigation Investment Decision Making: Organizational Response to Legislative Mandate," by L.A. Arendt, D.J. Alesch and W.J. Petak, 4/9/07 (PB2007-114768).
- MCEER-07-0003 "Seismic Behavior of Bidirectional-Resistant Ductile End Diaphragms with Unbonded Braces in Straight or Skewed Steel Bridges," by O. Celik and M. Bruneau, 4/11/07 (PB2008-105141).

- MCEER-07-0004 "Modeling Pile Behavior in Large Pile Groups Under Lateral Loading," by A.M. Dodds and G.R. Martin, 4/16/07(PB2008-105142).
- MCEER-07-0005 "Experimental Investigation of Blast Performance of Seismically Resistant Concrete-Filled Steel Tube Bridge Piers," by S. Fujikura, M. Bruneau and D. Lopez-Garcia, 4/20/07 (PB2008-105143).
- MCEER-07-0006 "Seismic Analysis of Conventional and Isolated Liquefied Natural Gas Tanks Using Mechanical Analogs," by I.P. Christovasilis and A.S. Whittaker, 5/1/07, not available.
- MCEER-07-0007 "Experimental Seismic Performance Evaluation of Isolation/Restraint Systems for Mechanical Equipment – Part 1: Heavy Equipment Study," by S. Fathali and A. Filiatrault, 6/6/07 (PB2008-105144).
- MCEER-07-0008 "Seismic Vulnerability of Timber Bridges and Timber Substructures," by A.A. Sharma, J.B. Mander, I.M. Friedland and D.R. Allicock, 6/7/07 (PB2008-105145).
- MCEER-07-0009 "Experimental and Analytical Study of the XY-Friction Pendulum (XY-FP) Bearing for Bridge Applications," by C.C. Marin-Artieda, A.S. Whittaker and M.C. Constantinou, 6/7/07 (PB2008-105191).
- MCEER-07-0010 "Proceedings of the PRC-US Earthquake Engineering Forum for Young Researchers," Edited by G.C. Lee and X.Z. Qi, 6/8/07 (PB2008-500058).
- MCEER-07-0011 "Design Recommendations for Perforated Steel Plate Shear Walls," by R. Purba and M. Bruneau, 6/18/07, (PB2008-105192).
- MCEER-07-0012 "Performance of Seismic Isolation Hardware Under Service and Seismic Loading," by M.C. Constantinou, A.S. Whittaker, Y. Kalpakidis, D.M. Fenz and G.P. Warn, 8/27/07, (PB2008-105193).
- MCEER-07-0013 "Experimental Evaluation of the Seismic Performance of Hospital Piping Subassemblies," by E.R. Goodwin, E. Maragakis and A.M. Itani, 9/4/07, (PB2008-105194).
- MCEER-07-0014 "A Simulation Model of Urban Disaster Recovery and Resilience: Implementation for the 1994 Northridge Earthquake," by S. Miles and S.E. Chang, 9/7/07, (PB2008-106426).
- MCEER-07-0015 "Statistical and Mechanistic Fragility Analysis of Concrete Bridges," by M. Shinozuka, S. Banerjee and S-H. Kim, 9/10/07, (PB2008-106427).
- MCEER-07-0016 "Three-Dimensional Modeling of Inelastic Buckling in Frame Structures," by M. Schachter and AM. Reinhorn, 9/13/07, (PB2008-108125).
- MCEER-07-0017 "Modeling of Seismic Wave Scattering on Pile Groups and Caissons," by I. Po Lam, H. Law and C.T. Yang, 9/17/07 (PB2008-108150).
- MCEER-07-0018 "Bridge Foundations: Modeling Large Pile Groups and Caissons for Seismic Design," by I. Po Lam, H. Law and G.R. Martin (Coordinating Author), 12/1/07 (PB2008-111190).
- MCEER-07-0019 "Principles and Performance of Roller Seismic Isolation Bearings for Highway Bridges," by G.C. Lee, Y.C. Ou, Z. Liang, T.C. Niu and J. Song, 12/10/07 (PB2009-110466).
- MCEER-07-0020 "Centrifuge Modeling of Permeability and Pinning Reinforcement Effects on Pile Response to Lateral Spreading," by L.L Gonzalez-Lagos, T. Abdoun and R. Dobry, 12/10/07 (PB2008-111191).
- MCEER-07-0021 "Damage to the Highway System from the Pisco, Perú Earthquake of August 15, 2007," by J.S. O'Connor, L. Mesa and M. Nykamp, 12/10/07, (PB2008-108126).
- MCEER-07-0022 "Experimental Seismic Performance Evaluation of Isolation/Restraint Systems for Mechanical Equipment – Part 2: Light Equipment Study," by S. Fathali and A. Filiatrault, 12/13/07 (PB2008-111192).
- MCEER-07-0023 "Fragility Considerations in Highway Bridge Design," by M. Shinozuka, S. Banerjee and S.H. Kim, 12/14/07 (PB2008-111193).

- MCEER-07-0024 "Performance Estimates for Seismically Isolated Bridges," by G.P. Warn and A.S. Whittaker, 12/30/07 (PB2008-112230).
- MCEER-08-0001 "Seismic Performance of Steel Girder Bridge Superstructures with Conventional Cross Frames," by L.P. Carden, A.M. Itani and I.G. Buckle, 1/7/08, (PB2008-112231).
- MCEER-08-0002 "Seismic Performance of Steel Girder Bridge Superstructures with Ductile End Cross Frames with Seismic Isolators," by L.P. Carden, A.M. Itani and I.G. Buckle, 1/7/08 (PB2008-112232).
- MCEER-08-0003 "Analytical and Experimental Investigation of a Controlled Rocking Approach for Seismic Protection of Bridge Steel Truss Piers," by M. Pollino and M. Bruneau, 1/21/08 (PB2008-112233).
- MCEER-08-0004 "Linking Lifeline Infrastructure Performance and Community Disaster Resilience: Models and Multi-Stakeholder Processes," by S.E. Chang, C. Pasion, K. Tatebe and R. Ahmad, 3/3/08 (PB2008-112234).
- MCEER-08-0005 "Modal Analysis of Generally Damped Linear Structures Subjected to Seismic Excitations," by J. Song, Y-L. Chu, Z. Liang and G.C. Lee, 3/4/08 (PB2009-102311).
- MCEER-08-0006 "System Performance Under Multi-Hazard Environments," by C. Kafali and M. Grigoriu, 3/4/08 (PB2008-112235).
- MCEER-08-0007 "Mechanical Behavior of Multi-Spherical Sliding Bearings," by D.M. Fenz and M.C. Constantinou, 3/6/08 (PB2008-112236).
- MCEER-08-0008 "Post-Earthquake Restoration of the Los Angeles Water Supply System," by T.H.P. Tabucchi and R.A. Davidson, 3/7/08 (PB2008-112237).
- MCEER-08-0009 "Fragility Analysis of Water Supply Systems," by A. Jacobson and M. Grigoriu, 3/10/08 (PB2009-105545).
- MCEER-08-0010 "Experimental Investigation of Full-Scale Two-Story Steel Plate Shear Walls with Reduced Beam Section Connections," by B. Qu, M. Bruneau, C-H. Lin and K-C. Tsai, 3/17/08 (PB2009-106368).
- MCEER-08-0011 "Seismic Evaluation and Rehabilitation of Critical Components of Electrical Power Systems," S. Ersoy, B. Feizi, A. Ashrafi and M. Ala Saadeghvaziri, 3/17/08 (PB2009-105546).
- MCEER-08-0012 "Seismic Behavior and Design of Boundary Frame Members of Steel Plate Shear Walls," by B. Qu and M. Bruneau, 4/26/08 . (PB2009-106744).
- MCEER-08-0013 "Development and Appraisal of a Numerical Cyclic Loading Protocol for Quantifying Building System Performance," by A. Filiatrault, A. Wanitkorkul and M. Constantinou, 4/27/08 (PB2009-107906).
- MCEER-08-0014 "Structural and Nonstructural Earthquake Design: The Challenge of Integrating Specialty Areas in Designing Complex, Critical Facilities," by W.J. Petak and D.J. Alesch, 4/30/08 (PB2009-107907).
- MCEER-08-0015 "Seismic Performance Evaluation of Water Systems," by Y. Wang and T.D. O'Rourke, 5/5/08 (PB2009-107908).
- MCEER-08-0016 "Seismic Response Modeling of Water Supply Systems," by P. Shi and T.D. O'Rourke, 5/5/08 (PB2009-107910).
- MCEER-08-0017 "Numerical and Experimental Studies of Self-Centering Post-Tensioned Steel Frames," by D. Wang and A. Filiatrault, 5/12/08 (PB2009-110479).
- MCEER-08-0018 "Development, Implementation and Verification of Dynamic Analysis Models for Multi-Spherical Sliding Bearings," by D.M. Fenz and M.C. Constantinou, 8/15/08 (PB2009-107911).
- MCEER-08-0019 "Performance Assessment of Conventional and Base Isolated Nuclear Power Plants for Earthquake Blast Loadings," by Y.N. Huang, A.S. Whittaker and N. Luco, 10/28/08 (PB2009-107912).

- MCEER-08-0020 “Remote Sensing for Resilient Multi-Hazard Disaster Response – Volume I: Introduction to Damage Assessment Methodologies,” by B.J. Adams and R.T. Eguchi, 11/17/08 (PB2010-102695).
- MCEER-08-0021 “Remote Sensing for Resilient Multi-Hazard Disaster Response – Volume II: Counting the Number of Collapsed Buildings Using an Object-Oriented Analysis: Case Study of the 2003 Bam Earthquake,” by L. Gusella, C.K. Huyck and B.J. Adams, 11/17/08 (PB2010-100925).
- MCEER-08-0022 “Remote Sensing for Resilient Multi-Hazard Disaster Response – Volume III: Multi-Sensor Image Fusion Techniques for Robust Neighborhood-Scale Urban Damage Assessment,” by B.J. Adams and A. McMillan, 11/17/08 (PB2010-100926).
- MCEER-08-0023 “Remote Sensing for Resilient Multi-Hazard Disaster Response – Volume IV: A Study of Multi-Temporal and Multi-Resolution SAR Imagery for Post-Katrina Flood Monitoring in New Orleans,” by A. McMillan, J.G. Morley, B.J. Adams and S. Chesworth, 11/17/08 (PB2010-100927).
- MCEER-08-0024 “Remote Sensing for Resilient Multi-Hazard Disaster Response – Volume V: Integration of Remote Sensing Imagery and VIEWS™ Field Data for Post-Hurricane Charley Building Damage Assessment,” by J.A. Womble, K. Mehta and B.J. Adams, 11/17/08 (PB2009-115532).
- MCEER-08-0025 “Building Inventory Compilation for Disaster Management: Application of Remote Sensing and Statistical Modeling,” by P. Sarabandi, A.S. Kiremidjian, R.T. Eguchi and B. J. Adams, 11/20/08 (PB2009-110484).
- MCEER-08-0026 “New Experimental Capabilities and Loading Protocols for Seismic Qualification and Fragility Assessment of Nonstructural Systems,” by R. Retamales, G. Mosqueda, A. Filiatrault and A. Reinhorn, 11/24/08 (PB2009-110485).
- MCEER-08-0027 “Effects of Heating and Load History on the Behavior of Lead-Rubber Bearings,” by I.V. Kalpakidis and M.C. Constantinou, 12/1/08 (PB2009-115533).
- MCEER-08-0028 “Experimental and Analytical Investigation of Blast Performance of Seismically Resistant Bridge Piers,” by S.Fujikura and M. Bruneau, 12/8/08 (PB2009-115534).
- MCEER-08-0029 “Evolutionary Methodology for Aseismic Decision Support,” by Y. Hu and G. Dargush, 12/15/08.
- MCEER-08-0030 “Development of a Steel Plate Shear Wall Bridge Pier System Conceived from a Multi-Hazard Perspective,” by D. Keller and M. Bruneau, 12/19/08 (PB2010-102696).
- MCEER-09-0001 “Modal Analysis of Arbitrarily Damped Three-Dimensional Linear Structures Subjected to Seismic Excitations,” by Y.L. Chu, J. Song and G.C. Lee, 1/31/09 (PB2010-100922).
- MCEER-09-0002 “Air-Blast Effects on Structural Shapes,” by G. Ballantyne, A.S. Whittaker, A.J. Aref and G.F. Dargush, 2/2/09 (PB2010-102697).
- MCEER-09-0003 “Water Supply Performance During Earthquakes and Extreme Events,” by A.L. Bonneau and T.D. O’Rourke, 2/16/09 (PB2010-100923).
- MCEER-09-0004 “Generalized Linear (Mixed) Models of Post-Earthquake Ignitions,” by R.A. Davidson, 7/20/09 (PB2010-102698).
- MCEER-09-0005 “Seismic Testing of a Full-Scale Two-Story Light-Frame Wood Building: NEESWood Benchmark Test,” by I.P. Christovasilis, A. Filiatrault and A. Wanitkorkul, 7/22/09 (PB2012-102401).
- MCEER-09-0006 “IDARC2D Version 7.0: A Program for the Inelastic Damage Analysis of Structures,” by A.M. Reinhorn, H. Roh, M. Sivaselvan, S.K. Kunnath, R.E. Valles, A. Madan, C. Li, R. Lobo and Y.J. Park, 7/28/09 (PB2010-103199).
- MCEER-09-0007 “Enhancements to Hospital Resiliency: Improving Emergency Planning for and Response to Hurricanes,” by D.B. Hess and L.A. Arendt, 7/30/09 (PB2010-100924).

- MCEER-09-0008 "Assessment of Base-Isolated Nuclear Structures for Design and Beyond-Design Basis Earthquake Shaking," by Y.N. Huang, A.S. Whittaker, R.P. Kennedy and R.L. Mayes, 8/20/09 (PB2010-102699).
- MCEER-09-0009 "Quantification of Disaster Resilience of Health Care Facilities," by G.P. Cimellaro, C. Fumo, A.M. Reinhorn and M. Bruneau, 9/14/09 (PB2010-105384).
- MCEER-09-0010 "Performance-Based Assessment and Design of Squat Reinforced Concrete Shear Walls," by C.K. Gulec and A.S. Whittaker, 9/15/09 (PB2010-102700).
- MCEER-09-0011 "Proceedings of the Fourth US-Taiwan Bridge Engineering Workshop," edited by W.P. Yen, J.J. Shen, T.M. Lee and R.B. Zheng, 10/27/09 (PB2010-500009).
- MCEER-09-0012 "Proceedings of the Special International Workshop on Seismic Connection Details for Segmental Bridge Construction," edited by W. Phillip Yen and George C. Lee, 12/21/09 (PB2012-102402).
- MCEER-10-0001 "Direct Displacement Procedure for Performance-Based Seismic Design of Multistory Woodframe Structures," by W. Pang and D. Rosowsky, 4/26/10 (PB2012-102403).
- MCEER-10-0002 "Simplified Direct Displacement Design of Six-Story NEESWood Capstone Building and Pre-Test Seismic Performance Assessment," by W. Pang, D. Rosowsky, J. van de Lindt and S. Pei, 5/28/10 (PB2012-102404).
- MCEER-10-0003 "Integration of Seismic Protection Systems in Performance-Based Seismic Design of Woodframed Structures," by J.K. Shinde and M.D. Symans, 6/18/10 (PB2012-102405).
- MCEER-10-0004 "Modeling and Seismic Evaluation of Nonstructural Components: Testing Frame for Experimental Evaluation of Suspended Ceiling Systems," by A.M. Reinhorn, K.P. Ryu and G. Maddaloni, 6/30/10 (PB2012-102406).
- MCEER-10-0005 "Analytical Development and Experimental Validation of a Structural-Fuse Bridge Pier Concept," by S. El-Bahey and M. Bruneau, 10/1/10 (PB2012-102407).
- MCEER-10-0006 "A Framework for Defining and Measuring Resilience at the Community Scale: The PEOPLES Resilience Framework," by C.S. Renschler, A.E. Frazier, L.A. Arendt, G.P. Cimellaro, A.M. Reinhorn and M. Bruneau, 10/8/10 (PB2012-102408).
- MCEER-10-0007 "Impact of Horizontal Boundary Elements Design on Seismic Behavior of Steel Plate Shear Walls," by R. Purba and M. Bruneau, 11/14/10 (PB2012-102409).
- MCEER-10-0008 "Seismic Testing of a Full-Scale Mid-Rise Building: The NEESWood Capstone Test," by S. Pei, J.W. van de Lindt, S.E. Pryor, H. Shimizu, H. Isoda and D.R. Rammer, 12/1/10 (PB2012-102410).
- MCEER-10-0009 "Modeling the Effects of Detonations of High Explosives to Inform Blast-Resistant Design," by P. Sherkar, A.S. Whittaker and A.J. Aref, 12/1/10 (PB2012-102411).
- MCEER-10-0010 "L'Aquila Earthquake of April 6, 2009 in Italy: Rebuilding a Resilient City to Withstand Multiple Hazards," by G.P. Cimellaro, I.P. Christovasilis, A.M. Reinhorn, A. De Stefano and T. Kirova, 12/29/10.
- MCEER-11-0001 "Numerical and Experimental Investigation of the Seismic Response of Light-Frame Wood Structures," by I.P. Christovasilis and A. Filiatrault, 8/8/11 (PB2012-102412).
- MCEER-11-0002 "Seismic Design and Analysis of a Precast Segmental Concrete Bridge Model," by M. Anagnostopoulou, A. Filiatrault and A. Aref, 9/15/11.
- MCEER-11-0003 "Proceedings of the Workshop on Improving Earthquake Response of Substation Equipment," Edited by A.M. Reinhorn, 9/19/11 (PB2012-102413).
- MCEER-11-0004 "LRFD-Based Analysis and Design Procedures for Bridge Bearings and Seismic Isolators," by M.C. Constantinou, I. Kalpakidis, A. Filiatrault and R.A. Ecker Lay, 9/26/11.

- MCEER-11-0005 “Experimental Seismic Evaluation, Model Parameterization, and Effects of Cold-Formed Steel-Framed Gypsum Partition Walls on the Seismic Performance of an Essential Facility,” by R. Davies, R. Retamales, G. Mosqueda and A. Filiatrault, 10/12/11.
- MCEER-11-0006 “Modeling and Seismic Performance Evaluation of High Voltage Transformers and Bushings,” by A.M. Reinhorn, K. Oikonomou, H. Roh, A. Schiff and L. Kempner, Jr., 10/3/11.
- MCEER-11-0007 “Extreme Load Combinations: A Survey of State Bridge Engineers,” by G.C. Lee, Z. Liang, J.J. Shen and J.S. O’Connor, 10/14/11.
- MCEER-12-0001 “Simplified Analysis Procedures in Support of Performance Based Seismic Design,” by Y.N. Huang and A.S. Whittaker.
- MCEER-12-0002 “Seismic Protection of Electrical Transformer Bushing Systems by Stiffening Techniques,” by M. Koliou, A. Filiatrault, A.M. Reinhorn and N. Oliveto, 6/1/12.
- MCEER-12-0003 “Post-Earthquake Bridge Inspection Guidelines,” by J.S. O’Connor and S. Alampalli, 6/8/12.
- MCEER-12-0004 “Integrated Design Methodology for Isolated Floor Systems in Single-Degree-of-Freedom Structural Fuse Systems,” by S. Cui, M. Bruneau and M.C. Constantinou, 6/13/12.
- MCEER-12-0005 “Characterizing the Rotational Components of Earthquake Ground Motion,” by D. Basu, A.S. Whittaker and M.C. Constantinou, 6/15/12.
- MCEER-12-0006 “Bayesian Fragility for Nonstructural Systems,” by C.H. Lee and M.D. Grigoriu, 9/12/12.
- MCEER-12-0007 “A Numerical Model for Capturing the In-Plane Seismic Response of Interior Metal Stud Partition Walls,” by R.L. Wood and T.C. Hutchinson, 9/12/12.
- MCEER-12-0008 “Assessment of Floor Accelerations in Yielding Buildings,” by J.D. Wieser, G. Pekcan, A.E. Zaghi, A.M. Itani and E. Maragakis, 10/5/12.
- MCEER-13-0001 “Experimental Seismic Study of Pressurized Fire Sprinkler Piping Systems,” by Y. Tian, A. Filiatrault and G. Mosqueda, 4/8/13.
- MCEER-13-0002 “Enhancing Resource Coordination for Multi-Modal Evacuation Planning,” by D.B. Hess, B.W. Conley and C.M. Farrell, 2/8/13.
- MCEER-13-0003 “Seismic Response of Base Isolated Buildings Considering Pounding to Moat Walls,” by A. Masroor and G. Mosqueda, 2/26/13.



**EARTHQUAKE ENGINEERING TO EXTREME EVENTS**

University at Buffalo, The State University of New York

133A Ketter Hall ■ Buffalo, New York 14260-4300

Phone: (716) 645-3391 ■ Fax: (716) 645-3399

Email: [mceer@buffalo.edu](mailto:mceer@buffalo.edu) ■ Web: <http://mceer.buffalo.edu>



**University at Buffalo** *The State University of New York*

ISSN 1520-295X